THEORETICAL STUDIES OF ELECTRONIC, VIBRATIONAL, AND MAGNETIC PROPERTIES OF CHEMISORBED SURFACES AND NANOALLOYS

by

MARISOL ALCÁNTARA ORTIGOZA

B.S., Universidad Nacional Autónoma de México, 2001

AN ABSTRACT OF A DISSERTATION

submitted in partial fulfillment of the
requirements for the degree

DOCTOR OF PHILOSOPHY

Department of Physics
College of Arts and Sciences

KANSAS STATE UNIVERSITY
Manhattan, Kansas
2007

Abstract

In this work we present a study of the geometric, electronic, vibrational and magnetic properties of several nanostructured systems for which experimental data call for a theoretical understanding. In order to investigate the effect of magnetic dipolar interactions on the magnetization of nanomagnets arranged in finite lattices, we utilize a phenomenological classical approach, which is based on the Landau-Lifshitz equation. Dipolar interactions lead to hysteretic behavior of the magnetization curves and established that the external field sweep rate, sample temperature, and shape anisotropy play a role in determining the specifics. Our results (derived from a classical approach) for magnets arranged in a square lattice suggest that stepped hysteresis curves do not have necessarily a quantum origin (quantum tunneling of the magnetization). We also find that in the square lattice small changes in the dipolar strength introduce sudden transitions in the magnetic hysteresis. For the examination of geometric vibrational and electronic structure of systems of interest, we turn to density functional theory (DFT), which is the leading technique for modeling nanoscale systems from first principles. We have applied DFT to either address some *old* queries of surface science, such as the dynamics of the CO-chemisorbed $Cu(001)$ surface, or to contribute to the forefront of hydrogen-based economy through the comprehension of the growth and diffusion of Pt islets on $Ru(0001)$, or to predict the geometric and electronic properties of materials to-be-created, as in the case of core-shell bimetallic nanoclusters. In the case of CO on $Cu(001)$, although the bond has been considered to be weak enough so as to treat the adsorbate and substrate separately, our calculations are able to reproduce measurements and provide evidence that the dynamics of the molecule is influenced by the substrate and vice versa, as well as by intermolecular interactions. Taking into account the adsorbate-substrate interplay, has furthermore clarified issues that were pending for the

clean surface and led to the correct interpretation of some features in the phonon dispersion of the chemisorbed surface. DFT has also directed us to the conclusion that the catalytic properties of few-atom Pt islets on Ru nanoclusters are preserved by the low probability of these islets to diffuse through the edges of the Ru nanoclusters. Moreover, the analysis of the $Ag_{27}Cu_7$ nanoalloy from *ab initio* methods has opened a wide panorama in terms of the geometry, coordination, energetics, and electronic structure of alloyed phases, in general, that may aid in the assembling on new materials.

THEORETICAL STUDIES OF ELECTRONIC, VIBRATIONAL, AND MAGNETIC PROPERTIES CHEMISORBED SURFACES AND NANOALLOYS

by

MARISOL ALCÁNTARA ORTIGOZA

B.S., Universidad Nacional Autónoma de México, 2001

A DISSERTATION

submitted in partial fulfillment of the
requirements for the degree

DOCTOR OF PHILOSOPHY

Department of Physics
College of Arts and Sciences

KANSAS STATE UNIVERSITY
Manhattan, Kansas
2007

Approved by:

Major Professor
Talat S. Rahman

Abstract

In this work we present a study of the geometric, electronic, vibrational and magnetic properties of several nanostructured systems for which experimental data call for a theoretical understanding. In order to investigate the effect of magnetic dipolar interactions on the magnetization of nanomagnets arranged in finite lattices, we utilize a phenomenological classical approach, which is based on the Landau-Lifshitz equation. Dipolar interactions lead to hysteretic behavior of the magnetization curves and established that the external field sweep rate, sample temperature, and shape anisotropy play a role in determining the specifics. Our results (derived from a classical approach) for magnets arranged in a square lattice suggest that stepped hysteresis curves do not have necessarily a quantum origin (quantum tunneling of the magnetization). We also find that in the square lattice small changes in the dipolar strength introduce sudden transitions in the magnetic hysteresis. For the examination of geometric vibrational and electronic structure of systems of interest, we turn to density functional theory (DFT), which is the leading technique for modeling nanoscale systems from first principles. We have applied DFT to either address some *old* queries of surface science, such as the dynamics of the CO-chemisorbed $Cu(001)$ surface, or to contribute to the forefront of hydrogen-based economy through the comprehension of the growth and diffusion of Pt islets on $Ru(0001)$, or to predict the geometric and electronic properties of materials to-be-created, as in the case of core-shell bimetallic nanoclusters. In the case of CO on $Cu(001)$, although the bond has been considered to be weak enough so as to treat the adsorbate and substrate separately, our calculations are able to reproduce measurements and provide evidence that the dynamics of the molecule is influenced by the substrate and vice versa, as well as by intermolecular interactions. Taking into account the adsorbate-substrate interplay, has furthermore clarified issues that were pending for the

clean surface and led to the correct interpretation of some features in the phonon dispersion of the chemisorbed surface. DFT has also directed us to the conclusion that the catalytic properties of few-atom Pt islets on Ru nanoclusters are preserved by the low probability of these islets to diffuse through the edges of the Ru nanoclusters. Moreover, the analysis of the $Ag_{27}Cu_7$ nanoalloy from *ab initio* methods has opened a wide panorama in terms of the geometry, coordination, energetics, and electronic structure of alloyed phases, in general, that may aid in the assembling on new materials.

Table of Contents

List of Figures

List of Tables

Acknowledgments

It is impossible to thank the many persons who made this work possible. But first and foremost, I would like to thank my major advisor, Prof. Talat S. Rahman, for accepting me in her research group at adverse times during my stay in KSU and opening a whole new thrilling world to me. I wish to thank her for her indefatigable spirit to keep that world spinning, her humaneness, her generosity, her thoughtfulness, and her immeasurable support.

I am indebted to my group colleagues and collaborators for providing me an encouraging and enjoyable environment to learn and grow, and very especially to Dr. Ahlam Al-Rawi for the support and the friendship she has given me. I am also profoundly grateful to Prof. Sergey Stolbov for his patience, his sound advise, his great efforts to explain everything clearly and simply, and for the greatness he exudes through his respectfulness and humility. I want to thank also to Prof. Abdelkader Kara for his kind assistance and Dr. John Spangler, to whom I consider by far the best professor I had in KSU throughout my graduate coursework, for providing me help, support, and inspiration. I am extremely grateful as well to Dr. Richard A. Klemm for his guidance, his support, and his extraordinary dedication to get me started and to wrap up my first project. It is my pleasure to also thank Dr. Klaus Peter Bohnen for mentoring me, giving me the opportunity to work and learn within his research group in the Forschungszentrum Karlsruhe (FZK) and taking the time and effort to make the necessary arrangements for my visits. No less, I want to thank Dr. Rolf Heid for his kind assistance, his patience, and his always brisk willingness to help, teach, and discuss. I am also very grateful to Dr. Sampyo Hong, former student colleague and current group member, for his kindness and indispensable assistance in countless occasions. Thanks also for their friendship and support to my former student colleagues Dr. Chandana Ghosh, Dr. Altaf Karim, and Dr. Faisal Mehmood; my student colleagues Handan Yildirim and Duy Le; and student visitor Ghazal Sadatshafaie.

I thank the members of my supervisory committee, Prof. Gary Wysin, Prof. Mick O'Shea, Prof. Christer Aaekeroy, and Prof. Larry Glasgow. I also take this opportunity to thank my former advisor, Prof. Horacio Martínez Valencia, Prof. Alejandro Amaya Tapia, and Dr. Pedro G. Reyes Romero for helping me and encouraging me to start my PhD in Kansas State University.

My hearty acknowledgement to the support personnel in the Physics Department, Jane Peterson, Peggy Matthews, Barbara Steward, Treva Singleton, Deanna Selby, Kim Coy, and Lisa Zecha; to the secretary of the Institut für Festkörperphysik, Mrs. Edith Maass; to two members of the Hauptabteilung Personal und Soziales (FZK), Mr. Gerd A. Aye and Mrs. Rike Bosbach; and last, but not least, to the support personnel of the Physics Department in University of Central Florida Pat Korosec, Monika Crittenden, Angie Roman, and Micheal Jiménez.

I desire to express my gratitude as well to the National Science Foundation and the Department of Energy for funding part of my research through several grants. I am very grateful also to the Forschungszentrum Karlsruhe for financial support during my stays in Karlsruhe, Germany.

I want to express my profound gratitude to the International Student Center of Kansas State University, notably to Dr. Donna Davis and Linda Bottom.

It is difficult to describe my gratitude to my husband, Víctor Manuel Rojas Guzmán. With his sacrifice of self, his heroism, his infinite caring, his enthusiasm, his encouragement, and his endless patience, he has helped me not only to go through the present enterprise, but has given a reason to endure life.

I wish to thank with all my heart and soul Mr. Clifford Conrad for the immense help and the selfless friendship he has given me since the very first day I arrived to Manhattan, Kansas. Without his wisdom, his hospitality, his empathy, his warmth, and his extraordinary sense of humor, Manhattan would have been a desolate place for me and my husband.

Also, I am extremely grateful to Prof. Torry Dickinson and Prof. Robert Schaeffer for their friendship, support, and generosity. I will always be grateful to them for bringing back one part of my life that had been missing.

I wish to express my gratitude to Conductor Prof. David Littrell for giving me the unique opportunity to join Kansas State University Orchestra and thus letting me enjoy one of the most beautiful experiences that may take place on the face of Earth.

I want to manifest my thankfulness to my friends and great people I had the pleasure to meet along the way, Arlette and Paul Conrad, Prof. Salomón Itza Ortiz, M.S. Erin White Itza, Prof. Lyman Baker, Nameer Baker, Jeanette and Angie Olivan, Mr. and Mrs. Fleming, Prof. Martin Almada, Prof. Marcial Antonio Riquelme Enciso, M.S. Andrea Pérez Mudski, M.S. Eduardo Orozco, Dr. William Windfield, Dwarka Klemm, Prof. Remigio Cabrera Trujillo, Dr. Luz María Díaz Rivera, Olga and Anna Stolbova, Omar de la Peña Seaman, Janet Vanessa Ruelas, Dr. Irina Sklyadneva, Prof. Bothina Hamad, Prof. Werner Keune, Mrs. Ingeborg Keune, Ernesto González, Juan Carlos Arteaga, and Karen S. Caballero Mora.

I thank the Rojas Guzmán family and the González del Ángel family, and particularly Arq. Ares Camacho Robles. Lastly, and most importantly, I wish to thank to my parents - Miguel Ángel Alcántara Sandoval and Ernestina Ortigoza Aranda - and my siblings - Miguel Ángle, Miguel Alonso, and Mariana - all of whom raised me, taught me, supported me, and loved me.

Dedication

To those friends and beloved ones who left this painful world during my journey and whom I could not say good-bye:

Guadalupe Sandoval Berrios de Alcántara

Graciela Alcántara Sandoval

Teacher Francisco Samuel Rojas Hernández

Professor Marcial Antonio Riquelme Enciso

To my husband:

Víctor Manuel Rojas Guzmán

To my parents:

Ernestina Ortigoza Aranda de Alcántara

and

Miguel Ángel Alcántara Sandoval

To my siblings:

Miguel Ángel, Miguel Alonso, Mariana, Marina Estefanía, and Miguel Sebastián

Preface

Provided that the mission of condensed matter physics is to understand the phenomena that emerge when a large number of nuclei and electrons interact with one another, it becomes understandable that such a discipline embraces an endless range of problems. Along with the desired comprehension of the world around us, there exists an unavoidable eagerness to manipulate these constituents to satisfy all sorts of human needs. Proof of the above is the fact that this year's physics Nobel Prize was awarded for the technology that is used to read data on hard disks and which made possible a striking miniaturization of hard disks. What is more, the 2007 Nobel Prize in chemistry has been awarded to Gerhard Ertl for his lifetime work in setting the foundation and development of modern surface chemistry. Surface science has seen its major advances over the last four decades. It involves, for instance, surface reconstruction, surface vibrations, chemical reactions, and catalysis at interfaces, hence playing a vital role in many processes, from the nitrogen fixation to fertilize the soil, to the reduction of pollutants contained in exhaust gases from vehicles and industries, to the hydrogen-based economy. There is, of course, a huge number of fundamental challenges inherent to these disciplines. In terms of the applicability of single-molecule-magnets as prospective memory devices, for example, serious problem arise from the memory loss due to the relaxation of the magnetization. This occurs mainly as a consequence of the one-body quantum tunneling of the magnetization but also from pair magnetic dipolar and exchange interactions which may be controllable. Moreover, energy converters and exhaust catalytic converters are exposed unavoidably to carbon monoxide molecules that poison their activity. For that reason, an unceasing search continues in order to find and understand catalysts that better manipulate, remove, or tolerate carbon monoxide. In the above spirit, the aim of our work is to combine experimental investigations with our computational studies, in order to contribute to the effort of disentangling part of these issues. Naturally, the character of the information that one wants to extract, the scope that one desires to reach, and the

resources that one can afford, determine the approach to be followed.

The atomistic modeling of matter is an enormously growing field. Its importance not only has been recognized in academia but also has largely reached industry and, most importantly, is nowadays pursuing aspects directly related to the human survival such as health and the environmental problems aforementioned.[1–3] Its central purpose is to provide means to "reproduce" experiments and isolate phenomena under highly controlled circumstances, so that real experiments may be understood. We shall see that part of the work presented here (Chapter 3, 5, and 6), for instance, falls within this category. The rest concerns another major use (Chapter 4) of the atomic modeling; namely, although most of the existing results obtained via atomistic modeling have been performed on the basis of experimental evidence, known materials, and observed phenomena; prediction of material with specific properties is becoming one of the most important aims and successful applications of this approach. Furthermore, some research quests are such that accomplishing related experiments is extremely difficult and/or expensive. The comprehension of the structural phases and dynamics of the interior of the Earth, for instance, stands among these cases since related experiments must deal with extremely high pressures difficult to reach in the laboratory,[4] whereas "reaching" high pressures with the atomistic modeling is a trivial task for solids as it only requires to reduce the corresponding lattice parameter. Modeling is also useful because it allows us to obtain fast answers as, for example, the crystal structure of a material, which represents a lengthy task for experimentalists.

It is important to note that modeling is not the same as simulating; simulation of reality - strictly speaking - is something that atomistic modeling cannot do. Rather, what atomistic modeling does is to isolate parts of reality, the parts that one considers important, and perform computations on those. As clearly exemplified in Chapter 5, it means that very often one has to make judgments of what parts of reality one would like to isolate to establish a reasonable model of reality. Indeed, the hardest part of computing is to know what to compute and to use the tools in a clever way.

The first step to adequately apply a particular modeling technique is to decide on the proper energetic description to be used in order to know whether the results generated by a given computation are reliable or even relevant. Typically, people distinguish three classes of modeling techniques: empirical or phenomenological,[5] semiempirical,[6] and *ab initio* or first principles,[7] or sometimes also called quantum mechanical models. Basically, these are three energy models that provide different approaches to the description of matter and thus must be used accordingly to the pursued objective. For example, to study the effect of magnetic dipolar interactions in the magnetization of finite arrays, first principles calculations are still prohibitively complex. The microscopic nature of the energy dissipation is still not clear and represents to date the focus of considerable research.[8–10] For that reason, in the case of magnetic dipolar interactions (Chapter 3), we use the phenomenological classical equation developed by Landau and Lifshitz[11] (later modified by Gilbert[12]), where the magnetization rate depends on an unknown damping parameter α that must be obtained experimentally but which provides a means to compare - at least qualitatively - measurements with theoretical calculations for different materials under various experimental conditions. Chapter 1 is thus devoted to present the Landau-Lifshitz and Landau-Lifshitz-Gilbert equations. We remark that rather complex explicit expressions for α for the different system of local spin moments arising from $p-d$ kinetic-exchange coupling of the itinerant-spin subsystem in ferromagnetic semiconductor alloys have been given recently and started opening a window for *ab initio* calculations.[10] However, to date, the damping coefficient α at a particular T value must be determined experimentally for each system.

The idea of empirical models for total energy calculations, on the other hand, is to take some form for the energy and fit it to any data one may have (sometimes that set of data is quantum mechanically computed). First principles studies, in contrast, leave the fitting aside and solve the Schrödinger equation for whatever problem is confronted. Yet, one may also use methods in between, semiempirical, which are essentially quantum mechanical informed but empirical in the parameters. The tight binding method,[13] for

example, fits into this category since we can think of it as parameterized solutions of the Schrödinger equation, that is, where the overlap integrals between wavefunction are not computed but are parameterized, saving computational time significantly. In the work related to the structure, energetics, and vibrational and electronic properties of chemisorbed surfaces and nanoalloys (Chapters 4 - 6), however, first principles calculations are feasible and also necessary to attain the desired information. Indeed, in modern computational material science and material applications, the first principles Density Functional Theory[7] (DFT) represents to date the most important and reliable tool to model a vast diversity of materials and phenomena. The purpose of Chapter 2 is therefore to provide an overview of the physics involved in DFT.

This dissertation is divided in four major subjects distributed in Chapters 3 - 6. In Chapter 3, we investigate the effect of interparticle dipolar interactions on three-dimensional and two dimensional ensembles magnets, each with spin $S = 5$, arranged in a cubic and squared lattice, respectively. In the case of the three and two dimensional systems, an array of $5 \times 5 \times 4$ and 5×5 magnets are considered, respectively. We employed the Landau-Lifshitz equation to solve for the magnetization curves for several values of the damping constant, the induction sweep rate, the lattice constant, the sample temperature, and the magnetic anisotropy.[14] Chapter 4 presents our *ab initio* calculations of the structure and electronic density of states (DOS) of the perfect core-shell $Ag_{27}Cu_7$ nanoalloy. Analysis of bond-length, average formation energy, heat of formation of $Ag_{27}Cu_7$ and $L1_2$ $Ag - Cu$ alloys are performed to provide an explanation for the relative structural and electronic stability of the former with respect to the other nanoalloys in the same family,[15] which may render $Ag_{27}Cu_7$ as a building block of novel materials or as a key model leading us to recognize the *ingredients* to create materials with specific properties. Analysis of the DOS of $Ag_{27}Cu_7$, $L1_2$ $Ag - Cu$ alloys and related systems provides insight into the effects of low coordination, contraction/expansion and the presence of foreign atoms on the DOS of Cu and Ag. Charge density plots of $Ag_{27}Cu_7$ are examined to attest the results drawn

from energetic and electronic structure considerations. The purpose of Chapter 5 is to initiate a study of the high carbon-monoxide-tolerance of recently synthesized Pt islets deposited on $Ru(0001)$ - in the course of their performance as hydrogen-oxidation catalyst - by carrying out first principles calculations of the geometry and energetics of the Pt atoms adsorbed on the $Ru(0001)$. We also calculate the energy barriers for diffusion of Pt monomers and dimers on the facets and through the edges of a superstructure modeling a Ru to understand the role played by the edges of Ru nanoparticles into the distribution of Pt atoms over Ru nanoparticles. Finally, in Chapter 6, the density functional perturbation theory formalism is applied to investigate the dynamics of one of the pioneering systems that has served to comprehend the coupling between molecules and metallic surfaces, namely, c(2x2)-CO/Cu(100). Knowledge of the vibrational dynamics of the system is a prerequisite[16] to obtain the preexponential factors[17] that determine the rate constants of carbon monoxide for diffusion, desorption, and dissociation, for instance. Such information, in turn, is thus closely related to the catalytic reactions mentioned above. Our calculated phonon dispersion is compared with Helium Atom Scattering data. Softening of the surface Rayleigh wave is addressed regarding the effect of CO on interlayer relaxations, changes in the force constants, and effects in other surface modes with respect to the clean surface.

Chapter 1

Theoretical Methods I : Magnetic Dynamics

1.1 Introduction : The phenomenological theory of Magnetic Precession Damping

Technological problems of interest for magnetic materials include reducing energy losses due to damping and developing materials with higher rates of remagnetization for weak driving fields.[12] The latter problem was of particular interest in the 1950's because at that time the so-called core-memory device (by Papian and Forrester) - which crystallized the random access memory (RAM) concept and preceded the RAM chip - was based on the switching of the magnetization of ferrite cores by electric currents and one of its major drawbacks was that reading is a destructive process. So every read access must be followed by a re-write access to retain the information, becoming a limiting factor for the computation rate.[12]

The rate of remagnetization in a ferromagnet is determined by damping mechanisms.[12] Damping of a physical system is accompanied by a deceleration of the macroscopic motion and a transfer of the kinetic and potential energy associated with macroscopic motion to kinetic energy of microscopic thermal motion (heat energy).[12] For a magnetization field, this can be through direct transfer of the energy of macroscopic motion to the energy of microscopic thermal motion in spin waves or by transfer of macroscopic energy of the magnetization field to other fields to which it is coupled, e.g., coupling of the magnetization

field to spin waves, eddy currents,[1] and lattice vibrations, and the effects of polycrystalline structure, strains, and crystal defects such as voids, interstitial atoms, and impurity atoms. [12] Within ferromagnets, when the external magnetic field is not strong enough to eliminate all domain walls,[2] the domain structure plays a leading role in the damping and the local rate of energy loss may vary by large amounts from point to point.[12]

As of 1955, a number of different damping mechanisms had been studied but (except for eddy currents in metallic ferromagnets) the dominant mechanisms had not yet been identified.[12] The Landau-Lifshitz phenomenological damping term in common use in 1955 could be used when the damping was small, but encountered problems for large damping.[12] In order to identify and understand the dominant damping mechanisms, Gilbert provided a new approach to the phenomenological theory by Landau-Lifshitz of the magnetic precession damping, which I will follow in the subsequent sections. Both approaches converge in the limit of small damping, as we shall see. The work was done in his PhD thesis (unpublished) in 1956 and reviewed later in 2004.[12]

By extending to electronic spin systems the Wangsness-Bloch model of nuclear spin magnetic relaxation by magnetic dipole coupling to a heat bath,[18] Fredkin and Ron showed that the damping term could be derived for large spin values and $\kappa = \hbar\gamma H/k_B T \ll 1$, where $\hbar$ and k_B are Planck's constant divided by 2π and Boltzmanns' constant, respectively, and in our case $H = B_i^{c,\text{eff}}$.[19] To the extent that electric quadrupole interactions could be neglected, α varies inversely with T for $\kappa \ll 1$, but depends upon κ otherwise.[19] More recently, a different derivation of the Gilbert damping term was derived from a spin Hamiltonian containing the interaction between the spin and the radiation field, which is induced by the precessing magnetization itself.[8,9] In that case, no explicit T dependence of α was given.

[1] An eddy current is that caused within a conductor when it moves across a stationary magnetic field, as well as when it is stationary and encounters a varying magnetic field. The current creates electromagnets with magnetic fields that oppose the effect of the applied magnetic field (Lenz's law). The stronger the applied magnetic field, the greater the greater the currents developed and the greater the opposing field.

[2] A domain wall is an interface separating magnetic domains, that is, a region within a material which has uniform magnetization.

1.2 Larmor Precession: Undamped and uncoupled magnetization in an external magnetic flux density

The starting point to understand magnetization processes is the phenomenological theory of the Larmor precession, which refers to the precession of the magnetic moment of a particle about the direction of an undamped and uncoupled magnetization field.[3] Classically, if a current density $\boldsymbol{J}(\boldsymbol{x})$ is in an external magnetic-flux density $\boldsymbol{B}(\boldsymbol{x})$, it experiences forces and torques according to Ampères's laws. The elementary torque law implies that the total torque on the current distribution is[20]

$$\boldsymbol{N} = \frac{d\boldsymbol{L}}{dt} = \int \boldsymbol{x} \times (\boldsymbol{J} \times \boldsymbol{B})\, d^3x \tag{1.1}$$

The angular momentum, $\boldsymbol{L}$, is defined as $\boldsymbol{L} = \boldsymbol{I} \cdot \boldsymbol{\omega}$, where $\boldsymbol{I}$ is the inertia tensor and $\boldsymbol{\omega} = [\omega_i]$ is a vector along the axis of rotation. The magnitude of $\boldsymbol{\omega}$ is $\omega = \frac{d\psi}{dt}$, where ψ is the angle between two lines perpendicular to the axis of rotation, one fixed in the volume containing the localized current distribution and the other fixed in space. If the external magnetic induction varies slowly over the region of the current, a Taylor series expansion can be utilized to find the dominant terms in the torque.[20] A component of $\boldsymbol{B}$ can be expanded around a suitable origin,

$$B_x(\boldsymbol{x}) = B_k(0) + \boldsymbol{x} \cdot \boldsymbol{\nabla} B_k(0) + \ldots \tag{1.2}$$

By inserting (1.2) into (1.1), we get an expansion for the torque, where the zeroth-order term in the expansion contributes. Keeping only this leading term, we have[20]

$$N = \int \boldsymbol{x}' \times [\boldsymbol{J} \times \boldsymbol{B}(0)]\, d^3x' \tag{1.3}$$

Writing out the triple product, we get

$$N = \int [(\boldsymbol{x}' \cdot \boldsymbol{B})\boldsymbol{J} - (\boldsymbol{x}' \cdot \boldsymbol{J})\boldsymbol{B}]\, d^3x' \tag{1.4}$$

[3] An uncoupled field is a field for which there is no coupling to other fields, such as the elastic strain field. An undamped field is a field for which internal energy losses (transfer of energy from macroscopic motion to microscopic thermal motion) and energy loss by transfer of energy to other fields are neglected.

The second integral vanishes for a localized steady current distribution.[20] Then, according to the following relation for each Cartesian component[20]

$$\boldsymbol{B}(0)\cdot\int \boldsymbol{x}' J_i d^3x' \equiv -\frac{1}{2}[\boldsymbol{B}(0)\times\int(\boldsymbol{x}'\times\boldsymbol{J})\,d^3x']_i, \tag{1.5}$$

the first integral can be written as[20]

$$\int(\boldsymbol{x}'\cdot\boldsymbol{B})\boldsymbol{J}\,d^3x' = -\frac{1}{2}[\boldsymbol{B}(0)\times\int(\boldsymbol{x}'\times\boldsymbol{J})\,d^3x'], \tag{1.6}$$

The leading term in the torque is therefore

$$\boldsymbol{N} = \frac{d\boldsymbol{L}}{dt} = \boldsymbol{\mu}\times\boldsymbol{B}(0) \tag{1.7}$$

where $\boldsymbol{\mu}$ is the magnetic moment of a magnetic dipole:[20]

$$\boldsymbol{\mu} = \int(\boldsymbol{x}\times\boldsymbol{J})\,d^3x \tag{1.8}$$

An angular moment is also associated with the current density $\boldsymbol{J}(x)$. The proportionality constant between the magnetic dipole moment and the angular momentum of $\boldsymbol{J}$ is known as the gyromagnetic ratio, γ,

$$\boldsymbol{\mu} = \gamma\boldsymbol{L} \tag{1.9}$$

Combining (1.8) and (1.9), we obtain that

$$\frac{d\boldsymbol{\mu}}{dt} = \gamma\,\boldsymbol{\mu}\times\boldsymbol{B}, \tag{1.10}$$

The first identity of Eq.1.1 remains valid in quantum mechanics when $\boldsymbol{L}$ and $\boldsymbol{N}$ are reinterpreted as operators in a Hilbert space, and can be used for spin systems by replacing the orbital angular momentum operator with the operator for the angular momentum associated with an electron spin.

The role of spin in the one-electron Dirac's theory is brought into focus if we evaluate the time derivative of the four-dimensional analogues of the Pauli spin matrices, $\boldsymbol{\sigma}$, for an electron exposed to a vector potential $\boldsymbol{A}$ but no potential ϕ .[21] Its Hamiltonian is thus given by[21]

$$H = c\boldsymbol{\alpha}\cdot(\boldsymbol{p}+\frac{e}{c}\boldsymbol{A}) + \beta mc^2 \tag{1.11}$$

where c is the speed of light; e, m, and $\boldsymbol{p}$ are the charge, mass and momentum of the electron; and $\boldsymbol{\alpha}$ and β are 4x4 matrices specified in terms of the 2x2 Pauli matrices; which in the *standard representation* are expressed as[21]

$$\boldsymbol{\alpha} = \begin{pmatrix} 0 & \boldsymbol{\sigma} \\ \boldsymbol{\sigma} & 0 \end{pmatrix},$$

$$\beta = \begin{pmatrix} \mathbf{1} & 0 \\ 0 & \mathbf{1} \end{pmatrix},$$

By a sequence of algebraic manipulations, it is possible to obtain that[21]

$$H\frac{d\boldsymbol{\Sigma}}{dt} + \frac{d\boldsymbol{\Sigma}}{dt}H = -2ec\boldsymbol{\Sigma} \times \boldsymbol{B} \tag{1.12}$$

where

$$\boldsymbol{\Sigma} = \begin{pmatrix} \boldsymbol{\sigma} & 0 \\ 0 & \boldsymbol{\sigma} \end{pmatrix},$$

In the nonrelativistic approximation $H \approx mc^2$, thus, the equation of motion for the one-electron spin operator $\boldsymbol{S} = \frac{\hbar}{2}\boldsymbol{\Sigma}$ becomes[21]

$$\frac{d\boldsymbol{S}}{dt} = -\frac{e}{mc}\boldsymbol{S} \times \boldsymbol{B} \tag{1.13}$$

A straightforward interpretation of this equation may be given: The time rate of the intrinsic angular momentum (spin) equals the torque produced by the applied magnetic filed. If a magnetic moment $\boldsymbol{\mu}$ is associated with the spin, the torque is $\boldsymbol{\mu} \times \boldsymbol{B}$.[21] Comparison with (1.13) shows that in the nonrelativistic approximation the magnetic moment operator for an electron is[21]

$$\boldsymbol{\mu} = -\frac{e}{mc}\boldsymbol{S} = -\frac{e}{2mc}g_s\boldsymbol{S} = \gamma_e\boldsymbol{S} \tag{1.14}$$

where γ_e is the gyromagnetic ratio of electrons and g_s is the electron spin g -factor; which, except for small radiative corrections, the value $g_s = 2$, is in agreement with the experimental measurements.[21]

In brief, one can obtain for electrons an equation parallel to that obtained in classical electrodynamics for the magnetic dipole moment of a current charge density, with the

gyromagnetic ratio for an electron spin,

$$\frac{d\boldsymbol{\mu}}{dt} = \gamma_e \boldsymbol{\mu} \times \boldsymbol{B}. \tag{1.15}$$

Thereby, from here on, no subscript will be used for the gyromagnetic ratio

1.3 Landau-Lifshitz equation

The first dynamic model for the precessional motion of the magnetization (or magnetic moment density) was proposed by Landau and Lifshitz in 1935. They suggested that the external magnetic field of Eq. (1.10) should take into account quantum-mechanical and anisotropy effects by means of an effective field $\boldsymbol{B}^{eff}$.[22] The applicability of Eq.1.10 is thus not limited to the torque exerted by an external magnetic field. Any torque on a magnetic moment, $\boldsymbol{M}$, can be written in the form of Eq.1.10 if we define an "effective" magnetic field,[12]

$$\boldsymbol{B}^{eff} = -[\boldsymbol{i}\frac{\partial U(\boldsymbol{M})}{\partial M_x} + \boldsymbol{j}\frac{\partial U(\boldsymbol{M})}{\partial M_y} + \boldsymbol{k}\frac{\partial U(\boldsymbol{M})}{\partial M_z}] \equiv -\frac{\partial U(\boldsymbol{M})}{\partial \boldsymbol{M}}, \tag{1.16}$$

where $U(\boldsymbol{M})$ is the potential energy of the system with respect to the work done by rotating the moment against whatever forces are present. The potential energy for a magnetic moment $\boldsymbol{M}$ in a magnetic field $\boldsymbol{B}^{eff}$ has the form

$$U = -\boldsymbol{M} \cdot \boldsymbol{B}^{eff}. \tag{1.17}$$

For a discrete set of magnetic moments, $\boldsymbol{M}_i$, where $i = 1, 2, ., n$, the equations of motion become

$$\frac{d\boldsymbol{M_i}}{dt} = \gamma_e \boldsymbol{M_i} \times \boldsymbol{B}^{eff}. \tag{1.18}$$

where

$$\boldsymbol{B}_i^{eff} = -\partial U(\boldsymbol{M}_1, \boldsymbol{M}_2, ..., \boldsymbol{M}_n)/\partial \boldsymbol{M}_i \tag{1.19}$$

is the effective field acting on the $i_t h$ moment and $U(\boldsymbol{M}_1, \boldsymbol{M}_2, ., \boldsymbol{M}_n)$ is a generalized potential energy that takes into account all interactions that can exert torque on the individual moments.[12]

Equations (1.18) and (1.19), interpreted as classical equations for a system of discrete magnetic moments $\boldsymbol{M}_i$ at points $\boldsymbol{r}_i$ in space, can be transformed into classical field equations by introducing a continuous field $\boldsymbol{M}(\boldsymbol{r})$ and setting $\boldsymbol{M}(\boldsymbol{r}_i) = \boldsymbol{M}_i/\Delta(\boldsymbol{r}_i)$, where $\boldsymbol{r}_i$ is the location of a lattice cell within which an electron with an unpaired spin is localized and $\Delta(\boldsymbol{r}_i)$ is the volume of a lattice cell.[12][4] It is assumed that the field is smooth on an atomic scale, i.e., that it does not have any "wiggles" over distances smaller than a few lattice cells (other than discontinuities that may occur at crystal boundaries) or the wiggles can be smoothed out by averaging over several adjacent lattice cells.[12] Substituting $\boldsymbol{M}(\boldsymbol{r}_i) = \boldsymbol{M}_i/\Delta(\boldsymbol{r}_i)$ into (1.18) and (1.19) and going into the limit $\Delta(\boldsymbol{r}_i) \to 0$, discrete arrays of magnetic moments become magnetization fields, sums become integrals, functions, $F(\boldsymbol{M}_1, \boldsymbol{M}_2, ..., \boldsymbol{M}_n)$, of a discrete array of magnetic moments $\boldsymbol{M}_i$ become functionals, $F[\boldsymbol{M}(\boldsymbol{r})]$, of the continuous field $\boldsymbol{M}(\boldsymbol{r})$,[5] and partial derivatives, $\partial U(\boldsymbol{M}_1, \boldsymbol{M}_2, ., \boldsymbol{M}_n)/\partial \boldsymbol{M}_i$, become functional derivatives, $\delta F[\boldsymbol{M}(\boldsymbol{r})]/\delta \boldsymbol{M}(\boldsymbol{r})$, defined by (see Appendix A)

$$\delta F[\boldsymbol{M}(\boldsymbol{r})] = \int d\boldsymbol{r}' \frac{\delta F[\boldsymbol{M}(\boldsymbol{r})]}{\delta \boldsymbol{M}(\boldsymbol{r}')} \delta \boldsymbol{M}(\boldsymbol{r}'), \tag{1.20}$$

for arbitrary infinitesimal vector field $\delta \boldsymbol{M}(\boldsymbol{r})$. This leads to a classical equation of motion for an undamped magnetization field[12]

$$\frac{\partial \boldsymbol{M}(\boldsymbol{r}, t)}{\partial t} = \gamma \boldsymbol{M}(\boldsymbol{r}, t) \times \boldsymbol{B}(\boldsymbol{r}, t) \tag{1.21}$$

where

$$\boldsymbol{B}(\boldsymbol{r}, t) = -\frac{\delta U[\boldsymbol{M}(\boldsymbol{r}, t)]}{\delta \boldsymbol{M}(\boldsymbol{r}')} \tag{1.22}$$

[4]This step assumes a model for which the spins are in a lattice array and that electrons with unpaired spins can be assigned to localized orbitals in the lattice cells. The generalization of this model to amorphous solids becomes more complicated, but presents no conceptual problems. The model would not be applicable to electrons in conduction bands, for which the orbitals cannot be well-localized. However, the electrons with unpaired spins that contribute to the magnetization fields of ferromagnets are all in narrow energy bands corresponding to d and f orbitals for which a representation of the wave function for a crystal using localized orbitals is a good approximation. A rigorous justification of the model would require a general theory of localized orbitals in solids, which was not available in 1955.[12]

[5]A functional $F[f(x)]$ differs from a function $f(x)$ in that a particular value of a function $f(x)$ depends on a particular value of the numerically valued independent variable x, whereas a particular value of a functional $F[f(x)]$ depends on the entire set values of the function $f(x)$.

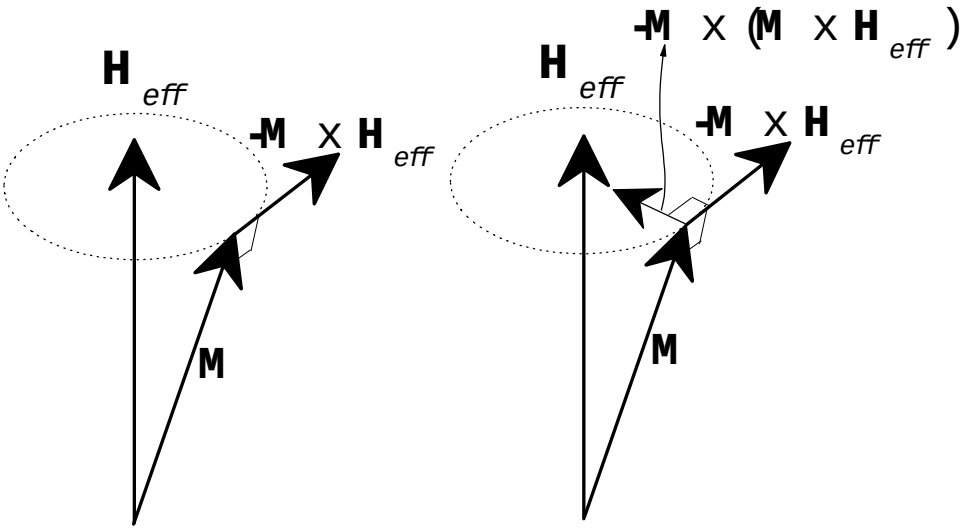

Figure 1.1: *(left) Undamped gyromagnetic precession (right) damped gyromagnetic precession proposed by Landau and Lifshitz*

is the effective field, and $U[\boldsymbol{M}(\boldsymbol{r},t)]$ is the generalized potential energy of the magnetization field.[12], which may include the energy of interaction with the external field, the demagnetizing energy, the exchange energy, the anisotropy energies, and the magnetoelastic energy. [12]

Substituting the external field by an effective field preserves the fact that the precessional dynamics of the magnetization results conservative, whereas, in reality, energy dissipation takes place within the dynamic magnetization processes. The potential energy of a magnetic moment (see Eq. 1.17) shows that it tends to orient itself parallel to the field in the position of lowest potential energy. Landau and Lifshitz introduced dissipation in a phenomenological way by considering an additional torque that aligns the magnetization in the direction of the effective field (see Fig.1.1). The additional torque is constructed so that the magnitude of the magnetization is preserved:

$$\frac{\delta \boldsymbol{M}}{\delta t} = -\gamma \boldsymbol{M} \times \boldsymbol{B}^{eff} - \frac{\lambda}{M} \boldsymbol{M} \times (\boldsymbol{M} \times \boldsymbol{B}^{eff}), \tag{1.23}$$

where $M = |\boldsymbol{M}|$ and λ is a phenomenological constant characteristic of the material.

1.4 Landau-Lifshitz-Gilbert equation

Details of the mechanisms for the transfer processes are too complex to be taken into account explicitly in the field equations. However, we can introduce into the field equations a phenomenological damping term that contains damping parameters that correspond to the rate of energy transfer and can be determined experimentally without knowing the details of the transfer mechanisms. The dependence of experimentally determined damping parameters on parameters that characterize different materials can often be used to identify the different mechanisms and how they might be controlled.[12] Damping of a physical system generates a force in opposition to the macroscopic driving force. When the two forces balance, the energy gain from the driving force is balanced by the energy loss from the damping force and a steady state is maintained.[12] If the damping force always increases or decreases as the rates of change of the dynamical variables that characterize the macroscopic motion increase or decrease, then when the driving force is constant the rates of change of the dynamical variables will increase or decrease until the driving and damping forces are equal and a steady-state condition is attained.[12] The simplest case, which commonly occurs when there are many different damping forces and resonance phenomena do not occur, is that the damping forces, $\boldsymbol{f}$, is directly proportional to the rates of change of the dynamical variables of the system.[12] For a system of discrete particles at positions $\{\boldsymbol{r}_i\}$, occupying a volume ΔV, and with a magnetic moment $\boldsymbol{M}(\boldsymbol{r_i}, t)\Delta V$, the dynamical variable is $\boldsymbol{M}(\boldsymbol{r}_i, t)$, $\psi = x, y, z$, and the damping forces are

$$\boldsymbol{f}(\boldsymbol{r}_i, t) = -\eta \frac{\partial \boldsymbol{M}(\boldsymbol{r}_i, t)}{\partial t}, \tag{1.24}$$

where η is a damping parameter characteristic of the material.

However, for the macroscopic magnetization field in which we are interested, they can be written as

$$\boldsymbol{f}(\boldsymbol{r}, t) = -\eta \frac{\partial \boldsymbol{M}(\boldsymbol{r}, t)}{\partial t} \tag{1.25}$$

A common way of introducing a damping term of this kind into classical equations of

motion for a physical system is to use a Lagrangian formulation of the equations of motion for the case when not all the forces acting on the system are derivable from a potential. In that case Lagrange equations for (1.24) can always be written in the form[23]

$$\frac{d}{dt}\Big(\frac{\partial L}{\partial \dot{\boldsymbol{M}}(\boldsymbol{r}_i,t)}\Big)-\frac{\partial L}{\delta \boldsymbol{M}(\boldsymbol{r}_i,t)}=\mathcal{Q}_i \tag{1.26}$$

or, for the macroscopic magnetization field, as

$$\frac{d}{dt}\Big(\frac{\delta L}{\delta \dot{\boldsymbol{M}}(\boldsymbol{r},t)}\Big)-\frac{\delta L}{\delta \boldsymbol{M}(\boldsymbol{r},t)}=\mathcal{Q} \tag{1.27}$$

where

$$L=T[\boldsymbol{M}(\boldsymbol{r},t),\dot{\boldsymbol{M}}(\boldsymbol{r},t)]-U[\boldsymbol{M}(\boldsymbol{r},t)] \tag{1.28}$$

is the Lagrangian containing the potential of the conservative forces, $\mathcal{Q}$ represents the forces in the not arising from a potential, and $\boldsymbol{M}(\boldsymbol{r},t)$ is the the dynamical variable. Damping forces as (1.24) may be derived in terms of a function $\mathcal{R}$, known as Rayleigh's dissipation function,[23] which for a system of discrete particles is defined as

$$\mathcal{R}=\frac{1}{2}\sum_i \eta\Big(\frac{\partial \boldsymbol{M}(\boldsymbol{r}_i,t)}{\partial t}\Big)^2, \tag{1.29}$$

while, for the macroscopic magnetization field in which we are interested, it becomes a functional(see Appendix A):

$$\mathcal{R}[\boldsymbol{M}]=\frac{\eta}{2}\int\int d\boldsymbol{r}'d\boldsymbol{r}\;\dot{\boldsymbol{M}}(\boldsymbol{r},t)\cdot\dot{\boldsymbol{M}}(\boldsymbol{r}',t)=\frac{\eta}{2}\Big(\int d\boldsymbol{r}'\dot{\boldsymbol{M}}(\boldsymbol{r}',t)\Big)\Big(\int d\boldsymbol{r}\dot{\boldsymbol{M}}(\boldsymbol{r},t)\Big)$$

$$=\frac{\eta}{2}\Big(\int d\boldsymbol{r}'\dot{\boldsymbol{M}}(\boldsymbol{r}',t)\Big)\Big(\int d\boldsymbol{r}'\dot{\boldsymbol{M}}(\boldsymbol{r}',t)\Big) \tag{1.30}$$

where $\dot{\boldsymbol{M}}(\boldsymbol{r},t)=\frac{\partial \boldsymbol{M}(\boldsymbol{r},t)}{\partial t}$.

Let us now calculate the differential of $\mathcal{R}$, $d\mathcal{R}$, due to an infinitesimal change $\delta\dot{\boldsymbol{M}}(\boldsymbol{r}',t)$

$$\mathcal{R}[\dot{\boldsymbol{M}}+\delta\dot{\boldsymbol{M}}]=\frac{\eta}{2}\Big(\int d\boldsymbol{r}'[\dot{\boldsymbol{M}}(\boldsymbol{r}',t)+\delta\dot{\boldsymbol{M}}(\boldsymbol{r}',t)]\Big)\Big(\int d\boldsymbol{r}'[\dot{\boldsymbol{M}}(\boldsymbol{r}',t)+\delta\dot{\boldsymbol{M}}(\boldsymbol{r}',t)]\Big)$$

$$= \frac{\eta}{2}\Big(\int d\boldsymbol{r}'[\dot{\boldsymbol{M}}(\boldsymbol{r}',t)+\delta\dot{\boldsymbol{M}}(\boldsymbol{r}',t)]\Big)\Big(\int d\boldsymbol{r}[\dot{\boldsymbol{M}}(\boldsymbol{r},t)+\delta\dot{\boldsymbol{M}}(\boldsymbol{r},t)]\Big)$$

$$= \frac{\eta}{2}\int\int d\boldsymbol{r}'d\boldsymbol{r}\Big(\dot{\boldsymbol{M}}(\boldsymbol{r}',t)\dot{\boldsymbol{M}}(\boldsymbol{r},t)+\delta\dot{\boldsymbol{M}}(\boldsymbol{r}',t)\dot{\boldsymbol{M}}(\boldsymbol{r},t)+\delta\dot{\boldsymbol{M}}(\boldsymbol{r},t)\dot{\boldsymbol{M}}(\boldsymbol{r}',t)+\delta\dot{\boldsymbol{M}}(\boldsymbol{r}',t)\delta\dot{\boldsymbol{M}}(\boldsymbol{r},t)\Big) \tag{1.31}$$

Keeping only the leading terms in $\delta\boldsymbol{r}'$ and $\delta\boldsymbol{r}$,

$$\mathcal{R}[\dot{\boldsymbol{M}}+\delta\dot{\boldsymbol{M}}] = \mathcal{R}[\dot{\boldsymbol{M}}] + \frac{\eta}{2}\Big[\Big(\int\int d\boldsymbol{r}'d\boldsymbol{r}\delta\dot{\boldsymbol{M}}(\boldsymbol{r}',t)\dot{\boldsymbol{M}}(\boldsymbol{r},t)\Big)+$$

$$+\Big(\int\int d\boldsymbol{r}'d\boldsymbol{r}\delta\dot{\boldsymbol{M}}(\boldsymbol{r},t)\dot{\boldsymbol{M}}(\boldsymbol{r}',t)\Big)\Big]. \tag{1.32}$$

Interchanging again $\boldsymbol{r}'$ and $\boldsymbol{r}$ in the second integral, one obtains

$$d\mathcal{R}[\dot{\boldsymbol{M}}] = \mathcal{R}[\dot{\boldsymbol{M}}+\delta\dot{\boldsymbol{M}}]-\mathcal{R}[\dot{\boldsymbol{M}}] = \frac{\eta}{2}\Big(2\int\int d\boldsymbol{r}'d\boldsymbol{r}\delta\dot{\boldsymbol{M}}(\boldsymbol{r}',t)\dot{\boldsymbol{M}}(\boldsymbol{r},t)\Big) \tag{1.33}$$

Hence, from (A.12)

$$\frac{\delta\mathcal{R}[\dot{\boldsymbol{M}}(\boldsymbol{r},t)]}{\delta\dot{\boldsymbol{M}}(\boldsymbol{r}',t)} = \eta\dot{\boldsymbol{M}}(\boldsymbol{r},t) \tag{1.34}$$

From this result and (1.25), it is clear that

$$\boldsymbol{f}(\dot{\boldsymbol{M}}(\boldsymbol{r},t)) = -\frac{\delta\mathcal{R}[\dot{\boldsymbol{M}}(\boldsymbol{r},t)]}{\delta\dot{\boldsymbol{M}}(\boldsymbol{r}',t)} \tag{1.35}$$

The component of the generalized force resulting from the dissipation force is then given by

$$\mathcal{Q} = \boldsymbol{f}(\dot{\boldsymbol{M}}(\boldsymbol{r},t))\cdot\frac{\delta\dot{\boldsymbol{M}}(\boldsymbol{r}',t)}{\delta\dot{\boldsymbol{M}}(\boldsymbol{r},t)} = -\frac{\delta\mathcal{R}[\dot{\boldsymbol{M}}(\boldsymbol{r},t)]}{\delta\dot{\boldsymbol{M}}(\boldsymbol{r}',t)}\frac{\delta\dot{\boldsymbol{M}}(\boldsymbol{r}',t)}{\delta\dot{\boldsymbol{M}}(\boldsymbol{r},t)} = -\frac{\delta\mathcal{R}[\dot{\boldsymbol{M}}(\boldsymbol{r},t)]}{\delta\dot{\boldsymbol{M}}(\boldsymbol{r},t)} \tag{1.36}$$

The Lagrange equations now become

$$\frac{d}{dt}\Big(\frac{\delta L}{\delta\dot{\boldsymbol{M}}(\boldsymbol{r},t)}\Big) - \frac{\delta L}{\delta\boldsymbol{M}(\boldsymbol{r},t)} + \frac{\delta\mathcal{R}[\dot{\boldsymbol{M}}(\boldsymbol{r},t)]}{\delta\dot{\boldsymbol{M}}(\boldsymbol{r}',t)} = 0 \tag{1.37}$$

and $\mathcal{R}$ is now a Rayleigh dissipation functional. The parameter η, in fact, quantifies the average damping throughout the sample. Namely, equation (1.30) implies that the distribution of energy loss due to damping mechanisms (the distribution of heat energy generated locally by damping) is uniform. Actually, this is not the case because local damping can be caused by a variety of nonuniform mechanisms: rapid spin reorientation in moving domain walls, random size and orientation of crystal grains, crystal defects, impurities, local strains, etc. A dissipation functional of the form

$$\mathcal{R}[\boldsymbol{M}] = \frac{1}{2}\sum_{i,j}\int\int d\boldsymbol{r}' d\boldsymbol{r}\; \dot{\boldsymbol{M}}_i(\boldsymbol{r},t)\,\eta_{ij}(\boldsymbol{r},\boldsymbol{r}')\,\dot{\boldsymbol{M}}_j(\boldsymbol{r}',t) \tag{1.38}$$

would take nonuniform damping into account; however, it is of little use because it is not possible to calculate or measure the matrix damping function $\eta_{ij}(\boldsymbol{r},\boldsymbol{r}')$ that replaces the single damping parameter η.[12]

Substituting (1.28) into (1.37) in order to separate the kinetic and potential energy contributions and using (1.34) and (1.22), we obtain

$$\frac{d}{dt}\frac{\delta T[\boldsymbol{M},\dot{\boldsymbol{M}}]}{\delta\dot{\boldsymbol{M}}} - \frac{\delta T[\boldsymbol{M},\dot{\boldsymbol{M}}]}{\delta\boldsymbol{M}} + [-\boldsymbol{B}(\boldsymbol{r},t) + \eta\dot{\boldsymbol{M}}(\boldsymbol{r},t)] = 0. \tag{1.39}$$

At this point, one encounters the problem that the kinetic energy T of a classical Lagrangian for a rotating object depends on dynamical variables that are not defined for quantum spin operators. Gilbert did not derive an expression for the kinetic energy of a rotating body in classical mechanics that would correspond to the spin of an elementary particle in quantum mechanics in a way that made physical sense.[12] Instead, he circumvented by means of the following argument.

If we set $\eta = 0$ in (1.39) then it becomes an equation for an undamped magnetization field, and should, therefore, be equivalent to (1.21).[12] We note that the damping term in (1.39) is an added *damping field* that can reduce the effective magnetic field and change the torque exerted on the magnetization field. It is reasonable to argue that, when $\eta \neq 0$, adding this same damping term to the effective field for the equation of motion for an

undamped magnetization field given by (1.21) gives a valid equation of motion for a damped magnetization field as follows,

$$\frac{\partial \boldsymbol{M}(\boldsymbol{r},t)}{\partial t} = \gamma \boldsymbol{M}(\boldsymbol{r},t) \times [\boldsymbol{B}(\boldsymbol{r},t) - \eta \dot{\boldsymbol{M}}(\boldsymbol{r},t)] = \gamma \boldsymbol{M} \times \boldsymbol{B} - \frac{\alpha}{M} \boldsymbol{M} \times \frac{\partial \boldsymbol{M}}{\partial t} \tag{1.40}$$

where $\alpha = \gamma \eta M$. It is of interest to compare (1.40) with the Landau-Lifshitz equation (1.23). Equation (1.23) can also be written in the same form as (1.40), by substituting the equality $\boldsymbol{M} \times \boldsymbol{B} = \gamma^{-1}[\frac{\partial \boldsymbol{M}}{\partial t} + (\frac{\lambda}{M})\boldsymbol{M} \times \boldsymbol{M} \times \boldsymbol{B}$ only in the second term of right side of (1.23)

$$\frac{\partial \boldsymbol{M}(\boldsymbol{r},t)}{\partial t} = \gamma\Big(1 + \frac{\lambda_2}{\gamma_2}\Big)[\boldsymbol{M} \times \boldsymbol{B}] - \frac{\lambda}{\gamma M}\Big(\boldsymbol{M} \times \frac{\partial \boldsymbol{M}}{\partial t}\Big) \tag{1.41}$$

$$= \gamma^*[\boldsymbol{M} \times \boldsymbol{B}] - \frac{\alpha}{M}\Big(\boldsymbol{M} \times \frac{\partial \boldsymbol{M}}{\partial t}\Big) \tag{1.42}$$

respectively, where

$$\alpha = \frac{\lambda}{\gamma} = \eta \gamma M \tag{1.43}$$

and

$$\gamma^* = \gamma(1 + \alpha^2). \tag{1.44}$$

We observe that the damping terms in Landau-Lifshitz and Gilbert equations are identical, the only difference between the two being that as the dimensionless damping parameter α increases in the Landau-Lifshitz form, the gyromagnetic ratio γ^* and, hence, the rate of precession of the spin also increases. The difference between the two equations is small when $\alpha^2 \ll 1$. For example, when ferromagnetic interactions are present, α/γ is generally expected to be $\ll 1$.[24]

Chapter 2

Theoretical Methods II: Matter from first principles

2.1 Introduction

2.1.1 The full quantum-mechanical problem

From the point of view of condensed matter physics, matter presents itself as an ensemble of particles which may be either in the gas or the condensed phase: solid or liquids. Ensembles of particles may be homogeneous or heterogeneous, ordered of amorphous. However, in all cases we can unambiguously describe the system by a number of nuclei and electrons interacting through Coulomb forces. Formally, we can write the Hamiltonian of such a system in the following general form:[25]

$$\hat{H} = -\sum_{I=1}^{P} \frac{\hbar^2}{2M_I}\nabla_I^2 - \sum_{i=1}^{N} \frac{\hbar^2}{2m}\nabla_i^2$$

$$+\frac{e^2}{2}\sum_{I=1}^{P}\sum_{J\neq I}^{P} \frac{Z_I Z_J}{|\boldsymbol{R}_I - \boldsymbol{R}_J|} + \frac{e^2}{2}\sum_{i=1}^{N}\sum_{j\neq i}^{N} \frac{1}{|\boldsymbol{r}_i - \boldsymbol{r}_j|} - e^2\sum_{I=1}^{P}\sum_{i=1}^{N} \frac{Z_I}{|\boldsymbol{R}_I - \boldsymbol{r}_i|} \tag{2.1}$$

where $\{\boldsymbol{R}_I\}$, $I = 1, ..., P$, is a set of P nuclear coordinates and $\{\boldsymbol{r}_i\}$, $i = 1, ..., N$, is a set of N electron coordinates. Z_I and M_I are the atomic numbers and masses of the atomic nucleus, respectively. Since electrons are fermions, the total electronic wave function must be antisymmetric with respect to exchange of two electrons. Nuclei can be fermions, bosons

or distinguishable particles, depending on the particular problem under examination. All the ingredients are perfectly known and, in principle, all the properties Schrödinger equation:

$$\hat{H}\Psi_n(\boldsymbol{r}, \boldsymbol{R}) = E_n\Psi_n(\boldsymbol{r}, \boldsymbol{R}) \tag{2.2}$$

In practice, however, this problem is almost impossible to treat in a full quantum-mechanical framework. Only in a few cases a complete analytic solution is available, and numerical solutions are also limited to a very small number of particles.[25]

There are several features that contribute to this difficulty. First, the Hamiltonian in Eq. 2.1 describes a multicomponent many-body system, where each component (each nuclear species and the electrons) obeys a particular statistics. Second, the complete wave function cannot be easily factorized because of coulombic correlations. In other words, the full Schrödinger equation cannot be easily decoupled into a set of independent equations so that, in general, we have to deal with $(3P + 3N)$ coupled degrees of freedom. The usual choice is to resort to some sensible approximations. The large majority of the calculations presented in the literature are based on (i) the adiabatic separation of nuclear and electronic degrees of freedom (adiabatic approximation) and (ii) the classical treatment of the nuclei.[25]

2.1.2 The adiabatic or *Born-Oppenheimer* approximation: Decoupling the electronic and nuclear problem

This approximation is based on the fact that the timescale associated to the motion of the nuclei is usually much slower than that associated to electrons. In fact, the small mass of the electrons as compared to that of the protons (the most unfavorable case) is about 1 in 1836, meaning that their velocity is much larger.[1] Unlike in thermodynamics, in quantum mechanics *adiabatic* is said of an infinitely slow change in the Hamiltonian of a system. [2] This approximation is then called "adiabatic" because the nuclear repulsion term of the

[1] The velocity is proportional to the typical frequency associated to either electrons or nuclei, which in turn is proportional to $m^{-\frac{1}{2}}$

[2] This definition is closer to the thermodynamic concept of a "quasistatic process"

total Hamiltonian, (2.1), suffers an infinitely slow change according to the time-scale of the electrons and the nuclei can be thus considered fixed particles in the electronic time-frame. In this spirit, it was proposed in the early times of quantum mechanics that the electrons can be adequately described as following instantaneously the motion of the nuclei, staying always in the same stationary state of the electronic Hamiltonian.[25] This stationary state will vary in time because of the coulombic coupling of the two sets of degrees of freedom but if the electrons were, for example, in the ground state, they will remain there forever. This means that as the nuclei follow their dynamics, the electrons instantaneously adjust their wave function according to the nuclear wave function and thus, their degrees of freedom are decoupled. Under the above conditions, the Born-Oppenheimer approximation comes in the fact that the full wave function can be factorized in the following way:[25]

$$\Psi(\boldsymbol{R}, \boldsymbol{r}, t) = \Theta_m(\boldsymbol{R}, t)\Phi_m(\boldsymbol{R}, \boldsymbol{r}) \tag{2.3}$$

where the electronic wave function $\Phi_m(\boldsymbol{R}, \boldsymbol{r})$, normalized for every $\boldsymbol{R}$, is the mth stationary state of the electronic Hamiltonian.

2.1.3 The decoupled electronic problem

The electronic Hamiltonian mentioned above,

$$\hat{h} = \hat{T}_e + \hat{U}_{ee} + \hat{V}_{ne} = \hat{H} - \hat{T}_n - \hat{U}_{nn}, \tag{2.4}$$

is obtained by considering that the kinetic energy operator, $\hat{T}_n$, vanishes provided that the nuclear positions $\{\boldsymbol{R}_I\}$ are fixed in the electronic problem under the Born-Oppenheimer approximation and by dropping the potential nuclear operator, $\hat{U}_{nn}$, since it becomes a constant for the same reason. $\hat{T}_e$ and $\hat{U}_{ee}$ are the kinetic and potential energy operators of electrons, and $\hat{V}_{ne}$ the electron-nuclear interaction, all explicitly written in (2.1).

The corresponding eigenvalue is noted $\epsilon_m(\boldsymbol{R})$:

$$\hat{h}\ \Phi_m(\boldsymbol{R}, \boldsymbol{r}) = \epsilon_m(\boldsymbol{R})\Phi_m(\boldsymbol{R}, \boldsymbol{r})$$

In this stationary electronic Schrödinger equation, the nuclear coordinates $\boldsymbol{R}$ enter as parameters. Also, in principle, m can be any electronic eigenstate. In practice, however, people conform themselves to obtain the solution for the ground state ($m = 0$) for the sake of simplicity and because it is enough to obtain many properties of matter.

2.1.4 The decoupled nuclear problem

Within the Born-Oppenheimer approximation, the lattice-dynamical properties of a system are determined by the eigenvalues ε and eigenfunctions $\Theta(\boldsymbol{R}, t)$ of the time-dependent Schrödinger equation[26]

$$i\hbar\frac{\partial\Theta(\boldsymbol{R},t)}{\partial t} = [\hat{T}_n + E(\boldsymbol{R})]\Theta(\boldsymbol{R},t), \tag{2.5}$$

or the stationary version,

$$[\hat{T}_n + E(\boldsymbol{R})]\Theta(\boldsymbol{R}) = \varepsilon\Theta(\boldsymbol{R}). \tag{2.6}$$

where $E(\boldsymbol{R}) = \hat{U}_{nn} + \epsilon_m(\boldsymbol{R})$ is the position-ion-dependent energy of the system, which is often referred to as the Born-Oppenheimer energy surface. In practice, $E(\boldsymbol{R})$ is the total ground-state energy of a system of interacting electrons moving in the field of fixed nuclei, whose Hamiltonian - which acts onto the electronic variables and depends parametrically upon R - is simply the electronic Hamiltonian plus the constant term accounting for the nuclear potential energy, $\hat{U}_{nn}$. As we shall see layer, the calculation of the equilibrium geometry and of the vibrational properties of a system thus amounts to computing the first and second derivatives of the Born- Oppenheimer energy surface, which in turn requires to solve the electronic problem, presented in the next section.

2.1.5 Range and breakdown of the Born-Oppenheimer approximation

This approximation does not always hold. Some molecules, for example, may have the nuclei moving too fast and/or the electrons moving too slow, in which case the vibration of the nuclei may couple to the electronic motion, the so-called vibronic coupling, and give

rise to non-radiative transitions between different electronic eigenstates. That is, radiative processes lead to the emission of light. The non-radiative simply redistribute the adsorbed energy among electronic excitations, i.e., the Auger effect, and lattice vibrations, ultimately converting the adsorbed light into heat. In the Born-Oppenheimer approximation, transitions can only arise through coupling with an external electromagnetic field and involve the solution of the time-dependent Schrödinger equation. This has been achieved, especially in the linear response regime, but also in a non-perturbative framework in the case of molecules in strong laser fields.[25] However, this is not the scope of this section, and electronic transitions will not be addressed.

2.2 Density Functional Theory: The electronic problem

2.2.1 Early instructive approaches

Introduction

The first key problem about the structure of matter is to solve the Schrödinger equation for a system of N interacting electrons in the external coulombic field created by a collection of atomic nuclei (and may be some other external field). It is a very difficult problem in many-body theory and, in fact, the exact solution is known only in the case of the uniform electron gas, for atoms with a small number of electrons and for a few small molecules. These exact solutions are always numerical. At the analytic level, one always has to resort to approximations.[25] However, the effort of devising schemes to solve this problem remains a very active field since the early establishment of quantum mechanics because the knowledge of the electronic ground state of a system gives access to many of its properties, for example, relative stability of different structures/isomers, equilibrium structural information, mechanical stability and elastic properties, pressure.temperature (P-T) phase diagrams, dielectric properties, dynamical (molecular or lattice) properties such as vibrational frequencies and spectral functions, (non-electronic) transport properties such as diffusivity, viscosity, ionic

conductivity and so forth. Excited electronic states (or the explicit time dependence) also give access to another wealth of measurable phenomena such as electronic transport and optical properties.

The Hartree approximation: electrons as distinguishable particles

The first approximation may be considered the one proposed by Hartree.[25] Such approximation artificially sets that electrons are not correlated; that is, regardless of their charge and fermionic nature, their probability to be at a particular state (spin and position) is not affected by that of the other electrons. If that were the case, then the *many-electron* wave function can be written as a simple product of *one-electron* wave functions. Each of these verifies a one-particle Schrödinger equation in an effective potential that takes into account the interaction with the other electrons in a mean-field way (we omit the dependence of the orbitals on $\boldsymbol{R}$ and the subscript m and consider only the electronic ground state):[25]

$$\Phi(\boldsymbol{R},\boldsymbol{r}) = \Pi_i \phi_i(\boldsymbol{r}) \tag{2.7}$$

Using the variational principle, one may focus on obtaining the ground state ($m = 0$) of the electronic Hamiltonian (2.4).[27] Namely, we require $\hat{h}$ to be stationary with respect to variations of the complete set of orbitals (2.7) from normality. Expressing the constraint of normalization, $\int d\boldsymbol{r}|\phi_i|^2 = 1$, for each ϕ_i with a Lagrange multipliers ε_i, the stationary condition,

$$\frac{\delta}{\delta\phi_i^*}\Big[< \hat{h} > -\varepsilon_i \int d\boldsymbol{r}\ \phi_i\ \phi_i^*\ \Big] = 0, \tag{2.8}$$

where $< \hat{h} > = < \Phi^*|\hat{h}|\Phi >$, leads to the one-electron *Hartree* equations for each $\phi_i(\boldsymbol{r})$,[28]

$$\Big(-\frac{\hbar^2}{2m}\nabla^2 + V_{eff}^{(i)}(\boldsymbol{R},\boldsymbol{r})\Big)\phi_i(\boldsymbol{r}) = \varepsilon_i\phi_i(\boldsymbol{r}) \tag{2.9}$$

where the effective potential on the i-electron is

$$V_{eff}^{(i)}(\boldsymbol{R},\boldsymbol{r}) = V(\boldsymbol{R},\boldsymbol{r}) + \int \frac{\sum_{j\neq i}^{N}\rho_j(\boldsymbol{r}')}{|\boldsymbol{r}-\boldsymbol{r}'|}d\boldsymbol{r}' \tag{2.10}$$

and the electronic density associated with particle j

$$\rho_j(\boldsymbol{r}) = |\phi_j(\boldsymbol{r})|^2 \tag{2.11}$$

The second term in the right-hand side (rhs) of equation (2.10) is the classical electrostatic potential generated by the charge distribution $\sum_{j\neq i}^{N} \rho_j(\boldsymbol{r})$. Notice that this charge density does not include the charge associated with particle i, so that the Hartree approximation is (correctly) self-interaction-free. In this approximation, the energy of the many-body system is not just the sum of the eigenvalues of equation (2.9) because the formulation in terms of an effective potential makes the electron-electron interaction to be counted twice. The correct expression for the energy is

$$E_H = \sum_{n=1}^{N} \varepsilon_n - \frac{1}{2} \sum_{i\neq j}^{N} \int\int \frac{\rho_i(\boldsymbol{r})\rho_j(\boldsymbol{r}')}{|\boldsymbol{r}-\boldsymbol{r}'|} d\boldsymbol{r} d\boldsymbol{r}' \tag{2.12}$$

The set of N coupled partial differential equations (2.9) can be solved by minimizing the energy with respect to a set of variational parameters in a trial wave function or, alternatively, by recalculating the electronic densities in equation (2.11) using the solutions of equation (2.9), then casting them back into the expression for the effective potential (equation 2.10), and solving again the Schrödinger equation. This procedure can be repeated several times, until self-consistency in the input and output wave function or potential is achieved. This procedure is called *self-consistent Hartree* approximation.

The Hartree-Fock approximation: Pauli's exclusion principle

A step beyond the Hartree approximation is to include the Fermi correlation among electrons, which so far have been treated as distinguishable particles whereas they obey Pauli exclusion principle (Fermi statistics for electrons). The Pauli principle requires the wavefunction, $\Phi(\boldsymbol{R}, \boldsymbol{r})$, to be antisymmetric under interchange of any two electrons, which the Hartree wavefunction (2.7) does not satisfy. An antisymmetric many-electron wavefunction

can be constructed via a Slater determinant of the one-electron wavefunctions:

$$\Phi(\boldsymbol{R},\boldsymbol{r}) = \frac{1}{\sqrt{N!}} \begin{vmatrix} \phi_1(\boldsymbol{r}_1,\sigma_1) & \phi_1(\boldsymbol{r}_2,\sigma_2) & \dots & \phi_1(\boldsymbol{r}_N,\sigma_N) \\ \phi_2(\boldsymbol{r}_1,\sigma_1) & \phi_2(\boldsymbol{r}_2,\sigma_2) & \dots & \phi_2(\boldsymbol{r}_N,\sigma_N) \\ \vdots & \vdots & \ddots & \vdots \\ \phi_N(\boldsymbol{r}_1,\sigma_1) & \phi_N(\boldsymbol{r}_2,\sigma_2) & \dots & \phi_2(\boldsymbol{r}_N,\sigma_N) \end{vmatrix} \tag{2.13}$$

This wave function introduces particle exchange in an exact manner.[25] The approximation is called *Hartree-Fock* (HF) or *self-consistent field* (SCF) approximation and has been for a long time the way of choice of chemists for calculating the electronic structure of molecules. In fact, it provides a very reasonable picture for atomic systems and, although many-body correlations (arising from the fact that, owing to the two-body Coulomb interactions, the total wave function cannot necessarily be written as an antisymmetrized product of single-particle wave functions) are completely absent, it also provides a reasonably good description of inter-atomic bonding.[25]

Using again the variational principle in reference to the constraint of normalization of each ϕ_i to make $\hat{h}$ stationary with respect to variations of the complete set of orbitals in (2.13) leads to the one-electron ground-state *Hartree-Fock* equations[28]

$$\Big(-\frac{\hbar^2}{2m}\nabla^2 + V(\boldsymbol{R},\boldsymbol{r}) + \int \frac{\sum_{\sigma',j=1}^{N} \rho_j(\boldsymbol{r}',\sigma')}{|\boldsymbol{r}-\boldsymbol{r}'|} d\boldsymbol{r}'\Big)\phi_i(\boldsymbol{r},\sigma)$$

$$-\sum_{j=1}^{N}\Big(\sum_{\sigma'}\int \frac{\phi_j^*(\boldsymbol{r}',\sigma')\phi_i(\boldsymbol{r}',\sigma')}{|\boldsymbol{r}-\boldsymbol{r}'|} d\boldsymbol{r}'\Big)\phi_j(\boldsymbol{r},\sigma) = \sum_{j=1}^{N}\lambda_{ij}\phi_j(\boldsymbol{r},\sigma) \tag{2.14}$$

Hartree-Fock equations look the same as Hartree equations, except for the fact that the exchange integrals introduce additional coupling terms in the differential equations and the self-interaction cancels exactly. Nowadays, the Hartree-Fock approximation is routinely used as a starting point for more elaborated calculations.[25]

2.2.2 The electronic density and correlations

Parallel to the development of the Hartree-Fock approach Thomas and Fermi proposed, at about the same time as Hartree (1927-1928), that the full electronic density was the fundamental variable of the many-body problem and derived a differential equation for the density without resorting to one-electron orbitals.[25] The Thomas-Fermi (TF) approximation was too crude because it did not include exchange and correlation effects and was also unable to sustain bound states because of the approximation used for the kinetic energy of the electrons. However, it set up the basis for the later development of density functional theory (DFT).[25]

The total ground state energy of an inhomogeneous system composed by N interacting electrons is given by by the expectation value of the electronic Hamiltonian (2.4)

$$E =< \Phi|\hat{T}_e + \hat{V}_{ne} + \hat{U}_{ee}|\Phi >=< \Phi|\hat{T}_e|\Phi > + < \Phi|\hat{V}_{ne}|\Phi > + < \Phi|\hat{U}_{ee}|\Phi > \tag{2.15}$$

where $|\Phi >$ is the ***unknown*** N-electron ground state wavefunction but for which no particular form is assumed this time, so that it includes the Fermi and Coulomb correlations. Let us concentrate now on the electron-electron interaction term, U_{ee}, which is the one that introduces many-body effects.

$$U_{ee} =< \Phi\ |\hat{U}_{ee}|\ \Phi >=< \Phi\ |\frac{1}{2}\sum_{i=1}^{N}\sum_{j\neq i}^{N}\frac{1}{|\boldsymbol{r}_i - \boldsymbol{r}_j|}|\ \Phi >$$

$$= \frac{1}{2}\int \frac{\sum_{\sigma,\sigma'} < \Phi|\Psi^{\dagger}_{\sigma}(\boldsymbol{r})\Psi^{\dagger}_{\sigma'}(\boldsymbol{r}')\Psi_{\sigma'}(\boldsymbol{r}')\Psi_{\sigma}(\boldsymbol{r})|\Phi >}{|\boldsymbol{r} - \boldsymbol{r}'|} d\boldsymbol{r}d\boldsymbol{r}' = \int \frac{\rho_2(\boldsymbol{r},\boldsymbol{r}')}{|\boldsymbol{r} - \boldsymbol{r}'|} d\boldsymbol{r}d\boldsymbol{r}' \tag{2.16}$$

where $\rho_2(\boldsymbol{r},\boldsymbol{r}')$ is the two-body density matrix expressed in real space, being Ψ and $\Psi^{\dagger}$ the creation and annihilation operators for electrons, which obey the anti-commutations relations $\{\Psi_{\sigma}(\boldsymbol{r}), \Psi^{\dagger}_{\sigma'}(\boldsymbol{r}')\} = \delta_{\sigma,\,\sigma'}\delta(\boldsymbol{r} - \boldsymbol{r}')$.[25] We then introduce the two-body direct corre-

lation function $g(\boldsymbol{r},\boldsymbol{r}')$ in the following way[25]

$$\rho_2(\boldsymbol{r},\boldsymbol{r}') = \frac{1}{2}\rho(\boldsymbol{r},\boldsymbol{r})\rho(\boldsymbol{r}',\boldsymbol{r}')g(\boldsymbol{r},\boldsymbol{r}') \tag{2.17}$$

where

$$\rho(\boldsymbol{r},\boldsymbol{r}') = \sum_{\sigma}\rho_{\sigma}(\boldsymbol{r},\boldsymbol{r}') \tag{2.18}$$

is the real-space one-body density matrix whose diagonal elements correspond to the electronic density: $\rho(\boldsymbol{r}) = \rho(\boldsymbol{r},\boldsymbol{r})$.[25] Writing explicitly,

$$\rho_{\sigma}(\boldsymbol{r},\boldsymbol{r}') =< \Phi|\Psi^{\dagger}_{\sigma}(\boldsymbol{r})\Psi_{\sigma}(\boldsymbol{r}')|\Phi >, \tag{2.19}$$

the electron-electron interaction is expressed as

$$U_{ee} = \frac{1}{2}\int\frac{\rho(\boldsymbol{r})\rho(\boldsymbol{r}')}{|\boldsymbol{r}-\boldsymbol{r}'|}d\boldsymbol{r}d\boldsymbol{r}' + \frac{1}{2}\int\frac{\rho(\boldsymbol{r})\rho(\boldsymbol{r}')}{|\boldsymbol{r}-\boldsymbol{r}'|}[g(\boldsymbol{r},\boldsymbol{r}')-1]d\boldsymbol{r}d\boldsymbol{r}' \tag{2.20}$$

The first term is the classical electrostatic interaction energy corresponding to a charge distribution $\rho(\boldsymbol{r})$. The second term includes correlation effects of both classical and quantum origin. Basically, $g(\boldsymbol{r},\boldsymbol{r}')$ takes into account the fact that the presence of an electron at $\boldsymbol{r}$ discourages a second electron to be located at a position $\boldsymbol{r}'$ very close to $\boldsymbol{r}$ because of the Coulomb repulsion. In other words, it says that the probability of finding two electrons (two particles with charges of the same sign, in the general case) is reduced with respect to the probability of finding them at infinite distance. This is true already at the classical level and it is further modified at the quantum level. Exchange further diminishes this probability in the case of electrons having the same spin projection, owing to the Pauli exclusion.[25]

Within the Hartree-Fock approximation (2.13), $g(\boldsymbol{r},\boldsymbol{r}')$ can be derived analytically[25]

$$g_X(\boldsymbol{r},\boldsymbol{r}') = 1 - \frac{\sum_{\sigma}|\rho^{HF}_{\sigma}(\boldsymbol{r},\boldsymbol{r}')|^2}{\rho^{HF}(\boldsymbol{r})\rho^{HF}(\boldsymbol{r}')} \tag{2.21}$$

and is called the *exchange hole* since it only accounts for Fermi correlations but not Coulomb correlations, provided that (2.13) only takes into account Pauli's exclusion principle. The calculation of $g(\boldsymbol{r},\boldsymbol{r}')$, in general, is a major problem in many-body theory and, up to

the present, it is an open problem in the general case of an inhomogeneous electron gas. Nevertheless, the energy of the many-body electronic system can always be written in the following way:[25]

$$E = T + V + \frac{1}{2}\int \frac{\rho(\boldsymbol{r})\rho(\boldsymbol{r}')}{|\boldsymbol{r}-\boldsymbol{r}'|} d\boldsymbol{r} d\boldsymbol{r}' + E_{XC} \tag{2.22}$$

where

$$V = \sum_{I=1}^{P} < \Phi | \sum_{i=i}^{N} V_{ne}(\boldsymbol{r}_i - \boldsymbol{R}_I) | \Phi >= \sum_{I=1}^{P} \int \rho(\boldsymbol{r}) V_{ne}(\boldsymbol{r} - \boldsymbol{R}_I) d\boldsymbol{r} \tag{2.23}$$

and

$$T =< \Phi | -\frac{\hbar^2}{2m} \sum_{i=1}^{N} \nabla_i^2 | \Phi >= -\frac{\hbar^2}{2m} \int [\nabla_r^2 \rho(\boldsymbol{r},\, \boldsymbol{r}')]_{\boldsymbol{r}'=\boldsymbol{r}}\, d\boldsymbol{r} \tag{2.24}$$

and E_{XC} is the exchange and correlation energy

$$E_{XC} = \frac{1}{2}\int \frac{\rho(\boldsymbol{r})\rho(\boldsymbol{r}')}{|\boldsymbol{r}-\boldsymbol{r}'|} [g(\boldsymbol{r},\boldsymbol{r}') - 1] d\boldsymbol{r} d\boldsymbol{r}' \tag{2.25}$$

2.2.3 Hohenberg-Kohn theorem

Hohenberg and Kohn[29] formulated and proved a theorem that put on solid mathematical grounds the ideas first proposed by Thomas and Fermi.[25]

THEOREM: The external potential is univocally determined by the electronic density, except for a trivial additive constant.

PROOF: We will suppose the opposite to hold, that the potential is not univocally determined by the density. Then one would be able to find two potentials V_{ne} and V'_{ne} such that their ground state density ρ is the same. Let Ψ and $E_0 =< \Psi|\hat{h}|\Psi >$ be the ground state and ground state energy of $\hat{h} = \hat{T}_e + \hat{U}_{ee} + \hat{V}_{ne}$, and Ψ' and $E'_0 =< \Psi'|\hat{h}'|\Psi' >$ the ground state and ground state energy of $\hat{h}' = \hat{T}_e + \hat{U}_{ee} + \hat{V}'_{ne}$ according to the variational principle,

$$E_0 < \langle \Psi'|\hat{h}|\Psi' \rangle = \langle \Psi'|\hat{h}'|\Psi' \rangle + \langle \Psi'|\hat{h} - \hat{h}'|\Psi' \rangle = E'_0 + \int \rho(\boldsymbol{r})(v_{ne}(\boldsymbol{r}) - v'_{ne}(\boldsymbol{r}))d\boldsymbol{r} \tag{2.26}$$

where we have also used the fact that different Hamiltonians have necessarily different ground states $\Psi \neq \Psi'$. This is straightforward to show since the potential is a multiplicative

operator. Now we can simply reverse the situation of Ψ and Ψ' (H and H') and obtain

$$E_0' < \langle \Psi | \hat{h}' | \Psi \rangle = \langle \Psi | \hat{h} | \Psi \rangle + \langle \Psi | \hat{h}' - \hat{h} | \Psi \rangle = E_0 - \int \rho(\boldsymbol{r})(v_{ne}(\boldsymbol{r}) - v_{ne}'(\boldsymbol{r}))d\boldsymbol{r} \tag{2.27}$$

Adding these two inequalities leads to an absurd conclusion: that $E_0 + E_0' < E_0' + E_0$ Therefore, there are no $v_{ne}(\boldsymbol{r}) \neq v_{ne}'(\boldsymbol{r})$ that correspond to the same electronic density for the ground state.

COROLLARY: Since $\rho(\boldsymbol{r})$ univocally determines $v_{ne}(\boldsymbol{r})$, it also determines the ground state wave function Ψ.

THEOREM: Let $\tilde{\rho}(\boldsymbol{r})$ be a non-negative density normalized to N. Then $E_0 < E_{v_{ne}}[\tilde{\rho}]$, for

$$E_{v_{ne}}[\tilde{\rho}] = F[\tilde{\rho}] + \int \tilde{\rho}(\boldsymbol{r}) v_{ne}(\boldsymbol{r}) d\boldsymbol{r} \tag{2.28}$$

with

$$F[\tilde{\rho}] = \langle \Psi[\tilde{\rho}] | \hat{T}_e + \hat{U}_{ee} | \Psi[\tilde{\rho}] \rangle \tag{2.29}$$

where $\Psi[\tilde{\rho}]$ is the ground state of a potential that has $\tilde{\rho}$ as its ground state density.

PROOF: We have

$$\langle \Psi[\tilde{\rho}] | \hat{h} | \Psi[\tilde{\rho}] \rangle = F[\tilde{\rho}] + \int \tilde{\rho}(\boldsymbol{r}) v_{ne}(\boldsymbol{r}) d\boldsymbol{r} = E_{v_{ne}}[\tilde{\rho}] \geq E_{v_{ne}}[\rho] = E_0 = \langle \Psi | \hat{h} | \Psi \rangle \tag{2.30}$$

The inequality follows from Rayleigh-Ritz's variational principle for the wave function, but applied to the electronic density. Therefore, the variational principle says

$$\delta \Big\{ E_{v_{ne}} - \mu \Big(\int \rho(\boldsymbol{r}) d\boldsymbol{r} - N \Big) \Big\} = 0 \tag{2.31}$$

and one obtains

$$\mu = \frac{\delta E_{v_{ne}}[\rho]}{\delta \rho} = v_{ne}(\boldsymbol{r}) + \frac{F[\rho]}{\delta \rho} \tag{2.32}$$

The knowledge of $F[\rho]$ implies that one has solved the full many-body Schrödinger equation.[25] It has to be remarked that $F[\rho]$ is a *universal* functional that does not depend explicitly on the external potential. It depends only on the electronic density. In

the Hohenberg-Kohn formulation, $F[\rho] = \langle\Psi|\hat{T}_e + \hat{U}_{ee}|\Psi\rangle$, where Ψ is the ground state wavefunction.

In Hohenberg-Kohn theorem the electronic density determines the external potential, but it is also needed that the density corresponds to some ground state antisymmetric wavefunction, and this is not always the case. However, DFT can be reformulated in such a way that this is not necessary, by appealing to the constrained search method.[25] By defining

$$F[\rho] = \min_{\Psi\to\rho}\langle\Psi|\hat{T}_e + \hat{U}_{ee}|\Psi\rangle\} \tag{2.33}$$

for non-negative densities such that $\int \rho(\boldsymbol{r})d\boldsymbol{r} = N$ and $\int|\nabla\rho^{\frac{1}{2}}(\boldsymbol{r})|^2 d\boldsymbol{r} < \infty$, which arise from an antisymmetric wave function, the search is constrained to the subspace of all the antisymmetric Ψ that give rise to the same density ρ.

If $F[\rho]$ is known, then DFT allows us to determine the electronic ground state density and energy exactly. The density determines univocally the potential, and this in turn determines univocally the many-body wave functions, ground and excited states, provided that the full many-body Schrödinger equation is solved. For the ground state, such a scheme was devised by Kohn and Sham and will be discussed in subsection (2.2.4). For excited states there are a few extensions and generalizations of Kohn-Sham (KS) theory, but only very recently these are beginning to be used with some degree of success.[25]

2.2.4 Kohn-Sham equations

We have seen that the interaction potential $U_{ee} = \langle\Phi|\hat{U}_{ee}|\Phi\rangle$ can be expressed in terms of the charge density, $\rho(\boldsymbol{r})$, by separating the electrostatic (classical Coulomb energy) and the Fermi and Coulomb correlation contributions.[25] The biggest difficulty is to deal with Coulomb correlations since the explicit form of the correlation function, $g(\boldsymbol{r}, \boldsymbol{r}')$, is in general unknown for inhomogeneous electron distributions. Although this issue is quite under control for many systems of interest,[25] the expression of the kinetic energy $\langle\Psi|\hat{T}_e|\Psi\rangle$ in terms of the electronic density is not known. The main problem with it is that the kinetic operator

is inherently non-local, though short-ranged.[25]

In 1965, Kohn and Sham[30] proposed the idea of replacing the kinetic energy of the interacting electrons with that of an equivalent non-interacting system, because the latter can be easily calculated. The density matrix $\rho(\boldsymbol{r}, \boldsymbol{r}')$ that derives from the (interacting) ground state is the sum of the spin-up and spin-down density matrices, $\rho(\boldsymbol{r}, \boldsymbol{r}') = \sum_s \rho_s(\boldsymbol{r}, \boldsymbol{r}')$ (for $s = 1, 2$). The latter can be written as

$$\rho_s(\boldsymbol{r}, \boldsymbol{r}') = \sum_{i=1}^{\infty} n_{i,s} \phi_{i,s}(\boldsymbol{r}) \phi_{i,s}^*(\boldsymbol{r}') \tag{2.34}$$

where $\{\phi_{i,s}(\boldsymbol{r})\}$ are the natural spin orbitals and $\{n_{i,s}\}$ are the occupation numbers of these orbitals, originally proposed by Löwdin in a 1955.[31] The kinetic energy can be written exactly as

$$T_e = \sum_{s=1}^{2} \sum_{i=1}^{\infty} n_{i,\,s} \langle \phi_{i,\,s} | -\frac{\nabla^2}{2} | \phi_{i,\,s} \rangle \tag{2.35}$$

In the following, it is assumed that the equivalent noninteracting system, that is, a system of non-interacting fermions whose ground state density coincides with that of the interacting system, does exist and is called the *non-interacting reference system* of density $\rho(\boldsymbol{r})$, which is described by the Hamiltonian

$$\hat{H}_R = \sum_{i=1}^{N} \Big(-\frac{\nabla_i^2}{2} + v_R(\boldsymbol{r}_i) \Big) \tag{2.36}$$

where the potential $v_R(\boldsymbol{r})$ is such that the ground state density of $\hat{H}_R$ equals $\rho(\boldsymbol{r})$ and the ground state energy equals the energy of the interacting system. This Hamiltonian has no electron-electron interactions and, thus, its eigenstates can be expressed in the form of Slater determinants

$$\Psi_s(\boldsymbol{r}) = \frac{1}{\sqrt{N!}} SD[\phi_{1,s}(\boldsymbol{r}_1) \phi_{2,s}(\boldsymbol{r}_2) \dots \phi_{N_s,s}(\boldsymbol{r}_{N_s}) \tag{2.37}$$

where the occupation numbers have been chosen to be 1 for $ileqN_s(s = 1, 2)$ and 0 for $i > N_s$. This means that the density is written as[25]

$$\rho(\boldsymbol{r}) = \sum_{s=1}^{2} \sum_{i=1}^{N_2} |\phi_{i,s}(\boldsymbol{r}_i)|^2 \tag{2.38}$$

while the kinetic term is

$$T_R[\rho] = \sum_{s=1}^{2} \sum_{i=1}^{N_s} \langle \phi_{I,s} | -\frac{\nabla^2}{2} | \phi_{I,s} \rangle \tag{2.39}$$

The single-particle orbitals $\{\phi_{i,s}(\boldsymbol{r})\}$ are the N_s lowest eigenfunctions of $\hat{h}_R = -(\nabla^2/2) + v_R(\boldsymbol{r})$, that is,

$$\Big\{ -\frac{\nabla^2}{2} + v_R(\boldsymbol{r}) \Big\} \phi_{i,s}(\boldsymbol{r}) = \varepsilon_{i,s} \phi_{i,s}(\boldsymbol{r}) \tag{2.40}$$

Using $T_R[\rho]$, the universal density functional can be rewritten in the following form:[25]

$$F[\rho] = T_R[\rho] + \frac{1}{2} \int \int \frac{\rho(\boldsymbol{r})\rho(\boldsymbol{r}')}{|\boldsymbol{r} - \boldsymbol{r}'|} d\boldsymbol{r} d\boldsymbol{r}' + E_{XC}[\rho] \tag{2.41}$$

where this equation defines the exchange and correlation energy as a functional of the density. The fact that $T_R[\rho]$ is the kinetic energy of the noninteracting reference system implies that the correlation piece of the true kinetic energy has been ignored and has to be taken into account somewhere else. In practice, this is done by redefining the correlation energy functional in such a way as to include kinetic correlations. Upon substitution of this expression for F in the total energy functional $E_v[\rho] = F[\rho] + \int \rho(\boldsymbol{r}) v(\boldsymbol{r}) d\boldsymbol{r}$, the latter is usually renamed the KS functional:

$$E_{KS}[\rho] = T_R[\rho] + \int \rho(\boldsymbol{r}) v(\boldsymbol{r}) d\boldsymbol{r} + \frac{1}{2} \int \int \frac{\rho(\boldsymbol{r})\rho(\boldsymbol{r}')}{|\boldsymbol{r} - \boldsymbol{r}'|} d\boldsymbol{r} d\boldsymbol{r}' + E_{XC}[\rho] \tag{2.42}$$

In this way the density functional is expressed in terms of the $N = N_\uparrow + N_\downarrow$ orbitals (KS orbitals), which minimize the kinetic energy under the fixed density constraint. In principle, these orbitals are a mathematical object constructed in order to render the problem more tractable and do not have a sense by themselves, but only in terms of the density. In practice, however, it is customary to consider them as single-particle physical eigenstates. It is usual to hear that the KS orbitals are meaningless and cannot be identified as single-particle eigenstates, especially in the context of electronic excitations. A rigorous treatment, however, shows that KS eigenvalues differences are a well-defined approximation to excitation energies.[25]

Minimizing the KS functional over all densities that integrate to N particles via the introduction of a Lagrange multiplier μ_R, it is shown that KS orbitals satisfy equation (2.40),

$$N = \int \tilde{\rho}(\boldsymbol{r}) d\boldsymbol{r} \tag{2.43}$$

$$\delta\{E[\tilde{\rho}(\boldsymbol{r})] + \mu(N - \int \tilde{\rho}(\boldsymbol{r}) d\boldsymbol{r}\} = 0 \qquad \Rightarrow \tag{2.44}$$

$$\delta E[\tilde{\rho}(\boldsymbol{r})] - \mu\delta \int \tilde{\rho}(\boldsymbol{r}) d\boldsymbol{r} = 0 \qquad \Rightarrow \tag{2.45}$$

$$\int \delta\tilde{\rho}(\boldsymbol{r})\Big\{\frac{\delta T_R[\tilde{\rho}]}{\delta\tilde{\rho}(\boldsymbol{r})} + v(\boldsymbol{r}) + \int \frac{\tilde{\rho}(\boldsymbol{r}')}{|\boldsymbol{r} - \boldsymbol{r}'|} d\boldsymbol{r}' + \frac{\delta E_{XC}[\tilde{\rho}]}{\delta\tilde{\rho}(\boldsymbol{r})} - \mu_R\Big\} d\boldsymbol{r} = 0 \tag{2.46}$$

For the minimizing (i.e., correct) density ρ,

$$\frac{\delta T_R[\rho]}{\delta\rho(\boldsymbol{r})} + v(\boldsymbol{r}) + \int \frac{\rho(\boldsymbol{r}')}{|\boldsymbol{r} - \boldsymbol{r}'|} d\boldsymbol{r}' + \frac{\delta E_{XC}[\rho]}{\delta\rho(\boldsymbol{r})} = \mu_R \tag{2.47}$$

The functional derivative $\frac{\delta T_R[\rho]}{\delta\rho(\boldsymbol{r})}$ can be quickly found by considering the non-interacting Hamiltonian $\hat{H}_R$ Eq.(2.36). Its ground state energy is E_0. Considering the following functional,

$$E_{v_R}[\tilde{\rho}] = T_R[\tilde{\rho}] + \int \tilde{\rho}(\boldsymbol{r}) v_R(\boldsymbol{r}) d\boldsymbol{r} \tag{2.48}$$

Then, clearly $E_{v_R}[\tilde{\rho}] \geq E_0$, and only for the correct density ρ we will have $E_{v_R}[\rho] = E_0$. Hence, the functional derivative of $E_{v_R}[\tilde{\rho}]$ must vanish for the correct density leading to

$$\frac{\delta T_R[\rho]}{\delta\rho(\boldsymbol{r})} + v_R(\boldsymbol{r}) = \mu_R \tag{2.49}$$

where μ_R is the chemical potential for the non-interacting system.

By comparison of (2.47) and (2.49), the effective potential v_R or v_{eff} is given by

$$v_{eff} = v(\boldsymbol{r}) + \int \frac{\rho(\boldsymbol{r}')}{|\boldsymbol{r} - \boldsymbol{r}'|} d\boldsymbol{r}' + \mu_{XC}[\rho](\boldsymbol{r}) \tag{2.50}$$

The exchange-correlation potential $\mu_{XC}[\rho](\boldsymbol{r})$ defined above is simply the functional derivative of the exchange-correlation energy $\frac{\delta E_{XC}[\rho]}{\delta\rho(\boldsymbol{r})}$. Notice the similitude between the KS and Hartree equations (equation 2.9). According to (2.49), the equations of the interacting electrons under the external potential $v(\boldsymbol{r})$ take the form of non-interacting electrons moving in an effective potential $v_{eff}(\boldsymbol{r})$. Thus, the KS orbitals must obey a set of equations as (2.9), the *Kohn-Sham equations* shown in (2.40) The solution of the KS equations has to be obtained by an iterative procedure. That is, one makes an initial guess (from scratch) for the KS orbitals to build an initial $\rho_0(\boldsymbol{r})$ which, in turn, is used to obtain the corresponding v^0_{eff} (and total energy E^0_{KS}). The equations are solved and a new set of KS orbitals is obtained to give place to a new $\rho_1(\boldsymbol{r})$, v^1_{eff}, and E^1_{KS}. The procedure is repeated until two consecutive $\rho_i(\boldsymbol{r})$ and $\rho_{i+1}(\boldsymbol{r})$ give rise to E^i_{KS} and E^{i+1}_{KS} that differ by less than certain desired and p-reestablished threshold value.

In the same way as Hartree and HF equations, until (2.49) is satisfied. As in these methods, the total energy cannot be written simply as the sum of the eigenvalues $\varepsilon_{i,s}$, but double counted terms have to be subtracted:[25]

$$E_{KS}[\rho] = \sum_{i=1}^{N_s}\sum_{s=1}^{2}\varepsilon_{i,s} - \frac{1}{2}\int\int\frac{\rho(\boldsymbol{r})\rho(\boldsymbol{r}')}{|\boldsymbol{r}-\boldsymbol{r}'|}d\boldsymbol{r}d\boldsymbol{r}' + \left\{E_{XC}[\rho] - \int\rho(\boldsymbol{r})\mu_{XC}[\rho](\boldsymbol{r})d\boldsymbol{r}\right\} \quad (2.51)$$

The main difference between the KS and Hartree equations is that the effective potential now includes exchange and correlation. Therefore, the computational cost is of the same order as Hartree, but much less than HF, which includes the exact non-local exchange. Now let us make some observations:

1. The correlation functional has to be modified to account for the missing part in the kinetic energy $T_R[\rho]$, which corresponds to a non-interacting system. The exchange functional remains unchanged.

2. Nothing ensures that the non-interacting reference system will always exist. In fact, there are examples like the carbon dimer C_2, which do not satisfy this requirement. In that case, a linear combination of Slater determinants that include single-particle eigenstates $\phi_{i,s}(\boldsymbol{r})$ with $i > N_s$ can be considered. This is equivalent to extending the domain of defini-

tion of the occupation numbers $n_{i,s}$ from the integer values 0 and 1 to a continuum between 0 and 1 to include excited single-particle states in the density.[25] Although there is nothing wrong, in principle, with minimizing the functional constructed with fractional occupation numbers, the minimization with respect to them is not justified.[25] The introduction of excited single-particle states does not mean that the system is in a true excited state. This is only an artefact of the representation. The true wave function is the correlated ground state.

3. The density of the non-interacting reference system is equal to that of the true interacting system. Up to here, the theory is exact. No approximation has been introduced into the electronic problem. All the ignorance about the many-fermion problem has been displaced to the $E_{XC}[\rho]$ term, while the remaining terms in the energy are well known.

2.2.5 Exchange and correlation

If the exact expression for the kinetic energy including Coulomb correlation effects, $T[\rho] = \langle \Psi[\rho] \,|\, \hat{T} \,|\Psi[\rho]\rangle$ (with $\Psi[\rho]$ being the interacting ground state of the external potential that has ρ as the ground state density), were known, then one could use the original definition of the exchange-correlation energy that does not contain kinetic contributions:

$$E^0_{XC}[\rho] = \frac{1}{2}\int\int \frac{\rho(\boldsymbol{r})\rho(\boldsymbol{r}')}{|\boldsymbol{r}-\boldsymbol{r}'|}[g(\boldsymbol{r},\boldsymbol{r}')-1]d\boldsymbol{r}d\boldsymbol{r}' \tag{2.52}$$

Then, provided that the ground state total energy is the same for the interacting and non-interacting system, the kinetic energy of the non-interacting system can be redefined in the following way:

$$E_{XC}[\rho] = E^0_{XC}[\rho] + T[\rho] - T_R[\rho]$$

It can be shown that the kinetic contribution to the correlation energy (the kinetic contribution to exchange is just Pauli's principle, which is already contained in $T_R[\rho]$ and in the density when adding up the contributions of the N lowest eigenstates) can be taken into account by averaging the pair correlation function $g(\boldsymbol{r},\boldsymbol{r}')$ over the strength of the

electron-electron interaction, that is,

$$E_{XC}[\rho] = \frac{1}{2}\int\int \frac{\rho(\boldsymbol{r})\rho(\boldsymbol{r}')}{|\boldsymbol{r}-\boldsymbol{r}'|}[\tilde{g}(\boldsymbol{r},\boldsymbol{r}')-1]d\boldsymbol{r}d\boldsymbol{r}' \tag{2.53}$$

where

$$\tilde{g}(\boldsymbol{r},\boldsymbol{r}') = \int_0^1 g_\lambda(\boldsymbol{r},\boldsymbol{r}')d\lambda \tag{2.54}$$

and $g_\lambda(\boldsymbol{r},\boldsymbol{r}')$ is the pair correlation function corresponding to the Hamiltonian $\hat{H} = \hat{T} + \hat{V} + \lambda\hat{U}_{ee}$. If the Fermi and Coulomb correlation are (artificially) separated, we can use Eq.(2.21) and write

$$\tilde{g}(\boldsymbol{r},\boldsymbol{r}') = 1 - \frac{\sum_\sigma|\rho_\sigma(\boldsymbol{r},\boldsymbol{r}')|^2}{\rho(\boldsymbol{r})\rho(\boldsymbol{r}')} + \tilde{g}_C(\boldsymbol{r},\boldsymbol{r}') \tag{2.55}$$

with $\rho_\sigma(\boldsymbol{r},\boldsymbol{r}')$ the spin-up and spin-down components of the one-body density matrix, which in general is a non-diagonal operator. For the homogeneous electron gas, the expression for the density matrix is well known, so that the exchange contribution to $\tilde{g}(\boldsymbol{r},\boldsymbol{r}')$ assumes an analytic closed form[25]

$$g_X(\boldsymbol{r},\boldsymbol{r}') = g_X(|\boldsymbol{r}-\boldsymbol{r}'|) = 1 - \frac{9}{2}\Big(\frac{j_1(k_F(|\boldsymbol{r}-\boldsymbol{r}'|)}{k_F|\boldsymbol{r}-\boldsymbol{r}'|}\Big)^2 \tag{2.56}$$

where $j_1(x) = [sin(x) - xcos(x)]/x^2$ is the first-order spherical Bessel function. The same function within the Hartree approximation is the constant function 1, because the approximation completely neglects both, exchange and correlation, so that one electron is insensitive to the location of the other electron. Within the HF approximation, the exchange is treated exactly, but the correlation is ignored. Therefore, the HF pair distribution only reveals the fact that the electrons with like spins do not like to be at the same place, and hence the HF pair correlation function is given by formula tending to the limit 1/2 for $\boldsymbol{r} \to 0$.

One then can define the exchange-correlation hole $\tilde{\rho}_{XC}(\boldsymbol{r},\boldsymbol{r}')$ in the following form:

$$E_{XC}[\rho] = \frac{1}{2}\int\int \frac{\rho(\boldsymbol{r})\tilde{\rho}_{XC}(\boldsymbol{r},\boldsymbol{r}')}{|\boldsymbol{r}-\boldsymbol{r}'|}d\boldsymbol{r}d\boldsymbol{r}' \tag{2.57}$$

where $\tilde{\rho}_{XC}(\boldsymbol{r},\boldsymbol{r}') = \rho(\boldsymbol{r}')[\tilde{g}(\boldsymbol{r},\boldsymbol{r}')-1]$

Then, $\tilde{E}_{XC}[\rho]$ can be written as the interaction between the electronic charge distribution and the charge distribution that has been displaced by exchange and correlation effects, that is, by the fact that the presence of an electron at $\boldsymbol{r}$ reduces the probability for a second electron to be at $\boldsymbol{r}'$, in the vicinity of $\boldsymbol{r}$. Actually, $\tilde{\rho}_{XC}(\boldsymbol{r},\boldsymbol{r}')$ is the exchange-correlation hole averaged over the strength of the interaction, which takes into account kinetic correlations.[25] The properties of $\tilde{g}(\boldsymbol{r},\boldsymbol{r}')$ and $\tilde{\rho}_{XC}(\boldsymbol{r},\boldsymbol{r}')$,

1. $\tilde{g}(\boldsymbol{r},\boldsymbol{r}') = \tilde{g}(\boldsymbol{r}',\boldsymbol{r})$ (symmetry)
2. $\int \tilde{g}(\boldsymbol{r},\boldsymbol{r}')\rho(\boldsymbol{r}')d\boldsymbol{r}' = N-1$ (normalization)
3. $\int \tilde{\rho}_{XC}(\boldsymbol{r},\boldsymbol{r}')d\boldsymbol{r}' = -1$,

mean that the exchange-correlation hole contains exactly *one* displaced electron. This sum rule is very important and it has to be verified by any approximation.[25]

2.2.6 The local density approximation

It was proposed by Kohn and Sham,[30] but the philosophy was already present in Thomas-Fermi theory.[25,28] The main idea is to consider general inhomogeneous electronic systems as locally homogeneous, and then to use the exchange-correlation hole corresponding to the homogeneous electron gas for which there are very good approximations and also exact numerical results. This means that (see Eq. 2.57)

$$\tilde{\rho}_{XC}^{LDA}(\boldsymbol{r},\boldsymbol{r}') = \rho(\boldsymbol{r})(\tilde{g}^h[|\boldsymbol{r}-\boldsymbol{r}'|,\rho(\boldsymbol{r})]-1) \tag{2.58}$$

with $\tilde{g}^h[|\boldsymbol{r}-\boldsymbol{r}'|,\rho(\boldsymbol{r})]$ the pair correlation function of the homogeneous gas, which depends only on the distance between $\boldsymbol{r}$ and $\boldsymbol{r}'$, evaluated at the density ρ^h, which locally equals $\rho(\boldsymbol{r})$. Within this approximation, the exchange-correlation energy density is defined as

$$\varepsilon_{XC}^{LDA}[\rho] = \frac{1}{2}\int \frac{\tilde{\rho}_{XC}^{LDA}(\boldsymbol{r},\boldsymbol{r}')}{|\boldsymbol{r}-\boldsymbol{r}'|}d\boldsymbol{r}' \tag{2.59}$$

and the exchange-correlation energy becomes

$$E_{XC}^{LDA}[\rho] = \int \rho(\boldsymbol{r})\varepsilon_{XC}^{LDA}[\rho]d\boldsymbol{r} \tag{2.60}$$

In general, the exchange-correlation energy density is not a local functional of ρ. From its very definition it is clear that it has to be a non-local object, because it reflects the fact that the probability of finding an electron at $\boldsymbol{r}$ depends on the presence of other electrons in the surroundings, through the exchange-correlation hole.

The exact expression would indicate to take $\rho(\boldsymbol{r}')$ instead of $\rho(\boldsymbol{r})$. However, this would render $E_{XC}^{LDA}[\rho]$ a non-local object that would depend on the densities at $\boldsymbol{r}$ and $\boldsymbol{r}'$, while the idea is to parameterize it with the homogeneous gas, which is characterized by only one density, and not two.

For the exchange energy density, the form deduced by Dirac is adopted:[25]

$$\varepsilon_X[\rho] = -\frac{3}{4}\left(\frac{3}{\pi}\right)^{1/3}\rho^{1/3} = -\frac{3}{4}\left(\frac{9}{4\pi^2}\right)^{1/3}\frac{1}{r_s} = -\frac{0.458}{r_s}au \tag{2.61}$$

where $\rho^{-1} = 4\pi r_s^3$ and r_s is the radius of the sphere that, on average, contains one electron. For the correlation, a widely used approximation is Perdew and Zunger's parameterization[32] of Ceperley and Alder quantum Monte Carlo results, which are essentially exact,[25]

$$\varepsilon_C[\rho] = \begin{cases} A\,ln\,r_s + B + C\,r_s\,ln\,r_s + Dr_s, & r_z \leq 1 \\ \gamma/(1+\beta_1\sqrt{r_s} + \beta_2 r_s), & r_s > 1 \end{cases}$$

For low densities, Perdew and Zunger have fitted a different (Padé) approximation to the Monte Carlo results.[25] Interestingly, the second derivative of the above $\varepsilon_C[\rho]$ is discontinuous at $r_s = 1$. Another popular parameterization is that of Hedin and Lundqvist.[33]

The LDA has been applied successfully for many systems of interest, especially those where the electronic density is quite uniform such as bulk metals, but also for less uniform systems as semiconductors and ionic crystals. There are a number of features of the LDA that are rather general and well established by now.[25] In Chapter 6 we will witness some of them.

1. It favors more homogeneous systems.

2. It overbinds molecules and solids.

3. For "good" systems (covalent, ionic and metallic bonds), geometries are good, bond lengths, bond angles and phonon frequencies are within a few percent, while dielectric properties are overestimated by about 10 %

4. For "bad" systems (weakly bound), bond lengths are too short (overbinding).

5. In finite systems, the XC potential does not decay as -e^2/r in the vacuum region, thus affecting the dissociation limit and ionization energies. This is a consequence of the fact that LDA fails to cancel the self-interaction included in the Hartree term of the energy, which is one of the most severe limitations of these approximations.

And, as we will see, LDA fails[25]

1. In atomic systems, where the density has large variations, and also the self-interaction is important.

2. In weak molecular bonds, for example, hydrogen bonds, because in the bonding region the density is very small and the binding is dominated by inhomogeneities.

3. In van der Waals (closed-shell) systems, because there the binding is due to dynamical charge-charge correlations between two separated fragments, and this is an inherently non-local interaction.

4. In metallic surfaces, because the XC potential decays exponentially, while it should follow a power law (image potential).

5. The energy band gap in semiconductors turns out to be very small. The reason is that when one electron is removed from the ground state, the exchange hole becomes screened, and this is absent in the LDA. On the other hand, HF also has the same limitation, but the band gap turns out to be too large.

There is not a unique and obvious way of improving the LDA.[25] The most popular approach has been to introduce semi-locally the inhomogeneities of the density, by expanding $E_{XC}[\rho]$ as a series in terms of the density and its gradients. This approach, known as generalized gradient approximation (GGA), has been quite successful in improving over

some features of the LDA, though there are many other cases in which LDA renders better results.[25,34]

2.2.7 Generalized gradient approximation

The exchange-correlation energy has a gradient expansion of the type

$$E_{XC}[\rho] = \int A_{XC}[\rho]\rho(\boldsymbol{r})^{4/3}d\boldsymbol{r} + C_{XC}[\rho]|\nabla\rho(\boldsymbol{r})|^2/\rho(\boldsymbol{r})^{4/3}d\boldsymbol{r} + \ldots \tag{2.62}$$

which is asymptotically valid for densities that vary slowly in space. The LDA retains only the leading term of equation (2.62). A straightforward evaluation of this expansion is ill-behaved, in the sense that it is not monotonically convergent, and it exhibits singularities that cancel out only when an infinite number of terms is re-summed.[25] In fact, the first-order correction worsens the results and the second-order correction is plagued with divergences.[25] The largest error of this approximation actually arises from the gradient contribution to the correlation term. Provided that the problem of the correlation term can be cured in some way, as the real space cut-off method proposed by Langreth and Mehl,[35] the biggest problem remains with the exchange energy.

The gradient expansion has to be carried out very carefully in order to retain all the relevant contributions to the desired order.[25] GGA expansions easily violate one or more of the exact conditions required for the exchange and the correlation holes. For instance, the normalization condition, the negativity of the exchange density (see above) and the self-interaction cancellation (the diagonal of the exchange density matrix has to be minus a half of the density). Perdew has shown that imposing these conditions to functionals that originally do not verify them results in a remarkable improvement of the quality of exchange energies.[25]

The basic idea of GGA is to express the exchange-correlation energy in the following form:[25]

$$E_{XC}[\rho] = \int \varepsilon_{XC}[\rho(\boldsymbol{r})]\rho(\boldsymbol{r})d\boldsymbol{r} + \int F_{XC}[\rho(\boldsymbol{r}), \nabla\rho(\boldsymbol{r})]d\boldsymbol{r} \tag{2.63}$$

where the function F_{XC} is required to satisfy a number of conditions for the exchange-correlation hole, such as sum rules, long-range decay and so on.[25] This cannot be done by considering directly the bare gradient expansion (2.62). What is needed from the functional is a form that mimics a re-summation to infinite order, and this is the main idea of the GGA, for which there is not a unique recipe,[25] and so not all the formal properties can be enforced at the same time, which differentiates one functional from another.[25] In Chapters 4 - 6, we use either one of the next two expressions:

1. Perdew-Wang '91 (PW91) exchange functional.[36]

$$\varepsilon_X = \varepsilon_X^{LDA}\Big(\frac{1 + a_1 s\, sinh^{-1}(a_2 s) + (a_3 + a_4 e^{-100s^2})s^2}{1 + a_1 s\, sinh^{-1}(a_2 s) + a_5 s^4}\Big)$$

where $a_1 = 0.19645$, $a_2 = 7.7956$, $a_3 = 0.2743$, $a_4 = -0.1508$, and $a_5 = 0.004$.

Perdew-Wang '91 (PW91) correlation functional.[36]

$$\varepsilon_C = \varepsilon_C^{LDA} + \rho H[\rho, s, t]$$

with

$$H[\rho, s, t] = \frac{\beta}{2\alpha} ln\Big(1 + \frac{2\alpha}{\beta}\frac{t^2 + At^4}{1 + At^2 + A^2t^4}\Big) + C_{c0}[C_c(\rho) - C_{c1}]t^2 e^{-100s^2}$$

and

$$A = \frac{2\alpha}{\beta}\Big[e^{-2\alpha\varepsilon_C[\rho]/\beta^2} - 1\Big]^{-1}$$

where $\alpha = 0.09$, $\beta = 0.0667263212$, $C_{c0} = 15.7559$, $C_{c1} = 0.003521$, $t = |\nabla\rho(\boldsymbol{r})|/(2k_s\rho)$ for $k_s = (4k_F/\pi)^{1/2}$, and $\rho\varepsilon_C[\rho] = \varepsilon_C^{LDA}[\rho]$.

2. Perdew-Burke-Ernzerhof (PBE) exchange-correlation functional.([37])

First, the enhancement factor F_{XC} over the local exchange is defined:

$$E_{XC}[\rho] = \int \rho(\boldsymbol{r})\varepsilon_X^{LDA}[\rho(\boldsymbol{r})]F_{XC}(\rho, \zeta, s)d\boldsymbol{r}$$

where ρ is the local density, ζ is the relative spin polarization and $s = |\nabla\rho(\boldsymbol{r})|/(2k_F\rho)$ is the dimensionless gradient,[25,36]

$$F_X(s) = 1 + \kappa - \frac{\kappa}{1 + \mu s^2/\kappa}$$

where $\mu = \beta(\pi^2/3) = 0.21951$ and $\beta = 0.066725$ is related to the second-order gradient expansion.[25,36] The correlation energy is written

The correlation functional is[25,37]

$$E_C^{GGA} = \int \rho(\boldsymbol{r})[\varepsilon_C^{LDA}(\rho,\zeta) + H[\rho,s,t]]d\boldsymbol{r}$$

with

$$H[\rho,s,t] = \left(\frac{e^2}{a_0}\right)\gamma\phi^3 ln\Big\{1 + \frac{\beta\gamma^2}{t}[\frac{1+At^2}{1+At^2+A^2t^4}$$

where $t = |\nabla\rho(\boldsymbol{r})|/(2k_s\rho)$ is a dimensionless density gradient, $k_s = (4k_F/\pi a_0)^{1/2}$ is the TF screening wave number and $\phi(\zeta) = [(1+\zeta)^{2/3} + (1-\zeta)^{2/3}]/2$ is a spin-scaling factor. The quantity β is the same as for the exchange term, $\beta = 0.066725$, and $\gamma = (1 - ln2)/\pi^2 = 0.031091$. The function A has the following form:

$$A = \frac{\beta}{\gamma}\Big[e^{-\varepsilon_C^{LDA}[\rho]/(\gamma\phi^3 e^2/a_0)} - 1\Big]^{-1}$$

So defined, the correlation correction term H tends to the correct second-order gradient expansion in the slowly varying (high-density) limit, $(t \to 0)$,[25] approaches minus the uniform electron gas correlation $-\varepsilon_C^{LDA}$ for rapidly varying densities $(t \to \infty)$,[25] thus making the correlation energy to vanish, and cancels the logarithmic singularity of ε_C^{LDA} in the high-density limit, thus forcing the correlation energy to scale to a constant under uniform scaling of the density. This GGA retains the correct features of LDA and combines them with the inhomogeneity features that are supposed to be the most energetically important. It sacrifices, in turn, the correct second-order gradient coefficients in the slowly varying limit, and the correct non-uniform scaling of the exchange energy in the rapidly varying density region.[25,37] GGA-PBE is very satisfactory from both the theoretical point of view, because it verifies many of the exact conditions for the XC hole and it does not contain any fitting parameters, and the applied point of view, as we will find in Chapter 6.

The general trends of GGA, concerning improvements over the LDA, are the following:[25]

1. They improve binding energies and also atomic energies.

2. They improve bond lengths and angles.

3. They improve energetics, geometries and dynamical properties of water, ice and water clusters.

4. Semiconductors are marginally better described within the LDA than in GGA, except for the binding energies.

5. For 4d-5d transition metals, the improvement of the GGA over LDA is not clear and will depend on how well the LDA does in the particular case. We have observed[38] with Hedin-Lundqvist-LDA that bulk Ag and the Ag(001) are well described by both LDA and GGA, while the CO adsorption site and binding energy trend is quite different, as in the case of Cu(001).

6. Lattice constants of noble metals (Cu, Ag, Au, Pt) are overestimated. The LDA values are very close to experiment, and thus any modification can only worsen them. However, we will see in Chapter 6 that the lattice dynamics of bulk Cu (and Ag)[38], as well as that of the (001) clean and CO-chemisorbed surfaces are described better by GGA than by LDA.

7. There is some improvement for the gap problem (and consequently for the dielectric constant), but it is not substantial because this feature is related to the description of the screening of the exchange hole when one electron is removed, and this feature is usually not fully taken into account by GGA.

8. They do not satisfy the known asymptotic behavior, for example, for isolated atoms: (a) $v_{XC}(\boldsymbol{r}) \sim -\mathrm{e}^2/r$ for $r \to \infty$, while $v_{XC}^{LDA,GGA}(\boldsymbol{r})$ vanish exponentially. (b) $v_{XC}(\boldsymbol{r}) \to$ const. for $r \to 0$, while $v_{XC}^{LDA}(\boldsymbol{r}) \to$ const., but $v_{XC}^{GGA}(\boldsymbol{r}) \to -\infty$.

There seems, then, to exist a limit in the accuracy that GGA can reach. The main aspect responsible for this is the exchange term, whose non-locality is not fully taken into account. A particularly problematic issue is that GGA functionals still do not compensate the self-interaction completely.[25]

2.3 Handling of the infinite electronic- and ionic- system: Periodicity

In the preceding section, we have seen that we can get around the electronic problem by solving as many one-particle KS-equations (see Eq. 2.40)as the number of electrons in the studied system (for magnetic system this amount is duplicated since wave functions with spin up and spin down a treated separately). However, this problem becomes computationally impossible since bulk and surface materials are composed of practically an infinite number of electrons moving in the static of potential of an infinite number of nuclei. Two difficulties must be overcome:[7] a wave function must be calculated for each of the infinite number of electrons in the system and, since each electronic wave function extends over the entire solid, the basis set required to expand (plane waves, for example) each KS-orbital is infinite. Both problems can be surmounted by performing calculation o periodic systems and applying Bloch.s theorem to the KS-orbitals.

2.3.1 Bloch's theorem

In a perfect crystal, the nuclei are arranged in a regular periodic array described by a set of Bravais lattice vectors $\{\boldsymbol{R}_i\}$. In an infinite system, the external potential and the charge density at a certain point $\boldsymbol{r}$ are thus invariant under translation by any of these lattice vectors $\{\boldsymbol{R}_i\}$. Therefore, the effective KS-potential in Eq. 2.40 (for the sake of clarity we will drop the subscript R in the KS-potential, and the spin and orbital number indices, s and i, respectively, in the KS-orbitals), rewritten here as,

$$\hat{h}_{KS}(\boldsymbol{r})\phi(\boldsymbol{r}) = \Big\{ -\frac{\nabla^2}{2} + v(\boldsymbol{r}) \Big\}\phi(\boldsymbol{r}) = \varepsilon\phi(\boldsymbol{r}) \tag{2.64}$$

is also periodic; that is,

$$v(\boldsymbol{r} + \boldsymbol{R}_i) = v(\boldsymbol{r}) \qquad \forall\, \boldsymbol{R}_i \tag{2.65}$$

The translation operator $\hat{T}_{\boldsymbol{R}_i}$ for each lattice vector $\boldsymbol{R}_i$ acts in the following manner on

any position-dependent function $f(\boldsymbol{r})$:[28]

$$\hat{T}_{\boldsymbol{R}_i} f(\boldsymbol{r}) = f(\boldsymbol{r} + \boldsymbol{R}_i) \tag{2.66}$$

and is then periodic as the KS-potential and the Hamiltonian, $\hat{h}_{KS}(\boldsymbol{r} + \boldsymbol{R}_i) = \hat{h}_{KS}(\boldsymbol{r})$, for which $\hat{T}_{\boldsymbol{R}_i}$ and $\hat{h}_{KS}$ commute.[28] Translation operators commute with each other as well, so

$$\hat{T}_{\boldsymbol{R}_i} \hat{T}_{\boldsymbol{R}_j} = \hat{T}_{\boldsymbol{R}_i + \boldsymbol{R}_j} \tag{2.67}$$

Therefore the eigenfunctions of $\hat{T}_{\boldsymbol{R}_i}$ must be also eigenfunctions of $\hat{h}_{KS}(\boldsymbol{r})$.

Consider thus that $c(\boldsymbol{R}_i)$ are the eigenvalues of $\hat{T}_{\boldsymbol{R}_i}$, then

$$\hat{T}_{\boldsymbol{R}_i} \phi(\boldsymbol{r}) = \phi(\boldsymbol{r} + \boldsymbol{R}_i) = c(\boldsymbol{R}_i)\phi(\boldsymbol{r}) \tag{2.68}$$

and, from (2.67), we obtain that

$$\hat{T}_{\boldsymbol{R}_i} \hat{T}_{\boldsymbol{R}_j} \phi(\boldsymbol{r}) = \hat{T}_{\boldsymbol{R}_i + \boldsymbol{R}_j} \phi(\boldsymbol{r}) = c(\boldsymbol{R}_i) c(\boldsymbol{R}_j) \phi(\boldsymbol{r}) = c(\boldsymbol{R}_i + \boldsymbol{R}_j) \phi(\boldsymbol{r}) \tag{2.69}$$

Since $\phi(\boldsymbol{r})$ is normalized to the same value as $\phi(\boldsymbol{r} + \boldsymbol{R}_i)$, $\hat{T}_{\boldsymbol{R}_i}$ must be unitary and $|c(\boldsymbol{R}_i)|^2 = 1$. Then, we can expand the translation operator[21]

$$\hat{T}_\xi \phi(x) = \phi(x - \xi) = \phi(x) - \frac{\xi}{1!}\phi'(x) + \frac{\xi^2}{2!}\phi''(x) \pm \cdots = exp\Big(- \xi \frac{\partial}{\partial x} \phi(x) \Big) \qquad \Rightarrow$$

$$\hat{T}_\xi \phi(x) = exp(-i\xi \hat{k}) \phi(x) \qquad \text{where} \qquad \hat{k} = \frac{1}{i} \frac{\partial}{\partial x} \tag{2.70}$$

and is proportional to the momentum operator p_x. Then, since displacements in three dimensions commute and may be carried out equivalently in any order, (2.70) is generalized to

$$\hat{T}_{\boldsymbol{R}_i} \phi(\boldsymbol{r}) = e^{i\hat{\boldsymbol{k}} \cdot \boldsymbol{R}_i} \phi(\boldsymbol{r}) = e^{i\boldsymbol{k} \cdot \boldsymbol{R}_i} \phi(\boldsymbol{r}) \tag{2.71}$$

leading us to Bloch's theorem,

$$\hat{T}_{\boldsymbol{R}_i} \phi(\boldsymbol{r}) = \phi(\boldsymbol{r} + \boldsymbol{R}_i) = e^{i\boldsymbol{k} \cdot \boldsymbol{R}_i} \phi(\boldsymbol{r}) \tag{2.72}$$

The eigenvalues of $\hat{T}_{\boldsymbol{R}_i}$, $e^{i\boldsymbol{k} \cdot \boldsymbol{R}_i}$, are "good" quantum numbers since $\hat{T}_{\boldsymbol{R}_i}$ commutes with $\hat{h}_{KS}(\boldsymbol{r})$. We can then label with the indices $\boldsymbol{k}$ and n to those which are simultaneously eigenfunctions of $\hat{T}_{\boldsymbol{R}_i}$ and $\hat{h}_{KS}(\boldsymbol{r})$, respectively.

2.3.2 The Plane-waves description of KS-orbitals

The KS orbitals are not periodic, however, it turns out that the function $u_{\boldsymbol{k}}(\boldsymbol{r}) = e^{-i\boldsymbol{k}\cdot\boldsymbol{r}}\phi_{n,\boldsymbol{k}}(\boldsymbol{r})$, has the periodicity of the lattice:

$$u_{\boldsymbol{k}}(\boldsymbol{r}+\boldsymbol{R}_i) = e^{-i\boldsymbol{k}\cdot[\boldsymbol{r}+\boldsymbol{R}_i]}\phi_{n,\boldsymbol{k}}(\boldsymbol{r}+\boldsymbol{R}_i) = e^{-i\boldsymbol{k}\cdot[\boldsymbol{r}+\boldsymbol{R}_i]}e^{i\boldsymbol{k}\cdot\boldsymbol{R}_i}\phi_{n,\boldsymbol{k}}(\boldsymbol{r}) = e^{-i\boldsymbol{k}\cdot\boldsymbol{r}}\phi_{n,\boldsymbol{k}}(\boldsymbol{r}) = u_{\boldsymbol{k}}(\boldsymbol{r}), \tag{2.73}$$

which means that $u_{\boldsymbol{k}}(\boldsymbol{r})$ can be expanded in a Fourier series over the reciprocal lattice vectors $\{\boldsymbol{G}_j\}$ (where $\boldsymbol{G}_j \cdot \boldsymbol{R}_i = 2\pi m$, and m is an integer)

$$u_{\boldsymbol{k}}(\boldsymbol{r}) = \sum_{\{\boldsymbol{G}_j\}} C_{(\boldsymbol{k},\boldsymbol{G}_j)}\, e^{i\boldsymbol{G}_j\cdot\boldsymbol{r}} \tag{2.74}$$

and $\phi_{n,\boldsymbol{k}}(\boldsymbol{r})$, according with (2.74), can thus expanded in terms of discrete plane-waves,

$$\phi_{n,\boldsymbol{k}}(\boldsymbol{r},\boldsymbol{k}) = \sum_{\{\boldsymbol{G}_j\}} c_{(\boldsymbol{k}+\boldsymbol{G}_j)}\, e^{i(\boldsymbol{k}+\boldsymbol{G}_j)\cdot\boldsymbol{r}} \tag{2.75}$$

KS-orbitals can also be expanded in a mixed set of plane waves and localized wavefunctions (see Chapter 6), which becomes useful to describe the localized parts of valence states. The plane wave expansion, however, has many advantages because the basis is orthonormal, is easy to integrate and does not depend on the positions of the nucleus. By inserting the expression for $\phi_{n,\boldsymbol{k}}$ in (2.75) in the KS equations (2.64) and multiplying from the left by $e^{i(\boldsymbol{k}+\boldsymbol{G}_i)\cdot\boldsymbol{r}}$ and integrating using the orthogonality of the plane waves,

$$\int_V e^{-i\boldsymbol{G}_i\cdot\boldsymbol{r}} e^{i\boldsymbol{G}_j\cdot\boldsymbol{r}} d\boldsymbol{r} = \delta_{ij},$$

a set of equations for the coefficients $c_{\boldsymbol{k}+\boldsymbol{G}_j}$ is obtained:

$$\frac{1}{2}|\boldsymbol{k}+\boldsymbol{G}_j|^2 c_{\boldsymbol{k}+\boldsymbol{G}_j} + \sum_{\boldsymbol{G}_i} V_{\boldsymbol{G}_j,\boldsymbol{G}_i} c_{\boldsymbol{k}+\boldsymbol{G}_i} = E(\boldsymbol{k}) c_{\boldsymbol{k}+\boldsymbol{G}_j} \tag{2.76}$$

where

$$V_{\boldsymbol{G}_j,\boldsymbol{G}_i} = \int_V v(\boldsymbol{r}) e^{i(\boldsymbol{G}_j-\boldsymbol{G}_i)\boldsymbol{r}} d\boldsymbol{r}$$

In principle, an infinite plane-wave basis set is required to expand the electronic wave functions. However, the coefficients $c_{\boldsymbol{k}+\boldsymbol{G}_j}$ for the plane waves with small kinetic energy

$(1/2)|\boldsymbol{k}+\boldsymbol{G}_j|^2$ are typically more important than those with large kinetic energy.[7] Thus the plane-wave basis set can be truncated to include only plane waves that have kinetic energies less than some particular cutoff energy, E_{cut}:

$$\frac{1}{2}|\boldsymbol{k}+\boldsymbol{G}_j|^2 < E_{cut}$$

In practice, several millions of plane waves are required for metallic systems and total energy convergence test must be performed to obtain reliable results. The situation worsens for metals with *semi-core* states which are more localized than the valence band states and require much more plane waves and the mixed-basis approach becomes more convenient.

2.3.3 The problem of an infinite number of k-points: k-point sampling

Electronic states are allowed only at a set of $\boldsymbol{k}$-points determined by the boundary conditions that apply to the bulk solid.[7]. The density of allowed $\boldsymbol{k}$ points is proportional to the volume of the solid. The infinite number of electrons in the solid are thus accounted for an infinite number of $\boldsymbol{k}$-points, and only a finite number of electronic states are occupied at each $\boldsymbol{k}$-point. The introduction of (2.75) reduces then the problem of calculating an infinite number of KS wave functions to one of calculating a finite number of KS wave functions at an infinite number of $\boldsymbol{k}$-points in the first Brillouin zone.[7,28] That is, once the coefficients $c_{\boldsymbol{k}+\boldsymbol{G}_j}$ in (2.76) are calculated, the KS-orbitals at a particular $\boldsymbol{k}$ point may be obtained. The charge density, however, comprehends the integration over the first Brillouin zone (BZ),[7,28]

$$\rho(\boldsymbol{r}) = \sum_{m}^{N_e^{BZ}} \int_{BZ} |\phi_{m,n,\boldsymbol{k}}(\boldsymbol{r},\boldsymbol{k})|^2 d\boldsymbol{k}$$

where m runs over the number of electrons in the BZ.

Since the effective potential is calculated iteratively from ρ, the occupied states at each $\boldsymbol{k}$-point contribute to the potential in the bulk solid so that, in principle, an infinite number of calculations are needed to compute it. However, the KS-wavefunctions at $\boldsymbol{k}$-points that are very close together are almost identical.[7] Hence it is possible to represent the electronic

wave functions over a region of $\boldsymbol{k}$ space by the wave functions at a single $\boldsymbol{k}$ point. Therefore, the electronic states at only a finite number of $\boldsymbol{k}$ points are required to calculate the electronic potential and hence to determine the total energy of the system. Several methods[39] have been devised to obtain accurate approximations to the electronic potential and the contribution to the total energy from material with filled electronic bands at special sets of $\boldsymbol{k}$-points in the Brillouin zone.[7,28] The electronic potential and the total energy are more difficult to calculate if the system is metallic because a dense set of $\boldsymbol{k}$-points is required to define the Fermi surface precisely.[7] To overcome the problem of partially filled bands, the Fermi level smearing technique is used.[40] This allows fractional occupation numbers (substitutes the Heaviside function Θ by a smooth function, see below).[41] In this case, the error induced by the inadequacy of the $\boldsymbol{k}$-point sampling is reduced by using a denser k-point mesh, for which reason convergence tests must be performed for the k-point mesh and the smearing parameter in each particular problem. The charge density (for non-spin polarized calculations) is therefore calculated as follows,

$$\rho(\boldsymbol{r}) = 2 \sum_{m,n,\boldsymbol{k}} w_{\boldsymbol{k}} \Theta(\varepsilon_F - \varepsilon_{n,\boldsymbol{k}}) |\phi_{n,\boldsymbol{k}}|^2 \tag{2.77}$$

where the $w_{\boldsymbol{k}}$ function is the weight of the value $\boldsymbol{k}$ on the calculation of ρ and the Heaviside function assures that the energy of the KS-orbitals is below the Fermi level.[40]

Chapter 3

Effect of dipolar interactions on the magnetization of square and cubic arrays of nanomagnets

3.1 Introduction

The need of smaller memory storage devices,[42–55] the interest in developing quantum computing,[56] and the hope for understanding the relationship between the macroscopic and microscopic magnetic behaviors has led intense research into the properties of nanoscale magnets.[42–73] Many issues still remain unclear and serious problems must be overcome in order for them to be technologically useful. Prominent among these is the loss of memory during magnetic relaxation.

Ferromagnetic nanodots are complex systems consisting of up to hundreds of magnetic atoms within a single dot.[46,52,53] In this case, interparticle interactions along with anisotropy effects dominate the dynamics of the systems, and control the magnetization processes.[49] Moreover, since interdot exchange interactions are negligibly small, the dynamics of the ferromagnetic nanodot arrangements are strongly influenced by dipolar interdot interactions.[54,55]

Single molecule magnets (SMM's) consist of clusters of only a few magnetic ions, and are thus among the smallest and simplest nanomagnets, but are also well-characterized systems exhibiting magnetic hysteresis.[68] In SMM's, the one-body tunnel picture of the magnetiza-

tion mostly explains this phenomenon in the sense that the sequence of discrete steps in those curves provides evidence for resonant coherent quantum tunneling.[69–71] Nevertheless, this one-body tunnel model neglects intermolecular interactions, and is not always sufficient to explain the measured tunnel transitions.[72,73] A close examination of the magnetization curves reveals fine structures which cannot be explained by that model. Wernsdorfer *et al.* suggest that these additional steps are due to collective quantum processes, called spin-spin cross relaxation (SSCR), involving pairs of SMM's which are coupled by dipolar and/or exchange interactions.[72,73] If dipolar and/or exchange interactions cooperate in the relaxation process, then one might hope to be able to better control such loss of magnetic memory.

Analyzing the relaxation of the magnetization is difficult for both SMM's and ferromagnetic nanodots. Besides dipolar interactions, many other factors may be involved in such processes. Geometric features, such as the shape and volume of the magnets, as well as the type of lattice on which they are placed, can directly influence the anisotropy barriers and the easy axis directions. In the case of SMM's, a quantum treatment has to be considered to show that resonant tunneling of the magnetization results in the discrete steps appearing in the low temperature T magnetization curves. Although in many SMM's the intercluster exchange interactions are negligible, as for ferromagnetic nanodots, in other SMM's, such interactions are comparable in strength to the dipolar interactions.[73] Besides the quadratic Heisenberg and quadratic anisotropic intramolecular exchange interactions, some SMM's are thought to contain intramolecular interactions of the Dzyaloshinskii-Moriya type.[74] Additional higher order, anisotropic spin exchange interactions further complicate the problem. Therefore, by studying models that deal with each one of these factors separately, one hopes to simplify the problem, to build up gradually a more realistic system, and at the same time, to elucidate how each of these factors contributes to the magnetization process.

With regard to SMM's, there have been recent approaches to the quantum dynamics of the low-T relaxation.[58,75–80] Prokof'ev and Stamp assumed a single relaxation mode,[75] in which the dipolar and hyperfine fields are frozen unless an SMM flips its spin. Then

by assuming the effective field around each SMM is that of randomly placed dipoles, they obtained an expression for the low-T decrease proportional to t^p of the magnetization of each SMM from its fully magnetized state,[75,81,82] where $p \approx 0.5 - 0.7$, but p might be as large as 0.7.[75–78]. This procedure was restricted to very small deviations of the magnetization from its saturated value, so it is not useful for studying the central portion of the hysteresis curves, for which the magnetization can be small. Moreover, as first argued for ferromagnets by Anderson,[24] the spin-spin and spin-lattice relaxation times can be very different, so that such simple behavior is not expected. In fact, experiments on SMM's have shown that an exponential relaxation of the magnetization is consistent with the data,[79,80] so that as a minimum, one requires two distinct relaxation times for SMM's, which could be very different from one another.[24]

The most commonly studied models of spin dynamics containing two distinct relaxation parameters are the Landau-Lifshitz (LL) equation and the Landau-Lifshitz-Gilbert (LLG) equations (see Chapter 1).[11,12,83] Early studies of square planar lattices of 9 to 36 ferromagnetic dots were made by Stamps and Camley.[84] In addition, Zhang and Fredkin (ZF) studied the LL model to obtain the zero-field time decay of the easy-axis magnetization of a three-dimensional (3D) cubic lattice of 12×12 × 12 Stoner-Wohlfarth particles interacting with each other via dipole-dipole interactions.[55] Since the size (or radius) of the Stoner-Wohlfarth particles was taken to be much less than the lattice constant, they could be treated as point-like magnetic moments, the classical analogue of SMM's. Using the LL equation, Kayali and Saslow (KS) recently also investigated the hysteresis curves at $T = 0$ for $N \times N$ two-dimensional (2D) square arrays with $2 \leq N \leq 14$ at a variety of applied magnetic field H and angles θ relative to the (100) edge of the square array. These curves exhibited hysteresis areas A_N, which KS showed to depend upon θ and N. They included anisotropy effects via an effective field proportional to the z-component of each dot's dipole moment. In order to study the magnetization of ferromagnetic dots, KS used an extremely large value for the damping coefficient, $\alpha/\gamma = 0.6$, a huge sweep rate, $\frac{\Delta B}{\Delta t} \sim 3000$ T/s, and a

small maximum external induction $B_{\rm max} = 2\mu_0 M_s$. Subsequently, Takagaki and Ploog (TP) also studied two-dimensional square arrays of ferromagnetic nanomagnets (or magnetic nanodots) at $T = 0$ with dipolar interdot interactions, but used the fourth-order Runge-Kutta procedure to iterate the LLG equation.[85] TP usually chose the iteration time interval to be much larger than in the second-order method used by KS, allowing TP to study larger values of N. In some cases, the same θ and N values were studied by both KS and TP, but the results presented were not identical. Not only were the A_N values different in the two calculations, the number of magnetization steps in the $M(H)$ hysteresis loops were also different, especially for $N = 5$, as noted by TP.[85]

In our studies of nanomagnet arrays, we used values of α/γ that varied from these values to values 12 orders of magnitude smaller. Depending upon the α values, we also varied the sweep rate $\frac{\Delta B}{\Delta t}$ from those values to the the much smaller $\sim 10^{-3}$ T/s, and varied $B_{\rm max}$ from much larger values (2 T), comparable to those reported in SMM experiments, [64,67] to those used by KS. Similarly, the lattice constants reported in the present work are in accordance with the near neighbor separation in the most extensively studied SMM crystals. We studied only the effects of the interparticle dipole-dipole interactions upon the magnetization curves for an ensemble of $N_c = 25$ 2D square crystals and $N_c = 100$ 3D cubic crystals each containing $N = 5 \times 5$ and $N = 5 \times 5 \times 4$ nanomagnets, respectively, all with the same magnetic moment. As in the ZF model of Stoner-Wohlfarth particles, we take the lattice parameter to be much greater than the nanomagnet size or radius. The strength of the dipole interactions is primarily determined by the lattice constant, a. We also consider that the damping coefficient α can also depend upon T.[18,19] The magnetic moment $\boldsymbol{M}_i^c$ of the ith nanomagnet within the cth crystal of our ensemble obeys

$$\frac{d\boldsymbol{M}_i^c}{dt} \equiv \gamma \boldsymbol{M}_i^c \times \boldsymbol{B}_i^{c,\rm eff} - \frac{\alpha}{M_s} \boldsymbol{M}_i^c \times \left(\boldsymbol{M}_i^c \times \boldsymbol{B}_i^{c,\rm eff} \right), \tag{3.1}$$

$$\boldsymbol{B}_i^{c,\rm eff} = \boldsymbol{B} + \left(\boldsymbol{B}_i^c \right)_{\rm dip}, \tag{3.2}$$

where γ is the gyromagnetic ratio, $M_s = \gamma S$ is the magnetic moment of an individual nanomagnet, and $(\boldsymbol{B}_i^c)_{dip}$ is the contribution to the effective magnetic induction $\boldsymbol{B}_i^{c,\text{eff}}$ at the ith nanomagnet within the cth crystal arising from dipole-dipole interactions between it and the other nanomagnets within the same crystal,

$$\left(\boldsymbol{B}_i^c\right)_{\text{dip}} = \frac{\mu_0}{4\pi} \sum_j{}' \frac{3(\boldsymbol{M}_j^c \cdot \boldsymbol{r}_{ij})\boldsymbol{r}_{ij} - r_{ij}^2 \boldsymbol{M}_j^c}{r_{ij}^5}, \tag{3.3}$$

where the prime indicates that the $j = i$ term is omitted.

3.2 Model system and calculation details

In the present work we consider two ensembles each of $N_c = 5 \times 5 = 25$ (square) of $N = 5 \times 5 \times 4 = 100$ (cubic) crystals (or configurations). Each nanomagnet has a ground state spin $S = 5$, which interact with one another only via dipolar interactions. Except when a strong anisotropy field is present, we assume that there is no long-range order in the T regime of interest, so that in the absence of an external magnetic field, the magnetization of each nanomagnet crystal is essentially zero. We note that long-range ordering was claimed to exist in the cubic system with Ising spin anisotropy.[76,86] In our studies only with a strong anisotropy field $\boldsymbol{H}_A$, hysteresis curves exhibiting a substantial zero-field magnetization were obtained for the applied magnetic induction $\boldsymbol{B} \,||\, \boldsymbol{H}_A$ after the system had been fully magnetized by $\boldsymbol{B}$. Therefore, each of the N_c system configurations $c = 1, \ldots, N_c$ is constructed to have a starting total magnetic moment $\boldsymbol{M}_c \approx 0$ at $\boldsymbol{B} = 0$. The hysteresis curves are obtained for each configuration, and these are then averaged over the N_c configurations. One then obtains the magnetization $\overrightarrow{\mathcal{M}}(B)$ curves, where $\overrightarrow{\mathcal{M}} = \langle \boldsymbol{M}_c \rangle_c / V$ is the configuration averaged magnetization, V is the crystal volume, and $B = |\boldsymbol{B}|$.

3.2.1 Ensemble of random spin configurations

In order to proceed, we first find a large number N_c of random spin configurations c of $N = 25,100$ spins, such that for each configuration, $\boldsymbol{M}_c / M_s \approx 0$ at $\boldsymbol{B} = 0$ and as $T \to \infty$,

where the total magnetic moment

$$\boldsymbol{M}_c(t,\boldsymbol{B}) \;=\; \sum_{i=1}^{N} \boldsymbol{M}_i^c(t,\boldsymbol{B}). \tag{3.4}$$

At the start of the iteration, we take $t = 0$, $\boldsymbol{B} = 0$, and $T \to \infty$ in the absence of the dipole-dipole (or any other inter-spin) interactions for configuration c. Then we select those configurations for which $|\boldsymbol{M}_c|/M_s \leq 0.1$, which we deem sufficiently close to $\boldsymbol{M}_c \approx 0$. Our resulting magnetization curves are based upon the average over N_c configurations, each one containing $N = 25,100$ similarly chosen nanomagnets.

We reiterate that N is the number of nanomagnets in each configuration, and N_c is the number of configurations studied. Although we have chosen both of these numbers to be 100 for the cubic system in order to obtain reliable statistics, N and N_c have completely different meanings. Finding many (N_c) configurations, each of which has an almost vanishing initial magnetization consumes a significant amount of computer time, especially if the number N of nanomagnets per configuration is not very large. However, choosing a rather small number N of nanomagnets reduces the time required to calculate the dipolar field at each nanomagnet due to all of its neighbors, which must be calculated at each integration time step of the LL equation, offsetting the large amount of computer time required to set up N_c initially nearly-nonmagnetic configurations.

3.2.2 Evolution of the magnetization versus field curves

In this model one increases the external magnetic induction $\boldsymbol{B}$ in discrete steps $\Delta\boldsymbol{B}$, until $\boldsymbol{B} = \boldsymbol{B}_{\max}$, where $B_{\max} = |\boldsymbol{B}_{\max}|$ has to be large enough to align every nanomagnet in its direction. How large $B_{\max}$ has to be generally depends upon T, the field sweep rate $\frac{\Delta B}{\Delta t} \equiv \frac{|\Delta \boldsymbol{B}|}{\Delta t}$, the lattice parameter a, and the crystal structure.[68] In addition, the steps $|\Delta\boldsymbol{B}|$ must be small enough to give rise to numerically smooth $\mathcal{M}(B)$ curves. We therefore set $|\Delta\boldsymbol{B}| = B_{\max}/N_B$, where the number of steps $N_B \gg 1$ should be on the order of 10^3. After each magnetic step, one allows each of the nanomagnets to relax for a fixed amount of time

Δt, which is chosen to be sufficiently small that the nanomagnets do not reach equilibrium. Otherwise, in the absence of a sufficiently strong anisotropy field, no hysteresis would result.

First, we choose one of our configurations c (e. g., $c = 1$) and set the moments of the nanomagnets equal to their values in this initially nonmagnetic configuration, $\{\boldsymbol{M}_i^{c=1}(t = 0, \boldsymbol{B} = 0)\}_{i=1,\ldots,N}$. That is, just after we turn on the magnetic induction in the x direction by the amount $\boldsymbol{B} = \Delta\boldsymbol{B}$, the nanomagnets have not yet precessed from their initial configuration. Then, we calculate the effective magnetic induction $\boldsymbol{B}_i^{c=1,\text{eff}}$ at each of the $i = 1, \ldots, N$ nanomagnets for $c = 1$. To do so, we must calculate the dipolar induction in Eq. (3) due to the presence of all the other nanomagnets.

Then, we let each of the nanomagnets evolve in the presence of its effective magnetic induction for a chosen fixed time interval Δt. To do this accurately, we break Δt up into N_t intervals $dt = \Delta t/N_t$. Obviously, this is extremely time consuming, because it is necessary to recalculate the effective induction at each nanomagnet after each time-integration step of width dt. Once the whole set of moments $\{\boldsymbol{M}_i^1(t = \Delta t, \boldsymbol{B} = \Delta\boldsymbol{B})\}_{i=1,\ldots,N}$ is obtained, we proceed to calculate the configuration magnetic moment, $\boldsymbol{M}_{c=1}(\Delta t, \Delta\boldsymbol{B})$, for this choice of fixed sweep rate, $\Delta B/\Delta t$, from

$$\boldsymbol{M}_c(t, \boldsymbol{B}) = \frac{\sum_{i=1}^N \boldsymbol{M}_i^c(t, \boldsymbol{B}) \exp[-\beta\mathcal{H}_i^c(t, \boldsymbol{B})]}{\sum_{i=1}^N \exp[-\beta\mathcal{H}_i^c(t, \boldsymbol{B})]}, \tag{3.5}$$

$$\mathcal{H}_i^c(t, \boldsymbol{B}) = -\boldsymbol{B}_i^{c,\text{eff}}(t, \boldsymbol{B}) \cdot \boldsymbol{M}_i^c(t, \boldsymbol{B}), \tag{3.6}$$

by setting $c = 1$, $t = \Delta t$ and $\boldsymbol{B} = \Delta\boldsymbol{B}$, where $\boldsymbol{B}_i^{c,\text{eff}}(t, \boldsymbol{B})$ is given from Eqs. (3.2) and (3.3), $\beta = 1/k_B T$, and k_B is Boltzmann's constant. Since $\left(\boldsymbol{B}_i^c\right)_{\text{dip}}$ as given by Eq. (3.3) in $\boldsymbol{B}_i^{c,\text{eff}}(t, \boldsymbol{B})$ contains a self-fieldless single sum, there is no site overcounting in Eq. (3.6).

We are interested in $\boldsymbol{M}_c(\boldsymbol{B}, \frac{\Delta B}{\Delta t})$. In this non-equilibrium situation, the $\boldsymbol{M}_i^c$, $\boldsymbol{B}_i^{c,\text{eff}}$ and hence $\mathcal{H}_i^c$ for each nanomagnet change after each time step dt at which they are evaluated, but the statistical weighting in Eqs. (3.5) and (3.6) is only evaluated at the end of each fixed interval Δt, which has a one-to-one correspondence with ΔB. Thus, this single-configuration average can be directly compared to those in different configurations after the same number

of intervals. Moreover, since $\Delta t = \Delta B \left(\frac{\Delta B}{\Delta t}\right)^{-1}$, $\boldsymbol{M}_c(t, \boldsymbol{B})$ for our purpose can be written as $\boldsymbol{M}_c(\frac{\boldsymbol{B}}{\Delta B/\Delta t}, \boldsymbol{B})$, which is effectively a function of $\boldsymbol{B}$ and $\frac{\Delta B}{\Delta t}$.

Next, we increase the external magnetic induction by another equal step $\Delta \boldsymbol{B}$, and let the nanomagnets precess during another equal time interval, Δt, under the action of the new effective induction. We continued increasing $\boldsymbol{B}$ in this equal step fashion a total of N_B times, until $\boldsymbol{B} = \boldsymbol{B}_{\max}$. At this point, the incremental induction direction is reversed, setting $\boldsymbol{B} = \boldsymbol{B}_{\max} - \Delta \boldsymbol{B}$ for the same time interval Δt, repeating the procedure $2N_B$ times, until $\boldsymbol{B} = -\boldsymbol{B}_{\max}$. After that, we reverse the incremental induction direction once again, setting $\boldsymbol{B} = -\boldsymbol{B}_{\max} + \Delta \boldsymbol{B}$ for the same time interval Δt, etc., and continue N_B times until $\boldsymbol{B} = 0$ is reached, or until the configuration magnetization hysteretic loop (if it exists) is closed. Then, one repeats the entire procedure above described for each of the other $N_c - 1$ configurations $c = 2, \ldots, N_c$, keeping the time intervals Δt and the subintervals dt constant for each step in each configuration. Once all of the calculations for each of the N_c configuration are finished, we average the results over the N_c configurations, obtaining,

$$\langle \boldsymbol{M}_c\Big(\frac{\mathbf{B}}{\Delta B/\Delta t}, \boldsymbol{B}\Big)\rangle_c \;\; = \;\; \frac{1}{N_c}\sum_{c=1}^{N_c} \boldsymbol{M}_c\Big(\frac{\boldsymbol{B}}{\Delta B/\Delta t}, \boldsymbol{B}\Big). \tag{3.7}$$

Then, the magnetization $\overrightarrow{\mathcal{M}}$ is easily calculated. Having tabulated $\overrightarrow{\mathcal{M}}$ for every external magnetic induction step with fixed $\frac{\Delta B}{\Delta t}$, T, a, M_s, α, and $B_{\max}$, we generate the magnetization curve $\mathcal{M}(B)$ for this set of parameters.

3.2.3 Variation of parameters

Unlike the parameters such as $B_{\max}$ and dt, which are details of the theoretical calculation, other parameters can in principle be varied in experiments in a variety of materials. Using the same initial dipole configurations we repeat the whole procedure with different values of α, $\frac{\Delta B}{\Delta t}$, T, and a. The only parameters that can be experimentally varied in studies on a particular sample are $\frac{\Delta B}{\Delta t}$ and T, since the other parameters are fixed. Nevertheless, the possibility of setting the nanomagnets further apart by varying the composition of the

non-magnetic ligand groups in SMM's, for example, justifies the study of the variation of a. Also, given that the damping term appearing in the LL equation is phenomenological, and that in most cases α should be determined experimentally, we have also examined its variation. We note that α is expected to depend inversely upon T, unless T is sufficiently low that thermal processes no longer dominate the relaxation.[55] We keep M_s fixed.

3.2.4 Integration of the LL equation for one nanomagnet

The magnetic moment of each nanomagnet is obtained by numerically integrating the LL equation. The time-evolution of one nanomagnet must be determined synchronously with all its neighbors in order to calculate the dipolar induction acting on each of them at a given time. To solve the LL equation for the ith nanomagnet in the cth crystal, we first rotate its coordinates at each time integration step such that $\boldsymbol{B}_i^{c,\mathrm{eff}}(t) \,||\, \hat{\boldsymbol{z}}(t)$. We then solve the resulting differential equations for either the coordinate spherical angles $\theta(t), \phi(t)$, or the components of $\boldsymbol{M}_i^c(t)$, as shown in Appendix B. The quantity relevant to each spherical angle or component of $\boldsymbol{M}_i^c(t)$ is $\int_{t_0}^{t} d\tau |\boldsymbol{B}_i^{c,\mathrm{eff}}(\tau)|$, which explicitly involves the past history of $|\boldsymbol{B}_i^{c,\mathrm{eff}}(t)|$. In order to decrease the computation time, we approximate this integral for small time integration steps $dt = t - t_0 \ll t_0$,

$$\int_{t_0}^{t} d\tau |\boldsymbol{B}_i^{c,\mathrm{eff}}(\tau)| \;\approx\; |\boldsymbol{B}_i^{c,\mathrm{eff}}(t_0)| dt. \tag{3.8}$$

In order to assure numerical accuracy of our results for the greatly different experimental parameters studied, we had to make appropriate choices for the numerical parameters used in the calculations, as discussed in the Appendix B. Generally, calculations with slow sweep rates require correspondingly small α/γ values. For the calculations leading to the results presented in Figs. 3.1, 3.2, and 3.6- 3.9, we take the numerical parameters $dt = 1 \times 10^{-4}$ s, $B_{\max} = 2.0$ T, $N_t = 1000$, and $N_B = 500, 1000$ and 4000, respectively, for the different sweep rates studied. For the calculations presented in Figs. 3-5, we take $dt = 6 \times 10^{-12}$ s, $B_{\max} = 22.5$ mT, $N_t = 1000$, and $N_B = 1250$.

3.3 Results and discussion: Cubic array

3.3.1 Effect of damping and maximum induction values on the hysteresis

We first neglect any anisotropy effects. In Fig. 3.1, we plotted the average over $N_c = 100$ configurations of the normalized magnetization at the lattice constant $a = 1.5$ nm, sweep rate $\frac{\Delta B}{\Delta t} = 0.005$ T/s, and temperature $T = 0.7$ K for four small damping rates $\alpha/\gamma = 3 \times 10^{-n}$, where $n = 10, 11, 12$, and 13. These results appear respectively from left to right (right to left) in the upper (lower) part of Fig. 1. The magnetization curves show hysteresis for all four of these α values. For the smallest α value we studied, $\alpha/\gamma = 3.0 \times 10^{-13}$, the hysteresis only occurs for external induction magnitudes exceeding 3.0 T, observed by setting $B_{\max}$ above that value, which is well beyond the domain pictured in Fig. 3.1. We also note that in Fig. 3.1, the central regions for $|\langle M \rangle/(NM_s)| < 0.8$ are non-hysteretic. For each of these four parameter value choices, the initial curve describing the first increase of the average magnetization from essentially 0 to its saturation value is indistinguishable from subsequent similar curves obtained after completing the full hysteresis paths. Hence, in this case, the main consequence of the choice of $N_c = 100$ configurations is the improvement in the statistics, reducing the noise that remains most evident in the curves corresponding to the smallest α values.

From the inset to Fig. 3.1, we see that although the height (in $< M > /(NM_s)$) of the hysteretic region decreases with decreasing α, the width (in B) of the hysteretic region increases faster with decreasing α, so that the overall area of the hysteretic region increases with decreasing α. From a computational standpoint, for the parameter values studied in Fig. 3.1, the smaller the value of α, the larger the required value of $B_{\max}$ to produce hysteresis. We also noticed that in these magnetization curves, the hysteresis sets in at the point of an abrupt change in slope in the initial curve, which describes the first increase of the average magnetization from 0 to its saturation value. Moreover, we conclude that $B_{\max}$ must be chosen to guarantee that the system reaches saturation at $B \leq B_{\max}$, because

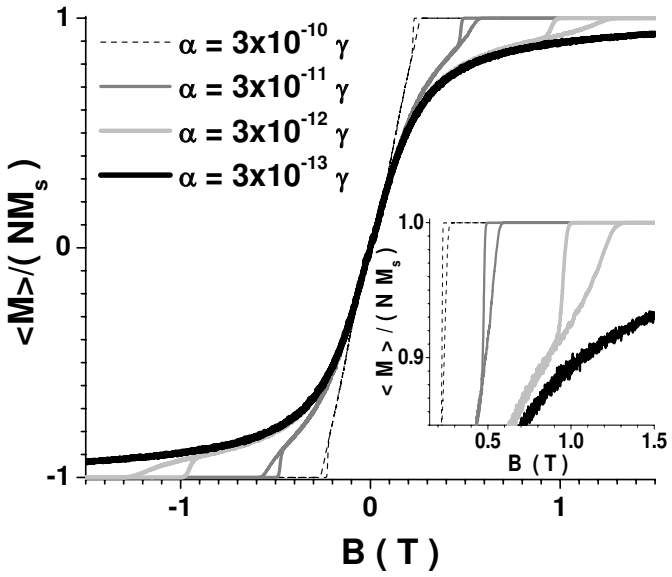

Figure 3.1: *Magnetization curves for* $N_c = 100$, $a = 1.5$ *nm*, $\frac{\Delta B}{\Delta t} = 0.005$ *From left to right for* $\mathcal{M} > 0$, $\alpha/\gamma = 3 \times 10^{-10}$ *(dashed),* 3×10^{-11} *(thin dark grey),* 3×10^{-12} *(light grey),* 3×10^{-13} *(thick black). The inset highlights the hysteretic region of the first three of these curves.*

of the different nature of the hysteresis present in each curve. For example, in Fig. 3.1 the hysteresis can occur only after saturation, but with smaller a values, if the system has not saturated by $B = B_{\max}$, then the magnetization will keep increasing for a number of subsequent $\Delta \boldsymbol{B}$ steps, even though the direction of $\Delta \boldsymbol{B}$ (but not of $\boldsymbol{B}$) has been reversed.

3.3.2 Effect of temperature on the hysteresis

Temperature-independent α

We first investigate the role of temperature that arises only from the statistics, Eq. (3.5), and present our results for a T-independent α in Fig. 3.2. In this figure, we have replotted the inset of Fig. 3.1, excluding the curve for $\alpha/\gamma = 3 \times 10^{-13}$, for which the hysteresis occurred for B too large to display on the same plot. Otherwise, the parameters are the same as in Fig. 3.1, except that we have compared our results (grey curves) for $T = 0.7$ K shown in Fig. 3.1 with those (black curves and circles) for $T = 0.1$ K. Since the evolution of

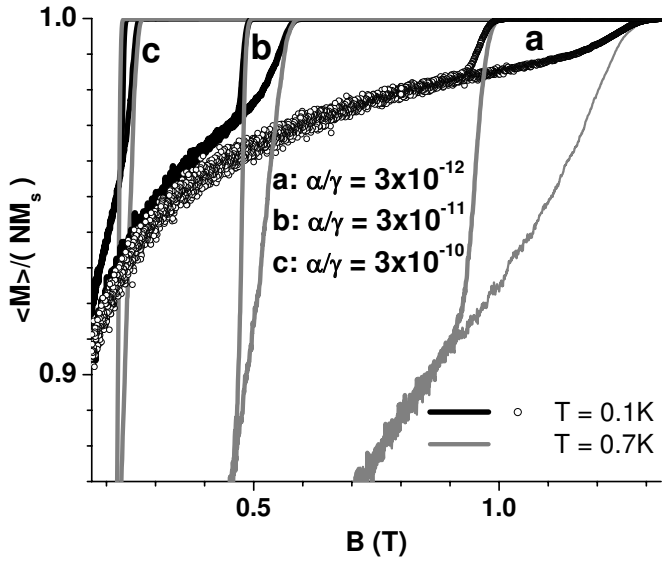

Figure 3.2: *Shown is the upper hysteretic region of the normalized magnetization curves at $T = 0.7$ K (grey) and $T = 0.1$ K (black, circles). The T-independent damping constants α/γ are 3×10^{-12} (a), 3×10^{-11} (b), and 3×10^{-10} (c). The other parameters are the same as in Fig. 1.*

the magnetization with $\boldsymbol{B}$ in this model is independent of T, we note from Fig. 3.2 that the departures of the magnetization curves from the points of saturation are the same at both T values, so that the widths (in B) of the hysteretic regions are nearly the same. However, the height in $< M > /(NM_s)$ of each hysteretic region decreases strongly with decreasing T, so that the overall area of each hysteretic region decreases with decreasing T. This particular result is in strong contrast to the existing experimental results on SMM's. Nevertheless, our results are reasonable from the point of view of the LL equation and the way T enters our calculation.

We remark that in Fig. 3.2, T only enters into the equations of motion when the average magnetic moment is evaluated from Eq. (3.5). As for the Brillouin function that describes the magnetization of a paramagnet in the absence of the dipole interactions, the initial slope of the magnetization at low B increases as T is lowered. This increases the alignment of the moment of each nanomagnet at decreasing T, so that the effect of the effective field is

is enhanced.

Temperature-dependent α

We now consider the effect of the temperature dependence of the damping constant α upon the magnetic hysteresis, focussing upon the case of correspondingly fixed very high sweep and damping rates. We assume that our choice of spin value, $S = 5$ for each nanomagnet, satisfies $S \gg 1$. In this limit, Fredkin and Ron showed that the damping of the nuclear spin precession by magnetic dipole coupling to a heat bath, as derived under the assumption of spin-orbit factorization by Wangsness and Bloch, could be readily extended to the spins in magnetic systems.[18,19] For $S \gg 1$, they found

$$\alpha(T)/\gamma \approx \frac{T_0}{T}, \tag{3.9}$$

where $T_0 = 2\hbar\Phi^1_{11}(1 - e^{-\kappa})S^2/k_B\kappa$,[19] and Φ^1_{11} is a rate constant (with units of s^{-1}), the expression for which is a complicated orbital integral arising from the interaction of the local spin with its surrounding molecular electronic orbitals in second-order perturbation theory,[18] and $\kappa = \hbar\gamma B^{\rm eff}/(k_B T)$. For $\kappa \ll 1$, $T_0 \to 2\hbar\Phi^1_{11}S^2/k_B$, which can be taken to be independent of T and $B^{\rm eff}$, so that $\alpha \propto T^{-1}$, but for $\kappa \gg 1$, $\alpha \propto 1/B^{\rm eff}$, which would completely change its effect. Here we only consider the case $\kappa \ll 1$, for which Eq. (3.9) holds for constant T_0. We note that, as in Figs. 3.1 and 3.2, T also affects the results for the magnetization from the statistics, Eq. (3.5).

In Fig. 3.3, we have shown our results, averaged over $N_c = 100$ configurations, of the normalized magnetization as a function of B in mT, for $a = 1.5$ nm, $\frac{\Delta B}{\Delta t} = 3000$ T/s, $\alpha(T)/\gamma = T_0/T$, $T_0 = 0.3K$, and $T = 5$ K. For the calculations presented in this figure, we used the numerical parameters $dt = 6 \times 10^{-12}$ s, $B_{\rm max} = 22.5$ mT, $N_t = 1000$, and $N_B = 1250$. Note that although a has the same value as in Figs. 3.1 and 3.2 , the sweep and damping ($\alpha(T)/\gamma = 0.06$) rates are six and at least eight orders of magnitude larger than in those figures, respectively. For these parameters, there are three regions of hysteresis in the pictured magnetization curve. The left inset is an enlargement of the upper hysteretic

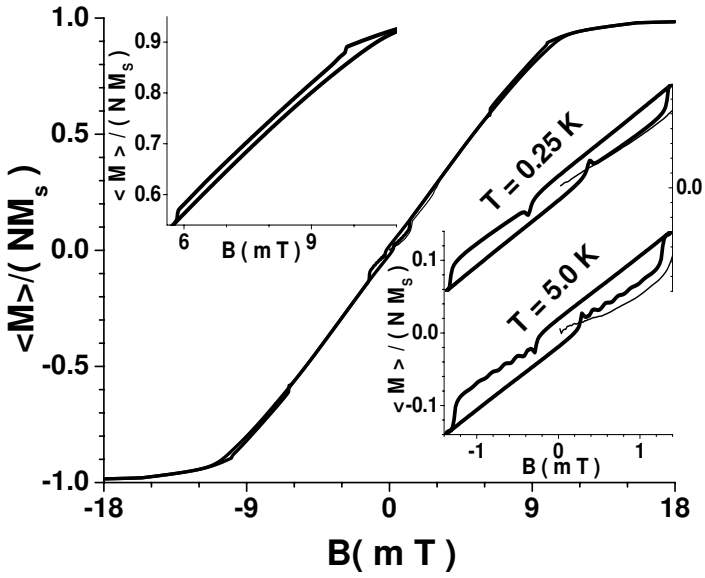

Figure 3.3: *The magnetization curves for* $N_c = 100$ *at* $T = 5$ *K,* $a = 1.5$ *nm, and* $\frac{\Delta B}{\Delta t} = 3000$ *T/s with* $B_{\max} = 22.5$ *mT and* $\alpha(T)/\gamma = T_0/T$ *for* $\hbar g \mu_B B^{eff}/(k_B T) \ll 1$ *and* $T_0 = 0.3$ *K are shown.*[19] *Left inset: details of the upper portion of the curve. Right inset: details of the central hysteretic portion of the curve shown, along with the central portion of the corresponding curve at* $T = 0.25$ *K. The thin curves beginning near to the origin represent the magnetization onsets.*

region, the mirror image of which occurs in the lower region of the pictured magnetization curve. In contrast to the behavior shown in Figs. 3.1 and 3.2 at the top of the upper hysteretic region, the magnetization does not rise abruptly to its saturation value, but first goes through an extended non-hysteretic region. In addition, there is a central hysteretic region, an enlargement of which is shown in the right inset, along with an enlargement of the same central hysteretic region obtained at $T = 0.25$ K with the same set of parameters. We note that at $T = 5$ K, the onset magnetization averaged over $N_c = 100$ configurations, pictured by the thin curve in the lower portion of the right inset, does not coincide with the thick curve corresponding to the central hysteresis loop region obtained subsequently to the attainment of the saturation value by the magnetization. In addition, we note that the thick central hysteresis loop exhibits reproducible oscillations with B-independent frequency f at $T = 5$K, which oscillations have disappeared at the lower $T = 0.25$ K value, for which $\alpha(T)/\gamma = 1.2$, pictured in the upper portion of the right inset.

In order to investigate further the differences between the starting magnetization curves and the curves obtained subsequent to saturation, in Fig. 3.4, we have shown the corresponding central hysteresis loop portion of the magnetization obtained for two individual configurations, using the same experimental and numerical parameters as in Fig. 3.3, except that $T = 10$ K, for which $\alpha(T)/\gamma = 0.03$. As in Fig. 3.3, T enters both through the statistical averaging and through the damping, $\alpha(T)$. In Fig. 3.4, the solid and open circles correspond to the starting magnetizations of the two configurations, and the coincident thick black and thin light grey curves correspond to the central hysteresis loop region of their respective magnetization curves obtained after saturation. Note that after the initial noisy regions, the starting magnetizations for these two configurations exhibit comparably large amplitude oscillations at the frequency $f/2$, the phases of which are very different. However, after the attainment of the saturation magnetization, these large amplitude oscillations are absent, and replaced by smaller amplitude oscillations at the frequency f, which are similar to the oscillations present in our results obtained at $T = 5$ K shown in the lower curves in the right inset of Fig. 3.3. We note that in the first oscillation present on both sides of the central post-saturation hysteresis loops obtained with these parameters at $T = 5$ and 10 K show additional small amplitude, higher frequency oscillations, which may be higher harmonics of f. In addition, the amplitudes of the fifth and sixth oscillations are larger at 10 K in 3.4 than at 5K in the lower right inset of Fig. 3.3.

We remark that the large amplitude oscillations present in the starting magnetizations shown in Fig. 3.4 are absent in Fig. 3.3. This occurs due to the randomness of the oscillation phases, which is averaged out in the $N_c = 100$ configurations studied in Fig. 3.3.

From Fig. 3.4, we therefore conclude that our starting configurations that were chosen to have $|M|/M_s \leq 0.1$, appropriate for SMM's, lead to starting magnetization curves that are very different from those that start at the saturation magnetization, but are subsequently identical. That is, after the attainment of saturation, all configurations are identical.

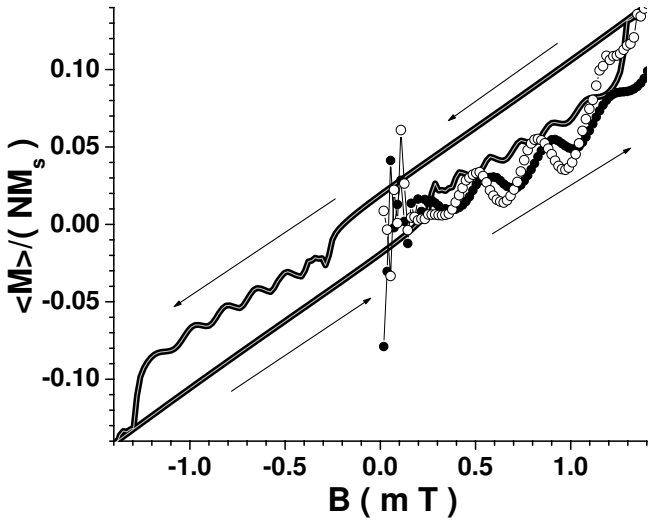

Figure 3.4: *The central loop and starting magnetization curves for two separate configurations, each with $N_c = 1$ (open and filled circles) at $T = 10$ K, $a = 1.5$ nm, and $\frac{\Delta B}{\Delta t} = 3000$ T/s with $\alpha(T)/\gamma = T_0/T$ for $\hbar g \mu_B B^{\rm eff}/k_B T \ll 1$ and $T_0 = 0.3$ K are shown.[19] The thin grey and thick black curves represent the identical behaviors of the central hysteretic loop portion of the magnetization for the same two configurations obtained after saturation. The arrows indicate the direction of the magnetization hysteresis. Here $B_{\rm max} = 22.5$ mT. See text.*

3.3.3 External field directed towards the crystal corners with $\alpha(T)$

We now consider the 3D case of the external magnetic induction directed from the crystal center to one of its corners, $\boldsymbol{B} = B(\hat{\boldsymbol{x}} + \hat{\boldsymbol{y}})/\sqrt{2}$, the (110) direction. In Fig. 3.5, we show the resulting central hysteresis region obtained from our calculations for $N_c = 50$, $N = 5 \times 5 \times 4$, $T = 10$ K, $a = 1.5$ nm, and $\frac{\Delta B}{\Delta t} = 3000$ T/s with $\alpha(T)/\gamma = 0.03$. In this case, it is sufficient to set $B_{\rm max} = 22.5$ mT, which leads to full saturation. We note that for this field direction, a small (-6 mT$< B <$6 mT) hysteresis region appears on either side of the origin, which is rather central to the full magnetization curve, but vanishes over a small region close to the origin. There are also tiny hysteresis regions near to saturation that appear as dots in the inset depicting the full magnetization curve.

The nearly central hysteretic regions shown in Fig. 3.5 exhibit reproducible jumps at specific B values, similar to those observed at low T in SMM's. However, we note that in this figure, we have taken $T = 10$ K, and have used a classical spin model. We also

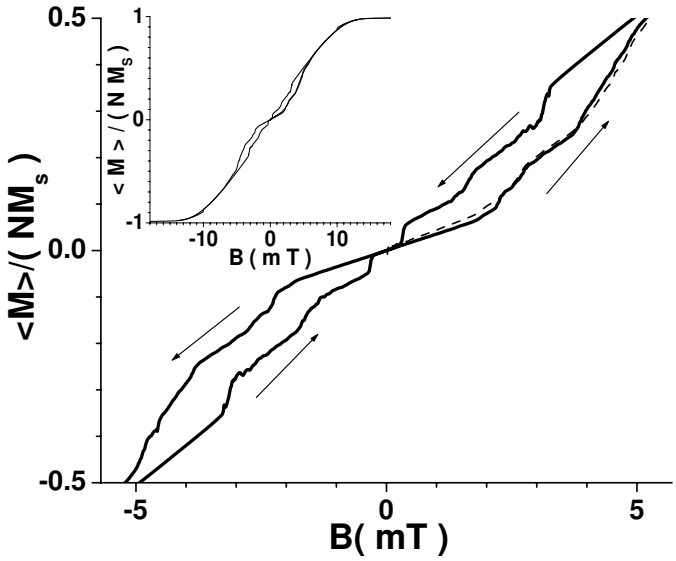

Figure 3.5: *The central loops (solid curves) of the magnetization curve for* $N_c = 50$, $N = 5 \times 5 \times 4 = 100$, *with* $\boldsymbol{B}$ *along the [110] direction* $[\boldsymbol{B}||(\hat{\mathbf{x}} + \hat{\mathbf{y}})/\sqrt{2}]$ *at* $T = 10\ K$, *with* $a = 1.5\ nm$, $B_{\max} = 22.5\ mT$, *and* $\frac{\Delta B}{\Delta t} = 3000\ T/s$ *with* $\alpha(T)/\gamma = T_0/T$, *and* $T_0 = 0.3\ K$. *The dashed curve is the starting magnetization curve. The arrows indicate the direction of the hysteresis. Inset: the full magnetization curve. See text.*

note that we have used a rather small sample ($N = 100$) with a fast sweep rate and a large damping coefficient in our calculations, and caution that such behavior might not be present in large single crystals, especially with much slower sweep rates. Nevertheless, this figure demonstrates that steps in the magnetization do not necessarily have a quantum origin, and that the sample shape can lead to unusual hysteresis effects.

3.3.4 Effect of sweep rate on the hysteresis

Fig. 3.6 shows the curves obtained for different induction sweep rates at a fixed, small damping rate (using the same numerical parameters as in Fig. 3.1), it is clear that stronger hysteresis is found for higher sweep rates, in agreement with experiments on a variety of nanomagnets, including SMM's. This shows that the reversibility of the process depends on how close to equilibrium the sweep rate allows the nanomagnet spins to reach. That is, although for different sweep rates the external induction is increased by the same amount

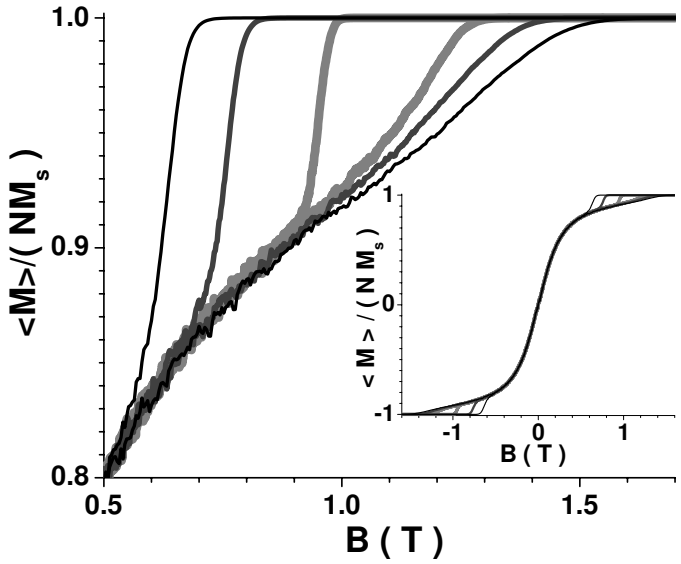

Figure 3.6: *Hysteretic region of $\mathcal{M}(B)$ at 0.7 K, $\alpha/\gamma = 3\times10^{-12}$, and a = 1.5 nm, for the sweep rates $\frac{\Delta B}{\Delta t}$ = 0.04 T/s (thin black), 0.02 T/s (dark grey), and 0.005 T/s (thick light grey). The inset shows the entire curves.*

$\Delta \boldsymbol{B}$, at higher sweep rates, the time Δt allowed for the nanomagnets to evolve towards equilibrium is less. This makes the process less reversible and the hysteresis loops larger.

We also note that at the much higher sweep and damping rates studied in Figs. 3.3 and 3.4, the magnetization also exhibits a central hysteretic region, which exhibits oscillations at T values not too low and/or damping constants not too large.

3.3.5 Effect of lattice constant on the hysteresis

In Fig. 3.7, we show hysteresis curves for two different values of the lattice constant a, obtained using the same numerical parameters as in Fig. 3.1 For weaker dipole-dipole interactions (larger a), the rise in the magnetization is steeper with increasing $\boldsymbol{B}$, and the rapid decrease in the magnetization from its saturation value upon decreasing $\boldsymbol{B}$ occurs at a smaller value of $|\boldsymbol{B}|$. Furthermore, we shall see that dipolar interactions do not promote hysteresis in these systems, but suppress it. Actually, the same conclusion was found recently for magnetic nanoparticles in the framework of the generalized mean-field approximation.[87]

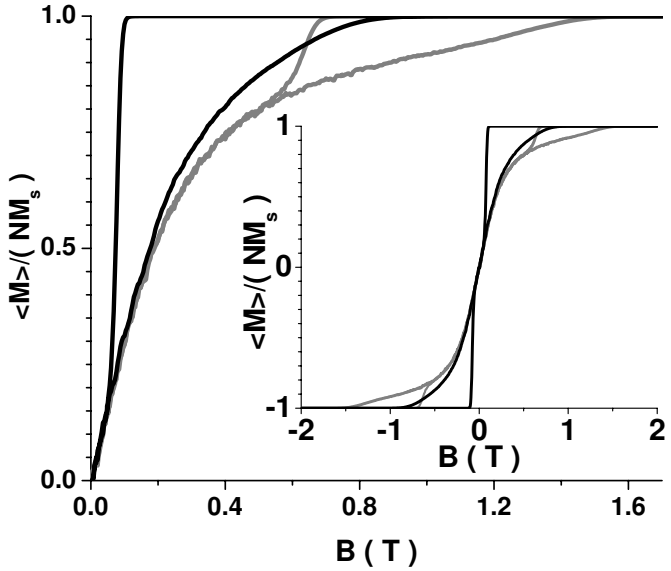

Figure 3.7: *Magnetization curves for lattice constants a = 1.5 nm (grey) and a = 2.5 nm (black). $\frac{\Delta B}{\Delta t} = 0.04$ T/s, $\alpha = 3 \times 10^{-12}\gamma$, T = 0.7 K.*

This peculiar hysteresis is easily understood by analyzing the LL equation. If the nanomagnet magnetization $\boldsymbol{M}_i^c$ is parallel to its local magnetic induction $\boldsymbol{B}_i^{c,\text{eff}}$, $d\boldsymbol{M}_i^c/dt = 0$, as it will remain thereafter, so that $\boldsymbol{M}_i^c$ has reached equilibrium. The only chance the system has to decrease its magnetization from its saturation value is through the combined weak dipolar induction, which strengthens with decreasing lattice parameter a. The dipolar induction can oppose the system from remaining completely magnetized, since it has small, but non-vanishing components. Therefore, even when $\boldsymbol{B}$ reaches its maximum (finite) amplitude B_{max} and the misalignments of each $\boldsymbol{M}_i^c$ with $\boldsymbol{B}$ are negligible, dynamic equilibrium will not generally have been attained due to the limited time allowed for relaxation before the next change in $\boldsymbol{B}$. There will remain a slight deviation between the directions of the $\boldsymbol{B}_i^{c,\text{eff}}$ and the $\boldsymbol{M}_i^c$ due to the presence of the $\boldsymbol{B}_i^{c,\text{dip}}$, which is especially important when B decreases from B_{max}.

Of course, it is harder to decrease $\mathcal{M}$ at the very beginning of the induction cycle. This

is precisely the cause of the hysteretic behavior, given that changes in $\boldsymbol{M}_i^c$ are proportional to $|\boldsymbol{M}_i^c \times \boldsymbol{B}_i^{c,\text{eff}}|$, which nearly vanishes when the direction of the incremental induction has just been reversed. We conclude then that the smaller the lattice parameter (the stronger the dipolar induction), the greater the deviation of $\boldsymbol{M}_i^c$ from the direction of $\boldsymbol{B}_i^{\text{eff}}$. Hence, the easier it is to decrease $\mathcal{M}$, making the magnetization curve less hysteretic. This is shown in Fig. ref4.7, in which the magnetization curves resemble those obtained for Mn_4 SMM's. [72] Those data show an abrupt decrease in $\mathcal{M}$ at nearly zero external induction that is not evident in the magnetization curves of other SMM's.[69]

It is important to note that the curves in Figs. 3.1 and 3.7 do not show the strong hysteresis observed experimentally in most SMM's, which is especially large in the central region of the $\mathcal{M}(B)$ curves. We remind the reader of our intent to focus upon the effects of the dipole-dipole interactions, whereas the most important features of SMM's involved in their low-T relaxation of the magnetization are generally thought to be their quantum structure and magnetic anisotropy. Nevertheless, for this entirely classical and magnetically isotropic system, we are indeed finding hysteretic curves. In addition, the sweep rates in Figs. 3.1, 3.2, 3.6, and 3.7 are comparable to those used in experimental SMM studies. At much larger sweep rates, such as were studied in Figs. 3.3- 3.5, an hysteretic central region was found. However, the sizes and T dependencies of these hysteretic regions were still respectively much smaller and qualitatively different than observed in SMM's.

3.3.6 Effect of spin anisotropy upon the hysteresis

It is straightforward to generalize our model to include some of the effects of magnetic spin anisotropy. Here we assume the nanomagnets contain sufficiently many spins that their quantum nature can be neglected. We note that SMM's at low T values behave as quantum entities, because of the small number of spins in each nanomagnet. In those systems, most workers have assumed the in addition to the isotropic Heisenberg and Zeeman interactions, the magnetic anisotropy terms could also be written in terms of components of the global spin

operator $\boldsymbol{S}$, with the overall dominant terms often written as $-DS_z^2 - E(S_x^2 - S_y^2)$.[88] However, portions sufficiently large for model comparison of the low-T magnetization curves of two Fe_2 SMM dimers have been studied experimentally.[89,90] In neither antiferromagnetic dimer case was any evidence for either of those types of spin anisotropy present.[91] In contrast, in one of those cases, strong evidence for a substantial amount of local, single-ion spin anisotropy, in which the individual spins within a dimer align relative to the dimer axis, is present in the data.[89,91] In addition, the global anisotropy in the ferromagnetic SMM Mn_6 is extremely weak.[92] Since the precise quantum nature of more complicated SMM's appears therefore to be poorly understood, we shall investigate the quantum features of the magnetic hysteresis curves in SMM's, including some effects of local spin anisotropy, in a subsequent publication.[93]

We therefore restrict our investigations of the role of magnetic anisotropy upon the magnetization curves of arrays of nanomagnets to the simplest classical model of spin anisotropy,

$$\boldsymbol{B}_i^{c,\mathrm{eff}} = \boldsymbol{B} + \boldsymbol{B}_{i,\mathrm{dip}}^{c} + \mu_0 \boldsymbol{H}_A, \tag{3.10}$$

where we take $\boldsymbol{B} = B\hat{\boldsymbol{x}}$ and studied the cases $\boldsymbol{H}_A = H_A\hat{\boldsymbol{x}}$ and $\boldsymbol{H}_A = H_A\hat{\boldsymbol{z}}$. This is the 3D analogue of the model studied by KS.[94] In this model, the magnetic anisotropy of each of the nanomagnets points in the same direction, and in our finite sized crystal consisting of $5 \times 5 \times 4$ nanomagnets on a cubic lattice, our chosen direction is one of the most general ones. We first performed two studies of the magnetic hysteresis in this model, for which the anisotropy field $\boldsymbol{H}_A$ is directed respectively along (100), $||\boldsymbol{B}$, and (001), $\perp \boldsymbol{B}$, and our results are shown in Figs. 3.8-3.9, respectively. For both anisotropy field directions, we take $N_c = 100$, $N = 5 \times 5 \times 4 = 100$, $\alpha/\gamma = 3 \times 10^{-12}$, $a = 1.5$ nm, $\frac{\Delta B}{\Delta t} = 0.04$ T/s, $T = 0.7$ K, and $B_{\mathrm{max}} = 2.0$ T. The sweep rates used in Figs. 3.8-3.9 are slightly faster than those used in SMM experiments but much slower than those used in the calculations of KS. Since $a = 1.5$ nm in these curves, these curves also represent the strongest realistic dipolar interaction we studied.

In Fig. 3.8, we show the portions of the parallel magnetization curves with $\boldsymbol{B}||\boldsymbol{H}_A||\hat{\boldsymbol{x}}$,

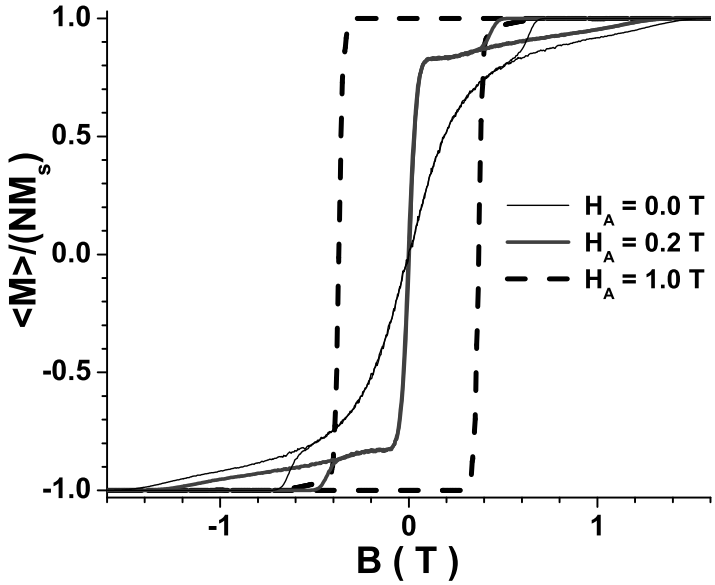

Figure 3.8: *Parallel 3D magnetization curves including different anisotropy field* $\boldsymbol{H}_A = H_A\hat{\boldsymbol{x}}$ *strengths, with the external induction* $\boldsymbol{B}||\boldsymbol{H}_A$. $\mu_0 H_A = 0$ *(thin black), 0.2 T (dark grey), and 1.0 T (thick dashed), respectively. For each curve,* $N_c = 100$, $N = 5\times5\times4 = 100$, $\alpha/\gamma = 3\times10^{-12}$, $a = 1.5$ *nm,* $\frac{\Delta B}{\Delta t} = 0.04$ *T/s,* $T = 0.7$ *K, and* $B_{\max} = 2.0$ *T.*

that exhibit the resulting regions of magnetic hysteresis for three H_A values. For the $\mu_0 H_A =$ 0, 0.2, and 1.0 T values shown, all three curves are hysteretic, but the two lower H_A values do not lead to a central hysteresis region. Nevertheless, the largest anisotropy value, $H_A = 1.0$ T, leads to a strong central hysteresis. We remark that the trends shown in Fig. 3.7 are rather different from those obtained for a single magnetic particle with magnetic anisotropy.[46]

In Fig. 3.9, we show the portions of the 3D perpendicular magnetization curves exhibiting the resulting regions of magnetic hysteresis for the five anisotropy fields $\mu_0 H_A = 0$, 1 mT, 12 mT, 0.5 T, and 1.0 T, with the magnetic induction $\boldsymbol{B}||\hat{\boldsymbol{x}} \perp \boldsymbol{H}_A||\hat{\boldsymbol{z}}$. In each case, hysteresis occurs near to magnetic saturation, but is absent in the central region for small magnetic induction. At $\mu_0 H_A = 1.0$ T, this is distinctly different from the large central hysteretic region observed for parallel anisotropy. Note that the slope $d\mathcal{M}/dB$ at small B is non-monotonic with increasing H_A, as it has a minimum at curve (c), corresponding to $\mu_0 H_A = 12$ mT.

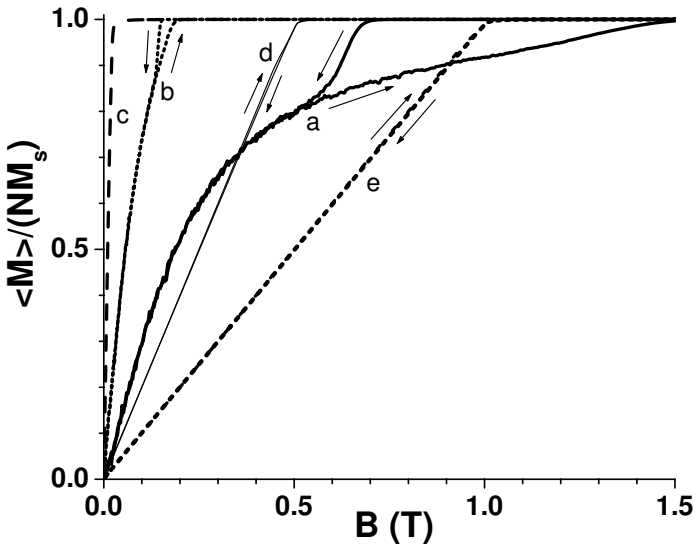

Figure 3.9: *Upper region of the 3D perpendicular magnetization curves with the external induction* $\boldsymbol{B} = B\hat{\boldsymbol{x}} \perp \boldsymbol{H}_A = H_A\hat{\boldsymbol{z}}$*, for different values of* H_A*. Curves (a)-(e) correspond to* $\mu_0 H_A = 0$*,* 1×10^{-3}*,* 1.2×10^{-2}*, 0.5, 1.0 T, respectively. The other parameters are the same as in Fig. 7. The arrows indicate the directions of the field sweeps.*

Thus, we conclude that it is possible to obtain a central hysteresis region using this classical model of dipolar interactions with constant spin anisotropy. However, our results suggest that such central hysteresis regions only arise for the magnetic induction parallel to the spin anisotropy direction, and for sufficiently strong anisotropy fields, $H_A \geq H_A^{\min}$, where 1.0 T$> \mu_0 H_A^{\min} > 0.2$ T.

3.4 Results and discussion: Square array

3.4.1 Introduction

To estimate the importance of the dipolar induction (especially when it becomes comparable to the external induction), the anisotropy and the sweep rate, we have[95] successfully reproduced one of the 2D calculations of KS.[94] The KS calculation we chose to reproduce was pictured in their Fig. 2(i), which was for $\theta = 45°$ and is shown here as the left panel of Fig. 3.10. We chose a and $\Delta B/\Delta t$ values consistent with those of KS, and since KS had

mentioned an anisotropy field in their Hamiltonian, but did not list any anisotropy parameters used in their calculations, we also varied the strength of the anisotropy field H_A. We obtained remarkably good agreement with their results of Fig. 2(i) with $\Delta B/\Delta t \approx 3000$ T/s, $a = 1.5$ nm, and $\mu_0 H_A \leq 0.75$ mT. Then, we changed some parameters to see how the results depend on the anisotropy strength, sweep rate, and lattice parameter.

Our calculations for a cubic lattice consisting of four 25-particle layers differ from those of KS in many ways.[94] They used a 2D square lattices of cylindrical nanodots (here, we take their 5×5 lattice with external induction aligned along an array's diagonal), included a shape-dependent anisotropy field perpendicular to the lattice, performed their calculations at $T = 0$, used a much larger damping constant than we generally did for 3D systems, and did not average their results over an ensemble of 2D samples, because such systems do not show variations in the resulting hysteresis loops for different initial states. Nevertheless, we both integrated the LL equation using the Runge-Kutta algorithm, and surprisingly, KS's system turned out to be very sensitive to the dipolar field strength. The effective induction they considered can be written as

$$\boldsymbol{B}_i^{c,\text{eff}} \;=\; \boldsymbol{B} + \boldsymbol{B}_{i,\text{dip}}^{c} + \mu_0 H_A \hat{\boldsymbol{z}}. \tag{3.11}$$

For lattice constant $a = 1.5$ nm, spin $S = 5$, and $V/a^3 = 0.5$, where V is the volume of the nanomagnet, the saturation magnetization is $M_s \approx 55$ Oe. Then, they took the dimensionless $dt = 5 \times 10^{-3}$, which implies a real time interval $dt = 5.17 \times 10^{-12}$ s. If the system evolves during 700 time steps dt for some fixed value of $\boldsymbol{B}$, then $\boldsymbol{B}$ is changed every $\Delta t \approx 3.62 \times 10^{-9}$ s. On the other hand, KS chose a maximum external induction $B_{\max} = 2\mu_0 M_s \approx 1.1 \times 10^{-2}$ T. In addition, they took fixed induction steps of magnitude $\Delta B = 2 \times 10^{-3} \mu_0 M_s \approx 1.1 \times 10^{-5}$ T. Therefore, we estimate their resulting sweep rate to be $\frac{\Delta B}{\Delta t} \approx 3 \times 10^3$ T/s, as in our 3D results shown in Figs. 3.3, 3.4.

In the absence of any specific information, we then had to induce the value of the anisotropy field that KS used to obtain their figure. Fortunately, as discussed in the following, the results are rather insensitive to it, unless H_A becomes comparable to $B_{\max}/\mu_0$. In

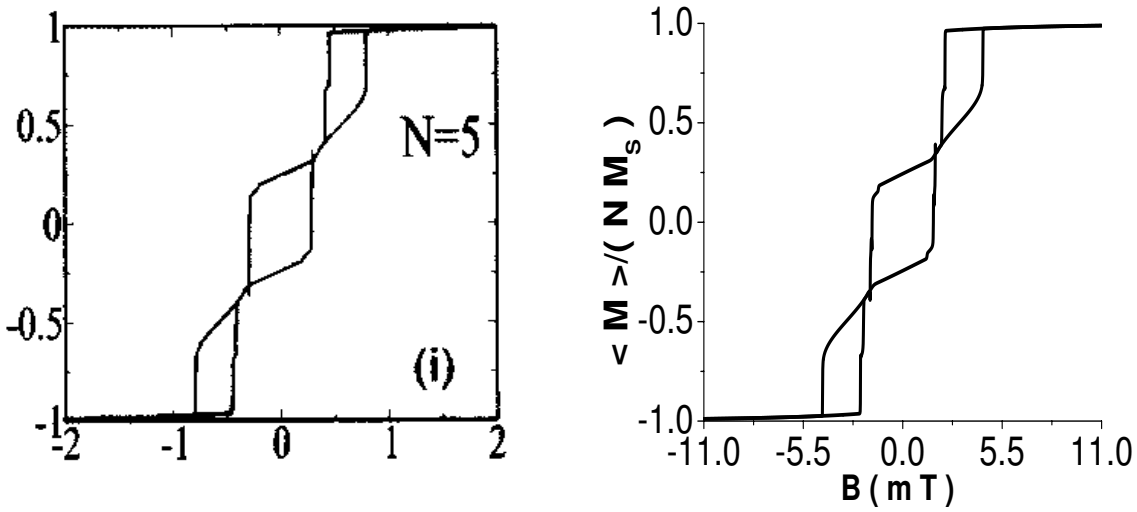

Figure 3.10: *(left) Hysteresis loop $\mathcal{M}(B)$ in units of M_s, for a weakly coupled array of 5×5 ferromagnetic nanodots in a square lattice on the xy plane, from Fig. 2(i) of KS. The external induction is applied along the array diagonal (45° from the x axis).*[94]*. (right) Our results calculated for $N_c = 1$ with 5×5 nanomagnets on a square lattice, $\alpha/\gamma = 0.6$, $T = 0K$, $\frac{\Delta B}{\Delta t} = 3000$ T/s, $\mu_0 H_A = 7.5 \times 10^{-4}$ T, $\boldsymbol{B} = B(\hat{\boldsymbol{x}} + \hat{\boldsymbol{y}})/\sqrt{2}$.*

the right panel of Fig. 3.10, our 2D calculation with $\mu_0 H_A = 0.75$ mT are shown, and by comparing that figure with Fig. 2(i) of KS pictured in the left panel of Fig. 3.10, we see that the agreement is remarkably good.

Later, Takagaki and Ploog (TP) used a fourth-order Runge-Kutta procedure to integrate the LL equations with $N \times N$ 2D nanomagnet lattices with magnetic anisotropy and dipole-dipole interactions.[85] They used a fixed time interval $dt = 0.1\hbar/(\gamma M_s)$, 20 times as fast as that used by KS,[94] and let the nanomagnets to interact until no further changes in the nanomagnet spin configurations were obtained. Some of their results appeared to differ qualitatively from the second-order Runge-Kutta results obtained for the same systems by Kayali and Saslow, both in the hysteresis area A_N and in the number of steps of the magnetization hysteresis loops. Since the numerical iteration techniques in those two papers

were different, one might first think that the differences could have arisen from inaccuracies in one or the other of the techniques. We had varied our iteration time interval (up to two orders of magnitude smaller) in other calculations to check our own accuracy, the excellent agreement between our results and those of KS provided strong evidence that those $N = 5$ KS results were also sufficiently accurate. In order to determine the source or sources of the apparent differences between the KS and TP results which were most prominent in a different $N = 5$ calculation, we varied the lattice parameter a, which was unspecified by TP, in order to determine if different a choices could account for their different results. We also reduced our iteration time interval dt by two orders of magnitude, in order to guarantee our own accuracy.

However, another possible source of the differences could be that *both KS and TP used apparently incompatible definitions of magnetic moment and magnetization*, which is defined to be the magnetic moment density,[20] or magnetic moment per unit volume (area) in a three (two)-dimensional array. KS plotted the array magnetization $M(H)$ with both M and H in units of M_s. However, *KS defined M_s to be both the nanodot saturation magnetization and the magnitude of the nanodot magnetic moment.*[94] On the other hand, *TP denoted M_H as the magnetization per lattice site, and plotted it in units of M_s*, which they also denoted as the magnitude of the nanodot magnetic moment.[85] However, *TP plotted the magnitude of the magnetic field H in the different units of M_s/a_{TP}^3*,[85] where a_{TP} is the TP lattice constant. These units used by TP are confusing and appear to be incompatible. Clearly, the magnetic field and the magnetization per volume do not have the same units.

Despite the dual character of M_j in the KS work, in their Eq. (3), M_j clearly represents the saturation magnetization of the jth nanodot.[94] Then, $M_j V_{\rm dot}^{KS}$ is that nanodot's magnetic moment, where $V_{\rm dot}^{KS} = \pi d R_d^2$ for a cylindrical nanodot of height d and radius R_d. The distance between the jth and ith nanodots is $a_{KS} r_{ij}$, where r_{ij} is dimensionless. Then, for an arbitrary nanodot magnetization, the strength of the dipolar interaction is $h_{\rm dip}^{\rm KS} = V_{\rm dot}^{KS}/a_{KS}^3$. SC had earlier presented this description without incurring any ambiguity between the

nanodot magnetization and magnetic moment.[84] However, *TP claimed their nanodots were circular with an infinitely small radius.*[85] Such nanodots have an unphysically divergent magnetization in the usual sense,[84] although the precise nanodot dimensions are irrelevant in TP's description of the dipolar interaction strength in terms of a_{TP} and M_s. Note that once $h_{\rm dip}$ is fixed, volume per se is irrelevant in the KS and TP calculations.

Here we show that **the different KS and TP results are not due to inaccuracies in either calculation or to different magnetic induction sweep rates $\Delta B/\Delta t$, but arise from different $h_{\rm dip}$ choices**, as TP effectively took $h_{\rm dip}^{TP} = V_{\rm dot}^{TP}/a_{TP}^3 = 1 = 2h_{\rm dip}^{KS}$ in their Eq.(3).[85] By taking the effective nanodot volume $V_{\rm dot}$ to be the same in each calculation, $V_{\rm dot}^{TP} = V_{\rm dot}^{KS}$, we accurately reproduce both the KS and TP $N = 5$ results using a values consistent with their different $h_{\rm dip}$ choices, $a_{\rm TP}/a_{\rm KS} = (h_{\rm dip}^{\rm KS}/h_{\rm dip}^{\rm TP})^{1/3} = 2^{-1/3}$.

3.4.2 Anisotropy field dependence of the hysteresis

We first investigated the effects of changing the strength of the anisotropy fields, and presented our results in Fig. 3.11. The most important issue about the results shown in Fig. 3.11 is the fact that the curve obtained by KS (the left panel of Fig. 3.10) is basically independent of the anisotropy field H_A for sufficiently small H_A. That is, there are no essential differences between that curve reproduced in the right panel of Fig. 10 with $\mu_0 H_A = 7.5$ mT, and the one with $H_A = 0$. Strong deviations from these essentially identical curves appear for $\mu_0 H_A \geq 4$ mT, however. Since identical behavior is obtained without any anisotropy, this implies that all hysteretic features (including the stepped magnetization and demagnetization) are due to the dipolar interaction. H_A becomes important only when it is comparable to $B_{\rm max}/\mu_0$ and tends to close the hysteresis loops, starting from the lower and upper loops. We note that by comparing Fig. 3.11 with Fig. 3.9, the details of the hysteresis obtained with $H_A = 0$ for $\boldsymbol{B}$ along the (110) direction are different in 3D and 2D samples. The hysteresis is much larger in the 2D case pictured in Fig. 11, and has a large loop in the central region that does not vanish at the origin, plus large loops that extend up to saturation. In the 3D

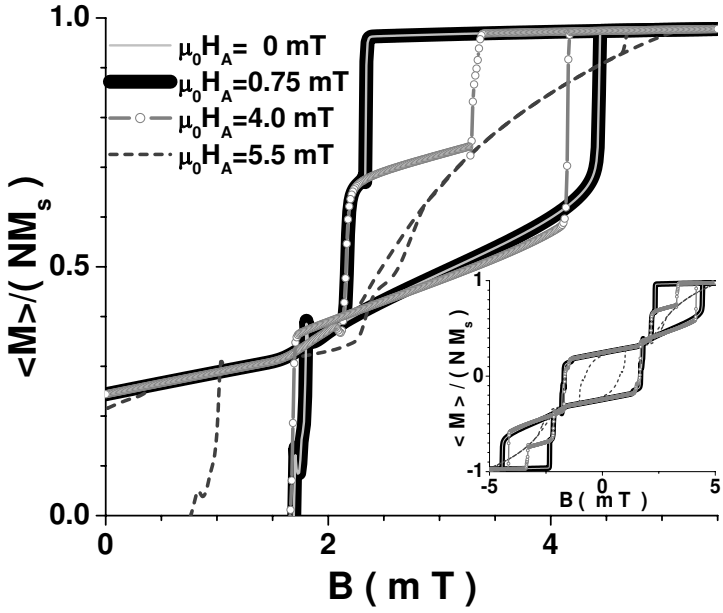

Figure 3.11: *Hysteresis loops for various strengths of H_A for 5×5 nanomagnets on a square lattice with $N_c = 1$. $S = 5$, $T = 0$ K, $a = 1.5$ nm, $\frac{\Delta B}{\Delta t} = 3000$ T/s, $\alpha/\gamma = 0.6$, $\boldsymbol{B} = B(\hat{\boldsymbol{x}} + \hat{\boldsymbol{y}})/\sqrt{2}$. The thin grey and thick black curves with $\mu_0 H_A = 0, 0.75$ mT, respectively, are nearly indistinguishable. The small grey circles and dashed curves correspond to $\mu_0 H_A = 4.0, 5.5$ mT, respectively. The inset shows the entire magnetization loops*

case constructed from four 2D planes each equivalent to that used in the calculation shown in Fig. 11, the magnitude of the hysteresis is reduced and its details have been greatly altered.

3.4.3 Induction sweep rate dependence of the hysteresis

In Fig. 3.12, we show our results for a single configuration of a square 2D lattice with $N = 5 \times 5$ for different sweep rates, keeping the other parameters fixed at $\mu_0 H_A = 0.75$ mT, $\alpha/\gamma = 0.6$, $a = 1.5$ nm, $S = 5$, $T = 0$, and $\boldsymbol{B} = B(\hat{\boldsymbol{x}} + \hat{\boldsymbol{y}})/\sqrt{2}$. From Fig. 3.12, we note that the hysteresis is nearly independent of induction sweep rate over the range 300 to 6000 T/s, distinctly different from the strong dependence found in 3D systems shown in Fig. 3.5

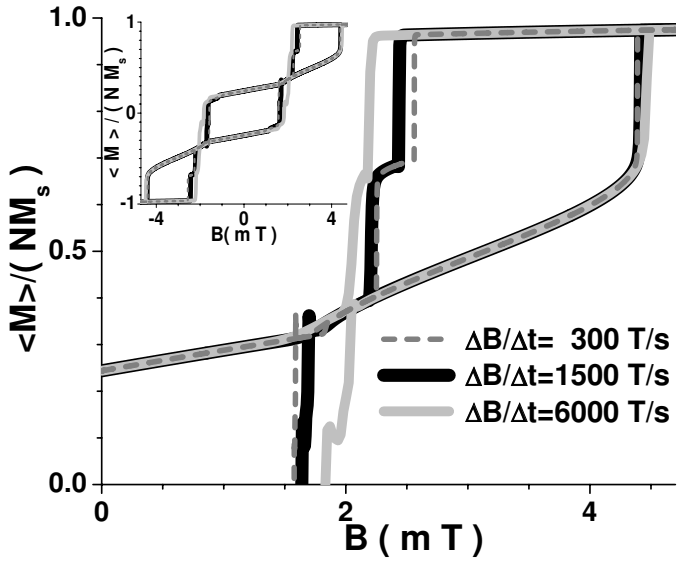

Figure 3.12: *Hysteresis loops for different induction sweep rates with* 5×5 *nanomagnets on a square lattice with* $N_c = 1$. $S = 5$, $T = 0$ K, $a = 1.5$ nm, $\mu_0 H_A = 0.75$ mT, $\alpha/\gamma = 0.6$. *The dashed grey, thick black, and light solid grey curves correspond to* $\frac{\Delta B}{\Delta t} = 300, 1500, 6000$ T/s, *respectively. The inset shows the entire curves.* $\boldsymbol{B} = B(\hat{\boldsymbol{x}} + \hat{\boldsymbol{y}})/\sqrt{2}$.

Results for $\theta = 0°$: Induction sweep rate dependence and accuracy check of the usage of the second-order Runge-Kutta integration method

Major differences appeared between the KS and TP results for the $N = 5$ square lattice calculations with $\theta = 0°$, which were Fig. 1(h) of KS and Fig. 7(d) of TP, shown here as Fig. 3.13 (a) and the dashed curve in Fig. 3.16 (a), respectively. Although nominally calculated for the same parameters N and θ, these hysteresis curves exhibit respectively four and three vertical steps on increasing and decreasing $\boldsymbol{B}$. In Fig. 3.13, we compare the KS results [Fig. 3.13 (a)] from their Fig. 1(h) with our results [Fig. 3.13 (b)] for $a = 1.5$ nm, $\Delta B/\Delta t = 3000$ T/s, evaluated using $dt = 5.17 \times 10^{-12}$ s (thick black curve) and $dt = 5.17 \times 10^{-14}$ s (thin white curve). As can readily be seen, these curves reproduce every feature of their curve, including the four vertical steps each upon increasing and decreasing $\boldsymbol{B}$, and there are no problems with the iteration accuracy.

In our previous results for two-dimensional arrays, we found that the hysteresis was nearly independent of the magnetic induction sweep rate $\Delta B/\Delta t$, provided that $h_{\rm dip} \propto a^{-3}$

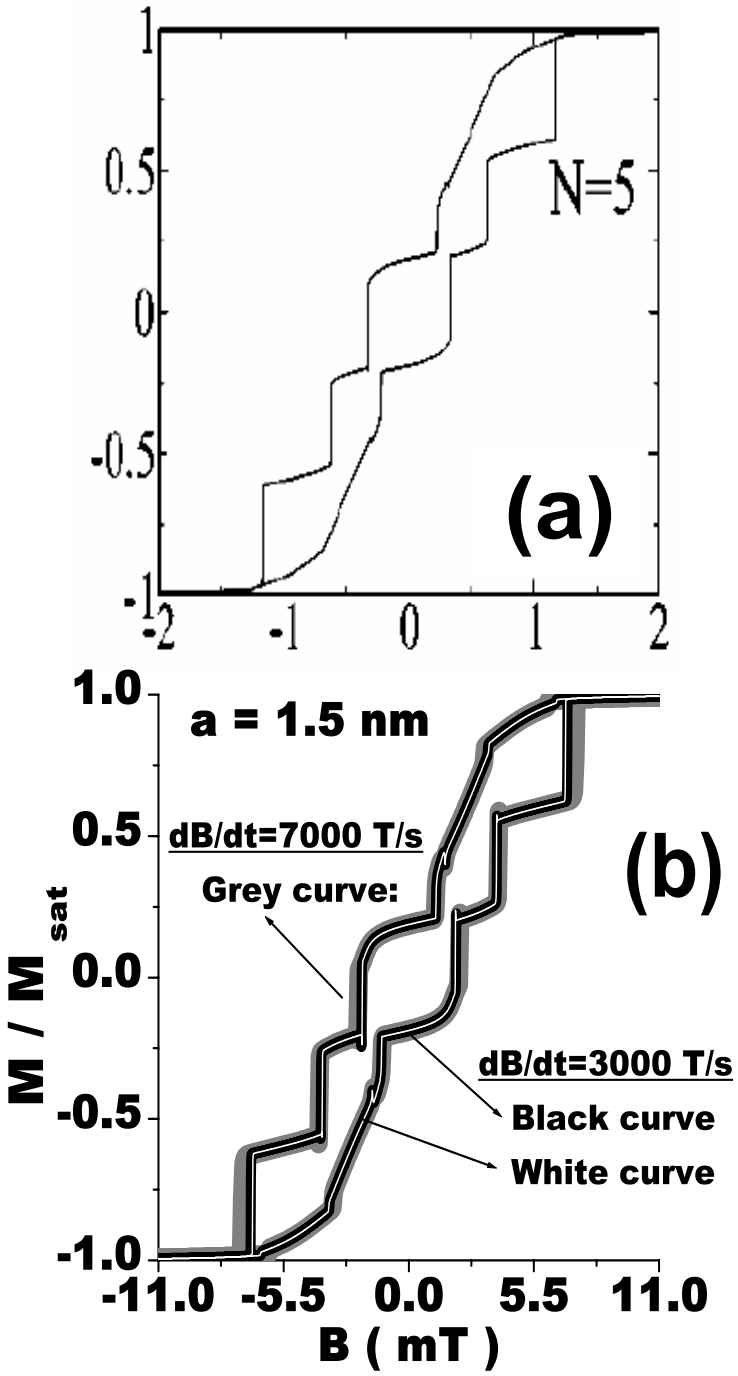

Figure 3.13: *(a): $M(H)$ hysteresis pattern from Fig. 1(h) of KS.*[94] *M and H are given in units of M_s, and $\theta = 0°$; (b): Our $M/M_{\rm sat}$ versus B results with $\theta = 0°$ for $a = 1.5$ nm. The thin white and thick black curves were both evaluated with $\Delta B/\Delta t = 3000$ T/s using $dt = 5.17 \times 10^{-14}$ s and $dt = 5.17 \times 10^{-12}$ s, respectively. The thick grey curve was evaluated with $dt = 5.17 \times 10^{-12}$ s and and $\Delta B/\Delta t = 7000$ T/s.*

was sufficiently large. Nevertheless, to check the case under study, we increased the sweep rate from $\Delta B/\Delta t = 3000$ T/s to 7000 T/s, using $dt = 5.17 \times 10^{-12}$ s, and presented the results as the thick grey curve in Fig. 3.13 (b). As expected, the curves with $\Delta B/\Delta t = 3000, 7000$ T/s are nearly identical, so that the sweep rate does not affect the magnetic hysteresis significantly, and is unlikely to account for the differences in the KS and TP results.

3.4.4 Lattice parameter dependence of the hysteresis

In Fig. 3.14, we have illustrated the effect of the lattice constant a upon the hysteresis. In this figure, we kept the other parameters fixed at $S = 5$, $T = 0$, $\frac{\Delta B}{\Delta t} = 3000$ T/s, $\mu_0 H_A = 0.75$ mT, $\alpha/\gamma = 0.6$, and $\boldsymbol{B} = B(\hat{\boldsymbol{x}} + \hat{\boldsymbol{y}})/\sqrt{2}$. As a is varied from 2.0 to 1.25 nm, the upper portions of the hysteresis curves appear from left to right, respectively. From Fig. 13, it is readily seen that the magnetization curves are very sensitive to a and hence to the strength of the dipolar interaction, which is proportional to a^{-3}. Our results for a=2.5 nm exhibit a smaller hysteresis shifted further to the left, and all indications of steps have disappeared. Although not shown in Fig. 3.14, as a is increased further to 3.0 nm, the hysteresis almost disappears entirely. We deduce that stronger dipolar interactions (smaller a) result in larger hysteresis loops and may increase the width of additional steps.

We then infer that contrary to the conclusion found for the 3D systems (based upon much smaller damping coefficients and much slower sweep rates), the dipolar interactions promote a hysteretic behavior in this 2D system.

Results for $\theta = 5°$ and $0°$ ($N = 5$): lattice parameter dependence in KS and TP calculations

We have showed that with decreasing a values (thus increasing h_{dip}) in two-dimensional arrays the area A_N of magnetic hysteresis increases, the hysteresis loops shift away from the central loop, and additional magnetization steps can also occur. Assuming both TP and KS plotted M and H in comparable units, we note that in comparing their $N = 5$,

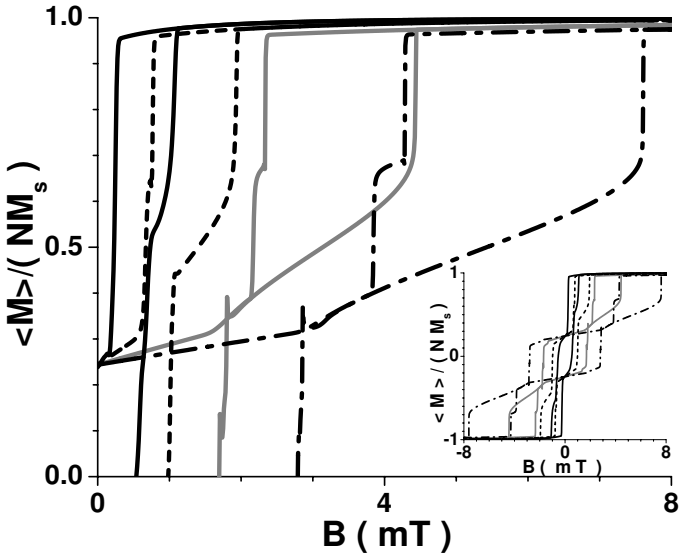

Figure 3.14: *Hysteresis loops for lattice parameters* $a = 2.5$ *nm (solid black),* $a = 2.0$ *nm (dashed black),* $a = 1.5$ *nm (solid grey), and* $a = 1.25$ *nm (dot-dashed black), for* 5×5 *nanomagnets on a square lattice with* $N_c = 1$. $S = 5$, $T = 0$ *K,* $\frac{\Delta B}{\Delta t} = 3000$ *T/s,* $\mu_0 H_A = 7.5 \times 10^{-4}$ *T,* $\alpha/\gamma = 0.6$. *The inset shows the entire curves.* $\boldsymbol{B} = B(\hat{\boldsymbol{x}} + \hat{\boldsymbol{y}})/\sqrt{2}$.

$\theta = 0°$ results, the KS $M(H)$ curve reached saturation at smaller M values than did the TP curve. This suggests that TP and KS scaled M differently. Since we had already checked one $N = 5$ curve of KS for accuracy, we first investigated further whether A_N might depend upon a in one of the $N = 5$ square arrays studied by either KS or TP. Since the $N = 5$ region of magnetic hysteresis is mostly localized around the origin in Fig. 2(g) of KS, we chose that case for study. In Fig. 3.15, we compare our results [Fig. 3.15 (b)] for the magnetization $M/M_{\rm sat}$ of a two-dimensional array with $N = 5$ and $\theta = 5°$ obtained for different a values with those [Fig. 3.15 (a)] presented in Fig. 2(g) by KS. In our calculations, the array saturation magnetization $M_{\rm sat} = M_s/(da^2)$ is different from the nanodot magnetization $M_s/V_{\rm dot}$. Figure 1 demonstrates that an excellent reproduction of the KS $\theta = 5°$ results is obtained using $\Delta B/\Delta t = 3000$ T/s and $a = 1.5$ nm, the same values that fit their $\theta = 45°$ results.[14] Furthermore, it is evident in Fig. 3.15 (b) that smaller a values lead to substantially larger hysteresis areas, consistent with our previous findings.

[14] We also checked the iteration accuracy for this figure by decreasing the iteration time interval dt a factor of 100, without any change in our results. Our results and those of KS provided strong evidence that those $N = 5$ KS results were also sufficiently accurate. On the other hand, we have seen that the induction sweep rate, which is unspecified in TP paper, seems not be explain the the apparent differences between the KS and TP results (in the $N = 5$ calculation).

In order to determine the source or sources of these, we varied the lattice parameter a, which was unspecified by TP, to reproduce the different TP results for $N = 5$ and $\theta = 0°$ keeping the sweep rate fixed at $\Delta B/\Delta t = 3000$ T/s, and varying a. A comparison of their Fig. 7(d) and our best fit to their results is presented in Fig. 3.16. The relevant TP results are shown as the dashed curve in Fig. 3.16 (a). Our best fit to that curve was obtained with $a = 1.2$ nm, and is pictured in Fig. 3.16 (b). Here we checked the accuracy of the TP calculation using our high accuracy time interval, $dt = 5.17 \times 10^{-14}$ s. We obtained excellent agreement with the TP results, even with the three vertical steps on increasing and decreasing $\boldsymbol{B}$. The different values of the lattice constant $\boldsymbol{a}$ used to fit the TP and KS curves, 1.2 nm and 1.5 nm, respectively, can account quantitatively for the strong, qualitative differences in the KS and TP hysteresis curves.

3.4.5 Abrupt change in the number of steps of the hysterisis loops with the lattice constant

In comparing Figs.Fig. 3.13 (b) and Fig. 3.16 (b), we see that there is a remarkable difference in the results obtained with only a 25% variation in a, as the number of steps changed by unity on both increasing and decreasing the field. Although we previously observed a smooth *increase* in step number with decreasing a for $\theta = 45°$, we wondered whether this *decrease* in step number with decreasing a for $\theta = 0°$, nominally opposite behavior to that for $\theta = 45°$, might occur abruptly or smoothly. Hence, we performed additional calculations with a values in the range 1.2 nm $< a <$ 1.5 nm to answer this question. Our results are pictured in Fig. 3.17. From these curves, it is evident that the qualitative change is abrupt, with

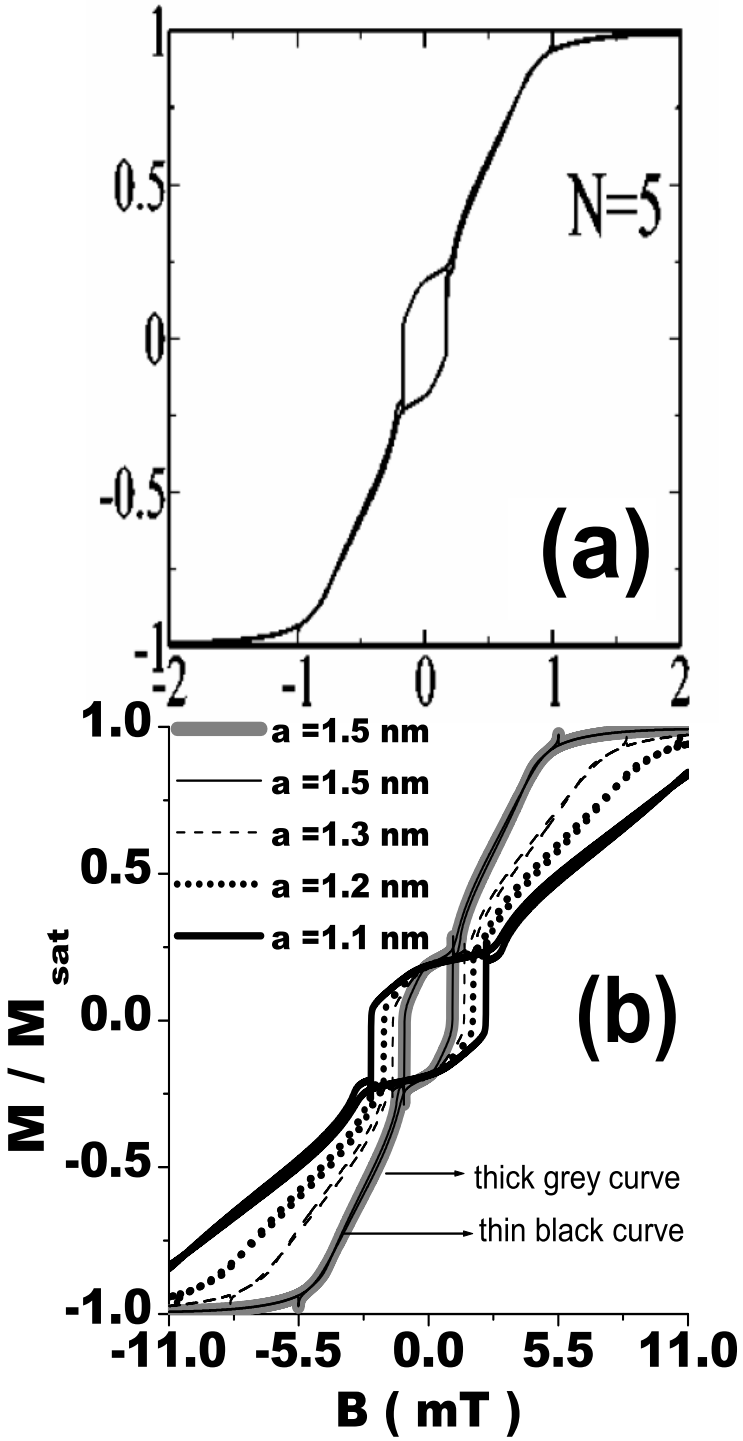

Figure 3.15: *(a): $M(H)$ hysteresis pattern from Fig. 2(g) of KS.*[94] *M and H are given in units of M_s, and $\theta = 5°$; (b): Our $M/M_{\rm sat}$ versus B results with $\theta = 5°$ for the a values listed and $\Delta B/\Delta t = 3000$ T/s. The thin black curve (inside the thick grey curve) was evaluated with $dt = 5.17 \times 10^{-14}$ s. All other curves were evaluated with $dt = 5.17 \times 10^{-12}$ s.*

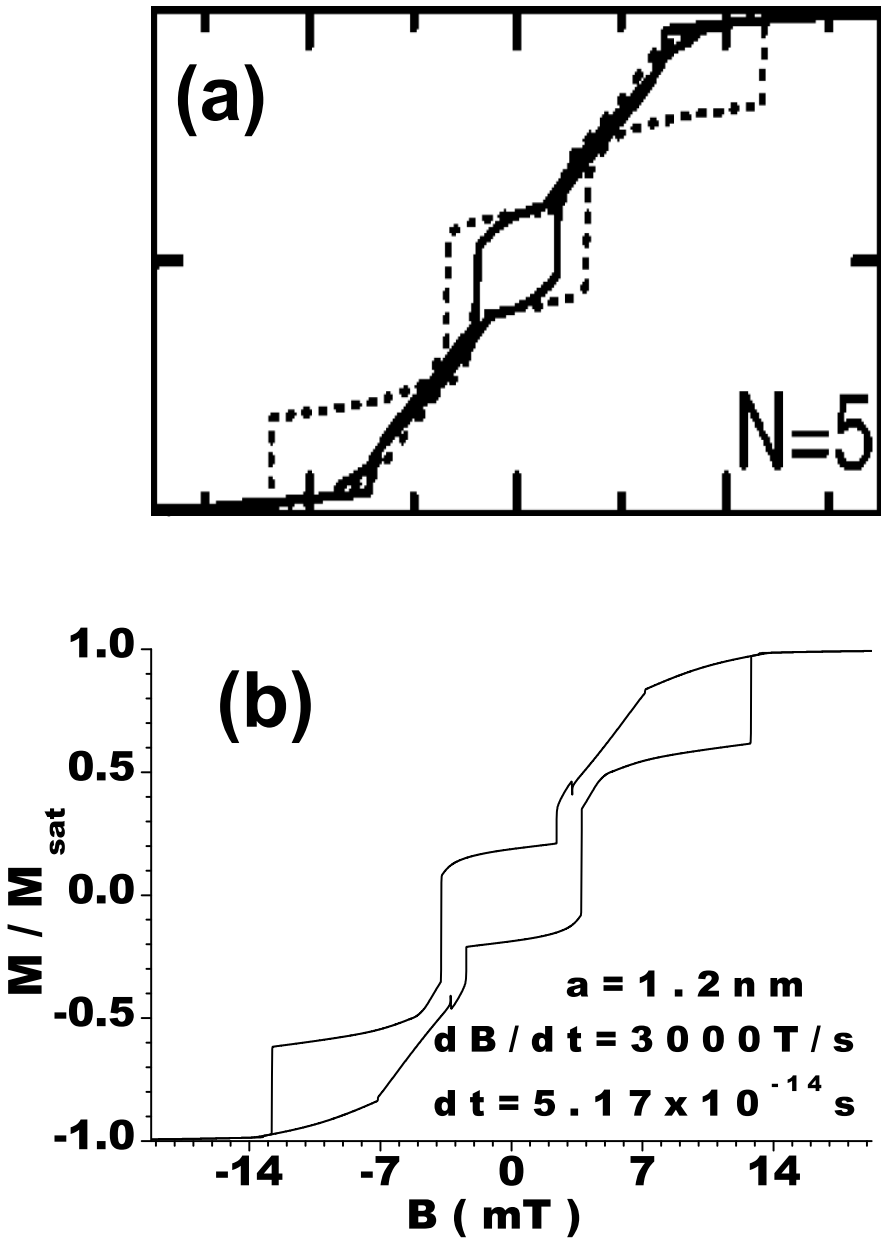

Figure 3.16: *(a): $M(H)$ hysteresis pattern (dashed) from Fig. 7(d) of TP.*[85] *M and H are given in units of M_s and M_s/a^3, and $\theta = 0°$. (b): Our $M/M_{\rm sat}$ versus B results with $\theta = 0°$ for $a = 1.2$ nm, $\Delta B/\Delta t = 3000$ T/s, and $dt = 5.17 \times 10^{-14}$ s.*

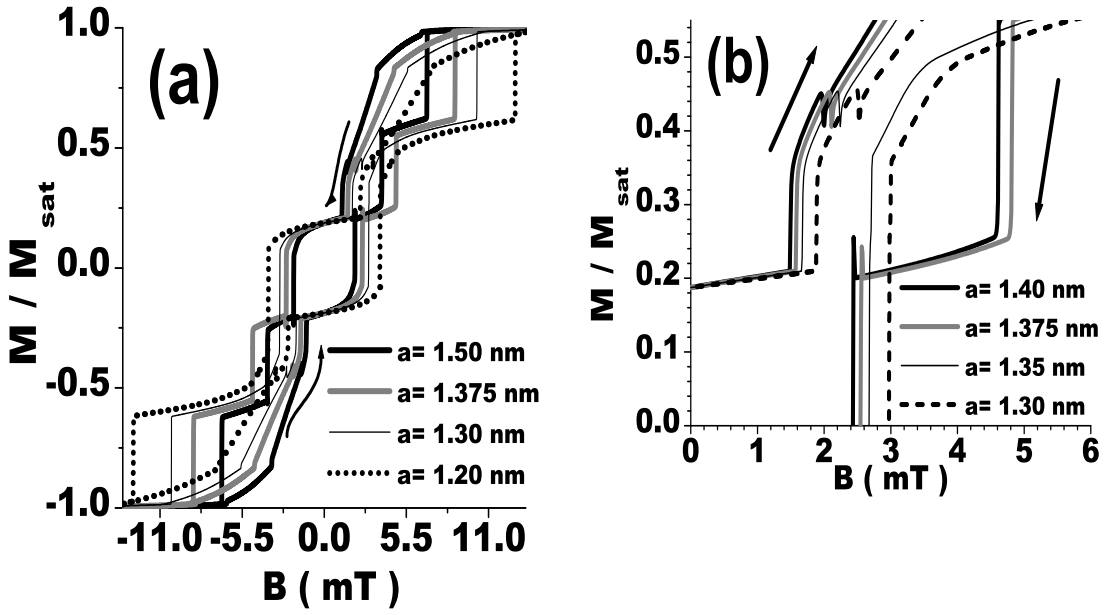

Figure 3.17: *(a): M/M_{sat} versus B for $\theta = 0°$, $N = 5$, $\Delta B/\Delta t = 3000\,T/s$, $dt = 5/17 \times 10^{-14}s$, and a values ranging from 1.2 nm to 1.5 nm. (b): Upper portion of the M/M_{sat} versus B curve for $\theta = 0°$, $N = 5$, $\Delta B/\Delta t = 3000\,T/s$, $dt = 5/17 \times 10^{-14}s$, and a values ranging from 1.30 nm to 1.40 nm.*

the extra step appearing at $a = a*$, where 1.35 nm $< a* <$ 1.375 nm. By comparing the Fig. 3.17 (a) curves for $a = 1.2$ nm and $a = 1.5$ nm, it appears that smaller a values lead to larger hysteresis areas. However, from Fig. 3.17 (b), we note that as a is decreased through $a*$, there is a dramatic decrease in the hysteresis area. Hence, the variation of the hysteresis area, A_N, as a function of the lattice parameter is non-monotonic - as it is with respect to the variation of the size of the array -[94] but may show an abrupt increase upon a small variation of the dipolar interaction strength, as shown in Fig. 3.18.

3.5 Summary

We first found $N_c = 100$ sample configurations with an overall magnetization close to 0. We then solved the Landau-Lifshitz equation for a 3D cubic lattice of $N = 5 \times 5 \times 4$ nanomagnets, subject to dipole-dipole interactions and spin anisotropy. These results should be

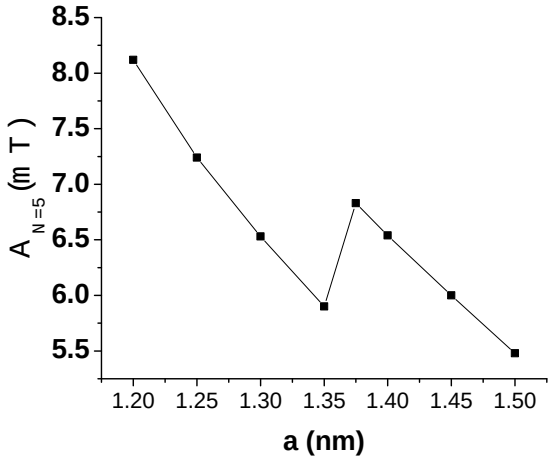

Figure 3.18: *Area of the magnetization hysteresis loops, $A_{N=5}$, versus the lattice parameter, a, of the 5×5 square array for $\theta = 0°$, $\Delta B/\Delta t = 3000\,T/s$, $dt = 5/17 \times 10^{-14}$ s.*

relevant for an array of Stoner-Wolfarth nanomagnets, and to some extent, single molecule magnets, although the quantum nature of the latter has so far been neglected. In the absence of spin anisotropy, we varied the magnetic induction sweep rate $\frac{\Delta B}{\Delta t}$, the damping constant α, the lattice constant a, and the temperature T. We also considered the effects of a T-dependent damping constant of the form $\alpha(T)/\gamma = T_0/T$ suggested by Fredkin and Ron. For slow sweep rates and small α relevant for experimental studies on single molecule magnets, magnetic hysteresis appears in the regions of the magnetization curves near to saturation, the area and onset magnetic induction strength of which increases with decreasing α and increasing sweep rate. With decreasing T, the onset magnetization magnitude of the hysteretic regions near to saturation decreases. With decreasing a corresponding to increased dipole-dipole interaction strengths, the onset of the hysteresis regions near to saturation appears at increasing magnetic induction magnitude.

At much larger sweep rates and damping constants, the magnetization curves attain saturation at much smaller applied magnetic induction strengths. The hysteretic regions just below saturation have moved somewhat below saturation, and a new central hysteretic region appears. As one follows the magnetization curve for a single configuration, the

starting curve exhibits oscillations at a rather constant (magnetic induction independent) frequency $f/2$, but the phase of the magnetization oscillations is a random function of the configuration. After the attainment of magnetic saturation, this central hysteretic region exhibits oscillations at f, twice that frequency, possibly with weak higher harmonics, for T not too low, which are independent of the configuration.

When the applied magnetic induction is in the (110) direction (from the sample center to one of its corners), magnetic hysteresis exhibiting steps and jumps appears within the central region, but vanishes at and very near to the origin. Although these step-like features are suggestive of the behavior seen in single molecule magnets, they are present at rather high T values, as they arise from the classical sample shape effects.

In the presence of the magnetic anisotropy field $\boldsymbol{H}_A$, an applied magnetic induction parallel to the anisotropy axis leads to a large central hysteresis region, provided that the magnitude of the spin anisotropy is sufficiently large. For the applied magnetic induction perpendicular to the magnetic anisotropy, no central hysteresis region is present, although a small amount of hysteresis near to saturation persists for sufficiently small spin anisotropy strength, and the slope of the magnetization curve at the origin is non-monotonic, exhibiting a maximum at a particular small value of the spin anisotropy strength. These effects for the spin anisotropy are qualitatively in agreement with those in many types of arrays of nanomagnets, including single molecule magnets.

We studied the simplified 5×5 2D square lattice with a perpendicular spin anisotropy field $\boldsymbol{H}_A$ using the same procedure, and for a particular set of parameters, obtained quantitative agreement with a hysteresis curve obtained for that system by Kayali and Saslow.[94] We showed that their hysteresis curve is basically independent of H_A until $\mu_0 H_A$ is on the order of the external induction. We also demonstrated that the magnetic hysteresis does not depend significantly upon the magnetic induction sweep rate, as opposed to the dependence we found in our 3D system. In addition, we found that the magnetization of the 2D system is very sensitive to variations in the lattice parameter a. Indeed, we have accounted for the

qualitative differences present in the calculations by Kayali and Saslow and by Takagaki and Ploog of the magnetization curves for square, 5×5 magnetic nanodot arrays with dipole-dipole interdot interactions with the magnetic field parallel to one of the array edges, by using different a values. Both of their calculations were sufficiently accurate and insensitive to the magnetic induction sweep rate. We note that the particular a values we used to fit the KS and TP curves, $a_{\rm KS} = 1.5$ nm and $a_{\rm TP} = 1.2$ nm, are in quantitative agreement with their different $h_{\rm dip}$ choices, $a_{\rm TP}/a_{\rm KS} = (h_{\rm dip}^{KS}/h_{\rm dip}^{\rm TP})^{1/3} = 2^{-1/3}$. We note that for the same nanodot magnetic moment M_s, comparing the same nanodot magnetization values requires setting $V_{\rm dot}^{\rm TP} = V_{\rm dot}^{\rm KS}$, so that the different a values arise solely from different dipolar interaction strength $h_{\rm dip}$ choices. In short, we have shown that there were two reasons for the apparent discrepancies in the KS and TP results. First, there was confusion created by both KS and TP. KS used two inequivalent definitions of M_s. TP used both an infinitely small nanodot volume and incompatible units for the magnetization and magnetic field. Second, the above exposé shows that even after these two differences are reconciled through proper definitions of the nanodot magnetization and magnetic moment, what sets the KS and TP calculations apart is their uses of different dipolar interaction strengths $\boldsymbol{h}_{\mathbf{dip}}$. The TP calculations based on twice the KS dipolar interaction strength naturally lead to qualitatively different behavior.

Finally, we noticed that although dipolar interactions also oppose the magnetization process in 2D systems by increasing the onset magnetic induction strength for the attainment of saturation as in 3D systems, their effect is opposite to that found for the 3D system with a much smaller damping coefficient and much slower sweep rate. We find that when qualitative changes in the $M(B)$ curves do not occur with decreasing lattice constants, the area of the hysteresis increases correspondingly. We also showed that at least one critical a value $a*$ can exist, at which qualitative changes in the $M(B)$ hysteresis curves appear, accompanied by an abrupt decrease in the hysteresis loop area upon a minuscule increase of the interaction strength.

Chapter 4

First principles calculations of the electronic and geometric structure of $Ag_{27}Cu_7$ Nanoalloy

4.1 Introduction

Small bimetallic nanoclusters often have physical and chemical properties that are distinct from that of their pure bulk counterparts and suggestive of novel applications.[15,96,97] Not surprisingly, materials assembled from finite-sized bimetallic clusters have been investigated intensively not only for their catalytic and optical properties,[98–108] but also for their ability to assemble into *cluster crystals*[109,110] and their possible applications in single-electron tunnelling devices.[15] Along with its high symmetry and relatively high melting temperature, one of the criteria for a cluster to be used as a potential building block for cluster-assembled materials is its chemical stability relative to other reagents and to other clusters of the same material. Also, major difficulties arise from the fact that clusters may tend to coalesce when assembled. This can be prevented in one of two ways - either by isolating the clusters in matrices or by coating them with surfactants.[110] An alternative route is to find nanoclusters that are naturally stable, i.e., nanoclusters whose intra-cluster interaction is stronger than the inter-cluster interaction allowing the clusters to keep their individual identity intact upon assembling. Even so, cluster-assembled materials could still be metastable against dissociation into their bulk phases.

Darby et al.[97], using many-body Gupta potentials, studied the structure and stability (as reflected by the total energy) of a wide variety of Cu_xAu_y nanoclusters with up to 56 atoms and $x/y = 1, 3$; corresponding to the well-known $x : y$ ratios that result in stable ordered bulk phases at low-temperatures.[111] They found that the geometry of the cluster is influenced by the tendency to maximize the number of $Cu - Au$ and $Au - Au$ bonds. Rossi et al.[15], on the other hand, proposed a new family of 34-atom bimetallic alloys using the genetic global optimization technique (GGO).[15] These nanoalloys are characterized by a perfect core-shell structure in which the *smaller* atoms (Cu or Ni) compose the core whereas, the relatively larger, Ag atoms lie on the surface. They find the nanoalloys to be energetically and thermodynamically more stable than pure clusters Ni_{34}, Cu_{34}, and Ag_{34},[15] and attribute the relative stability of the nanoalloy structures to the supplanting of the inner Ag atoms by *smaller* atoms (Cu or Ni) thereby reducing the internal strain in Ag_{34}, or the replacement of outer Cu atoms by *larger* atoms (Ag) to reduce the external strain in Cu_{34}. As we shall see later, the most stable of the 34-atom $Ag - Cu$ nanoalloy family proposed by Rossi et al,[15] $Ag_{27}Cu_7$, provides a hint that it is not the $x : y$ ratio that guarantees the stability of either bulk or nano-alloys, rather it is the maximization of the number of *optimized* $Cu - Cu$ and $Cu - Ag$ bonds.

Among a set of possible core-shell nanoclusters modelled by many-body interatomic potentials, Rossi et al.[15] chose the compositions corresponding to their most stable structures for some selected sizes and *locally* optimized the structures using density functional theory (DFT) to confirm the trends given by the GGO and to single out the clusters with high electronic stability, namely, the width of HOMO-LUMO (Highest Occupied Molecular Orbital - Lowest Unoccupied Molecular Orbital) gap. They determined the thermodynamic stability of the chosen structures through calculations of the melting temperatures from molecular dynamics simulations and of temperature-dependent probabilities of the global minima by harmonic thermodynamics.[112] Among the 34-atom family of nanoclusters, they found $Ag_{27}Cu_7$ and $Ag_{27}Ni_7$ to have the least excess energy with respect to bulk atoms

(the lowest heat of formation), strong electronic stability (large HOMO-LUMO gap), and relatively high melting temperatures.[15] For these particular clusters they have proposed a structure with D_{5h} symmetry in which the 7 core-Cu atoms form a decahedral structure while the 27 shell-Ag atoms are placed in an anti-Mackay overlayer.

Experiments and heat of formation calculations have shown that $Ag-Cu$ alloys generally tend to segregate.[113–115] In a sense, the core-shell structure of $Ag_{27}Cu_7$ nanoalloy is itself segregated. In order to understand how its particular geometry implicitly stabilizes it, a detailed examination of the relative strengths and lengths of the $Ag-Cu$, $Cu-Cu$, and $Ag-Ag$ bonds is needed. For bulk $Cu-Au$ alloys the presence of a dip in the electronic DOS near the Fermi level was also considered to be a signature of alloy stability.[113] Interestingly, such a dip is not found in bulk $Au-Ag$ alloys.[111,113] Moreover, in the case of crystalline solids, the structural stability is linked to the absence of phonon instabilities.[116] The purpose of this paper is to carry out a full investigation of the relationship between the geometric and electronic structure of $Ag_{27}Cu_7$ nanoalloy and related bulk systems to get insights into the various factors that may impact their stability. That is, through examination of the formation energy, the density of states near the Fermi level, the HOMO-LUMO gap, and the charge density distribution, we develop criteria which may lead to chemical and electronic stability of $Ag_{27}Cu_7$. To obtain additional insights into the structure-stability relationship, we have also carried out calculations of the bond-length, the electronic structure, and the phonon dispersion of Ag_3Cu and Cu_3Ag bulk alloys in their Ll_2 phase.

The rest of the chapter is organized as follows: Section 4.2 contains the computational details, while Section 4.3 is a summary of our results and is divided in subsections 4.3.1 and 4.3.2. Subsection 4.3.1 analyzes the geometry and bond coordination of the atoms in the $Ag_{27}Cu_7$ nanoalloy and those in the bulk $Ag-Cu$ Ll_2 alloys, for insights into proposed stability criteria. In Subsection 4.3.2, we examine our calculated DOS of $Ag_{27}Cu_7$ and of the bulk systems (Cu_3Ag and Ag_3Cu), and the charge density distribution of $Ag_{27}Cu_7$. Finally, in Section 4.4 we summarize our conclusions, and discuss how the relation between structure

and stability in $Ag_{27}Cu_7$ nanoalloy can be understood in terms of a specific hierarchy in bond strength and the capability of the structure to provide the bond lengths for which that hierarchy is satisfied.

4.2 Computational Details

Periodic super-cell calculations are performed in the framework of density functional theory.[117] Our calculations are based on the pseudopotential approach and the plane wave method (Quantum ESPRESSO: opEn-Source Package for Research in Electronic Structure, Simulation, and Optimization).[118] Ultra-soft pseudo-potentials[119] used here are generated consistently with GGA schemes. For the GGA functional the expression introduced by Perdew, Burke, and Ernzerhof (PBE) has been introduced.[120] Integrations up to the Fermi surface are performed by using a broadening technique[41] with smearing parameter of 0.2 eV (0.147 Ry). Below we provide some specifies of the calculations as relevant to a particular system.

4.2.1 Calculation of bulk systems

We have performed extensive convergence tests for lattice constants, bulk moduli and total energies of bulk Cu, Ag, Ag_3Cu , and Cu_3Ag . To obtain the minimum energy configuration with zero stress based on total energy differences of 1 mRy, as well as, convergence up to the third and second digit in the lattice parameter (in a.u.), and the bulk modulus (in Mbar), respectively, the calculations demand a k-point sampling of 145 Monkhorst-Pack special points[121] (corresponding to a $16 \times 16 \times 16$ Monkhorst-Pack grid) for the integrations over the Brillouin zone (BZ). Furthermore, the plane wave kinetic energy cut-off, E_{cut}, and the energy at which the charge density Fourier expansion is truncated, E_ρ, had to be set equal to 680 eV (50Ry) and 8160 eV (600 Ry), respectively. These convergence criteria surpass by far most of those reported in the literature, but are necessary to obtain reliable results in the present case, as we will see.

The lattice dynamics of Ag_3Cu and Cu_3Ag bulk alloy at arbitrary wave-vectors is obtained by the Perturbational DFT (DFPT) which is based on the linear response theory.[122–124] To determine the force constants we use a $2 \times 2 \times 2$ q-point mesh in the BZ of the Ll_2 structure.[123] Phonon dispersion curves are obtained by the standard Fourier interpolation method.[123]

4.2.2 Calculation of $Ag_{27}Cu_7$ nanoalloy and isolated atoms

Since in the unrelaxed configuration of $Ag_{27}Cu_7$ the separation between the most distant atoms was about 8.7 Å, we locate the nanoalloy inside a cubic super-cell with side length of 24 Å. In this manner we ensure that as a result of periodic boundary conditions, the atoms at the edges of neighboring clusters are at least 15 Å apart, thereby isolating the clusters from each other. The same cubic box is used to model and calculate the total energy of isolated Cu and Ag atoms, using a spin-polarized calculation.

In this work the Broyden-Fletcher-Goldfarb-Shanno (BFGS) algorithm[125] is used to minimize the nanoalloy total energy as a function of atomic positions.[118] At equilibrium, forces on the nanocluster atoms are required to be below 6.5×10^{-4} eV/A (2.6×10^{-5} Ry/au). Given the large dimensions of the super-cell used for the nanoalloy and the free atom calculations, integrations over the BZ can be accurately performed using only 1 k-point. To confirm this, we have tested the total energy convergence using 24 special k-points to find that the total energy changes by only 4×10^{-5} eV while forces on each atom remain below 8×10^{-3} eV/A. For the nanoalloy, E_{cut} and E_ρ are 680 eV and 8160 eV, respectively, as mentioned above. Since these parameters surpass the demands for convergence in other systems involving copper or silver, and using the same DFT code,[126,127] we expect them to work well for the nanoalloys of interest here. While these demands for convergence make the calculations very cpu intensive, it is worth mentioning that we find the total energy and even the geometry of the nanoalloy to be severely affected if we were to use the default values of $E_{cut} = 340$ eV and $E_\rho = 1360$ eV in the code. For example, with the latter choice, the fully relaxed

D_{5h} structure (resulting from E_{cut} = 680 eV and E_{ρ} = 8160 eV) is no longer stable and displays intra-layer dislocations of up to 1 Å and forces which cannot be lowered below 2.5×10^{-2}eV/A.

4.3 Results and Discussion

Since the nanoalloy presents several opportunities for comparison of its properties and development of criteria for its stability, we find it beneficial to divide this section into two subsections, each of which consists of several parts. In subsection 4.3.1, we concentrate on issues related to the geometry, the distribution of bond lengths, the atomic coordination, and the formation energy of the nanoalloy. We first introduce a notation in subsection 4.3.1.1 that classifies the atoms in $Ag_{27}Cu_7$ according to their location within the nanoalloy. In 4.3.1.2, we inspect how the local coordination of the atoms in the nanoalloy relates to the bond lengths. Since there is hardly any experimental data on $Ag_{27}Cu_7$ and since calculations of the phonon density of states of the nanoalloy from first principles is still a challenge, we have included in subsection 4.3.1.3 our results for the structure and dynamics of bulk alloys, Ag_3Cu and Cu_3Ag, to gain insights and draw stability criteria for the nanoalloy of interest here. The average formation energy of $Ag_{27}Cu_7$ nanoalloy and stability considerations are analyzed in subsection 4.3.1.4.

In subsection 4.3.2 we focus on the electronic DOS and the local charge density of the nanoalloy. Subsection 4.3.2.1 contains the electronic DOS of the $Ag_{27}Cu_7$ nanoalloy and includes for comparison also those of bulk alloys, Ag_3Cu and Cu_3Ag. The local charge density distribution in the nanoalloy is summarized in subsection 4.3.2.2.

4.3.1 Geometry, bond coordination, and stability considerations

4.3.1.1 Geometric Structure of $Ag_{27}Cu_7$ nanoalloy

The initial configuration we adopted for $Ag_{27}Cu_7$[128] nanoalloy nicely relaxes towards the D_{5h} symmetry after energy minimization, as seen from the plots in Fig. 4.1. Accordingly,

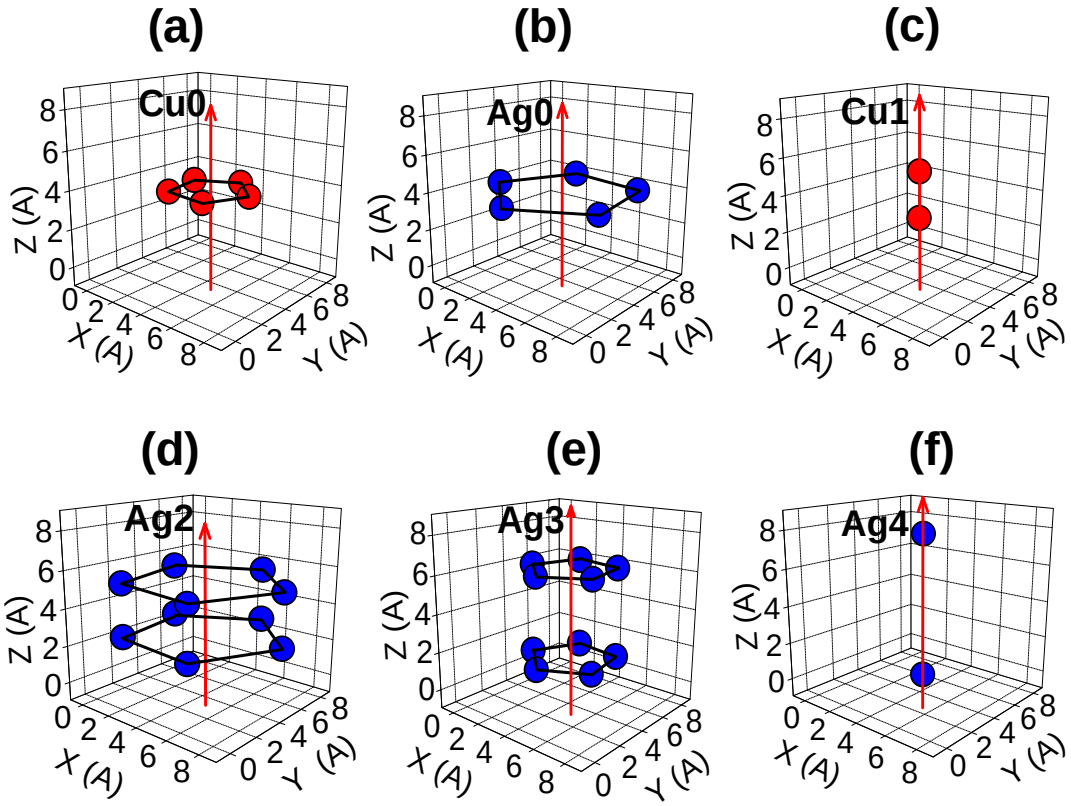

Figure 4.1: *Three-dimensional picture of the six types of non-equivalent atoms. The red arrow represents the 5-fold rotation axis. (a) Five $Cu0$ atoms sitting on the mirror plane of the cluster, $z_0 = 3.88$ Å. Note that the z_i-coordinates are given with respect to the reference frame used in the figure and will define later interlayer distances; (b) The five $Ag0$ atoms also sit on the mirror plane, $z_0 = 3.88$ Å; (c) Two $Cu1$ atoms sitting on the 5-fold rotation axis symmetrically located above and below the mirror plane, $z_1 = 5.17$ Å and $z_{-1} = 2.59$ Å. Notice that $Cu0$-pentagon fits in the $Ag0$-pentagon; (d) Ten $Ag2$ atoms form two pentagons symmetrically located above and below the mirror plane, $z_2 = 5.31$ Å and $z_{-2} = 2.44$ Å; (e) Ten $Ag3$ form two pentagons symmetrically located above and below the mirror plane, $z_3 = 6.24$ Å and $z_{-3} = 1.52$ Å; (f) The two $Ag4$ atoms sit on the 5-fold rotation axis symmetrically located above and below the mirror plane, $z_4 = 7.76$ Å and $z_{-4} = 0$ Å.*

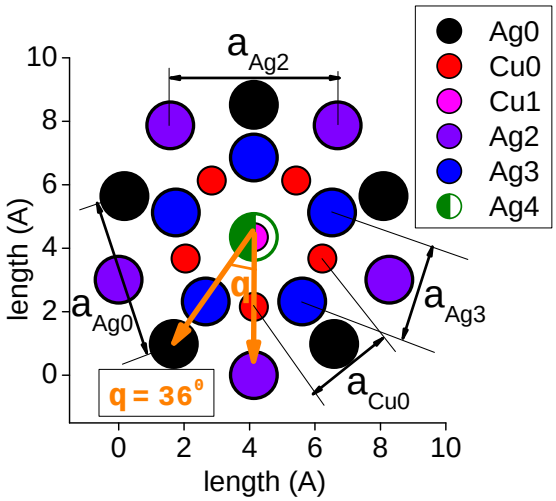

Figure 4.2: Top view *of $Ag_{27}Cu_7$ nanoalloy, perpendicular to the mirror plane. The side length of each pentagon as a_{M_n} (see text).*

there are only 6 types of non-equivalent atoms: 4 types of Ag and 2 types of Cu atoms. This leads to a natural and useful classification of the atoms that refers to their distance from the mirror plane: Cu layer 0 ($Cu0$), Ag layer 0 ($Ag0$), Cu layer ±1 ($Cu1$), Ag layer ±2 ($Ag2$), Ag layer ±3 ($Ag3$), Ag layer ±4 ($Ag4$), as shown in Fig. 4.1. Layer 0, which lies on the mirror plane, consists of two pentagonal structures; the smaller one is made of copper atoms ($Cu0$) and fits in the larger one that is composed of silver atoms ($Ag0$) (Fig. 4.1(a) and (b)). The *single-atom layers*, layers ±1 and ±4, sit on the 5-fold rotation axis (see Fig. 4.1(c) and (f)). The other two pentagonal layers, ±2 and ±3, are centered at the 5-fold symmetry axis (Fig. 4.1(d) and (e)). The radii of $Ag2$ and $Cu0$ pentagons are parallel to each other, but rotated 36° with respect to the $Ag0$ and $Ag3$ pentagons, as shown in Fig. 4.2. Since the layers are symmetric with respect to a mirror plane, the cluster can be characterized by only five of them, say, the central layer (layer 0) and those above this (layers 1 to 4). Ultimately, the symmetry of $Ag_{27}Cu_7$ allows us to fully describe its geometric structure by 8 parameters: the interlayer distances ($d_{01} = 1.341$, $d_{12} = 0.052$, $d_{23} = 0.992$, $d_{34} = 1.512$ Å) and the pentagons. side length ($a_{Cu0} = 2.584$, $a_{Ag0} = 4.897$,

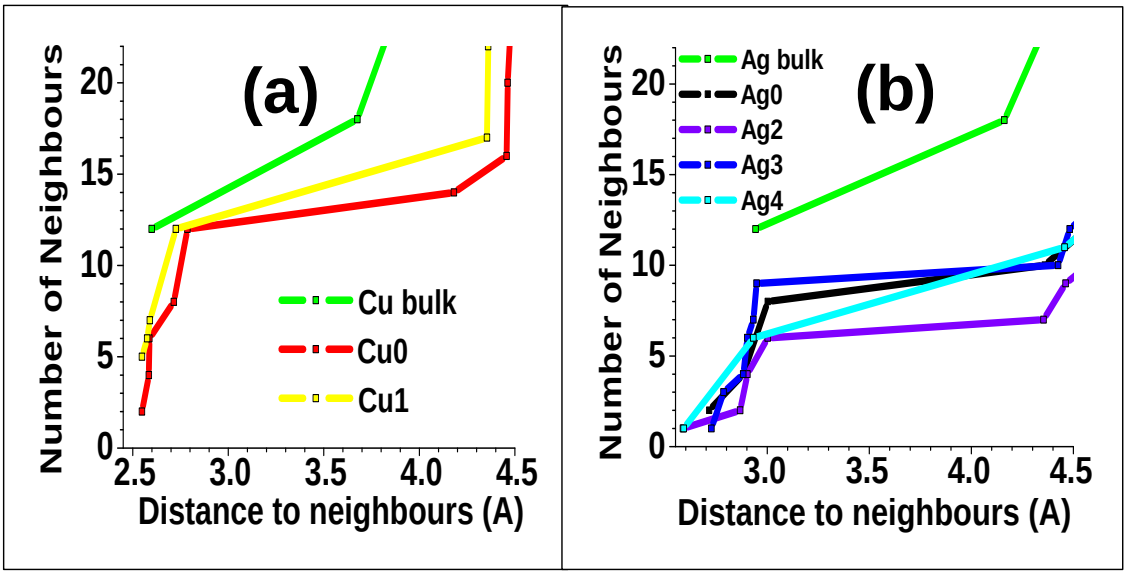

Figure 4.3: *(a) Bond coordination for Cu atoms of $Ag_{27}Cu_7$ compared with Cu bulk; (b) bond coordination for Ag atoms of $Ag_{27}Cu_7$ compared with Ag bulk.*

a_{Ag2} = 5.115, a_{Ag3}= 2.948 Å, as shown in Fig. 4.2). The dislocations in the D_{5h} structure, as present in our initial configuration,[128] relaxed into the perfect D_{5h} structure under the stringent criterion that the apothem of each pentagon can be well defined up to 0.0003 Å, while interlayer distances are well defined up to 0.0001 Å. The interatomic bond lengths for the 34 atoms in the cluster, in the relaxed geometry, are summarized in Table 4.1, and discussed in detail below.

4.3.1.2 Neighbor distances in $Ag_{27}Cu_7$: a comparison with bulk Ag and bulk Cu values

Despite the perfect D_{5h} symmetry of the cluster, Table 4.1 shows an intricate hierarchy of NN in the optimized structure. For example, for $Ag3$ the 1^{st} NN atoms ($Cu1$) are at 2.726 Å while their 6^{th} nearest neighbors are at 2.948 Å, all within a separation of 3.0 Å. Figs. 4.3 (a) and (b) show a comparison between the bond coordination of atoms in the $Ag_{27}Cu_7$

Table 4.1: *This table contains six sets of 2-column "sub-tables" showing the distance (d) from each type of atom in the nanoalloy to all its neighbors. In the right column of each sub-table appears the type of neighbor which is being referred and the number of such equivalent atoms at the same distance is shown as a subscript. Notice that here equivalent atoms are not considered being so if they do not belong to the same layer.*

$Cu0$		$Ag0$		$Cu1$		$Ag2$		$Ag3$		$Ag4$	
Type (NN)	d (Å)	Type (NN)	d (Å)	Type (NN)	d (Å)	Type (NN)	d (Å)	Type (NN)	d (Å)	Type (NN)	d (Å)
$Cu1^1$	2.55	$Cu0^2$	2.72	$Cu0^5$	2.55	$Cu0^1$	2.59	$Cu1^1$	2.73	$Cu1^1$	2.59
$Cu\text{-}1^1$	2.55	$Ag3^1$	2.88	$Cu\text{-}1^1$	2.58	$Ag\text{-}2^1$	2.87	$Cu0^2$	2.79	$Ag3^5$	2.93
$Cu0^2$	2.58	$Ag\text{-}3^1$	2.88	$Ag4^1$	2.59	$Ag3^2$	2.90	$Ag0^1$	2.88	$Cu0^5$	4.46
$Ag2^1$	2.59	$Ag2^2$	3.00	$Ag3^5$	2.73	$Ag0^2$	3.00	$Ag2^2$	2.90	$Ag2^5$	4.99
$Ag\text{-}2^1$	2.59	$Ag\text{-}2^2$	3.00	$Ag2^5$	4.35	$Cu1^1$	4.35	$Ag4^1$	2.93	$Cu\text{-}1^1$	5.17
$Ag0^2$	2.72	$Cu1^1$	4.36	$Ag0^5$	4.36	$Cu0^2$	4.46	$Ag3^2$	2.95	$Ag0^5$	5.69
$Ag\text{-}3^2$	2.79	$Cu\text{-}1^1$	4.36	$Ag\text{-}3^5$	4.43	$Ag\text{-}3^2$	4.68	$Cu\text{-}1^1$	4.43	$Ag\text{-}3^5$	6.72
$Ag3^2$	2.79	$Ag3^2$	4.77	$Ag\text{-}2^5$	5.13	$Ag4^1$	4.99	$Cu0^2$	4.48	$Ag\text{-}2^5$	6.87
$Cu0^2$	4.18	$Ag\text{-}3^2$	4.77	$Ag\text{-}4^1$	5.17	$Ag2^2$	5.12	$Ag\text{-}2^2$	4.68	$Ag4^1$	7.76
$Ag4^1$	4.46	$Ag0^2$	4.90			$Cu\text{-}1^1$	5.13	$Ag\text{-}3^1$	4.72		
$Ag\text{-}4^1$	4.46	$Cu0^2$	5.28			$Ag3^2$	5.73	$Ag0^2$	4.77		
$Ag2^2$	4.46	$Ag4^1$	5.69			$Ag\text{-}2^2$	5.86	$Ag3^2$	4.77		
$Ag\text{-}2^2$	4.46	$Ag\text{-}4^1$	5.69			$Cu0^2$	6.43	$Cu0^1$	5.26		
$Ag3^2$	4.48	$Cu0^1$	6.36			$Ag\text{-}3^2$	6.81	$Ag\text{-}3^2$	5.56		
$Ag\text{-}3^2$	4.48	$Ag3^2$	6.79			$Ag\text{-}4^1$	6.87	$Ag2^2$	5.73		
$Ag3^1$	5.26	$Ag\text{-}3^2$	6.79			$Ag3^1$	6.92	$Ag\text{-}3^2$	6.71		
$Ag\text{-}3^1$	5.26	$Ag2^2$	7.04			$Ag0^2$	7.04	$Ag\text{-}4^1$	6.72		
$Ag0^2$	5.28	$Ag\text{-}2^2$	7.04			$Ag\text{-}3^1$	7.84	$Ag0^2$	6.79		
$Ag0^1$	6.36	$Ag0^2$	7.92			$Ag2^2$	8.28	$Ag\text{-}2^2$	6.81		
$Ag2^2$	6.43	$Ag2^1$	8.64			$Ag0^1$	8.64	$Ag2^1$	6.92		
$Ag\text{-}2^2$	6.43	$Ag\text{-}2^1$	8.64			$Ag\text{-}2^2$	8.76	$Ag\text{-}2^1$	7.84		

nanoalloy and that of atoms in bulk Ag and bulk Cu. Notice from Table 4.1 that the local coordination of Cu atoms in $Ag_{27}Cu_7$ seems, in fact, not dramatically different from that in bulk Cu regarding the number of first and second NN. The $Cu0$ atoms, for example, have 12 neighbors within a distance of 2.548 and 2.786 Å, and another twelve between 4.181 and 4.482 Å. Silver atoms, on the other hand, find themselves in unusual atomic environments: at distances 3 Å (bulk Ag nearest neighbors distance) $Ag2$ and $Ag4$ atoms have barely acquired 6 neighbors, while $Ag3$ and $Ag0$ atoms get 9 and 8 NN, respectively. Between 4.2-4.5 Å, at which bulk Ag atoms already have 18 NN, $Ag0$, $Ag3$ and $Ag4$ atoms have acquired only 11 neighbors, while $Ag2$ atoms have only 7 NN, finding themselves as the most under-coordinated atoms of the cluster. Most importantly, we notice that the NN bond lengths between Cu atoms contract by as much as 2% with respect to the value in bulk (2.599 Å). Such contraction may be expected for Cu atoms in low coordination environments, such as on the surface layer of $Cu(100)$ (inward contraction of around 3 %[116]), and not in $Ag_{27}Cu_7$ because of their high coordination (12) as in bulk Cu. Interestingly, for the shell Ag atoms, which have much lower local coordination than the core Cu atoms, the $Ag-Ag$ NN bond lengths are only 2.6 % shorter than those in bulk Ag (2.943 Å). If coordination alone were a measure, one might have expected the most under-coordinated Ag atoms, $Ag2$ and $Ag4$, to undergo a larger contraction, as found on Ag surfaces.[116] Instead, in $Ag_{27}Cu_7$, $Ag2$ and $Ag4$ form short bonds of about 2.59 Å with their neighboring Cu atoms, as seen from Table 4.1. These bond lengths are in fact very close to the smallest $Cu-Cu$ bond lengths (2.55 Å) and considerably smaller than the smallest $Ag-Ag$ bond lengths (2.87 Å). Indeed, it follows from Table 4.1 that in $Ag_{27}Cu_7$ the first NN of every Ag atom is a Cu atom, pointing to the reality that finite sized structures of these elements may not follow straightforwardly the behavior of infinite and/or semi-infinite systems and the relationship between bond coordination number and bond stiffening might be subtler in nanoalloys. Two conclusions may, nevertheless, be drawn from the above: 1) the fact that $Cu-Cu$ bond lengths in $Ag_{27}Cu_7$ contract almost as much as $Ag-Ag$ bond lengths suggests that Cu atoms are more sensitive than Ag

atoms to either low coordination, or local geometry, or chemical environment; 2) the low coordination of the Ag atoms appears to be significantly compensated by the formation of short bond lengths with Cu atoms. To discriminate between the above mentioned effects of local coordination, geometry, and environment, the conclusions about bond lengths in the $Ag_{27}Cu_7$ nanoalloy need to be put on firmer grounds through examinations of details of the electronic structure and the charge density distribution, and their implications for nanoalloy stability. We will turn to this in Sections 4.3.1.4 and 4.3.2. But before we do that, it is interesting to examine the structural stability of related bulk alloys, Ag_3Cu and Cu_3Ag, for which some information already exists and hence can serve as reference points. The relationship between the composition of $Ag_{27}Cu_7$ and Ag_3Cu is obvious. The other alloy is chosen to establish whether preponderance of Cu and/or its effect on bond lengths is a key for understanding the structural stability of these alloys.

4.3.1.3 Structure, phonons, and heat of formation of Cu_3Ag and Ag_3Cu bulk alloys

In considerations of structural stability of bulk alloys, it is essential that the heat of formation be negative and that the phonon spectrum be well defined. $Ag-Cu$ alloys, unlike $Au-Cu$ and $Au-Ag$ alloys, are known for their tendency to segregate and have a miscibility gap beyond the eutectic temperature of the material.[113–115] Earlier calculations[113–115] have shown that $Ag-Cu$ alloys possess a positive heat of formation regardless of the chosen ratio of Ag to Cu.[113,114] In particular, the heat of formation per atom was found to be about 70 meV for Ag_3Cu (60 meV, in this work) and 80 meV for Cu_3Ag (64 meV, in this work), pointing to the structural instability of these $Ag-Cu$ bulk alloys.[114]

It has, however, been pointed that even with a positive heat of formation presence of a well-defined phonon spectrum may serve as an indicator of alloy stability under special formation conditions, for example, using non-equilibrium techniques.[129–132] Indeed, among a variety of immiscible noble-transition metal alloys, some - particularly those that mix fcc and hcp metals - have shown mutual solid solubility.[133] Kong et al.[129] have calculated

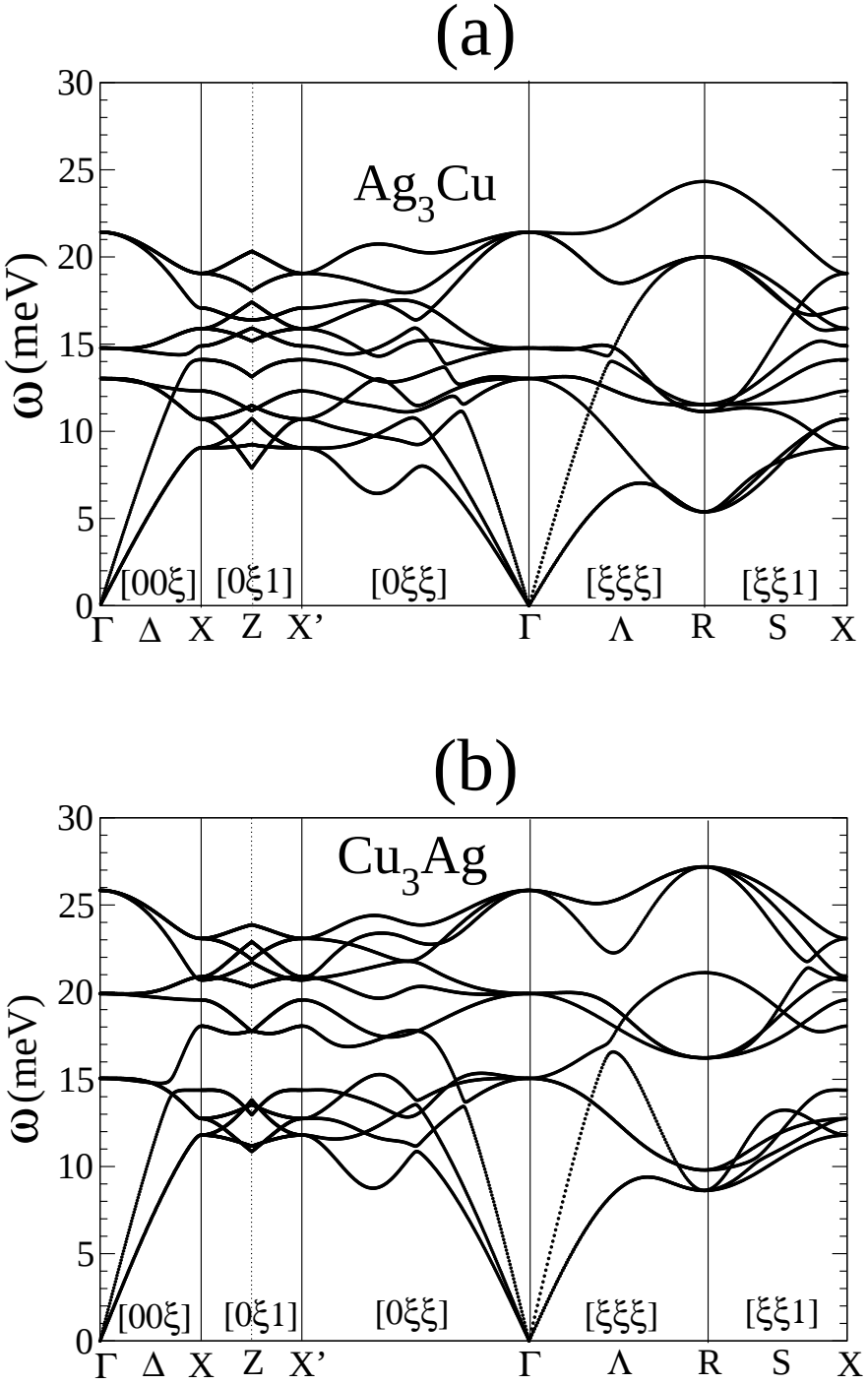

Figure 4.4: *Calculated phonon spectra of the hypothetical $L1_2$ phase of (a) Ag_3Cu and (b) Cu_3Ag bulk alloys.*

the phonon spectra of several structures of the equilibrium immiscible Ag_xRu_y alloys, for $x/y = 1/3$ and 3, to find that only the $L1_2$ and $D0_{19}$ phases of Ru_3Ag may be stable. In Ref.[129], phonon-stable/unstable structures were associated with the presence of relatively high charge density bridging NN atoms of the same/different element. We will come to charge density implications later in Section 4.3.2.2. For the present discussion, we note that, regardless of the structure of the stable phases, the phonon-stable $Ag-Ru$ alloys are all Ru-rich and have smaller lattice parameter than the corresponding Ag-rich structures, owing to the fact that typical bond lengths in bulk Ru are smaller than those in bulk Ag. Moreover, Kong et al. were able to remove the phonon instabilities, when present, by artificially increasing the external pressure; i.e., by simply reducing the equilibrium lattice parameter.

In the above spirit, we now turn to the calculation of the structure and the lattice dynamics of Ag_3Cu and Cu_3Ag bulk alloys using DFT and DFPT methods. We find the bond-length for Ag_3Cu to be 2.87 Å and that of Cu_3Ag to be 2.70 Å. For reference, note that our calculated bond lengths for bulk Cu and Ag are 2.59 and 2.94 Å, respectively. Note also that the shortest $Ag-Cu$ bond lengths in $Ag_{27}Cu_7$ are around 2.6 Å. The bond-lengths in bulk alloys Ag_3Cu and Cu_3Ag are thus larger than the shortest $Ag-Cu$ bond-length in the nanoalloy and that in bulk Cu and may imply lack of overlap of the d-orbitals for its $Ag-Cu$ and $Cu-Cu$ bonds (as we shall see), pointing to the structural instability of these bulk alloys. Our calculated phonon dispersion curves (Fig. 4.4) of Ag_3Cu and Cu_3Ag, showing the absence of unstable modes, however, suggest that these alloys may be stable and obtainable by non-equilibrium techniques.[129]

Phonon dispersion curves are furthermore a measure of the contribution of the vibrational entropy to the free energy of a given system.[134] The vibrational entropy integrates the vibrational DOS weighted by a factor that falls off as the frequency of phonons increases. Thus, vibrational entropy plays a larger role in minimization of the free energy for systems whose (well-defined) phonon dispersion curves display notable contributions and shifts of the

density of states towards the lower frequency range.[115] For example, bulk Cu_3Au ($L1_2$) has larger vibrational entropy than either bulk Au or Cu.[135] Our calculated phonon dispersion for bulk Ag_3Cu (see Figs. 4.4(a)) is softer than that of bulk alloy (Figs. 4.4(b)), bulk Ag,[136] and bulk Cu,[136] indicating that the vibrational entropy of Ag_3Cu is larger than that of the bulk Ag and Cu. Regardless, the vibrational entropic contribution to the reduction of the free energy is small[115] (typically less than 5 meV at room temperature) compared to the positive heat of formation (∼60 meV) found for this bulk alloy. Instead, the presence of stiffer vibrational DOS of Cu_3Ag, compared to that of Ag_3Cu, reflects stronger bonds in the former which may provide stability if created by the techniques mentioned above.[129–132]

4.3.1.4 Formation energy of $Ag_{27}Cu_7$

In Ref.[15] the thermodynamic stability of a given nanoalloy is evaluated via considerations of its melting temperature and its relative energetic stability is established through comparison of the heat of formation. Remarkably, although clusters with increasing binding energies per atom do not necessarily have higher melting temperatures,[137] $Ag_{27}Cu_7$ came out with both the highest melting point and the least heat of formation. In terms of stability and minimum-energy structures, however, it is important to know also the output given by the average formation energy, which measures the dissociation or *cohesive* energy of the nanoalloy, and to analyze the meaning, implications, and scope of these two energetic considerations. Thus, to estimate the average strength of the bonds, we calculate the so-called average *formation energy per atom*, E_{form}, which is defined as,

$$E_{form}(Ag_{N_1}Cu_{N_2}) = \frac{E(Ag_{N_1}Cu_{N_2}) - N_1E(Ag_{free}) - N_2E(Cu_{free})}{N}, \tag{4.1}$$

where $N = N_1 + N_2$ and $E(Cu_{free})$ and $E(Ag_{free})$ are the energies of isolated Cu and Ag atoms, respectively. We find $E_{form}(Ag_{27}Cu_7)$ to be 2.17 eV. Since no experimental data on this particular binary nanocluster exists, we turn to the formation energy of related systems for comparison. For example, our calculated cohesive energy of bulk Ag, Ag_3Cu, Cu_3Ag, and Cu are 2.51, 2.66, 3.06, and 3.34 eV, respectively, implying that $E_{form}(Ag_{27}Cu_7)$ is

smaller than all these bulk values. Note that the higher cohesive energy of bulk Ag_3Cu as compared to that of bulk Ag signals a stronger $Ag-Cu$ bond than the usual $Ag-Ag$ one. In fact, from the results presented in Ref.[15], one finds that the average formation energy per atom of the 34-atom family decreases monotonically from ∼2.6 to ∼2.0 eV as the Ag content increases from 0 to 34. Considerations of formation energy alone would thus imply that in this family of nanoalloys the $Cu-Cu$ and $Cu-Ag$ bonds are stronger than the $Ag-Ag$ bonds and that $Ag_{27}Cu_7$ is not the most stable structure. It is thus surprising that a related quantity, i.e. the heat of formation (defined as in Eq. 4.1, but substituting $E(Cu_{free})$ and $E(Ag_{free})$ by the cohesive energy of Cu and Ag, respectively), plotted as function of the Ag/Cu ratio in Ref.,[15] shows a minimum at this intermediate composition ($Ag_{27}Cu_7$) - a result that stands in contrast to that found in $Ag-Cu$ bulk alloys.[113–115] n reality, the formation of intricately tailored structures as $Ag_{27}Cu_7$ is not expected to occur simply by melting the parent compounds. Thus measures like heat of formation have to be supplemented by others such as the dynamical stability of the alloy as displayed by its vibrational modes. Nevertheless, we find that the heat of formation of the $Ag_{27}Cu_7$ is 9 times larger than that of Ag_3Cu, but this suggestion of instability might be misleading since the heat of formation not only measures the strength of the bonds but also weighs the energetic cost(gain) of breaking(forming) single element bulk bonds to form(from breaking) binary bonds. In reality, the formation of intricately tailored structures as $Ag_{27}Cu_7$ is not expected to occur simply by melting the parent compounds. Thus measures like heat of formation have to be supplemented by others such as the dynamical stability of the alloy as displayed by its vibrational modes. The heat of formation is perhaps more of an indicator of the life-time of the nanoalloy, say, against clustering and the eventual formation of segregated metallic bulk Cu and Ag, if one ignores the energy barriers needed to actually break all bonds in the nanoalloy.

On the experimental side, in addition, we note that the pure clusters Ag_7^- (Ref. 47) and Ag_{19}^+ (Ref.[138]) were found to have dissociation energy of 2.73 eV and 2.88 eV, which are very

close to the experimentally observed cohesive energy of bulk Ag (2.94 eV). The formation of pure cluster structures, such as Ag_7^- and Ag_{19}^+, may thus be seen to be energetically more favorable than the nanoalloys. Perhaps, the possible disintegration of $Ag_{27}Cu_7$ into pure-element clusters may be argued against on the basis of the strength of the $Ag-Cu$ bond. To estimate the strength of the bonds in the 34-atom nanoalloys and understand what distinguishes $Ag_{27}Cu_7$ in its family of nanoalloys, we turn to Fig.2 of Ref.[15]. Rossi et al. show that as the amount of Cu increases up to ∼20 % (starting from Ag_34), the heat of formation is reduced or kept constant, implying that small amounts of Cu atoms immersed among Ag atoms (in the nanoalloys $Ag_{34-n}Cu_n$ as n decreases from 7 to 1) create $Cu-Ag$ and $Cu-Cu$ bonds that are stronger than those in bulk Cu and are able not only to counterbalance the cost of the cohesive energy of the newly added Cu atom, but also to increasingly stabilize the nanoalloy. Fig.2 of Ref.[15] shows also that if the content of Cu increases beyond 7 atoms, the heat of formation increases again, with the implication that the strength of the bonds is not able to compensate the bulk Cu cohesive energy for an additional atom. In conclusion, $Ag_{27}Cu_7$ possesses the composition and geometry that maximizes the number of $Cu-Cu$ and $Cu-Ag$ bonds using the minimum number of Cu atoms.

The structural stability considerations presented above are derived entirely from the energetics of $Ag_{27}Cu_7$. The contributions of vibrational entropy could be important[112] and may lead to a minimum of the free energy (as a function of the Ag/Cu ratio) which is different from that in the plot of Rossi et al. They, however, argue against such a possibility.[15] Calculations of the phonon frequencies of these nanoalloys from first principles, as presented in section A.3 for the Ll_2 bulk alloys, is obviously desirable. Such a study may also serve as an indicator of stable compositions. However, the resulting contributions of the vibrational entropy to the free energy are expected to be small and should not change the conclusions drawn from the mean vibrational frequencies using Lennard-Jones potentials.[15]

4.3.2 Electronic structure and charge density distribution

4.3.2.1 Electronic DOS of $Ag_{27}Cu_7$ nanoalloy and Ll_2 $Ag-Cu$ alloys

To obtain the electronic DOS of bulk Cu_3Ag and Ag_3Cu alloys and $Ag_{27}Cu_7$ nanoalloy from *ab initio* electronic structure calculations, the discrete states are broadened using Gaussian functions of width 0.14 eV. The resulting DOS of $Ag_{27}Cu_7$ is shown in Fig. 4.5(a)-(c), while that of the bulk alloys is presented in Fig. 4.5(d) and (e). First of all, the HOMO-LUMO gap (Δ in Fig. 4.5(a)) of $Ag_{27}Cu_7$ is found to be 0.77 eV in the ground state, which is only slightly smaller than that reported by Rossi et al,[15] 0.82 eV. As expected, the *s*-states have negligible contributions and the displayed structures have mostly *d*-character between -5.5 and -1.7 eV. Fig. 4.5(b) shows that the centroid of the nanoalloy valence band red-shifts ~ 1 eV as compared to bulk Ag, and blue-shifts ~ 0.5 eV with respect to bulk Cu. Fig. 4.5(c) shows that even though the amount of Cu in the $Ag_{27}Cu_7$ nanoalloy is ~ 4 times less than that of Ag, it contributes to shift the centroid of the valence band to lower binding energies. As shown in Fig. 4.5(c)-(e) and in Refs.[111,139], the role of Cu is, in general, to enhance the DOS at the top of the valence band and to shift the centroid to lower binding energies, while the effect of Ag is the opposite. Similar results have been reported for $Au-Pd$ nanoclusters,[140] in which the increasing content of Au on Pd clusters reduces the density of states at the Fermi level. Fig. 4.5(b) and (c) show in addition that the valence band of the nanoalloy is as broad as that of either pure bulk constituents - a point worth of noticing since atoms in a low coordinated environment generally exhibit a valence band narrowing.[140] Pure Ag clusters and Cu_3Au surfaces,[141,142] for example, have shown this effect. The hybridization of Ag and Cu states in $Ag_{27}Cu_7$ thus compensates the *d*-band narrowing that each atom undergoes.

In general, the features in the electronic DOS that discriminate stable alloy phases are not yet fully understood. Although it is well accepted[113] that the dip in the DOS at the Fermi level is related to the stability of a particular alloy phase, there is no obvious correlation

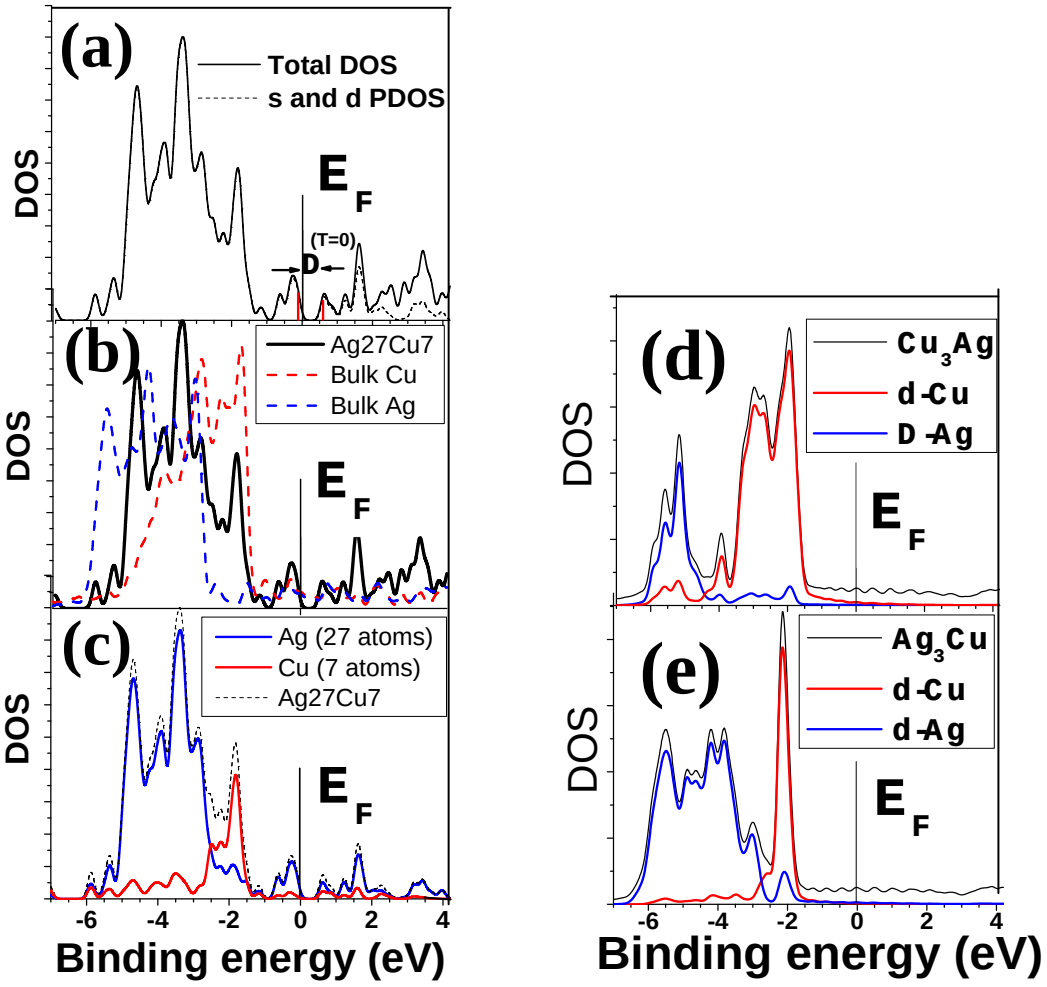

Figure 4.5: *(a) Total and projected electronic DOS of $Ag_{27}Cu_7$. The later corresponds to the contribution of s and d atomic states between -7 and 4.2 eV from the Fermi level, E_F, which is set equal to 0. The s-contribution is negligible up E_F. The HOMO-LUMO gap in the ground state, $\Delta = 0.77$ eV, is highlighted in red; (b) comparison between the total DOS of $Ag_{27}Cu_7$ and that of Ag and Cu bulk; (c) contribution from the core (Cu) and shell (Ag) atoms to the projected DOS of $Ag_{27}Cu_7$; (d) DOS of Cu_3Ag showing the d-contribution from each species to the total DOS of the alloy in the $L1_2$ phase; (e) DOS of Ag_3Cu showing the d-contribution from each species the total DOS of the alloy in the $L1_2$ phase.*

between the two since stable and ordered $Cu-Au$ alloys present a dip in the DOS while $Au-Ag$ alloys do not.[113] In the former the dip in the DOS changes position, width and depth with composition, and structure, and has been found to be related to the electronic specific heat.[111] Kokko et al.[111] noticed also that the dip is considerably lessened in the layered $CuAuI$ phase (which reduces the $Au-Cu$ bond) with respect to Cu_3Au and Au_3Cu. Also, based on their electronic specific heat calculations, they infer that the dip is even smoother in the disordered phases. In this work, we find that the nanoalloy $Ag_{27}Cu_7$ displays hardly any dip while the Ll_2 $Ag-Cu$ alloys display one (compare Fig. 4.5(a), (d) and (e)) similar to, but broader than, that found in stable $Cu-Au$ alloys.[111] Yet, from considerations of the heat of formation, the $Ag-Cu$ alloys are marked as being immiscible. Furthermore, we find that the DOS of the Ag atoms (Fig. 4.5(b) and (c)) in $Ag_{27}Cu_7$ resembles to some extent that of bulk Ag, despite being highly under coordinated, while that of the fully coordinated Cu atoms is strikingly different from bulk Cu presumably, since half of its neighbors are Ag atoms.

In order to understand the correlation between the Ag/Cu content ratio, the consequent decrease/increase of the bond lengths, and the structure of the electronic DOS, we turn to examination of the changes experienced by the DOS of individual Ag and Cu atoms in a set of environments (some natural, some artificial): $Ag_{27}Cu_7$ nanoalloy, a free standing Ag and Cu monolayer, bulk $Ag-Cu$ alloys, and bulk Ag and Cu (Figs. 4.6-4.8). For the bulk systems, we consider also the effect on the DOS (Fig. 4.7 of expanding and contracting the lattice constant from the equilibrium value found in our DFT calculations. The DOS of Ag and Cu atoms in Figs. 4.6-4.8 allow comparison on a *one-to-one* basis and not as percentile contributions as presented in Fig. 4.5.

From Figs. 4.6(a) and (b), we note that as the content of Ag and consequently the lattice parameter in the two bulk alloys decrease, an increasingly sharper peak is generated at intermediate energies since the bottom of the d-band remains almost unchanged most states from the top of the bulk Ag band (Fig. 4.6(e)) retract to lower energies. Despite

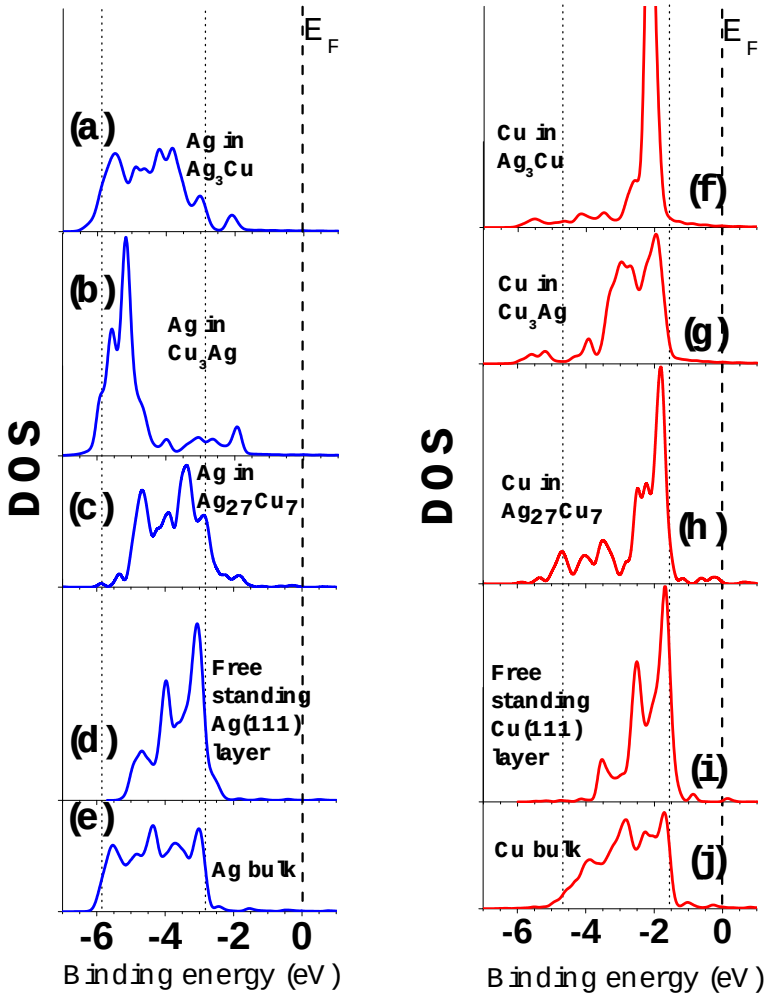

Figure 4.6: *Electronic DOS (d-band) of Cu and Ag atoms situated in various environments and bond lengths, l; (a) Ag atoms in Ag_3Cu (l = 2.87 Å); (b) Ag atoms in Cu_3Ag (l = 2.70 Å); (c) Ag atoms in $Ag_{27}Cu_7$; (d) Ag atoms in Å free standing $Ag(111)$ monolayer (l = 2.94 Å); (e) Ag atoms in bulk (l = 2.94 Å); (f) Cu atoms in Ag_3Cu (l = 2.87 Å); (g) Cu atoms in Cu_3Ag (l = 2.70 Å); (h) Cu atoms in $Ag_{27}Cu_7$; (i) Cu atoms in Å free standing $Cu(111)$ monolayer (l = 2.59 Å); (j) Cu atoms in bulk (l = 2.59 Å).*

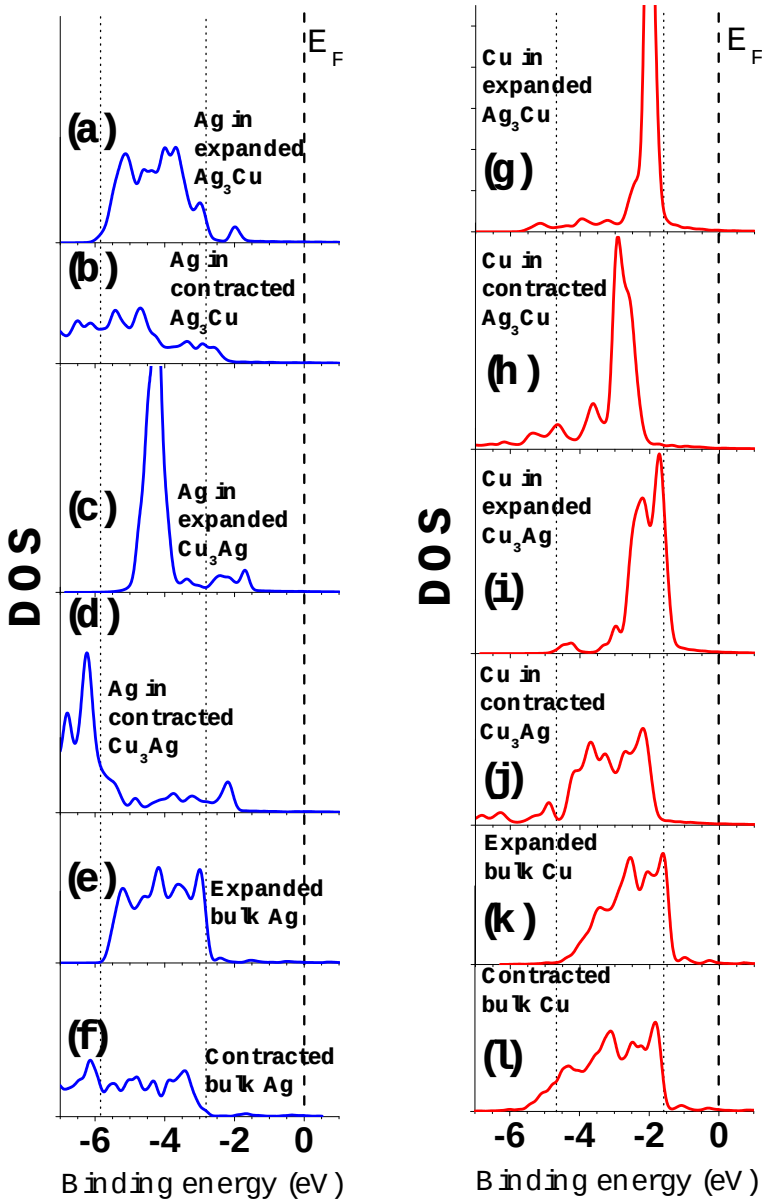

Figure 4.7: *Electronic DOS (d-band) of Cu and Ag atoms situated in an expanded/contracted bond length, l, in pure bulk and $L1_2$ bulk Ag-Cu alloys: (a) Ag atoms in expanded Ag_3Cu with $l = l_{Ag_{bulk}} = 2.94$ Å; (b) Ag atoms in contracted Ag_3Cu with $l = l_{Cu_{bulk}} = 2.59$ Å; (c) Ag atoms in expanded Cu_3Ag with $l = l_{Ag_{bulk}}$; (d) Ag atoms in contracted Cu_3Ag with $l = d(Cu0\text{-}Cu1) = 2.55$ Å; (e) Ag atoms in bulk Ag expanded by 8%; (f) Ag atoms in contracted Ag bulk with $l = l_{Cu_{bulk}}$; (g) Cu in expanded Ag_3Cu with $l = l_{Ag_{bulk}}$; (h) Cu in contracted Ag_3Cu with $l_{Cu_{bulk}}$; (i) Cu in expanded Cu_3Ag with $l = l_{Ag_{bulk}}$; (j) Cu in contracted Cu_3Ag with $l = d(Cu0 - Cu1)$; (k) Cu in expanded bulk Cu with $l = l_{Cu_3Ag} = 2.70$ Å; (l) Cu in contracted with $l = d(Cu0 - Cu1)$.*

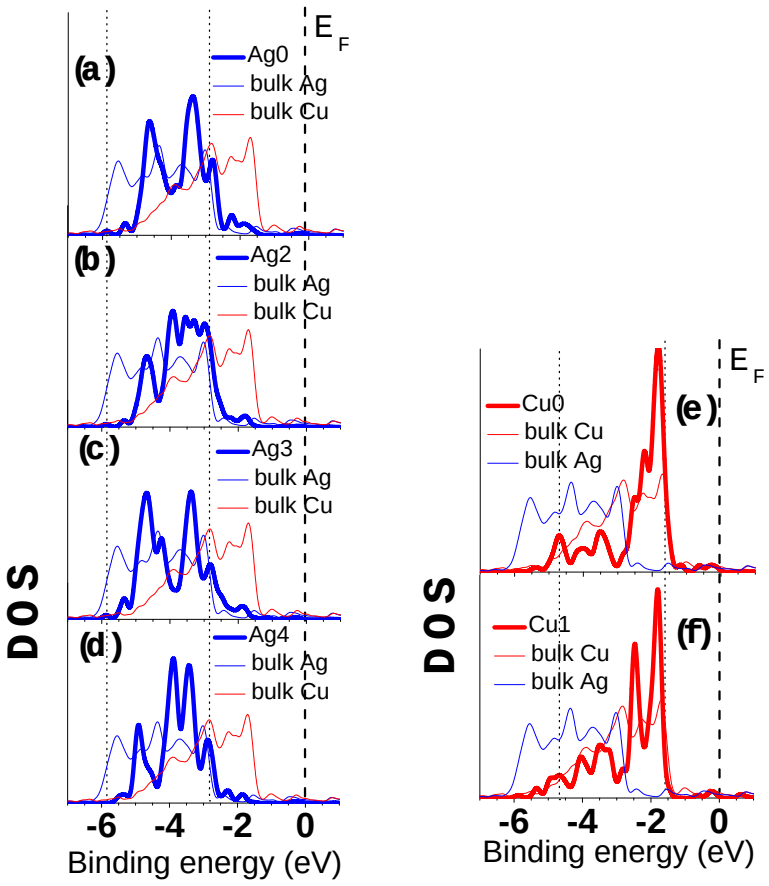

Figure 4.8: *The PDOS of the six non-equivalent types of atoms in the $Ag_{27}Cu_7$ nanoalloy is compared with the DOS of pure bulk Cu (black lines) and Ag (blue lines). E_F is shifted to 0 for all of them; (a) Ag0; (b) Ag2; (c) Ag3; (d) Ag4 (e) Cu0; (f) Cu1.*

the later feature, a few states appear between -1.5 and -2.5 eV, above the range of the DOS of bulk Ag, and hybridize with Cu states. We will see below that the appearance of the higher energy states is related purely to the presence of Cu, whereas the depletion of the top of the Ag d-band is not only due to the presence of Cu but also to the overlap of $Ag-Ag$ orbitals at distances smaller than the bond-length of bulk Ag. To isolate the effect of the bond length, we turn to the DOS in Fig. 4.7 for Ag and Cu atoms in bulk environments with bond lengths different from the equilibrium values. In order to maintain a reference point, we have taken the lattice constant of expanded Ag_3Cu and Cu_3Ag to be that of bulk Ag, leading to an expansion of 2.4 % in the former and 8.9 % in the latter. Similarly, to infer the effect of lattice contraction we have used the lattice constant of bulk Cu for Ag_3Cu (contraction of 9.8 %) and the bond-length of $Cu0-Cu1$ for Cu_3Ag (contraction of 5.5 %. By comparing Figs. 4.6(e) and 4.7(f), we find that contraction of $Ag-Ag$ bonds pushes the bottom of the Ag d-band to lower energies and depletes the top of the band, while comparison of Figs. 4.6(a) with 4.7(b) and 4.6(b) with 4.7(d) indicates that the contraction of $Ag-Cu$ bonds also pushes the bottom of the Ag d-band to lower energies and significantly lessens the highest features of the DOS of Ag d-band in bulk alloys. We also conclude from Figs. 4.7(b) and 4.7(d), and Fig. 4.6(e), 4.6(a) and 4.6(b) that the presence of Cu is responsible for the appearance of Ag states above the top of the bulk Ag band hence improving the overlap with the Cu d-band. On the other hand, as seen from Figs. 4.6(e) and 4.7(e), the expansion of $Ag-Ag$ bonds depletes the bottom of the DOS and slightly enhances the DOS at the top. Similarly, the expansion of the $Ag-Cu$ in the bulk alloys depletes the bottom of the DOS and enhances the highest peaks of the DOS (compare 4.6(a) with 4.7(a) and 4.6(b) with 4.7(c)). The same effect of expansion, though augmented, is caused on the DOS of Ag by low coordination, as in the case of a free standing (111) monolayer (Fig. 4.6(d)), in which the 6-coordination of Ag atoms causes a strong depletion at the bottom and enhancement at the top of the d-band. From the above, we conclude that the low coordination of Ag atoms in the $Ag_{27}Cu_7$ nanoalloy can indeed

account for the depletion of the bottom of the d-band (Fig. 4.6(c)). On the other hand, the reduction of the DOS at the top of the d-band of $Ag0$ (Fig. 4.8(a)), $Ag3$ (Fig. 4.8(c)), and $Ag4$ (Fig. 4.8(d)) atoms, suggests that the presence of Cu at such short distances overpowers their low coordination and no enhancement of the DOS at the top of the Ag d-band occurs, nevertheless, as seen in bulk alloys, the hybridization of Cu and Ag states is at the same time improved by Cu by setting off the occupation of states above the top of the d-band of bulk Ag (see Fig. 4.6(c) and Figs. 4.8(a)-(d)).

We now turn to the issue of the DOS of Cu atoms in the $Ag_{27}Cu_7$ nanoalloy which differ prominently from that of bulk Cu. We consider three different aspects that may influence their electronic structure: the conspicuously disparate overall geometry, the presence of Ag, and the existence of bond lengths longer than that of bulk Cu. To understand each one of these we first note that if $Cu-Ag$ bonds are longer than that of bulk Cu, then the bottom of the d-band of Cu is strongly depleted and an increasingly sharper peak at the top is created, which slightly shifts towards higher energies (compare Figs. 4.6(f) with 4.7(g) and 4.6(g) with 4.7(i)). As already noted for the Ag atoms, the effect of expanding $Cu-Cu$ bonds is similar to that of Cu atoms in a low coordinated environment (compare Fig. 4.7(k) and 4.6(i) with 4.6(j)), that is, the bottom of the Cu d-band (states below $\sim$3.5 and $\sim$ 4.0 eV in Figs. 4.6(i) and 4.7(k), respectively) is entirely extinguished. Interestingly, the d-band of the free monolayer is sharply localized at the top edge, resembling that of $Cu0$ (Fig. 4.8(e)) and $Cu1$ (Fig. 4.8(f)) atoms notwithstanding their full coordination in $Ag_{27}Cu_7$. Contracting $Ag-Cu$ bonds in bulk alloys reduces the DOS at the top, which is pushed to lower energies, and enhances the bottom of the d-band, thus improving the $Ag-Cu$ hybridization, as seen by comparing Figs. 4.6(f) with 4.7(b), 4.6(g) and 4.7(j). Similar features are found by contracting the $Cu-Cu$ bond is bulk Cu (compare Figs. 4.6(j) and 4.7(l)). More importantly, note in Figs. 4.7(j) that even when $Cu-Cu$ and $Cu-Ag$ bonds in bulk Cu_3Ag are shorter than that of bulk Cu, the region from $\sim$ 4.0 eV - $\sim$ 5.0 eV is nevertheless strongly quenched, suggesting that the presence of Ag also strongly depletes

most of the bottom of the d-band of Cu atoms (something similar occurs in $Au-Cu$, see Ref.[111]). Observe also that presence of Ag introduces states below the bottom of the DOS of bulk Cu (Figs. 4.6(f)-(h) and 4.7(g)-(j)), which hybridize with Ag. From the above, we conclude first that the sharp peak (Fig. 4.6(h)) at the top of the DOS of Cu atoms in $Ag_{27}Cu_7$ nanoalloy, characteristic of low-coordination (Figs. 4.6(i)), can only be accounted for by the relatively long distances ($\sim$ 2.7-2.8) between Cu atoms and half of their *nearest neighbors* - all Ag atoms - (see Figs. 4.3(a) and Table I), seemingly leading to a weak interaction of the Cu atoms with those *far-lying* Ag neighbors, as occurs for Cu atoms in bulk Ag_3Cu and Cu_3Ag alloys. The DOS of Cu atoms in bulk Ag_3Cu (Figs. 4.6(f)) thus indicates that the strength of the $Ag-Cu$ bond is considerably weak for Cu atoms; in fact, expanding the lattice parameter (Figs. 4.7(g)) changes insignificantly the DOS of Cu. Second, the effect of the Ag environment on the DOS of Cu atoms in $Ag_{27}Cu_7$ is connected with the depletion of states between 2.5 and 3.5 below the Fermi level, i.e., the dip around 3.0 eV in Fig 4.6(h), 4.6(e) and (f). We note in addition that the DOS of $Ag_{27}Cu_7$ below the dip (3.5 eV) is remarkably high, as compared to that of bulk alloys (see Figs. 4.6(f) and (g)) - despite the low Cu content - and generates a much stronger hybridization between Cu and Ag states, contrasting that observed in bulk alloys (see Figs. 4.5(c)-(e)); interestingly, the DOS of states of Cu atoms at 3.5 eV below the Fermi level in the compressed lattice of bulk Ag_3Cu (Figs. 4.7(b)) is almost as high as that of Cu atoms in $Ag_{27}Cu_7$ and also results in a stronger hybridization between Cu and Ag states compared to that found in equilibrium bulk Ag_3Cu bulk. In the third place, we conclude that the *optimum* $Cu-Ag$ bonding in $Ag_{27}Cu_7$ comes about in terms of the electronic DOS through the shortening of $Ag-Cu$ bonds that allows the hybridization of the d-states of Cu and Ag atoms, suppressing by this means the dip featuring in the DOS of Cu_3Ag and Ag_3Cu alloys.

Finally, we remark that although the DOS of Ag atoms is not changed as drastically as that of Cu atoms in bulk $Ag-Cu$ alloys - suggesting that Cu is more sensitive than Ag to the chemical environment -, the vulnerability of Cu to the presence of Ag is intermixed with

long bond-length effects. That is, the presence of Cu depletes the top of the Ag d-band as much as Ag depletes the bottom of Cu d-band. However, the short $Ag-Ag$ and $Ag-Cu$ bonds (with respect to bulk Ag) as present in both bulk alloys broaden the d-band of Ag atoms, compensating in this manner the effect of the Cu atoms. On the other hand, the $Cu-Cu$ and $Cu-Ag$ bond lengths induced in both bulk alloys never become shorter than that of bulk Cu, rather it is quite the opposite. As a result, narrowing of the d-band of Cu atoms is triggered, aggravating the depletion caused by the presence of Ag atoms and, hence, exaggerating the actual chemical susceptibility of Cu to the Ag environment. In summary, the electronic DOS is found unambiguously related to the bond lengths held in a particular geometry.

If we were to extrapolate the above results to related systems, we would speculate that the dip in the DOS identifies less stable phases of noble metal alloys. For example, the stability $Au-Ag$ alloys and the absence of a dip in their DOS may be attributed to the fact that the lattice parameter of bulk Au and Ag are nearly identical and that the d-band of bulk Ag lies within that of bulk Au, assuring significant d-band hybridization. Likewise, the hybridization between Cu and Au states is strong in bulk $Au-Cu$ alloys because the d-band of Cu also lies within that of bulk Au, albeit in the region near its Fermi level, while that of Ag lies deeper. The overlap between the bands of Ag and Cu, on the other hand, is relatively small resulting in weaker $Cu-Ag$ hybridization in bulk $Cu-Ag$ alloys. The dip in the DOS of $Au-Cu$ is probably not a sign of stability, rather it may be a sign that structures and/or compositions allowing shorter $Au-Cu$ would be more stable (amorphous phases, perhaps). The heat of formation of bulk Cu_3Au, for example, is negative because the strength of the $Au-Cu$ bond is larger than that of bulk Cu and Au, even at the distances dictated by the $L1_2$ phases, but which are not necessarily the distances at which the strength of all three $Au-Cu$, $Au-Au$, and $Cu-Cu$ bonds is optimized with the corresponding hierarchal importance, as exemplified by $L1_2$ bulk $Ag-Cu$ alloys whose long $Ag-Cu$ bonds contrast the significantly short ones found in the $Ag_{27}Cu_7$ nanoalloy.

4.3.2.2 Charge density distribution of $Ag_{27}Cu_7$ nanoalloy

The first aspect that comes to mind in Fig. 4.9-4.14 of the plotted charge densities of the nanoalloy $Ag_{27}Cu_7$ is that Ag atoms barely supply charge to the surface of the nanoalloy. The question is whether the surface charge depletion coincides with charge redistribution from Ag atoms to Cu atoms since two neighboring metals with significantly different work function can give rise to electron transfer from one metal to the other, as reported in calculations of Pd clusters on $Au(111)$ by Sánchez et al,[142] in correspondence with a work function difference of ~ 0.3 eV. Here, the work function of Cu is larger than that of Ag by ~ 0.2 eV. Indeed, Figs. 4.9 and 4.10 display higher charge density around Cu atoms than around Ag atoms.

The plot of the charge density in a plane passing through 10 Ag and Cu atoms in Fig. 4.9 illustrates that the $Cu0$-$Ag2$ and $Cu1$-$Ag4$ bonds are linked by the highest bonding charge density, corresponding indeed to the shortest $Ag-Cu$ bond lengths (~ 2.58 Å), and implying that they are stronger than the $Cu1$-$Cu1$ (2.58 Å), $Cu0$-$Cu0$ (2.58 Å) bonds and even the $Cu0$-$Cu1$ bonds (2.55 Å), in that order (see Figs. 4.9 and 4.10). The next strength of bonding charge density occurs for $Cu0$-$Ag0$ bonds, followed by $Cu1$-$Ag3$ bonds, as shown in Figs. 4.9 and 4.10. In this case, the bond lengths are 2.72 and 2.73 Å, respectively. Notice that, in the second set of bonds, the charge density is considerably lower than in $Cu0$-$Ag2$ and $Cu1$-$Ag4$ bonds, which supports the assumption that $Ag-Cu$ interactions die out very rapidly (see Section 4.3.2.1). The third place in bonding charge density corresponds to $Cu0$-$Ag3$ (Fig. 4.11) bonds and the shortest $Ag-Ag$ bonds: $Ag0$-$Ag3$ and $Ag2$-$Ag2$ bonds (Fig. 4.9) whose bond lengths are 2.79, 2.87 and 2.89 Å, respectively (Table 4.1). The first might influence very little $Cu0$ atoms since the bond is quite large. However, this bonding charge density appears as large as that of $Ag0$-$Ag3$, which is 0.1 Å further apart. The next in bonding charge density is the $Ag2$-$Ag3$ bond (Fig. 4.12), whose length is 2.90 Å, followed by the $Ag3$-$Ag4$ bond (Fig. 4.9), whose length is 2.93 Å. The latter bond length is close to that of the $Ag0$-$Ag3$ bond (and almost identical to the bond length of bulk Ag);

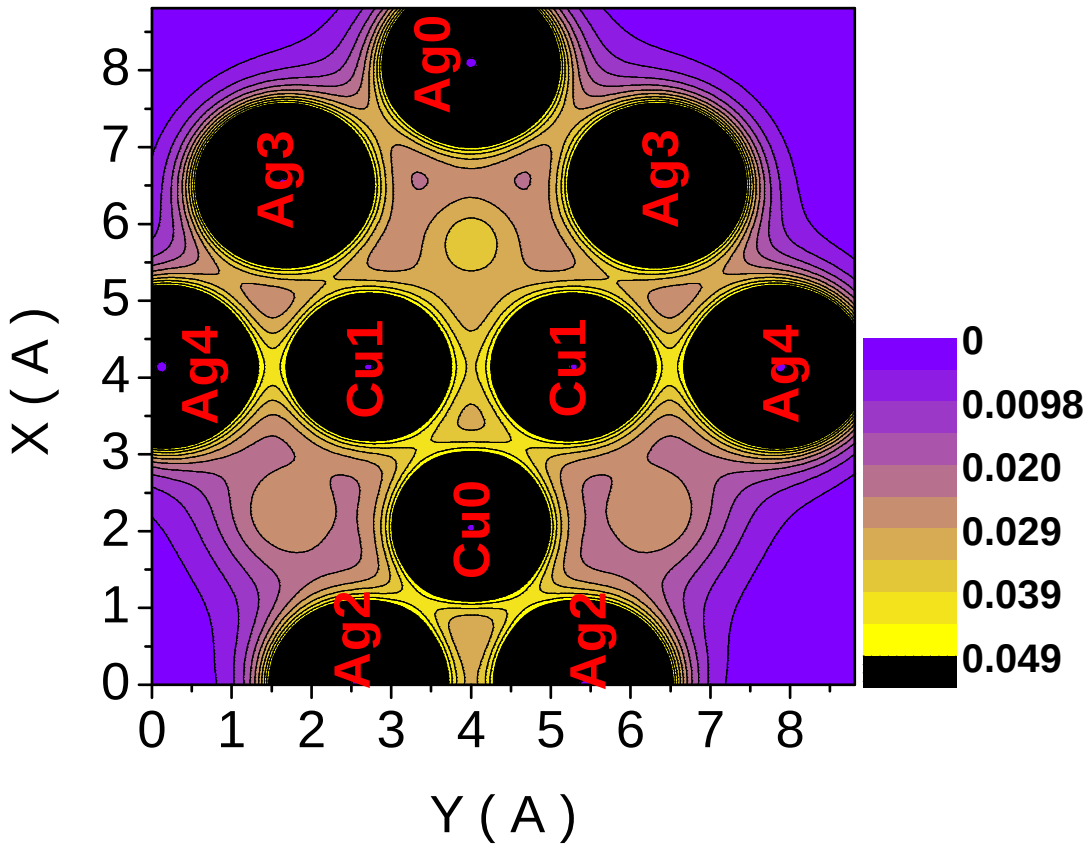

Figure 4.9: *2D Charge density plot at a plane that contains the 5-fold rotation axis of $Ag_{27}Cu_7$ nanoalloy and is, therefore, perpendicular to its mirror plane. Atoms labelled with red color are precisely centered on that plane.*

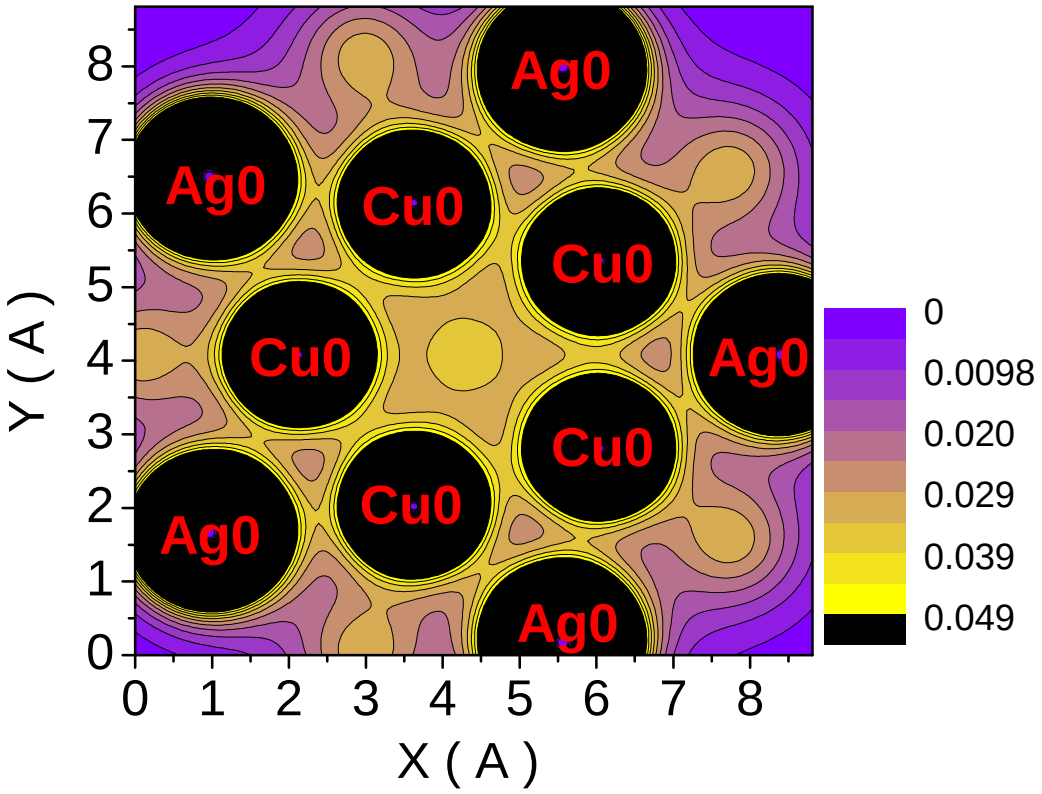

Figure 4.10: *2D Charge density plot at the mirror plane of $Ag_{27}Cu_7$. Atoms labelled with red color are precisely centered on that plane.*

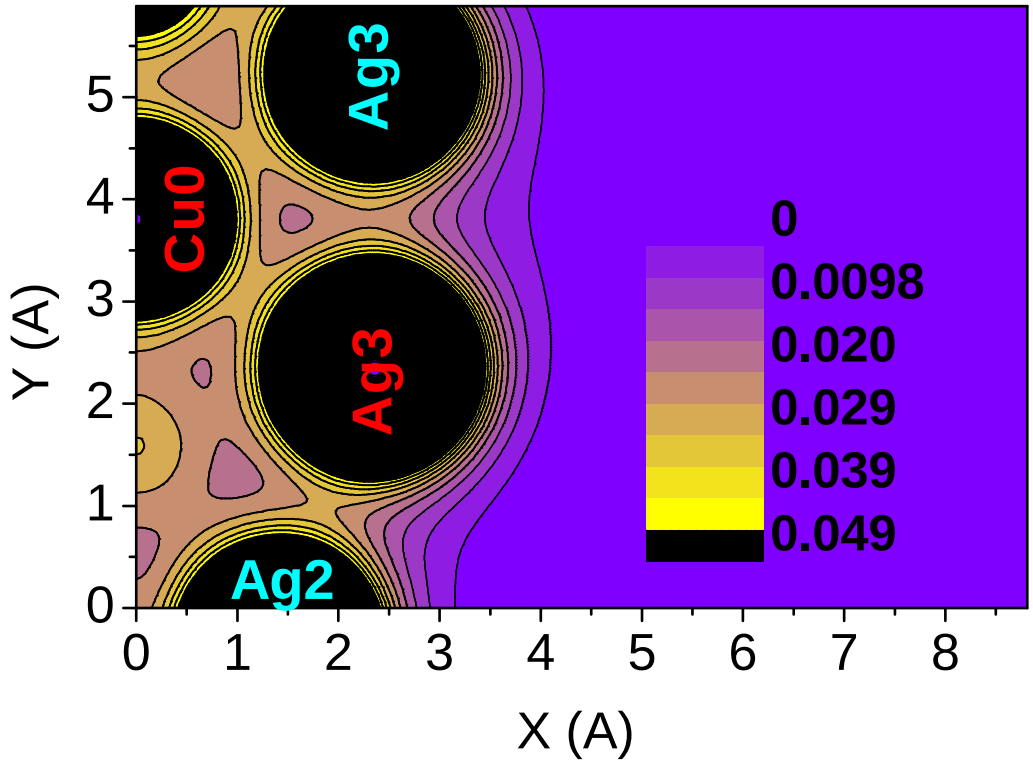

Figure 4.11: *2D Charge density plot at a plane that contains the positions where Cu*0 *and Ag*3 *atoms (labeled with red color) are centered. Atoms labelled with blue color are depicted in the section but are not centered precisely on that plane.*

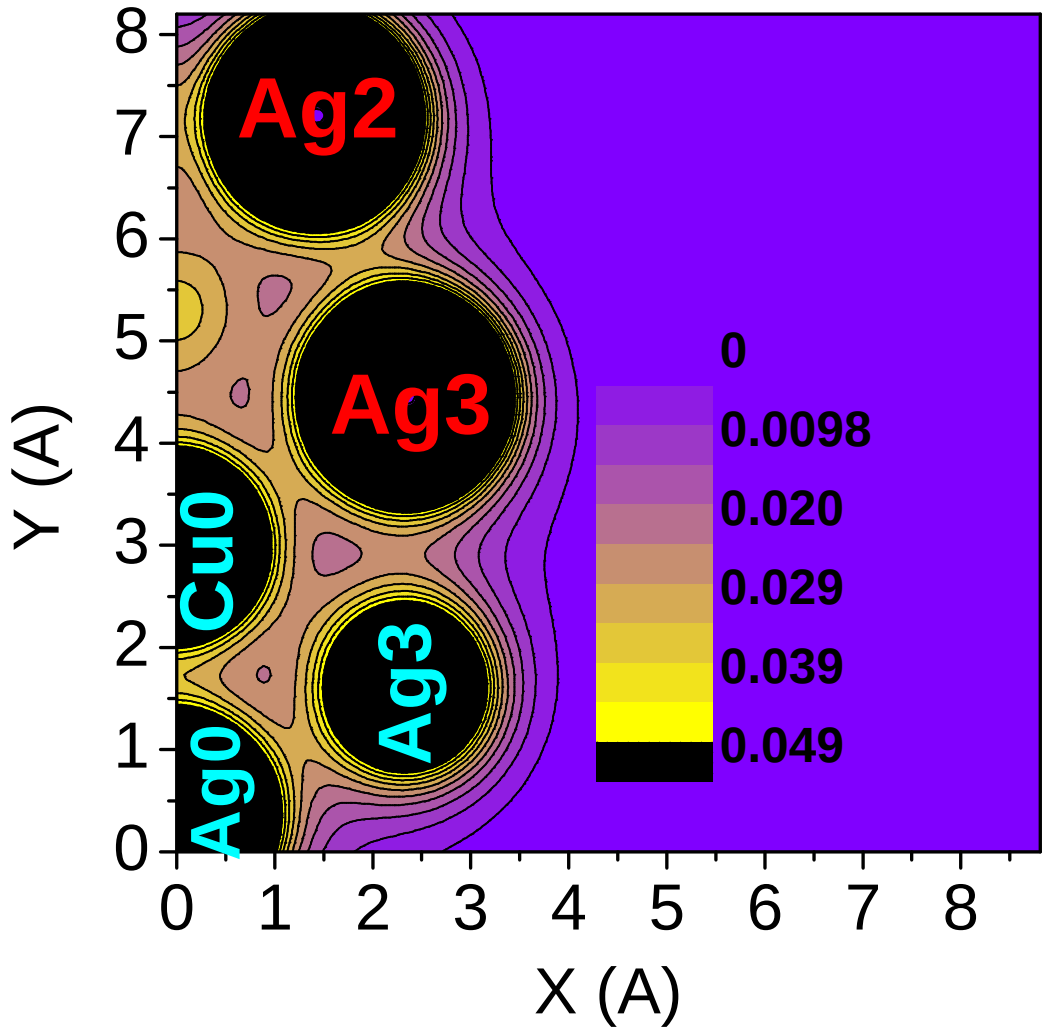

Figure 4.12: *2D Charge density plot at a plane that contains the positions where Ag2 and Ag3 atoms (labeled with red color) are centered. Atoms labelled with blue color are depicted in the section but are not centered precisely on that plane.*

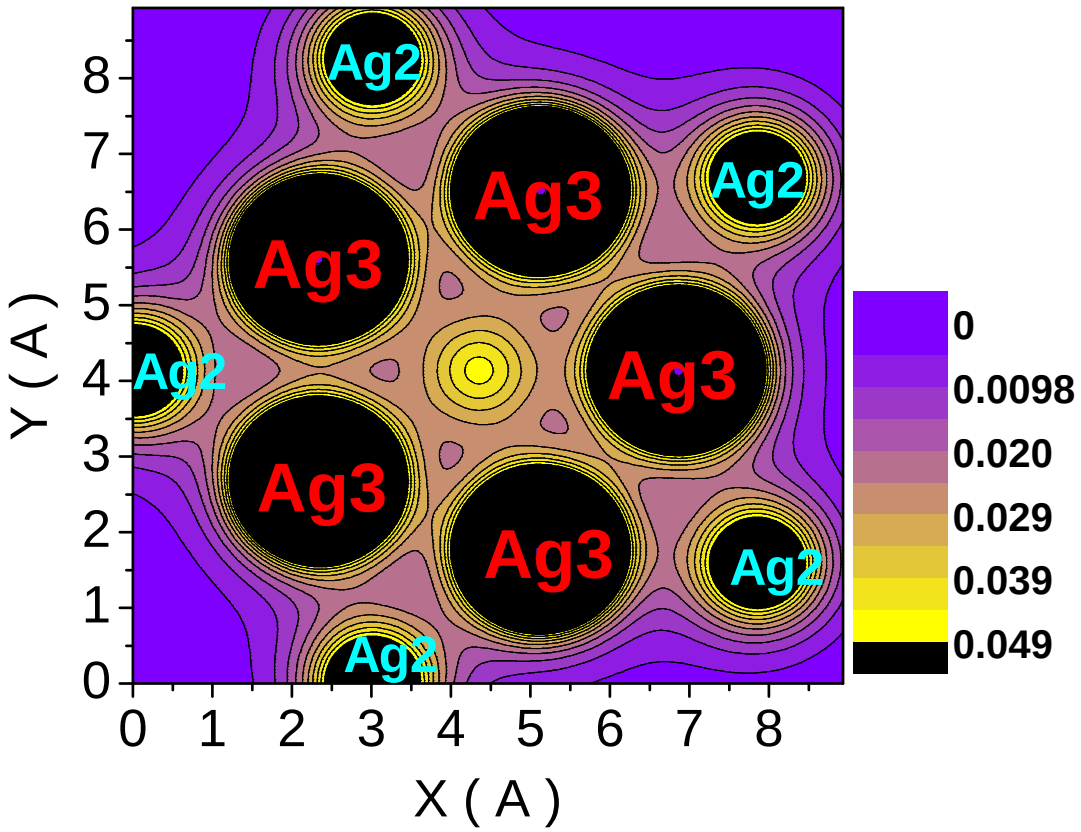

Figure 4.13: *2D Charge density plot at a plane which is parallel to the mirror plane of $Ag_{27}Cu_7$. The pentagonal layer composed of Ag3 atoms (labeled with red color) is contained in this plane. Atoms labelled with blue color are depicted in the section but are not centered precisely on that plane.*

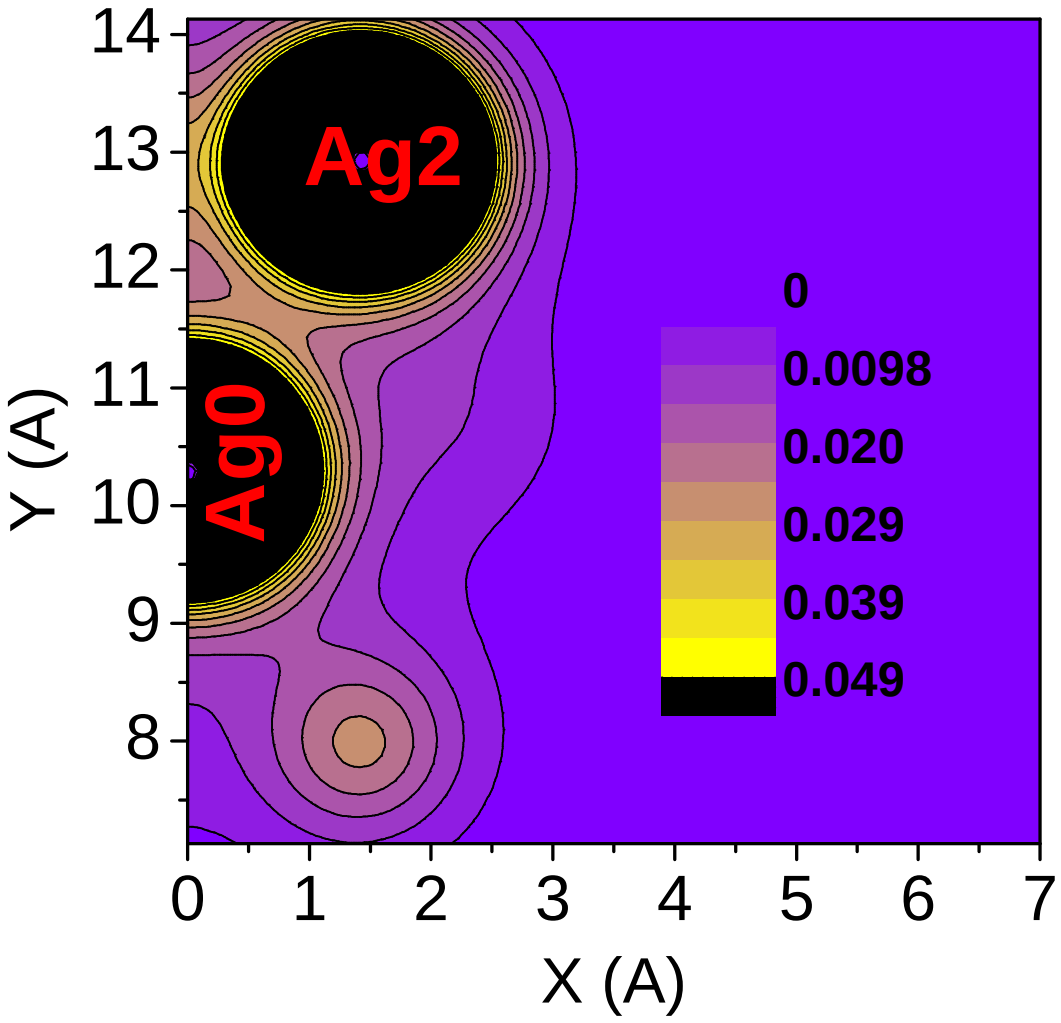

Figure 4.14: *2D Charge density plot at a plane that contains the positions where Ag*0 *and Ag*2 *atoms (labeled with red color) are centered. Atoms labelled with blue color are depicted in the section but are not centered precisely on that plane.*

however, the charge density bridging these atoms is slightly weaker. Note that $Ag3$-$Ag3$ bonds (Fig. 4.13) are only slightly longer (2.95 Å) but the bonding charge density around it is less than that around the $Ag3$-$Ag4$ bonds. The charge density around the $Ag0$-$Ag2$ bond (Fig. 4.14) is substantially lower than that around $Ag3$-$Ag3$, consistent with a larger bond length, 3.0 Å. The next larger bond lengths are more than $\sim$ 4 Å, which are expected to provide much weaker direct interactions that will not be discussed here.

In reference to the importance of bond strength and length hierarchies in alloys, mentioned in subsection 4.3.2.1, we turn to the discussion in 4.3.1.3 of Ref.[129] in which $Ag-Ru$ phonon-stable structures were associated with a high charge density bridging atoms of the same element, whereas phonon-unstable structures were associated with a high charge density bridging atoms of different elements. Instead, following the arguments above, we propose that their charge density plots indicate that Ag-rich structures do not allow for strong $Ru-Ru$ bonds and so, although strong $Ru-Ag$ and $Ag-Ag$ bonds are present, the structure is unstable. Additional support to our assertion comes from the fact that phonon instabilities are not present in some Ru-rich structures,[129] while those in Ag-rich structures disappear by reducing the equilibrium lattice parameter.[129] Besides, Ag-rich structures with reduced lattice parameter show clearly that the charge density bridging $Ru-Ru$ bonds is enhanced (see Fig. 4.3(e) of Ref.[129]). The above suggests that in $Ag-Ru$ alloys the strength hierarchy is in the following order: $\{Ru-Ru,\ Ag-Ru,\ Ag-Ag\}$. In fact, relatively large differences between the strength of $Ru-Ru$ and $Ag-Ru$ bonds and a pronounced deep dip in the DOS can be expected to explain all their results simultaneously.

4.4 Summary and Conclusions

We have presented DFT calculations of the $Ag_{27}Cu_7$ nanoalloy to understand its structure and relative stability via considerations of its energetics, electronic DOS, and charge density distribution. The local coordination of Cu atoms seems not dramatically different from that in bulk Cu regarding the number of first and second NN, whereas Ag atoms find

themselves in a very low-coordinated environment but, in return, form $Ag-Cu$ bonds as short as the shortest $Cu-Cu$ bonds. On the other hand, the electronic structure of the Cu atoms in $Ag_{27}Cu_7$ deviates much more from that of atoms in bulk Cu, as compared to the corresponding case of Ag atoms in this nanoalloy.

Related bulk alloys, Ag_3Cu and Cu_3Ag, have positive heat of formation and form larger bonds than the shortest ones found in the $Ag_{27}Cu_7$. However, we find that the resulting interatomic bonds in these bulk alloys are sufficiently strong to make their cohesive energy larger than that of bulk Ag and display stable phonon dispersion curves.

From our analysis of the geometric and electronic structure, we conclude that the relative stability of $Ag_{27}Cu_7$, among its nanoalloy family, is the result of the maximization of the number of $Cu-Cu$ and $Cu-Ag$ bonds, using the minimum number of Cu atoms. The core-shell $Ag-Cu$ nanoalloys do not behave differently from $Ag-Cu$ bulk alloys regarding the segregation tendency and the migration of Ag to the surface, as pointed earlier,[143] since $Ag_{27}Cu_7$ is segregated by construction. Furthermore, the segregated structure is the attribute that leads to its relative stability, provided that the core-shell structure allows $Cu-Cu$ and $Cu-Ag$ pairs to approach and form bonds nearly as strong as they can be, at almost no expense of either contracting the typical $Ag-Ag$ bond or (most importantly) stretching the typical $Cu-Cu$ bond.

The HOMO-LUMO gap of $Ag_{27}Cu_7$ is found to be 0.77 eV. The DOS of $Ag_{27}Cu_7$ shows similar features as those of $Ag-Cu$ bulk alloys. We find that the novel features of the DOS of full-coordinated Cu atoms in $Ag_{27}Cu_7$ atoms are caused by the relatively long distance separating Cu atoms from half of its first NN. Short $Ag-Cu$ bond-lengths, on the other hand, improve the hybridization of Cu and Ag states; explaining why the hybridization of Cu and Ag states in the $Ag_{27}Cu_7$ nanoalloy is stronger than in $Ag-Cu$ bulk alloys. The observed differences in electronic DOS between $Ag_{27}Cu_7$ and $L1_2$ alloys arise not only because of low-coordination and geometry differences but mainly because the symmetry enforces long $Cu-Cu$ and $Cu-Ag$ bonds, unlike the situation in $Ag_{27}Cu_7$.

In $Ag_{27}Cu_7$, the charge density along $Ag-Cu$ bonds whose length is $\sim$ 2.6 Å is even larger than that around $Cu-Cu$ bonds, and certainly larger than those bridging $Ag-Ag$ atoms. Nevertheless, $Ag-Cu$ bonds whose length is of the order of that in bulk Ag_3Cu, or even Cu_3Ag, are surrounded by an appreciably quenched charge density, explaining why the DOS of Cu atoms show low coordination features. We infer a hierarchy of bond strength, $\{Cu-Cu$, $Cu-Ag$, and $Ag-Ag\}$, correlated to a bond length order, $\{Ag-Ag$, $Cu-Ag$, and $Cu-Cu\}$ so that, the actual strength of the bonds in a particular structure becomes the signature of a relaxed geometry, which may or may not satisfy the above hierarchy, let the strongest bonds to realize, and thus be stable.

Chapter 5

First principles study of the formation of Pt islands on Ru nanoparticles

5.1 Introduction

Direct methanol fuel cells (DMFC) are considered a promising means for energy conversion in "hydrogen-based economy" because they work at low temperature and use liquid methanol as fuel, which is easy to deliver and store. In DMFC, the same anode is used as a catalyst for both methanol reforming and for the oxidation of hydrogen obtained by that reforming. Although the carbon monoxide released in the course of this reaction is supposed to be oxidized by hydroxyl radicals obtained from admixed water, it still severely poisons the commonly used Pt anode by blocking the Pt sites and, in this way, reducing the rate of hydrogen electro-oxidation. Similarly, in proton exchange fuel cells operating with pre-reformed gas, the anode is poisoned by carbon monoxide molecules, inevitably present in hydrogen obtained from hydrocarbons.

It is known[144] that $PtRu$ alloys are more tolerant to CO poisoning than pure Pt, though their tolerance is still unsatisfactory. Another disadvantage of these catalysts is still the high content of expensive platinum. It has been recently found that nanoclusters of Ru exposed to spontaneous Pt deposition are much more tolerant to CO than commercial $PtRu$ catalysts[145,146]. In addition, it is commercially advantageous that the content of Pt on these novel materials is significantly reduced with respect to $Ru-Pt$ alloys. Brankovic et al.[145,146]

deposited Pt on $\sim$2.5 nm size Ru nanoparticles and found that the 1:20 ratio ($PtRu_{20}$), which corresponds to $\sim$0.1 monolayer (ML) coverage, surpass substantially the catalytic performance of $PtRu$ and Pt_2Ru_3 in the presence of CO. This feature was attributed to the *spillover* effect, in terms of the tendency of CO to leave the Pt and diffuse towards Ru. It was assumed[146] that Pt atoms form two dimensional (2D) islands on the facets of the Ru nanoparticles, although, the actual arrangement of the deposited Pt atoms was not determined because of experimental limitations.[146] Since the first step in obtaining a systematic understanding of the enhanced reactivity of this catalyst is the determination of its surface structure, we have proceeded to do the same theoretically using *ab initio* structure calculations in this work.

We first notice that the resulting structure of deposited Pt atoms will be determined by the balance between the propensity of the atoms to increase the number of chemical bonds and the stress caused by a misfit in the $Ru-Ru$ and $Pt-Pt$ bond lengths. Competition between these two factors may, at a critical size of a Pt island, cause crossover between 2D and three dimensional (3D) growth mode or island-substrate atom exchange.[147,148] Experimentally, the bond length of bulk Ru and Pt phase are of 2.706 Å and 2.775 Å, respectively. The size mismatch between Ru and Pt is not large, and so it is not obvious which growth mode is preferred by Pt. Experimentally, rather large ($\sim$2.5 nm) Pt monolayer islands on $Ru(0001)$[149] have been obtained by Pt vapor deposition at coverages as low as 0.03 ML. On the other hand, it has been found that under spontaneous deposition Pt forms 2 - 3 layer islands of 3 - 10 nm diameter on $Ru(0001)$.[150] As noted above, Pt coverage is critical for the catalytic properties of the Ru nanoparticles[145]; island size effects - tuned by Pt coverage - have also been reported for methanol electro-oxidation.[151] All the above suggests that the correlation between catalytic activity and coverage has implications on how Pt arranges itself on the Ru nanoparticles, as we shall see later. The arising question is, which structure of Pt atoms on Ru faceted clusters is energetically the most favorable?While the focus of this work is not on understanding the catalytic reactivity of the $Pt-Ru$ nanoparticles,

we notice that previous calculations indicate that the CO adsorption energies on various binary $Pt-Ru$ systems, ranging from $Pt(111)$ to 1ML of Pt on $Ru(0001)$, are reduced upon lowering Pt content.[152] Kopper et al.[152] proposed that 1 ML of Pt deposited on $Ru(0001)$ surface might be the best $H2/CO$ oxidation catalyst due to the reduced binding energy of CO to Pt and the consequent increment of available active Pt sites.

Since Ru nanoclusters in Refs.[145,146] have well developed facets divided by edges, both formation of Pt islands on Ru facets and Pt diffusion over Ru nanoparticle edges are of interest. To gain insight into the former, we have examined the energetics of Pt islands, as a function of size, on the $Ru(0001)$ surface. To this end, we carry out first principles calculations of the geometry and formation energy of Pt islands whose size ranges from 1 to 9 atom, as well as that of 1ML of Pt, adsorbed on $Ru(0001)$. Furthermore, to assess the possibility of diffusion of Pt atoms and dimers, we simulate two edges of a Ru nanoparticle using a superstructure described in the next section and calculate diffusion barriers of Pt atoms on its (0001) and $(\bar{1}101)$ facet and across its edges. The rest of this chapter is organized as follows: Section 5.2 presents the computational details, Section 5.3 contains our results and provides some discussion about Pt islands on $Ru(0001)$ (subsection 5.3.1) and of Pt diffusion on the (0001) facet and across the edges of our Ru nanostructure (subsection 5.3.2). Section 5.4 summarizes our results and conclusions.

5.2 Computational details

In this paper periodic supercell calculations have been carried out within the density functional theory (DFT) framework[29,30] using the plane wave pseudopotential method[153] - embodied into the ESPRESSO code (previously known as PWSCF)[154] - with ultrasoft pseudopotentials.[155] We have used a kinetic energy cutoff of 25 Ry for the wave functions and 100 Ry for the charge density to obtain convergent results with sufficient computational accuracy of the lattice constant of bulk Ru and Pt. Brillouin zones were sampled with either the $(4 \times 3 \times 1)$ or the $(3 \times 3 \times 1)$ Monkhorst-Pack k-point meshes,[39] depending

on the size of the supercell, as we will see. Since the main uncertainty of DFT comes from the exchange-correlation potential, we have used two different approximations for the exchange-correlation functional: the Perdew and Wang generalized gradient approximation (GGA)[36] and the Perdew, Burke, and Ernzerhof (PBE) modified GGA[37], and compared some of the results obtained using these two approximations. To achieve force relaxation of the studied structures, the total energy of the system and the forces acting on each atom are obtained after each self-consistent electronic structure and minimized by the Broyden-Fletcher-Goldfarb-Shanno (BFGS) algorithm.[156] At equilibrium, forces on each atom are required to be below 0.3 mRy/au. The diffusion barriers for monomers and dimers on the Ru superstructure are obtained by the direct dragging method. The 3D graphics presented in this work were generated by the *Xcrysden* program.[157]

We note that in the calculations of the geometry and formation energy of Pt islands the usage of supercells may introduce contributions from island-island interactions, as a result of the imposed periodicity of the system. This is particularly true for the largest islands in the 3×4 and 4×4 supercells in which edge-atoms of neighboring islands are as close as third nearest neighbors (NN) of the $Ru(0001)$ surface. A simple way to estimate this spurious interaction is to consider that between two Pt atoms adsorbed on the surface the interaction energy, E^{int}, defined as changes in the total energy of the dimer on $Ru(0001)$ as the $Pt-Pt$ distance varies. Roughly, $E^{int} = E(2Pt/Ru) - 2E(1Pt/Ru)$, where $E(2Pt/Ru)$ is the adsorption energy of 2 Pt atoms on $Ru(0001)$ in a 4×4 supercell and $E(1Pt/Ru)$ is the adsorption energy of 1 Pt atom on the same surface and supercell. Our results provide that E^{int} = -0.203, +0.074, and -0.018 eV, as the separation between the two Pt atoms increases from 1^{st} to 2^{nd}, and 3^{rd} NN bond length, respectively. The interaction between 3^{rd} NN is thus expected to be 10 times smaller than that of 1^{st} NN; accordingly, E_{form}, as calculated in this work, can be reliable up to $\pm$ 0.02 eV for the largest islands.

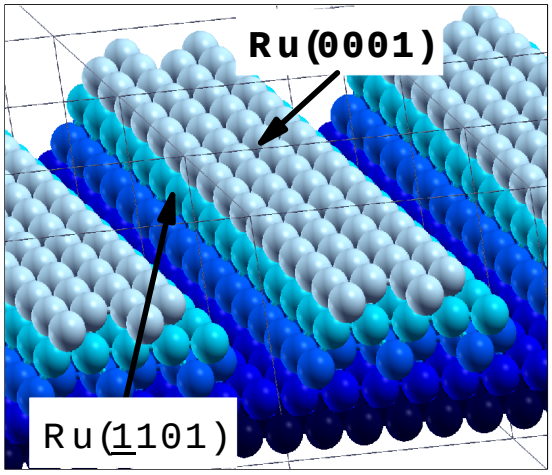

Figure 5.1: *Model of a faceted Ru nanoparticle exposing a (0001) facet and two ($\bar{1}101$) facets. Different colors distinguish the five layers parallel to the (0001) surface constituting the structure.*

5.2.1 2D *Pt* islands on *Ru*(0001)

The facets of *Ru* nanoparticles are first modeled by a 5 layer *Ru*(0001) slab, which is the surface known to have the lowest energy.[158] *Pt* adatoms are placed on only one side of the slab. To avoid the interaction between surfaces and *Pt* adatoms of neighboring periodic supercells we have imposed a 15 Å vacuum layer, whereas to reduce the interaction between deposited *Pt* islands, the (0001) surface unit cells is extended to either (3×4) or (4×4) structures depending on the island size. The (3×4) and (4×4) supercells contained 60 and 80 *Ru* atoms, respectively, plus *Pt* atoms forming the island. Their corresponding surface Brillouin zone is sampled with a $(4 \times 4 \times 1)$ and $(3 \times 4 \times 1)$ k-point mesh, respectively.

5.2.2 Monomer and dimer on faceted superstructure

To model *Pt* diffusion through the nanoparticles edges we have taken into consideration the *Ru*(0001) and *Ru*($\bar{1}$101) surfaces, which are among the most stable *Ru* surfaces.[146,158] We consider a periodic 3D superstructure containing 116 *Ru* atoms and made of a 4-atom wide *Ru*(0001) facet and two *Ru*($\bar{1}$101) facets (see Fig. 5.1). The construction of this *Ru*

supercell, which has 7×4 in-plane periodicity, is achieved by stacking five $Ru(0001)$ layers: two of 7×4, one of 6×4, one of 5×4, and one of 4×4 atoms. The so obtained edges, on each side of the $Ru(0001)$ are different, say edge A and B. Atoms forming edge A (edge B) are contiguous to hcp (fcc) hollow sites of the (0001) facet. The bottom two layers (see Fig. 5.1) were not allowed to relax to guarantee the stability of the superstructure. We impose a 15 Å vacuum layer between periodic superstructures along the direction perpendicular to the surface, as in the system described previously. The Brillouin zone is sampled with a $(2 \times 3 \times 1)$ k-point mesh. The adsorption energy and diffusion barriers of Pt monomers and dimers are calculated on the (0001) and the $(\bar{1}101)$ facets.

5.3 Results and Discussion

To determine in-plane slab periodicity, we have calculated bulk lattice parameters using PW and PBE approximation for the exchange-correlation functional. The bond lengths of bulk Ru and Pt are found to be 2.706(2.744PBE) and 2.77(2.82PBE) Å, respectively, while the c/a ratio of bulk Ru is found to be 1.585 (PBE) Å.

5.3.1 Pt islands on $Ru(0001)$

We have calculated the optimized geometric structure and energetics of 1 to 5 Pt atom islands adsorbed on $Ru(0001)$ using the (3×4) supercell and that of 1 to 9 Pt atom island on $Ru(0001)$ using the (4×4) supercell. The relaxed structure of one Pt monolayer on $Ru(0001)$ has been also obtained. To characterize the energetics and stability of a given Pt island, we obtained its formation energy, which is defined as: $E_{form} = E(Ru+Pt) - E(Ru) - nE(Pt_{at})$. Here $E(Ru + Pt)$ is the energy of Ru slab adsorbed with a n-atom Pt island, while $E(Ru)$ and $E(Pt_{at})$ denote the energy of the clean Ru slab and the energy of a free Pt atom, respectively. The structure with lowest average formation energy per Pt atom, E_{form}/n, will thus be distinguished as the energetically most favorable one. Fig. 5.2(a) presents the dependencies of E_{form}/n on the size of the island, n, for n = 1-5 using a (3×4) supercell,

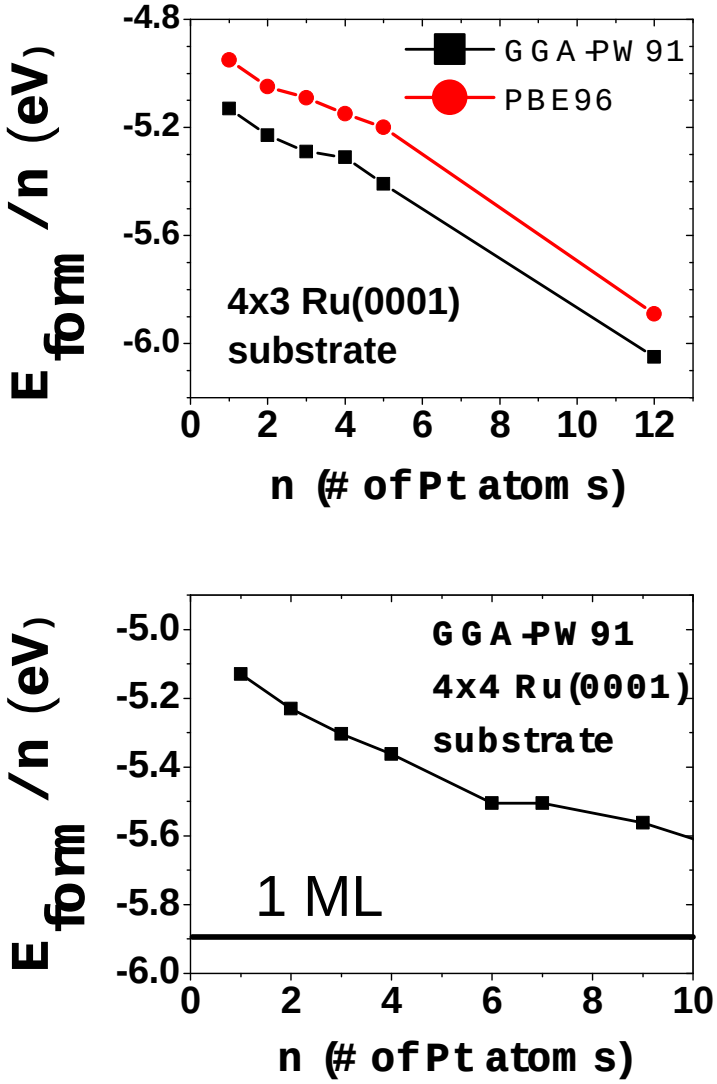

Figure 5.2: *The upper panel shows the average formation energy per atom, E_{form}/n, as a function of the size of the islands, n, for n = 1 - 5 using a (3x4) supercell, as provided by PBE and GGA. The lower panel shows also E_{form}/n vs. n using instead a (4x4) supercell, for n =1 - 4, 6, 7, and 9.*

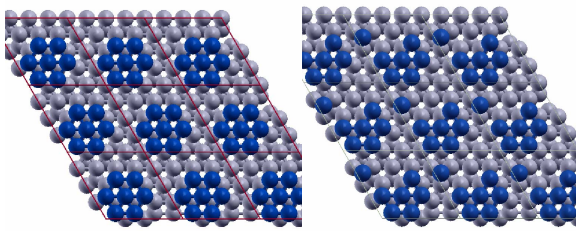

Figure 5.3: *Two configurations of a 7-atom Pt island (blue) on Ru(0001) (grey) showing the detachment of one Pt atom. The configuration in the right panel has lower E_{form}/n than the configuration in the left panel by ∼0.14 eV (see text).*

as provided by PBE and GGA. Fig. 5.2(b) displays the dependencies of E_{form}/n on n using a (4×4) supercell, for n = 1-4, 6, 7 and 9. Note that the values $n = 12$ and $n = 16$ represent a coverage of 1ML of Pt in the (3×4) and (4×4) supercells, respectively. We find that both PBE and GGA provide the same qualitative dependence: the larger island, the stronger the bonds, indicating that the full monolayer provides lowest E_{form}/n. The effect of atom detachment (from Pt islands) on E_{form} has been studied as well. Fig. 5.3 shows two configurations considered for the 7-atom Pt island adsorbed on $Ru(0001)$. We find that the detachment (transition from the left to the right configuration in the figure) causes an increase in E_{form} from -38.55 eV to -37.52 eV. Similar results have been obtained for the islands of other sizes. The increment of energy per Pt atom upon detachment, however, does not depend significantly on the island size and vary in the range of 0.11 - 0.14 eV. For instance, for a 2-atom Pt island, detachment leads to an increase in E_{form} from -10.46 eV to -10.24 eV, while for a 3-atom island, the energy increases from -15.88 eV to -15.52 eV upon the detachment.

The well-known tendency of many-atom systems to form as many interatomic bonds as possible leads to 2D, layer by layer growth. For binary systems, however, this can be

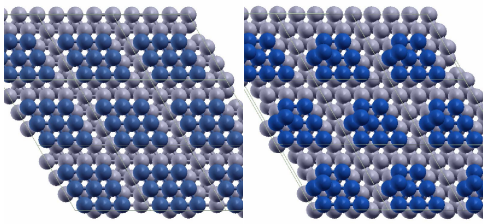

Figure 5.4: *Two configurations of a 9-atom Pt island (blue) with 2D(left) and 3D(right) structure on Ru(0001) (grey) (see text).*

overpowered by other factors and growth of multilayer islands may occur instead of wetting. For instance, the misfit between the typical bond lengths of the adatoms and the substrate may cause tensile or compressive stress as the adatom cluster grows larger and may, at certain point, induce the 2D/3D crossover, favoring the formation of multilayer islands. We have therefore performed calculations for some 3D Pt islands on Ru(0001) and found that the 2D islands are more stable that 3D ones. For example, two configurations of a 9-atom Pt island with 2D and 3D structures (see Fig. 5.4) were found to have E_{form} = -50.06 eV and -48.54 eV, respectively. Analyses of the above results point that Pt atoms tend to form the configurations that provide the maximum number of bonds regardless of their chemical nature until they form at least one single monolayer. There still remains the question: why, despite the misfit, no 2D/3D crossover occurs? In order to grasp some understanding of the issue, we note first that

In the 2D Pt islands under consideration, the number of NN fluctuates from 3 (single atom) to 9 (full monolayer). Decrease in the number of NN usually causes reduction of the equilibrium interatomic distances. Indeed, we find that for a free standing Pt monolayer, in which every Pt atom has only 6 nearest neighbors, the equilibrium $Pt - Pt$ NN distance is much shorter ($\sim$2.6 Å) than that in bulk Pt ($\sim$2.8 Å) and even shorter than the $Ru - Ru$

NN distance in bulk Ru ($\sim$2. Å). The misfit in low dimensional structures is thus not well defined because of the dependency on the coordination number of the atoms in question.

For these surface alloys, there is also the issue of stress induced by the bond-length misfit between the Pt nanostructures and the Ru surface atoms, neither one of which is expected to be at the bulk value, given the diversity of their local geometric environment. For the Pt atoms on the top of a hcp metal such as Ru, there is also an incommensurability in bulk structure. We find that the bulk NN bond length of Pt atoms certainly decreases when they arrange in an hcp structure. In that case, the bulk bond length misfit (PBE) between Pt and Ru decreases from $\sim$2.8 to $\sim$1.4 %. Furthermore, the surface *interlayer* distance in $Pt(111)$ expands to 2.49 Å ($\sim$1.0 % with respect to bulk), while that of the hypothetical $Pt(0001)$ contracts to 2.39 Å notwithstanding that *intralayer* NN distances are 1.8 % smaller than in the fcc bulk.

In summary, the formation of larger 2D islands appears to be favored because of the increasing number of bonds achieved by this means, while the aforesaid bond-length misfit seems to be mitigated by the low-coordination of Pt atoms and the hcp structure of the Ru substrate.

5.3.2 Pt diffusion on (0001) facet and through edges of a Ru nanostructure

From the above, we have gained an understanding of the tendency of Pt atoms to form 2D islands, wetting the $Ru(0001)$ surface rather than clustering in multiple 2D or 3D structures. The experimental evidence, however, suggests that Pt islands maintain small size on Ru nanoparticles,[146] say $\sim$0.5 nm (5 to 7 atoms), for 0.1 ML coverage. The difference in the characteristic of Pt surface alloys on $Ru(0001)$ and on Ru nanoparticle is part of the reason for the substantial reactivity of Pt adatoms on Ru nanoclusters and not on Ru surfaces. If Pt atoms were to make as many bonds as possible on the Ru nanoparticle as they do on the Ru surface, one would expect that, even for low coverage ($\sim$0.1 ML), a large island should totally cover one of the facets of the Ru nanoparticles. For example, a Ru nanoparticle of

Table 5.1: *Adsorption energy (in eV) of a Pt monomer on various sites of the* (0001) *and* ($\bar{1}$101) *facets of our Ru nanoparticle model (see numbering notation in Fig. 5.5)*

0001 fcc		0001 hcp		($\bar{1}$101)	
Label (Fig. 5.5)	E_{ads} (eV)	Label (Fig. 5.5)	E_{ads} (eV)	Label (Fig. 5.5)	E_{ads} (eV)
1	4.94	4	4.86	1	5.66
2	4.93	5	4.77	2	4.92
3	5.05	6	4.78		

2.5 nm with the proposed cubo-octahedral structure[146] - a 14-faceted structure - could hold roughly ∼7 (∼4) *Pt* atoms per squared (triangular) facet for homogeneous coverage of 0.1 ML (∼70 *Pt* atoms), whereas the same coverage coalesced into a single island could totally cover one of the squared facets, which seems not to be the case.[146]

One main difference between the *infinite* surface and the nanoparticle is that the latter exhibits edges dividing its facets. It is hence natural that they prevent *Pt* coalescence on the *Ru* nanoparticles. If this is true, 2D islands are formed on each facet, but they do not join together into a large unique island because the edges prevent those initial small islands from diffusing to other facets, thus persisting as few-atom 2D islands. Support for the aforesaid reasoning will be attained below by comparing the barrier for *Pt* atoms to diffuse on a (0001) facet with that for *Pt* to diffuse across the edges towards a ($\bar{1}$101) facet.

Pt Monomers

The *Ru* nanostructure used for the above purpose is displayed in Fig. 5.1. It possesses 3 fcc (fcc1, fcc2, fcc3) and 3 hcp (hcp4, hcp5, hcp6) non-equivalent hollow sites on the (0001) facet, as shown in Fig. 5.5(a). *Pt* monomers sit at those sites with different adsorption energies (see Table 5.1) and, as expected, they prefer to sit at fcc hollow sites.

In addition, *Pt* monomers preferably sit on sites surrounded by 2 edge atoms (hcp4 and fcc3), rather than on those surrounded by only one (hcp6 and fcc1) or none (hcp5, fcc2) edge atom. Note that the adsorption energy of a monomer on the (0001) facet is lower than on the infinite surface (5.13 eV). Across edge *A*, the first ($\bar{1}$101) available site is a 4-fold

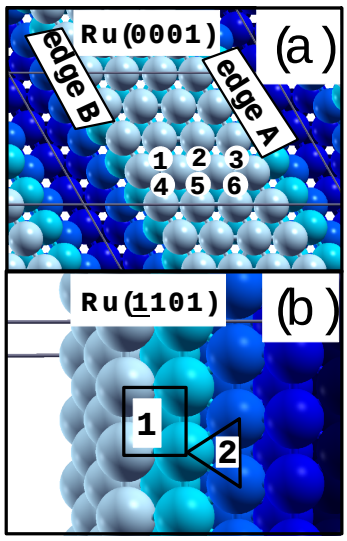

Figure 5.5: *Adsorption sites of Pt monomers (red) on the (0001) facet of the Ru nanoparticle model (blue). Numbers "1", "2" and "3" indicate fcc sites and "4", "5", "6" indicate hcp sites. (b) Adsorption sites of Pt monomers on the ($\bar{1}101$) facets of the Ru nanoparticle model. Numbers "1" and "2" indicate four-fold and three-fold hollow sites, respectively.*

hollow site, denoted by "1" in Fig. 5.5(b), whose adsorption energy, 5.66 eV, is substantially higher than that on fcc sites of the (0001) facet. Across edge B, the first ($\bar{1}101$) available site is a 3-fold hollow site, denoted by "2" in Fig. 5.5(b), whose adsorption energy is 4.92 eV. The above results, incidentally, suggest that there may be a propensity of Pt to deposit on ($\bar{1}101$) facets in the long range.

The calculated diffusion barriers,ΔE, through edge A, appears to be highly asymmetric (see Fig. 5.6(a)): $\Delta E(\text{fcc3} \rightarrow \text{"1"}) = 0.49$ eV and $\Delta E(\text{"1"} \rightarrow \text{fcc3}) = 1.10$ eV.

The diffusion barrier through edge B comprises two processes - one on the (0001) facet (fcc1 $\rightarrow$ hcp4) and one effectively across the edge (hcp4 $\rightarrow$ "2") - given that it is surrounded by hcp hollow sites on the (0001) side. As shown in Fig. 5.6(b) and (c), the activation energy barriers for monomer diffusion on the (0001) facet and through the edges are found to be comparable.

In order to estimate the probability of Pt diffusion entailed by these barriers, we have

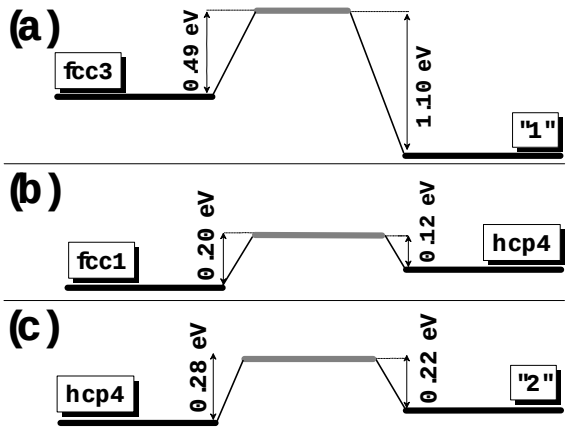

Figure 5.6: *Energy barrier for the diffusion of a Pt monomer (a) across the edge A (see Fig. 5.5): fcc3 ⟷ type "1" site, (b) on the (0001) facet: fcc1 ⟷ hcp4, and (c) across the edge B: hcp4 ⟷ type "2" site.*

roughly calculated the diffusion rate of Pt monomers. The latter, dominated by the exponential of the energy barrier, is given by $R = D_0 e^{-\frac{\Delta E}{k_B T}}$, where k_B is the Boltzmann constant, T is the temperature, and D_0 is the diffusion prefactor[17] whose typical values are of the order of $\sim 10^{12}\ s^{-1}$. We obtain that, at room temperature, the diffusion rate through edge B ($\sim 2 \times 10^8$ and $\sim 2 \times 10^7\, s^{-1}$, for "2" → hcp4 and hcp4 → "2", respectively) is comparable to that on the (0001) facet ($\sim 4 \times 10^8$ and $\sim 1 \times 10^{10}\ s^{-1}$, for fcc1 → hcp4 and hcp4 → fcc1, respectively). On the other hand, the diffusion rate through edges A ($\sim 3 \times 10^{-7}$ and $\sim 6 \times 10^3\ s^{-}1$, for "1" → fcc3 and fcc3 → "1", respectively) is found to be several orders of magnitude lower than that through edges B or that on the (0001) facet. In summary, our results indicate that edges A compel Pt monomers to remain on the facet where they are initially adsorbed, but not so edges B. In real Ru nanoparticles we might thus expect that Pt monomers may diffuse across some edges and may not across some others.

Pt dimers

The results of previous sections indicate that clustering of 2D islands on the facets and monomer diffusion across the edges are expected to occur readily. Yet, in order for Pt

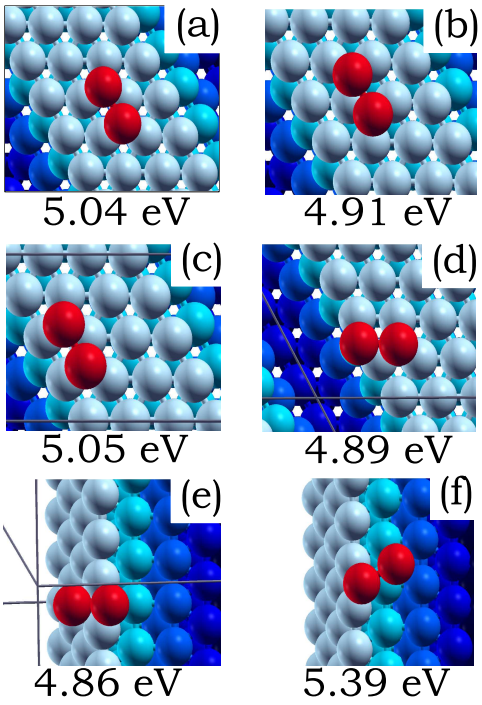

Figure 5.7: *Adsorption sites and E_{form}/n (n = 2) of Pt dimers (red) on the facets of the Ru nanoparticle model (blue). (a) Top view of the* (0001) *facet showing a dimer at fcc2 sites. (b) Top view of the* (0001) *facet showing a dimer at hcp5 sites. (c) Top view of the (0001) facet showing a dimer at fcc1 sites. (d) Top view of the (0001) facet showing a dimer with one atom at a fcc1 site and the other beyond the edge of the same facet. The coordination number of the atoms is 5 and 4, respectively. (e) Top view of the ($\bar{1}$101) facet showing a dimer with one atom at a hcp4 site and the other at a type "2" hollow site. (f) Top view of the ($\bar{1}$101) facet showing a dimer at a type "2" and type "1" hollow sites of the same facet.*

islands to coalesce and form larger islands, they would have to diffuse through the edges. We therefore turn to the calculation of the energy barrier for a dimer to diffuse from fcc to hcp sites (on the (0001) facet) and through edge B, the *easy* edge for monomers to cross. Some of the sites that Pt dimers may adopt on the (0001) and the ($\bar{1}$101) facets, as well as the corresponding average formation energies per atom, are shown in Fig. 5.7. We find that E_{form}/n of the dimer increases ($\sim$ 0.12 eV) with respect to that of the monomer, suggesting that dimers would preferably form rather than diffuse as monomers through the

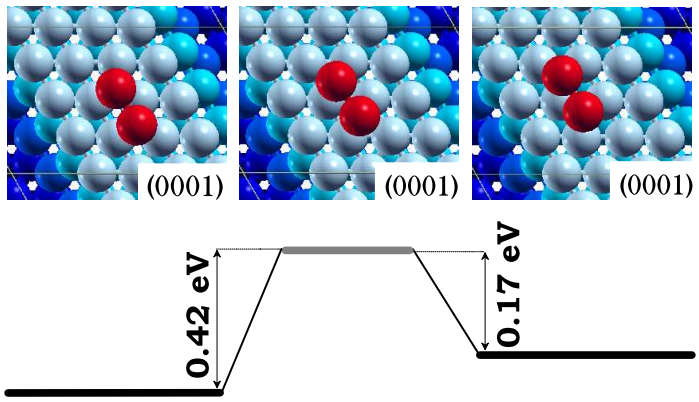

Figure 5.8: *The upper three panels from left to right illustrate initial, transition, and final states, respectively, of the diffusion of a dimmer (red) from fcc to hcp sites, as seen from the top of the (0001) facet (blue). The lower panel shows the corresponding barriers of this process and the inverse, from hcp to fcc sites.*

easy edges. As in the case of monomers, dimers prefer to sit on fcc sites on the (0001) facet (see Fig. 5.7(a) and (b)); similarly, the adsorption energy of Pt dimers at fcc sites near edge B (only one edge-atom neighbor) and in the middle of the Ru stripe is almost the same (see Fig. 5.7(a) and (c)). On the (0001) facet, when one of the atoms in the dimer comes closer to the edge and its coordination is reduced from 5 to 4 (compare Fig. 5.7(c) and (d)), E_{form}/n drops $\sim$ 0.16 eV, suggesting that there is a higher barrier for Pt dimers to approach the edges to the point where its atoms become more undercoordinated. On the $(\bar{1}101)$ facet, analogously, E_{form}/n is 0.52 eV lower for a dimer across the (0001) and $(\bar{1}101)$ edges (see Fig. 5.7(e)) than for a dimer sitting on the $(\bar{1}101)$ facet close to the edge (see Fig. 5.7(f)). As shown in Fig. 5.8, the barrier for the dimer to diffuse from hcp to fcc sites is similar to that for monomers while is 2.5 times smaller for the inverse process, from fcc to hcp. The diffusion rates (1.4×10^9 and $8.8\times10^4\ s^{-1}$, correspondingly) thus differ by four orders of magnitude, indicating that dimers are most of the time at fcc sites. This presents another indication that Pt dimers (or larger islands) would not leave the (0001) facet since, for it to diffuse across edge B, it must be on hcp sites. As shown in Fig. 5.9, the diffusion across edge B comprises two stages. The initial state of the first stage corresponds to the configuration

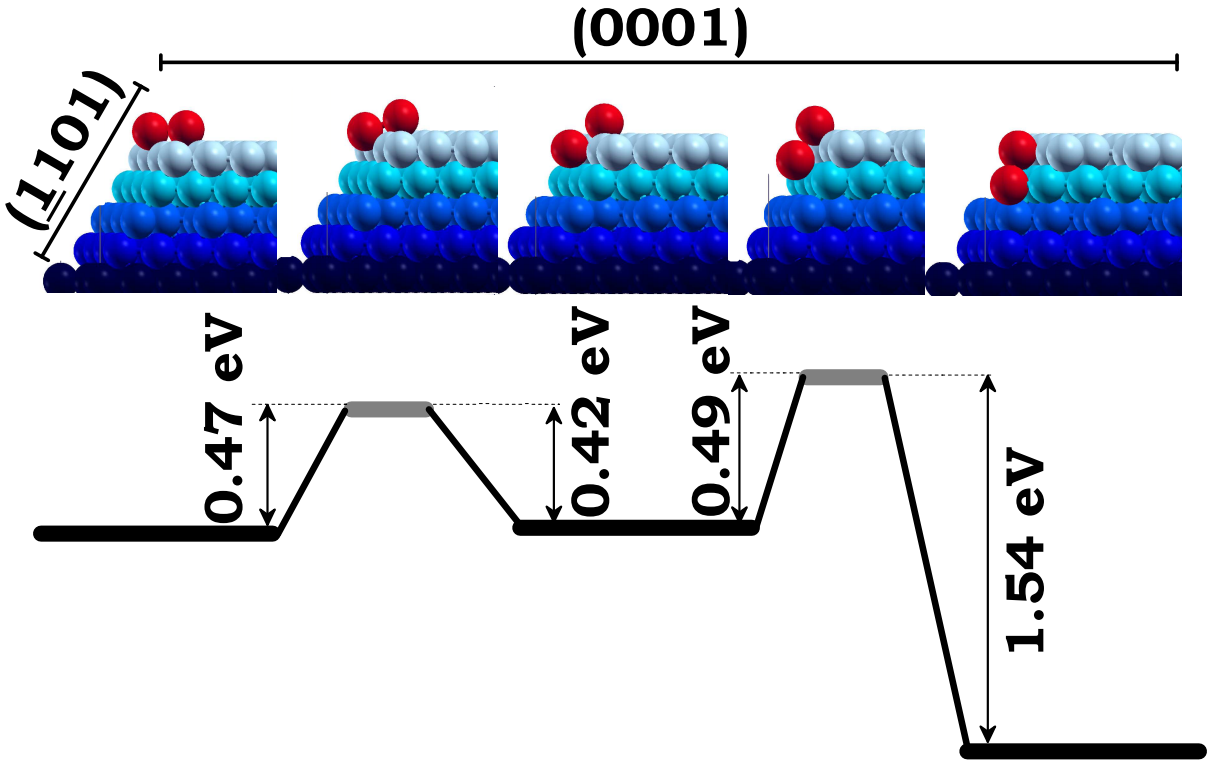

Figure 5.9: *The upper five panels from left to right illustrate the two-step diffusion of the dimmer (red) across the edge intersecting the (0001) and the ($\bar{1}$101) facets (blue). First, third, and fifth upper panels are local minimum energy configurations of the dimmer and the second and forth upper panels are transition states. The lower panel shows the barrier for the dimmer to diffuse back and forth from either local minimum energy configuration (see text).*

shown in Fig. 5.7(d) in which one atom is on a fcc1 site and the other is slightly beyond the edge whereas, in the final state, the atom at the fcc1 site diffuses to a hcp4 site and the other moves to a type "2 " site (see Fig. 5.5(b)) of the $(\bar{1}101)$ facet, as shown in Fig. 5.7(e). The energy barriers for the dimer to diffuse back and forth from the initial and final states are shown in Fig. 5.9 while the corresponding diffusion rates for these processes are low ($\sim 10^4$). Indeed, the energy barriers of the first stage are very similar to those for dimer diffusion from fcc to hcp sites (see Fig. 5.8) and for monomer diffusion through edge A (see Fig. 5.6). Notice also that the final state described above is only an intermediate stage of the diffusion towards the $(\bar{1}101)$ facet. For the second stage, the initial state is naturally the configuration shown in Fig. 5.7(e) while the final state corresponds to that shown in Fig. 5.7(f), in which both atoms sit on the $(\bar{1}101)$ facet. The energy barrier to move from the initial to the final state (see Fig. 5.9) produces also a low diffusion rate of $6\times10^3\,s^{-1}$, while the inverse process, whose barrier is 3 times larger, provides a diffusion rate of $\sim1.4\times10^{-14}\,s^{-1}$, indicating that dimers like monomers on the $(\bar{1}101)$ facets will most likely remain there. In short, edge B, which offers a low-barrier diffusivity path to monomers, renders to Pt dimmers two energy barriers for facet-to-facet diffusion, each representing a diffusion rate at least three orders of magnitude lower than those of the monomer. We expect the diffusion rates of trimers and other n-mers of Pt on Ru nanoparticle facets to be even lower than that found here for dimers.

5.4 Summary

We have calculated from first principles the energetics and geometry of Pt islands deposited on $Ru(0001)$, as well as the energy barriers for diffusion of Pt monomers and dimers through the edges intersecting the (0001) and $(\bar{1}101)$ facets of a superstructure modeling a nanoparticle. We find that the low coordination of Pt atoms composing the islands and the hcp structure of the substrate promote that Pt islands adsorbed on the $Ru(0001)$ grow as large as possible up to 1ML and avoid the 2D/3D crossover. Nevertheless, we have proposed

that, in experiment, *Pt* atoms arrange homogeneously over the facets of *Ru* nanoparticles by spontaneous deposition and form 2D islands on each facet, but they do not join together into a large unique island because the edges of the *Ru* nanoparticles prevent the initial islands from diffusing to other facets, persisting thus as few-atom 2D islands. Our calculated barriers indicate that there may be some edges in the *Ru* nanoparticles for which the diffusion rate *across-edge* is several orders of magnitude lower than the diffusion rate *on-facet*, even for monomers. For those edges that may offer low diffusion barriers to monomers, our calculated barriers for dimers suggest that dimers or larger islands, whose formation is more probable than the monomer diffusion, remain in the facet where they were formed since the diffusion rate *across-edge* is several orders of magnitude lower than that of monomers.

Chapter 6

First-principles study of the surface phonon dispersion of c(2x2)-CO on Cu(001)

6.1 Introduction

Comprehension of the coupling between molecules and metallic surfaces have attracted much interest in the last three decades[159,160] because of the insight it provides into chemisorption and diffusion processes,[161] which ultimately control phenomena such as catalysis and corrosion. In this regard, *ab initio* numerical methods based on the density-functional theory (DFT) represent, to date, the most robust and accurate approach to model, understand, and predict the geometrical, electronic, and dynamical properties of chemisorbed surfaces, as well as many other systems. Of particular relevance in this work is the density-functional perturbation theory (DFPT), which furnishes a powerful and comprehensive framework to deal with perturbations in the ionic positions since it provides access to the dynamics of the adsorbate and the substrate in the entire surface Brillouin zone (SBZ) while taking into consideration all inter-atomic couplings within the system.[116] On the experimental side, different spectroscopic techniques, such as infrared-reflection absorption spectroscopy (IRRAS) and Raman and electron energy loss spectroscopy (EELS), have provided a vast amount of data on vibrational modes whose frequencies exceed ∼20 meV.[162] Inelastic Helium Atom Scattering (HAS) has instead been the leading technique for measuring frequencies below

$\sim$20 meV, particularly those arising from fluctuations of the surface-molecule bond, as manifested in the frustrated translation (FT) modes of adsorbed molecules.[16]

The CO/Cu(100) system, has been widely studied because of its structural symmetry, relatively simple electronic structure, and experimental approachability.[163] Low Energy Electron Diffraction (LEED) and Near-Edge x-ray Adsorption Fine Structure (NEXAFS) measurements show that CO adsorbs on Cu(001) with the C end bound atop Cu surface atoms and the molecular bond oriented normal to the surface, forming a c(2x2) overlayer at half monolayer, $\theta = 0.5$ ML (see Fig. 6.2(a)).[160,164–166] Vibrational modes of CO on Cu(001) have also been extensively studied experimentally[167] and theoretically at the center of the SBZ,[34,159] the Γ-point (see Fig. 6.2(b)). Many of the calculations available in the literature have used a cluster model for the substrate[168–173] and applied the *frozen-phonon* or *finite differences* (FD) method[174] to determine ν_1 and ν_2, while ignoring the role of the substrate (*frozen substrate* method). To our knowledge, no attempt to obtain theoretically the phonon dispersion relations of the chemisorbed surface has so far been carried out, while the latter has been assessed experimentally only in the low frequency range by HAS.[16]

The vibrational modes of CO on the Cu(001) surface may be divided into two groups according to their polarization. The first group involving displacements perpendicular to the surface are the C-O and the Cu-CO stretch modes, whose frequencies are denoted by ν_1 and ν_2, respectively. The second group involves mostly horizontal displacements derived from the rotational and translational motions of the free CO molecule that become frustrated upon adsorption on the Cu surface.[16] The four modes among this group consist of two frustrated rotation (FR) modes and two frustrated translation (FT) modes, whose frequencies are denoted by ν_3 and ν_4, respectively. Notice that straight atop adsorption of the molecule on the (001) surfaces of fcc metals causes degeneracy in the two FR and FT modes at Γ.[16]

Lewis and Rappe[175] computed the frequencies of all six modes at Γ, treating both the adsorbate and the substrate on equal footing, using the local density approximation (LDA) of the density functional theory (DFT) and the finite differences (FD) method. They found

reasonable agreement with experiment for the Rayleigh wave of the substrate, and for ν_1 and ν_3, but not for ν_2 and ν_4. They also found the molecule-substrate bond to be anharmonic with respect to horizontal displacements and that the introduction of anharmonicity effects in the force constants shifted ν_4 very close to the experimental value.[175] Favot et al.[34], applying the DFPT method with GGA, obtained values of ν_1 and ν_2 at the Γ point to be in agreement with the experimental data, but ν_3, ν_4 and the frequencies of the substrate modes were not reported. They compared the capabilities of LDA and GGA to describe c(2x2)-CO/Cu(100), and found that LDA fails to find the top site as the preferred adsorption site of the molecule, while GGA reproduces it correctly. In this work, through examination of the dispersion of the phonons of c(2x2)-CO/Cu(100) using DFPT with both approximations, we show that apart from predicting the wrong adsorption site, LDA produces negative frequencies for the FT mode almost everywhere in the sampled regions of the SBZ (except in the vicinity of Γ), suggesting - against the experimental evidence - that the CO-c(2x2) overlayer is unstable under the FT mode distortion. There are indications that this situation is derived from the strong overestimation of the C-Cu bond strength,[34,176] which makes the LDA potential energy surface favor the hollow site to atop for CO on Cu(001). Meanwhile, the dispersion of the FT mode obtained from GGA reproduces quantitatively well HAS measurements without need to adjust the involved force constants to incorporate anharmonic effects.[175]

The different scenario exhibited by GGA regarding the C-Cu interaction calls also for revisiting the softening of the Rayleigh wave (RW), with respect to the clean surface, observed in HAS measurements upon CO adsorption.[16] It has been partially explained by the mass overloading of *covered* Cu atoms. Namely, Ellis et al.[16] obtained a dispersion relation that underestimates the observed softening by keeping intact the force constants of the clean surface and simply taking into account the mass overloading of *covered* atoms. In turn, previous LDA DFT calculations[175] did not find considerable changes in the force constants of surface Cu atoms while reasonable agreement with experiment was obtained for the fre-

quency of the *back-folded* RW at Γ, leaving the mass overloading as the main reason for the softening of the RW. It is not straightforward to interpret or classify the softening as due to either fact. On the one hand, only one of the two Cu surface atoms in the unit cell adsorbs and carries CO whereas the RW refers to the vibration of the first layer (mainly) which is represented by both surface atoms in the unit cell. On the other hand, upon CO chemisorption *covered* and *bare* atoms relax in opposite directions. Namely, *covered* atoms not only drag a CO molecule but also relax outwards, while bare atoms remain relaxed inwards with respect to bulk interlayer spacing, as occurs for the clean surface. Understanding of the softening of the RW becomes even more complex since structural features and changes in the force constants of the substrate are a matter of disagreement between LDA and GGA and, in spite of that, both reproduce well HAS measurements of the RW.

The rest of this work is organized as follows: Section 6.2 contains the computational details for the present calculations. Section 6.3 is a summary of results concerning the structure of bulk Cu, clean Cu(001), and c(2x2)-CO/Cu(100). In Section 6.4, we present our results and discussion of the dynamics of all three systems. Chapter 7 contains the concluding remarks of this study.

6.2 Computational details

Periodic super-cell calculations are performed on the basis of the DFT formalism and the pseudopotential approach.[116] The present results are derived from the mixed basis (MB) technique,[177] which reduces significantly the size of the basis set to describe valence states that are strongly localized near atomic sites. Using norm-conserving pseudotentials (NCPP), we obtain results within both LDA and GGA. The former is applied through the Hedin-Lundqvist[33] parametrization of the exchange-correlation functional, whereas GGA is introduced via the expression by Perdew, Burke, and Ernzerhof.[120]

The radius around Cu sites, at which the d-type local functions are smoothly cut off, r_{cutoff}, is 2.3 au for both LDA and GGA. The r_{cutoff} of s- and p- type local functions is

1.2 and 1.08 au, respectively, for C and O in both LDA and GGA. In the present GGA calculations, d-type basis functions are included in the description of the valence states of C atoms. The maximum kinetic energy, E_{max}, of the plane waves used to describe valence states has been set to 20 Ry for LDA and increased up to 33 Ry for GGA to reach convergence of the CO bond length and the atomic forces in c(2x2)-CO/Cu(001). The energy at which the Fourier expansion of the charge density is truncated, G_{max}, has been set to 50 Ry for both LDA and GGA.

The clean and the CO-chemisorbed Cu(001) surfaces are simulated with symmetric slabs inside a tetragonal unit cell containing either 9 (for LDA) or 7 (for GGA) layers of Cu. In the chemisorbed surface, CO molecules are symmetrically located on each side of the slab. Periodically repeated slabs are separated by a distance equivalent to 9 and 11 layers, correspondingly. Integrations inside the SBZ are done over discrete meshes of 8x8x8, 8x8x1, and 6x6x1 k-points for bulk Cu, clean Cu, and CO-c(2x2)-Cu(001), respectively. Integrations up to the Fermi surface at an irreducible set of k-points are obtained using the broadening technique for the level occupation,[178] where the Gaussian smearing parameter, $\overline{\Sigma}$, is set to 0.2 eV.

To find the binding energy of a molecule in the c(2x2) overlayer, we have taken into account the direct interaction among the molecules. We have thus calculated the total energy of CO molecules in a free standing two dimensional c(2x2) array as in the c(2x2)-CO/Cu(001) system, using the same super-cell employed in the chemisorbed system, as well as all other parameters. The direct-interaction energy among molecules in the above two dimensional array is thus the difference between the total energy of one molecule in the array and that of an isolated molecule. The latter is modelled using a large super-cell of 19x19x21 au, so as to limit integration over only 1 k-point.

Minimization of the slab total energy as a function of the atomic positions is based upon the reduction of Hellmann-Feynman forces[7] below 10^{-3} Ry/au, using the Broyden-Fletcher-Goldfarb-Shanno (BFGS) algorithm.[179]

The calculation of the lattice dynamical matrices at specific q-points of the SBZ is based on the lineal response theory embodied within DFPT,[116,122] as developed by Heid and Bohnen.[180] Studies of the dynamics of CO/Cu(001) have also been performed using the plane-wave technique and ultra-soft pseudopotentials with the Quantum ESPRESSO package[118], which essentially provides the same results when LDA is used, but overestimates the frequency of the FT mode when GGA is used. For the sake of clarity, those results will not be presented here. Calculations of the dynamical matrices at specific q-points are performed applying a convergence criterion of 0.02 meV in the phonon energies. For bulk Cu, Cu(001), and c(2x2)-CO/Cu(001), they are calculated at the q-points of a 4x4x4, a 4x4x1, and a 2x2x1 mesh, respectively. The real-space force constants in these systems are obtained by the standard Fourier transform of the corresponding dynamical matrices.[181] The force constants of both surfaces are then matched with those of bulk Cu to model a clean and a chemisorbed asymmetric slab of 50 and 800 layers, respectively, and used to obtain the frequencies at arbitrary q-points. Surface modes in the clean surface have been identified as those whose amplitude weight in the two outermost layers is larger than 20%. In the chemisorbed slab, surface modes and resonances have been identified as those whose amplitude weight in the 6 outermost atoms (including C and O) is larger than 20 and 5%, respectively.

In order to reliably compare the results given by inclusive DFPT calculations and those by the FD-*frozen substrate* (FD-FS) method, we have computed ν_1 and ν_2 using the later method within LDA. The 2x2 force constant matrix that primarily controls the C-O and CO-Cu stretch modes is obtained from the forces developed on C and O as their vertical equilibrium position on Cu(001) is independently modified by *finite differences* of ± 0.04 Å while keeping the Cu slab fixed.

Table 6.1: *Lattice constant (*a*) and bulk modulus (*B*) of bulk Cu.*

	Theory				Experiment
	LDA		GGA		
	NCPP	AE	NCPP	AE	
	This work	Ref.[182]	This work	Ref.[182]	Refs.[125,183,184]
a (Å)	3.57	3.52	3.68	3.62	3.61
B (GPa)	170	192	128	151	138

6.3 Structural properties

6.3.1 Bulk Cu

Convergence tests of the lattice constant and bulk modulus have been performed extensively. As shown in Table 6.1, the lattice parameter of bulk Cu is found in good agreement with all-electron (AE) calculations, which are the ultimate test for pseudopotentials methods. Nevertheless, our calculated bulk modulus (B), falls below that provided by AE calculations.[182] Discrepancies with AE calculations in this respect are expected since B involves the derivative of the energy with respect to the volume, being thus more responsive to the differences between AE and PP calculations than the lattice parameter. As for agreement with experiment,[125,183,184] LDA underestimates the lattice constant and yields, therefore, larger bulk modulus. GGA overcorrects LDA, though it reproduces better the experimental bulk modulus than does LDA. Our results for bulk Cu are also in good agreement with those obtained by pseudopotential calculations reported in studies of relevance to this work.[34,175]

6.3.2 Clean Cu(001)

The relaxation of the interlayer distances normal to the surface of Cu(001) has been extensively studied theoretically.[34,116,161,175,185] Nevertheless, before conducting our study on the CO-chemisorbed surface, it is essential to test the applied methodology with interrelated and well characterized systems, as is the clean Cu(001) surface; which, furthermore, will serve as a reference to appraise the extent to which CO chemisorption affects it. The top view of Cu(001) and the (1x1) SBZ are shown in Figs. 6.1(a) and (b), respectively. Notice

Table 6.2: *Percentage change of the interlayer spacing of the outermost layers of Cu(100) compared to the bulk situation.*

	Theory[1]		Experiment	
	LDA	GGA	SPLEED[2]	MEIS[3]
Δd_{12}	-2.57	-2.82	-1.2	-2.4
Δd_{23}	+0.55	+0.58	+0.9	+1.0
Δd_{34}	+0.30	fixed	-	-

[1]This work [2]Ref.[187] [3]Ref.[186]

in Table 6.2 that both LDA and GGA produce an inwards relaxation of the surface layer of $\sim 3\%$, as shown in Table 6.2. These results are in agreement with earlier pseudopotential calculations[34,116,161,175,185] and with surface structure measurements via the medium ion energy scattering (MEIS) technique (see Table 6.2).[186]

6.3.3 c(2x2)-CO/Cu(001)

The c(2x2) structure exhibited by the CO adlayer on Cu(001) is illustrated in Fig. 6.2(a). Notice there that the primitive super-cell contains two atoms per layer, and that these are non-equivalent in odd numbered layers since CO sits directly above only one of them. Accordingly, atoms in the first layer are referred either as *covered* or *bare* atoms. To our knowledge there is no experimental characterization of the substrate geometry after CO adsorption. The present work and previous calculations[34,175] indicate that the first and third layers rumple, but not the second layer atoms. As shown in Table 6.3, there are differences in the interlayer relaxations of the Cu(001) surface upon CO adsorption as predicted by LDA and GGA. In both cases, CO raises the original inwards contraction of *covered* atoms and makes them relax slightly outwards with respect to the bulk situation. GGA, however, finds that such outwards relaxation is two times larger than predicted by LDA. Additionally, LDA indicates that the inwards relaxation of bare atoms is also slightly lessened by CO, while, according to GGA, bare atoms undergo an inwards relaxation stronger ($\sim$ -4.0%) than that of atoms in the clean surface. We notice that similar trends were found in Refs.[34] and[175]; even though, there are moderate differences regarding the spacing among deeper

(a)

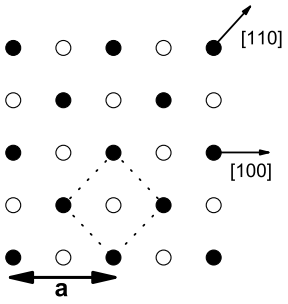

(b)

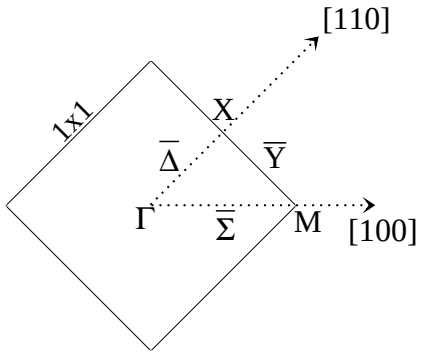

Figure 6.1: *(a) The top view of the Cu(100) surface. First layer atoms are represented by filled circles and second layer atoms are represented by open circles. (b)The corresponding (1x1) surface Brillouin zone of Cu(100).*

(a)

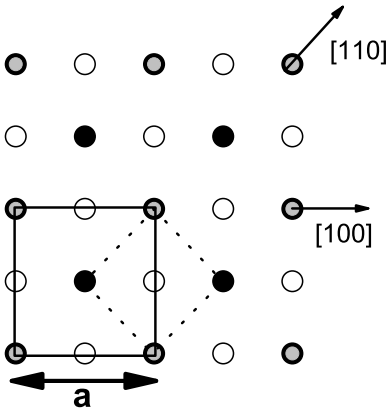

(b)

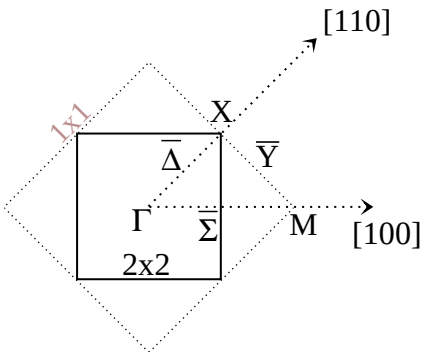

Figure 6.2: *(a) The top view of the surface shows CO (grey circles), and first (filled circles) and second (open circles) layer atoms of Cu(100). The 1x1 (dashed line) and the c(2x2) (solid line) surface unit cells are underlined. (b) The corresponding (1x1) (dotted line) and c(2x2) surface Brillouin zones (solid line) showing the* Γ*, X, and M points; and the* $\overline{\Delta}$*,* $\overline{\Sigma}$*, and* $\overline{Y}$ *directions.*

Table 6.3: *Percentage change of the interlayer spacing of the outermost Cu layers of c(2x2)-CO on Cu(100) compared to the bulk situation; bond-length of CO, d_{C-O}, when it is adsorbed on Cu(001) (on Cu), isolated (free) CO, and in a free-standing c(2x2) mesh (mesh); and bond-length of the C-Cu bond, d_{Cu-C}. Label A distinguishes the interlayer Cu spacing referred to atoms that have CO directly above, while B accounts for the those which do not.*

	Theory					Experiment
	LDA			GGA		
	This work	Ref.[175]	Ref.[34]	This work	Ref.[34]	Refs.[164],[a] [189],[b] and [160c]
Δd_{12}	$+0.34^A$ -2.17^B	$+0.50^A$ -1.56^B	$+1.4^A$ -2.7^B	$+1.32^A$ -4.41^B	$+2.0^A$ -4.1^B	-
Δd_{23}	-0.17^A $+0.64^B$	$+0.44^A$ $+1.39^B$	$+0.1^A$ $+1.2^B$	$+0.02^A$ $+0.71^B$	$+0.2^A$ $+1.7^B$	-
Δd_{34}	-0.15^A -0.96^B	$+0.72^A$ -0.40^B	-	-0.44^A -1.12^B	-	-
d_{C-O}(Å)^{chemisorbed}	1.16	1.14	1.15	1.16	1.16	1.15^a
d_{C-O}(Å)^{mesh}	1.14	-	-	1.15	-	-
d_{C-O}(Å)^{free}	1.14	1.12	1.36	1.14	1.15	1.13^b
d_{Cu-C}(Å)	1.83	1.85	1.82	1.88	1.88	1.90 ± 0.01^a

layers (see Table 6.3). As for C-O and Cu-C bond lengths, for which experimental data are available, Table 6.3 shows that GGA gives better agreement with experiment than LDA. Note that the molecular bond-length is enlarged after chemisorption,[176,188] in agreement with experiment.

The results of our calculated interaction energy among molecules in the free standing c(2x2) array also point to difficulties in the application of LDA to this system: LDA finds it to be attractive by ∼45 meV, while GGA shows it to be repulsive by ∼75 meV. Experiments[160,190] suggest that, even below a coverage of one-half monolayer, the interaction of chemisorbed CO molecules is repulsive and estimated to be ∼20 meV at 0.5 ML,[160] albeit for chemisorbed CO on Cu(001). It is also known that the binding energy of the molecule to the surface is strongly overestimated by LDA , while GGA substantially improves agreement with the experimental value,[34,191] 0.57 eV.[160] Our GGA calculation produces a chemisorption energy of 0.75 eV, which takes into account the above (repulsive) direct interactions among molecules.

Table 6.4: *Calculated real space atomic force constants of bulk Cu corresponding to first NN, in units of dyn/cm. Experimental values*[192] *(at 49 K) were obtained by fitting the measured frequencies.*

	Theory[1]		Experiment
	LDA	GGA	NIS
XX	15941	12226	13278
XY	17897	13595	14629
ZZ	-1801	-1037	-1351

[1]This work

6.4 Lattice dynamics

6.4.1 Bulk Cu

Figure 6.3 shows that the calculated phonon dispersion of bulk Cu is in reasonable agreement with neutron inelastic-scattering measurements (NIS).[192,193] GGA dispersion curves appear in closer agreement with experimental data than those of LDA, though. At the zone boundaries, where differences in the force constants become conspicuous in the phonon dispersion, LDA provides a stiffer phonon spectrum by ∼2.5 meV as compared to experiment, while that of GGA is softer by ∼1.5 meV. Indeed, as shown in Table 6.4, LDA overestimates the real space force constants between first nearest neighbors (NN) XX, XY, and ZZ by ∼20, ∼22 and ∼33%, respectively; while GGA underestimate them by ∼8, ∼7, and ∼23%, respectively.

6.4.2 Cu(001)

The phonon dispersion of Cu(001) has been studied at length using DFPT methods recently.[116,126] Repeating this calculation is, however, a testing ground for the computational methodology that is being used, but, above all, it is imperative to obtain a commensurable comparison with the chemisorbed surface. Our calculated dispersion along the $\overline{\Sigma}$ ([100]), $\overline{\Delta}$ ([110]), and $\overline{Y}$ directions (see Fig. 6.1(b)) is shown in Figs. 6.4 (LDA) and 6.5 (GGA) and compared to HAS and EELS measurements.[194–196] Observe that surface phonons are labelled in accordance with the notation introduced by Allen et al.[197] In agreement with

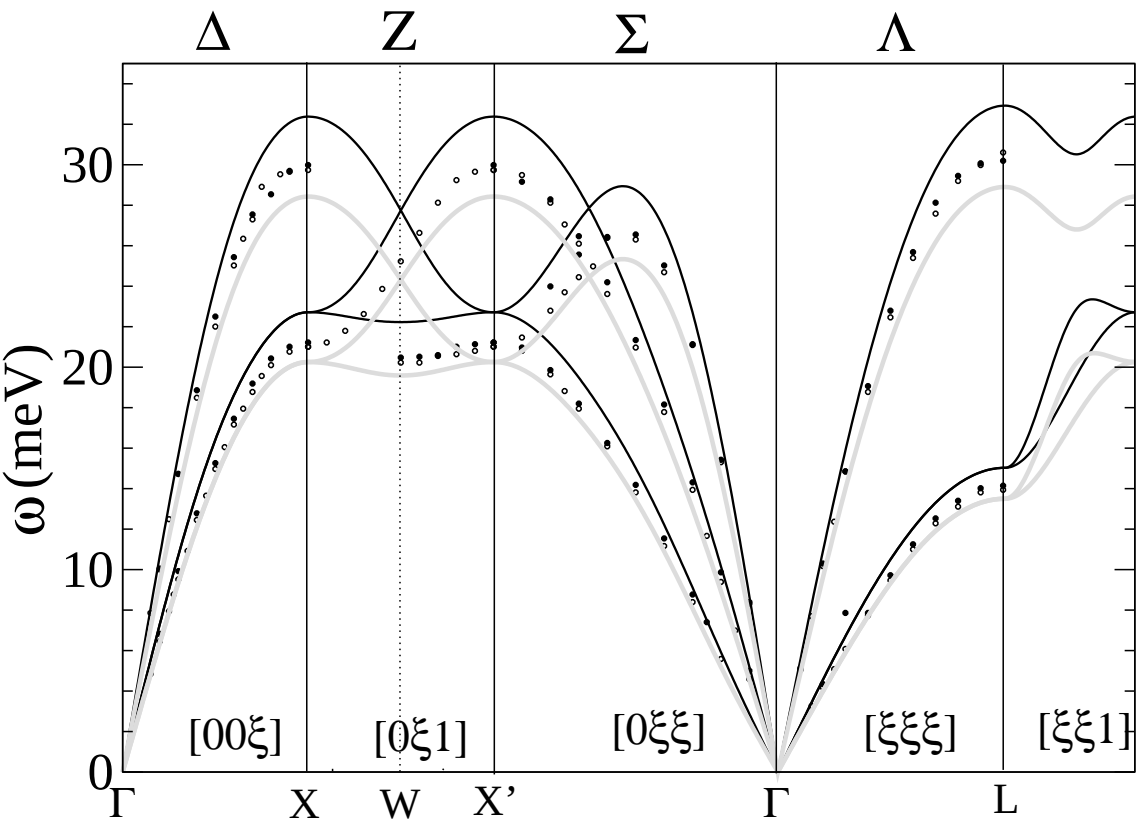

Figure 6.3: *LDA(black line) and GGA(grey line) phonon spectrum of bulk Cu. Experimental data, open*[193] *and filled*[192] *circles, are taken from NIS measurements at room temperature and 49K, respectively.*

Table 6.5: *Frequencies (in meV) of the surface modes of Cu(100) at the high symmetry points X and M (see Fig. 6.2 (b)). The main polarization (SH, L, or V) is denoted in parenthesis and the superscript indicates the layer showing largest amplitude weight.*

		Theory			Experiment	
		LDA		GGA		
		This work	Ref.[116]	This work	Ref.[195]	Ref.[196]
X	$S_1(SH^1)$	9.7	9.9	9.1	-	-
	$S_4(V^1)$	14.6	14.0	13.5	13.4	-
	$S_5(SH^2)$	15.6	15.0	14.3	-	-
	$S_6(L^1)$	27.0	26.1	24.1	25.2	-
M	$S_1(V^1)$	18.7	19.9	16.9	25.2	16.8
	$L_1(L^1)$	22.3	-	20.1	20.2	20.5
	$S_2(V^2)$	22.3	21.1-21.7	20.0	20.3	-

their work and as seen in Figs. 6.4 and 6.5, a large number of surface modes come out in the phonon dispersion of Cu(001), especially along $\overline{Y}$. In the subsections below, however, we describe only those which are of interest in the discussion of the chemisorbed surface; their frequencies at high symmetry q-points (X and M) are summarized in Table 6.5 and compared with those reported in Ref.[116] and experiment.

We find that, in the top layer, *intralayer* force constants among first NN are ∼12 (LDA) and 7-10% (GGA) softer than in bulk Cu, whereas, in the second layer, *intralayer* force constants among first NN differ from bulk values by less than 1%. In turn, the *interlayer* force constants coupling the first and second layers via first NN stiffen by ∼15-17% and 20-22% in LDA and GGA, respectively. Experimentally,[195,196] such stiffening has been estimated to be ∼20%, on the average. Finally, force constants coupling second-third, and third- forth layers are found to soften by ∼4 and ∼2%, respectively.

Surface modes along $\overline{\Delta}$

Along $\overline{\Delta}$, S_1 is the surface mode of lowest energy, as shown in Figs. 6.4 and 6.5. It is totally localized in the first layer at the X point. However, it is undetectable by scattering techniques since its polarization is shear horizontal (SH) all along. Above S_1, it appears the RW - S_4 in Allen's notation -, which is a surface mode essentially vertically (V-) polarized,

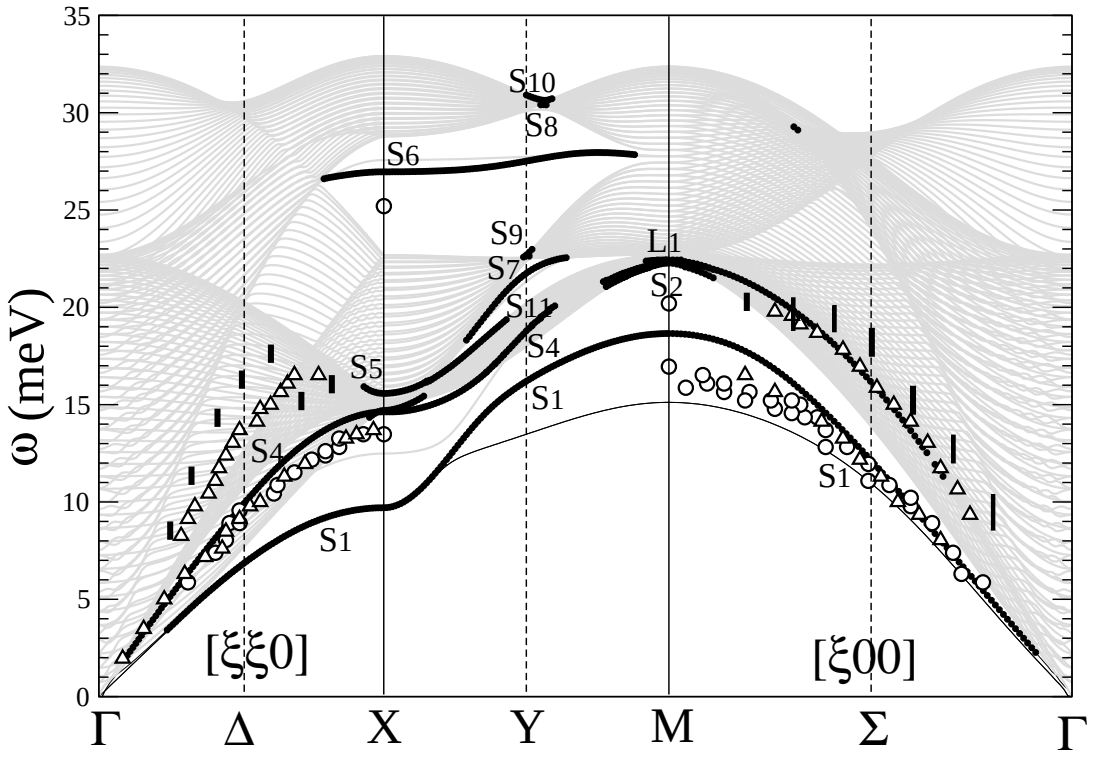

Figure 6.4: *LDA phonon dispersion of Cu(001), modelled by a 50-layer slab. Theoretical surface modes (filled circles) are compared with HAS (open triangles) and EELS (open circles) measurements taken from Refs.*[194–196] *Bulk terminated modes are not highlighted (see text). Thin rectangles show regions where weak resonances are found (see text).*

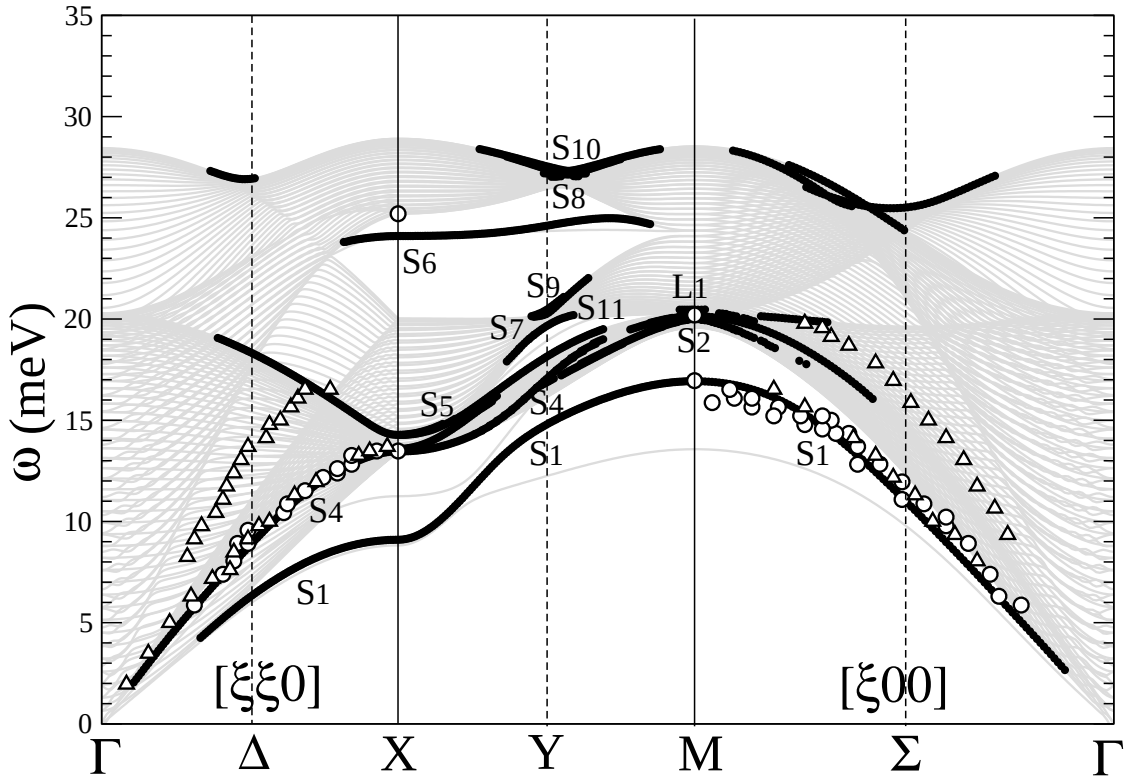

Figure 6.5: *GGA phonon dispersion of Cu(100), modelled by a 50-layer slab. Theoretical surface modes (filled circles) are compared with HAS (open triangles) and EELS (open circles) measurements taken from Refs.*[194–196] *Bulk terminated modes are not highlighted see text).*

although a longitudinal (L-) contribution is also present. Its amplitude weight is greatest at the first layer but it dies out well below the first two layers. Right above S_4, there appears a SH mode, S_5, with dominant displacement in the second layer. Finally, S_6 is found inside the spectrum gap, close to the zone boundary, and with predominant L-polarization in the first layer. We note that, above S_4, LDA shows also a resonance in the first and second layers and with mixed L- and V- polarization that follows closely HAS measurements. It is not plausible, nevertheless, to associate it with the experimental data since the amplitude weight in the two outermost layers contributes, at most, ∼12%. The reason why DFPT does not reproduces such L- polarized mode, sharply detected in HAS experiments, remains an open question to date (A similar situation existed for the Cu(111) surface, though in this case the issue has been resolved just recently.[198]).[116,126]

Surface modes along $\overline{Y}$

We observe that S_4, which is vertically polarized at X, develops into a predominantly SH-mode as it crosses $\overline{Y}$.[197] Similarly, S_1, which along $\overline{\Delta}$ is SH- polarized, changes rapidly to V- polarization along this direction. Notice in Figs. 6.4 and 6.5 that no experimental data is available for comparison.

Surface modes along $\overline{\Sigma}$

The mode with lowest frequency along $\overline{\Sigma}$ is the first-layer RW (see Figs. 6.4 and 6.5), known as S_1 in Allen's notation.[197] It is mainly V-polarized at the M-point, acquiring an additional L-polarization as it approaches to the Γ-point. In the second layer, we find the V-polarized mode S_2. GGA indicates that it prevails along $\overline{\Sigma}$, reaching one-quarter way to Γ (see Fig. 6.5) with either V- or mixed V-L polarization. LDA, on the other hand, finds that it is more delocalized and very rapidly becomes a resonance that runs throughout $\overline{\Sigma}$ (see Fig. 6.4). This mode thus soon forms part of a band of bulk resonances along $\overline{\Sigma}$ (see Fig. 6.4) whose maximum amplitude weight comes from either the second and first layers (with V- and L- polarization, respectively) when close to the SBZ boundary, or first layer

(with mixed V-L mixed polarization) when close to Γ. There are other two more modes at M that were not described in Allen's work. The first, L_1, is a L-polarized mode that, in LDA, becomes a resonance more rapidly than S_2. GGA finds it to persist as a dispersionless mode one-quarter way along $\overline{\Sigma}$ (see Figs. 6.5); it barely matches a couple of experimental points, though. The second one is just a SH-degenerate pair of L_1 at M. The degeneracy with the latter is broken outside M but the SH-mode persists all along $\overline{\Sigma}$ in LDA and up to the mid point of the same in GGA (see Figs. 6.4 and 6.5). Notice that because of its SH-character, by no means could it be associated to the HAS measurements matching so well our LDA points (see Fig. 6.4).

6.4.3 c(2x2)-CO/Cu(001)

In our calculations, we find that the force constants coupling C-O, C-Cu, O-Cu, C-C, and O-O are stiffer in LDA than in GGA. In particular, those between C-C (between neighboring molecules) and C-Cu are, respectively, 20 and 40% larger. The force constants given by both LDA and GGA reflect that the *in-plane* interactions between neighboring molecules are much smaller than the *out-of-plane* ones, which arise from the perturbation of the C-O bond length. This fact is reflected in the strong (weak) dispersion of the C-O stretch mode (all other modes), as shown later (see Figs. 6.6 and 6.7). As regards the substrate, LDA indicates that the chemisorption of CO has little impact on the force constants mediating the interaction between *bare* atoms and their first NN in the second layer, whereas those mediating the interaction between *covered* atoms and their first NN in the second layer, YY, YZ, ZY, and ZZ, are mildly softened by 12, 12, 24 and 6%, respectively, as compared to the clean surface. GGA, in contrast, finds that CO chemisorption modifies the force constants of not only *covered* atoms but also of *bare* ones. Naturally, the major effect occurs on *covered* atoms, whose corresponding force constants are softened by 40, 20, 38, and 14%, respectively, while those of *bare* atoms are stiffened by 14, 14, 14, and 9%, respectively. Unlike *interlayer* force constants, *intralayer* force constants between *bare* atoms and their first NN *covered*

Table 6.6: *Frequencies (in meV) at* Γ *of the adsorbate and surface vibrational modes of* $c(2x2) - CO/Cu(001)$.

	Theory								Exp.
	LDA					GGA			HAS IRRAS
	This work[1]	This work[3]	Ref.[175]2	Ref.[341]	Ref.[191]3,4	This work[1]	Ref.[341]	Ref.[191]3,4	Refs.[16] Ref.[162]
ν_1	265.6	268.1	261.7	259.8	268.8	257.7	251.2	262.6	258.5
ν_2	54.6	45.9	52.9	54.2	49.6	47.4	47.2	44.4	42.8
ν_3	34.4	-	35.0	-	-	33.3	-	-	35.6
ν_4	2.1	-	1.7[5]	-	-	3.7	-	-	3.9
S_1	15.8	-	16.0	-	-	14.2	-	-	15.2
L_1	22.6	-	-	-	-	20.2	-	-	-
S_2	23.1	-	23.2	-	-	20.4	-	-	-

[1]DFPT. [2]DFT-FD. [3]DFT-FD-FS. [4]Substrate not relaxed. [5]3.4 meV with anharmonic correction.

atoms are barely altered by CO chemisorption. Namely, they are ∼5(GGA) or ∼8%(LDA) stiffer than would be if CO were not present. Tables 6.6 and 6.7 summarize the frequencies obtained at Γ and X, respectively, and compare them with those found in experiment and former studies, when available. The characterization of the vibrational modes displayed by CO and the Cu(001) substrate is presented below.

CO modes

(a) Dispersion of the C-O internal stretch mode (ν_1): LDA and GGA find that the C-O stretch mode disperses inside the SBZ (see Figs. 6.6 and 6.7) by ∼10 meV at X, as noted from Table 6.7. No contribution from the substrate is observed, as can be expected from the frequency range in which ν_1 lies. At Γ, small differences are found in the calculated frequencies depending on whether LDA or GGA is used, whether the FD or the DFPT method is applied, and whether the substrate is frozen (FS) or not. The agreement with experiment is in general reasonable.

(b) Dispersion of the Cu-CO stretch mode (ν_2): As seen in Figs. 6.6 and 6.7, our calculations show that the CO-substrate stretch mode disperses at most by ∼0.4 meV over the

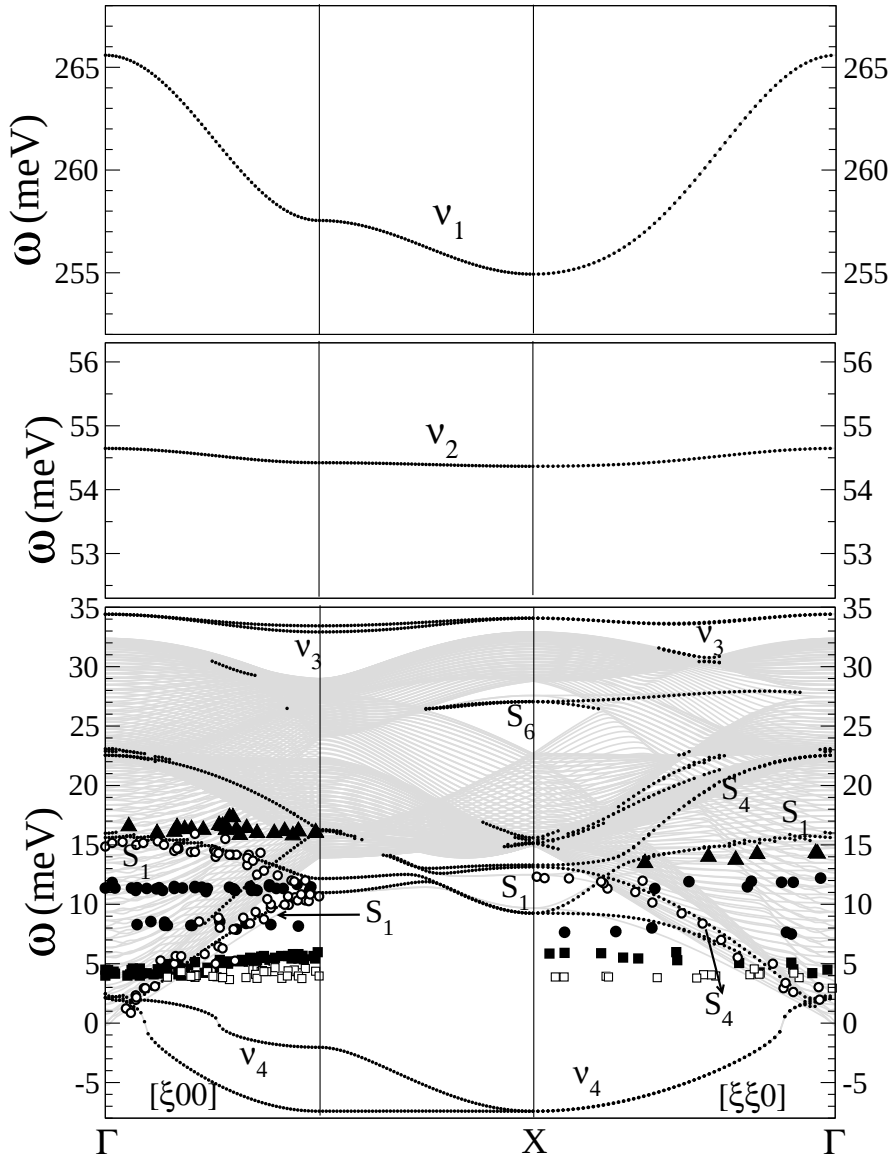

Figure 6.6: *LDA phonon dispersion of c(2x2)-CO/Cu(100), modelled by a Cu 50-layer slab. Filled circles denote theoretical surface modes. Experimental data are taken from Ref.*[16]*: Filled circles and triangles were associated with multi-phonon processes. Open circles correspond to the substrate Rayleigh wave. Squares were associated with the FT mode of CO on the perfect c(2x2) structure (filled) and on defects in the adlayer at lower coverage (open).*

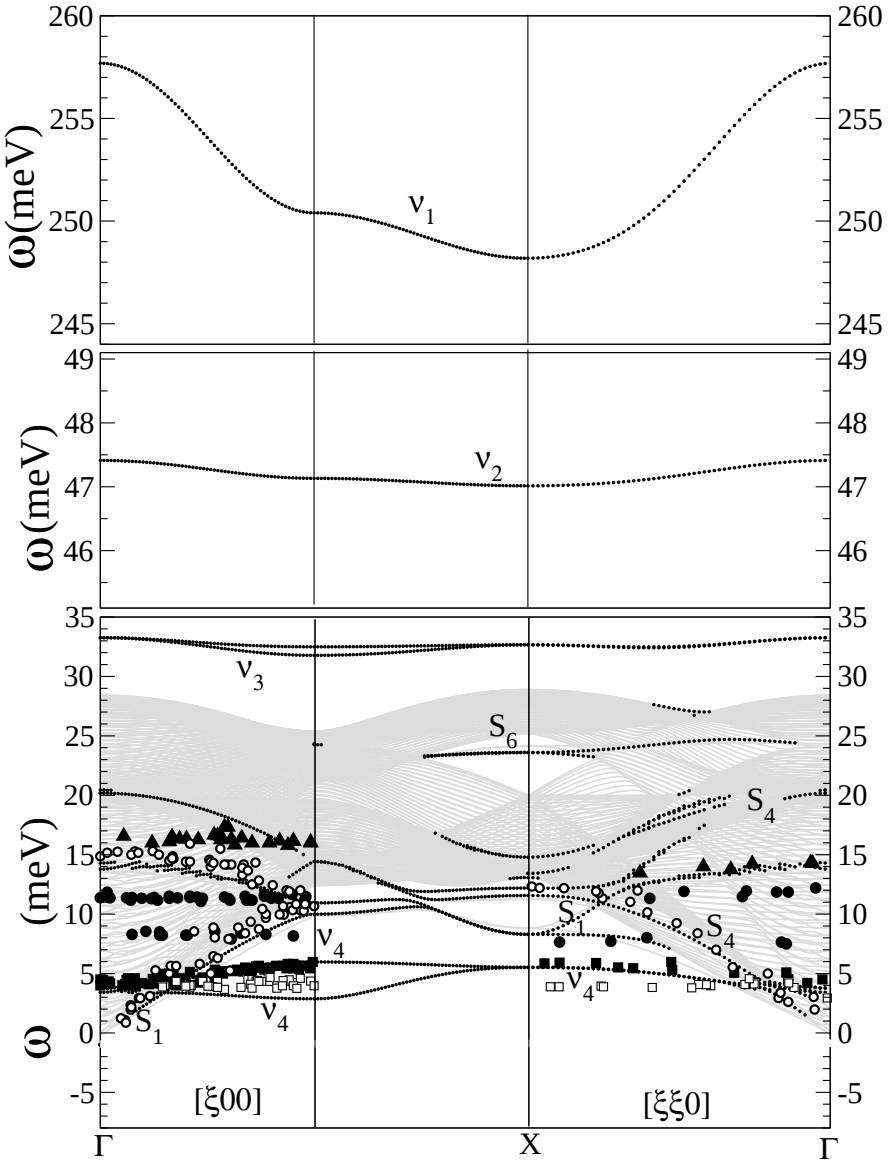

Figure 6.7: *GGA phonon dispersion of c(2x2)-CO/Cu(100), modelled by a Cu 50-layer slab. Filled circles denote theoretical surface modes. Experimental data are taken from Ref.*[16]*: Filled circles and triangles were associated with multi-phonon processes. Open circles correspond to the substrate Rayleigh wave. Squares were associated with the FT mode of CO on the perfect c(2x2) structure (filled) and on defects in the adlayer at lower coverage (open).*

Table 6.7: *Frequencies (in meV) at X of the adsorbate and surface vibrational modes of c(2x2)-CO/Cu(001).*

	Theory		Experiment
	LDA	GGA	HAS
	This work	This work	Ref.[16]
ν_1	254.9	248.2	-
ν_2	54.4	47.0	-
ν_3	34.1	32.7	-
ν_4	-7.4	5.5	5.8
S_1	9.3	8.3	-
S_4	13.1	11.6	12.3
	13.3	12.2	
S_5	15.2	13.1	-
	15.6	14.8	
S_6	27.1	23.6	-

sampled region of the SBZ, in both LDA and GGA. It is found to involve an additional C-O stretching of the C-O bond and to be coupled to an out-of-phase vibration of the Cu atom, which carries ∼33% of the amplitude. LDA, however, predicts ν_2 ∼12 meV higher than the experimental value, while GGA finds it to be only ∼5 meV higher, as summarized in Table 6.6.

(c) Frustrated Rotation of CO (ν_3): As seen in Table 6.6, the experimental value of ν_3 at Γ is well reproduced by both LDA and GGA. At Γ, LDA and GGA agree that the contribution of the substrate to the vibrational amplitude reaches only ∼3%, while those of C and O are ∼75 and ∼21%, respectively. Close to X, at which the substrate contribution is maximal, the first and second layers contribute no more than 7%. Figs. 6.6 and 6.7 show that the FT mode is nearly dispersionless but splits visibly along the edge of the SBZ and along the $\overline{\Sigma}$ direction The maximum splitting reaches ∼0.7 meV at the zone boundary. The branch with lowest energy has shear horizontal (SH) polarization (displacement perpendicular to propagation direction).

(d) Frustrated Translation of CO (ν_4): Significant differences are seen in Figs. 6.6 and 6.7 between LDA and GGA in relation to the dispersion of the FT mode. It is apparently

well described at Γ by LDA[175] because it estimates ν_4 only ∼2 meV below the experimental value. Nonetheless, it is unstable almost everywhere outside Γ. GGA, on the other hand, is able to reproduce ν_4 in excellent agreement with the experimental assessment, as shown in Table 6.7. GGA presents no instabilities, and shows remarkable agreement with the HAS data set, indicating stability of the c(2x2) overlayer (See Fig. 6.7).[16] Bagus and Wöll (private communication of Ref.[167]) have performed cluster calculations and found that, opposite to the FR mode, the amplitude of O in the FT mode is larger than that of C by 60%. By inspection of the displacement vectors (in GGA) along the main polarization, we observe that the amplitude of O at Γ is about two times larger than that of C. Considering the total amplitude weight of molecule, as we have been doing so far, C and O contribute ∼20 and ∼80% (all along the sampled SBZ), respectively, which is indeed opposite to the FR mode.

At Γ, the FT mode perturbs the Cu-C bond length but not so the CO-CO bond length. Outside Γ, nevertheless, particularly at zone boundaries, CO-CO bond lengths are perturbed and the effects of the interaction among molecules come about. The longitudinal (L-) polarized (atomic displacement along the propagation direction) branch and the SH- branch of the FT mode split along $\overline{\Sigma}$ and along the edge of the SBZ, but not along $\overline{\Delta}$. Fig. 6.8 shows the displacement patterns of the L- and SH- modes at the zone boundaries to illustrate that such is the case since the displacement pattern of the FT in both polarizations is equivalent along $\overline{\Delta}$, whereas, along $\overline{\Sigma}$, the L-mode involves CO-rows vibrating one against the other and the SH-mode involves the shearing vibration of CO-rows. The displacements occurred in the L- and SH-modes along $\overline{\Sigma}$, thus, set different perturbations to the intermolecular distance. Notice that, for example, each molecule has four CO first NN. At the zone boundary along $\overline{\Sigma}$, in the L-mode, two of the corresponding bond-lengths do not change, one distends, and the other one contracts; while, in the SH-mode, two of these do not change and the other two distend. Interestingly, GGA indicates that the SH-branch has lower frequency than the L-branch and even than the frequency at Γ. Both branches result negative in LDA, as mentioned before; however, it may be worth to mention that the LDA L-branch has lower

energy. Close to the zone boundaries, the amplitude weight of the substrate in the FT mode is small (∼3%) given that its frequency falls below the bulk band. However, both LDA and GGA find that the FT mode couples to the substrate in the vicinity of Γ in the sense that bulk modes whose frequency is close to ν_4 include a contribution from a FT motion of the molecule. In fact, the amplitude weight of CO in these mode, as a function of their frequency, shows a Gaussian-like behavior (which half-band width is ∼0.12 meV) and so ν_4 has been taken as the frequency that peaks this function. Notice, however, that such harmonic resonant coupling is manifested only by the symmetric broadening of the mode since ν_4 itself is independent of the dynamics of the substrate. Namely, fixing the substrate (by artificially increasing the mass of Cu atoms) eliminates the broadening but changes ν_4 negligibly. The L-branch of the FT mode and the RW do hybridize at their crossing point giving rise to two L-polarized FT modes that are split by ∼0.4 meV and show different degrees of contribution from the vertical vibration of the surface.

Substrate modes along $\overline{\Sigma}$

Notice that modes proper to clean Cu(001) from the zone boundary of the c(2x2) SBZ to M are *back-folded* along Σ from the zone boundary of the c(2x2) SBZ to Γ (see Fig. 6.1).

(a) S_1. The RW, S_1, increases its frequency along Σ, until it reaches the zone boundary and matches, except for a 1 meV gap, the *back-folded* S_1, which has its maximum at Γ and decreases its frequency along Σ. The gap between the RW branches at the zone boundary may be explained by the fact that the higher (lower) branch corresponds to a mode whose amplitude weight is primarily vertical in *bare* atoms (*covered* atoms dragging the molecule to some extent), involving also a small contribution from the L-polarized vibration of *covered* (*bare*) atoms. In fact, it matches that of the RW of the clean surface, suggesting that *bare* atoms are not affected. Nevertheless, we will see that this is not the case and mass overloading does not alone softens the RW. At Γ, where the softening with respect to the clean surface is maximal, the *back-folded* S_1 mode corresponds to an *out-of-phase* vibration between *covered* and *bare* atoms. In this case, the contribution of *bare* atoms is 50% larger

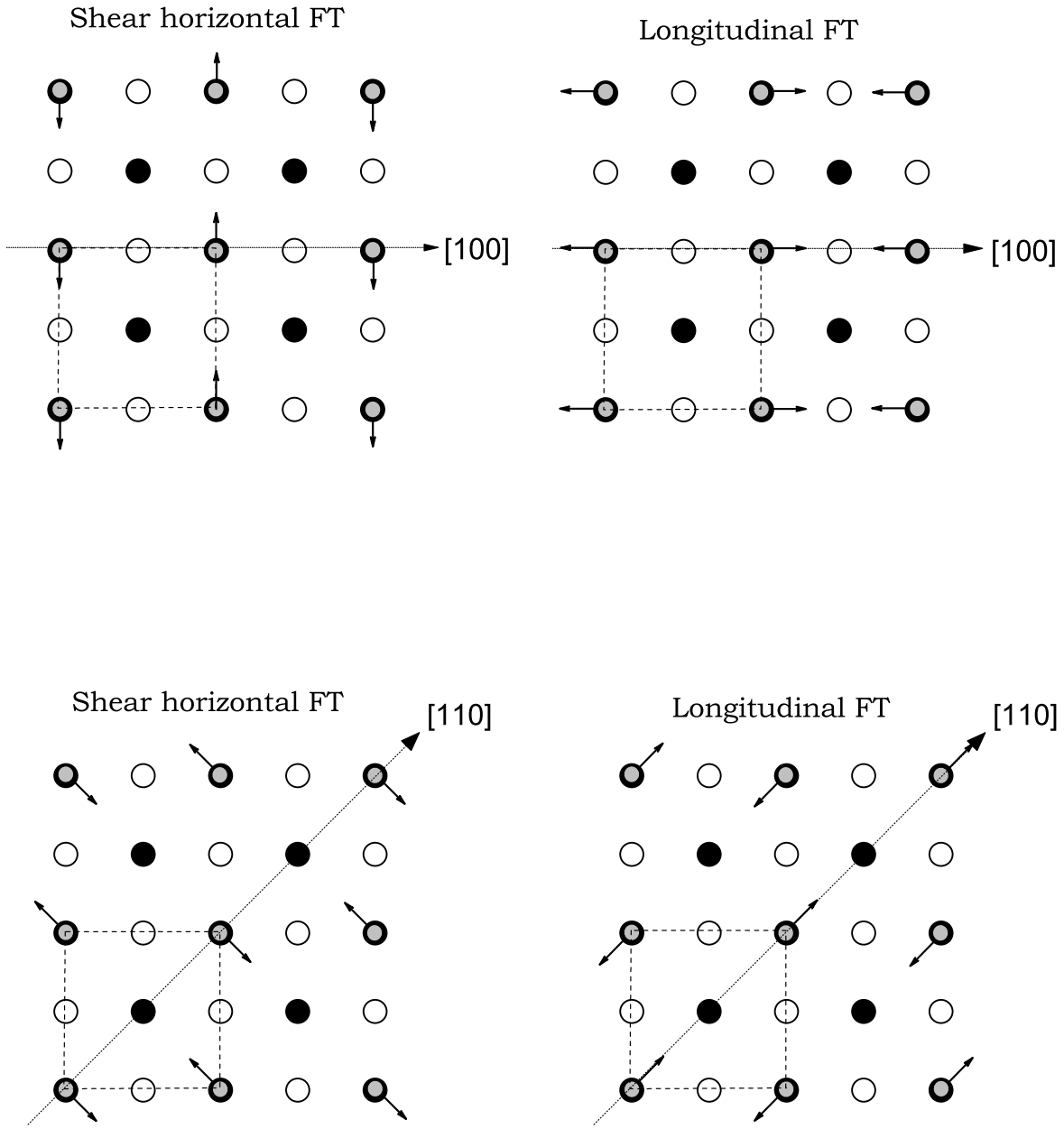

Figure 6.8: *Displacement patterns of the FT. Filled and open circles represent first and second layer atoms, respectively. Small grey circles symbolize CO: (upper-left) SH-mode at the zone boundary of the c(2x2) SBZ along* $\overline{\Sigma}$*. (upper-right) L-mode at the zone boundary of the c(2x2) SBZ along* $\overline{\Sigma}$*. (lower-left) SH-mode at X (along* $\overline{\Delta}$*). (lower-right) L-mode at X (along* $\overline{\Delta}$*).*

than that of *covered* atoms and CO molecules are dragged parallel to the latter. Close to Γ, S_1 is broadened and appears as a finite-width resonance whose maximum amplitude weight can be as low as 6% in the first two layers, yet detectable by HAS. We observe that, although LDA and GGA predict different effects of CO chemisorption on the force constants of the first layer, in both cases S_1 softens by ∼16% at Γ, overestimating in fact HAS measurements (∼10%).

(b) S_2. This mode only appears *back-folded* from M to Γ. It steeply disappears outside Γ, as soon as it immerses into the bulk band. At Γ, S_2 is well inside the bulk band even though no coupling to bulk modes is observed. In fact, it appears to be more localized in the chemisorbed surface than in the clean surface (at M).

(c) L_1 *and the corresponding SH-branch.* In the clean surface these modes arise close to the zone boundary so that in the chemisorbed surface they appear mainly as *back-folded* modes. At Γ the *back-folded* L_1 and its degenerate SH pair stiffen very slightly (1.3 and 0.5% in LDA and GGA, respectively). They are not totally localized in the first or second layers but exhibit a significant contribution of ∼60% to the amplitude weight from deeper layers. Outside Γ, the *back-folded* L_1 disappears rapidly while the *back-folded* SH mode disperses and becomes more localized towards the zone boundary. There, it matches the branch that originally appears in the clean surface but vanishes rapidly back to Γ.

Substrate modes along $\overline{\Delta}$

Modes proper to the clean surface along $\overline{Y}$ are back-folded to $\overline{\Delta}$ in the c(2x2) SBZ (see Fig. 6.1 (b)).

(a) S_1 *and the corresponding L-branch.* S_1 is totally localized in the first layer and the CO overlayer. The latter vibrates *in-phase* with *covered* atoms but with much smaller amplitude. S_1 softens at X by ∼5, and ∼8% in LDA and GGA, respectively (see Table 6.7). LDA and GGA find also a L-polarized degenerate pair of S_1 at X. Such mode corresponds to S_1 along $\overline{Y}$, which is *back-folded* along $\overline{\Delta}$ in the chemisorbed SBZ. The degeneracy is broken outside X. The *back-folded* S_1 remains L-polarized as it goes across $\overline{\Delta}$ towards Γ up

to the crossing point with the RW, where it becomes V-polarized. It is slightly softened around the zone boundary, just as much as S_1 at X; nonetheless, the softening becomes stronger, similar to that of the RW, right after crossing the RW and the transitioning to V-polarization.

(b) S_4. This is the RW along $\overline{\Delta}$. It is mostly localized (∼60-70%) in the first layer and, to lesser degree, in the molecule. At X, S_4 splits by ∼0.2 and ∼0.6 meV in LDA and GGA, respectively. Regarding the first layer, only *covered* (*bare*) atoms contribute to the mode with lower (higher) energy. Notice that in this case, both branches are softened with respect to the clean surface at X by 8.2 and 11.0%, in LDA, and by 9.6 and 15.0%, in GGA, while HAS measurements[16] find ∼8.2% softening. We also obtain the *back-folded* S_4, originally arising along $\overline{Y}$ in the clean surface. It is V-polarized close to the zone boundary. In GGA, it broadens and becomes a resonance as soon as it immerses into the bulk band, reappearing as a surface mode close to Γ with mixed L- and SH-polarization. In LDA, S_4 remains highly localized in the surface and changes smoothly to L-polarization.

(c) S_5. This mode is strongly localized in the second layer with mixed SH- and L-polarization. It rapidly becomes a resonance along $\overline{\Delta}$ towards Γ. At X, S_5 splits by 0.4 and 1.7 meV in LDA and GGA, respectively (see Table∼6.7). LDA shows that the lower branch softens by 7.1% while the other - bearing ∼25% contribution from deeper layers - does not change at all. In GGA both branches are totally localized in the second layer. One of these softens by 8.4% and the other stiffens by 3.5%. LDA presents also a resonance at 15.4 meV.

(d) S_6. This mode is found together with a degenerate SH pair at X. Note in Figs. 6.6 and 6.7 that the degeneracy is broken inside the SBZ. LDA and GGA find that S_6 - and the SH-branch - remain nearly dispersionless and involve an additional V- second layer vibration, as occurs in the clean surface. These modes are, incidentally, more localized in the first layer of the chemisorbed surface than in that of Cu(001). At the right end of the bulk band gap (see Figs. 6.6 and 6.7), S_6 slightly softens and becomes a resonance while it penetrates the bulk band. The SH branch, in contrast, extends well inside the bulk band

and becomes more localized at the top two layers. According to GGA, S_6 softens at X by 2.0%, while LDA predicts no softening.

6.5 Summary

First-principles calculations of the structure and lattice dynamics of bulk Cu, Cu(001) and c(2x2)-CO/Cu(100) surfaces have been presented. The structure and lattice dynamics of bulk Cu and Cu(001) are found to be in good agreement with earlier results. In both cases, however, GGA is in better agreement with experiment than LDA. For the chemisorbed surface, significant differences arise between both approximations concerning structure and lattice dynamics, as summarized below.

We find that CO-modes are influenced by molecule-substrate and molecule-molecule interactions. The C-O stretch mode disperses by ∼10 meV along $\overline{\Delta}$, indicative of CO-CO interactions. Inspection of the displacement vectors in our DFPT calculations confirms that the C-O stretch mode is independent of the dynamics of the substrate. The value of ν_1 is found to be in good agreement with experiment, regardless of the approximation used for the exchange correlation functional.

Nevertheless, the results obtained for ν_2, ν_4, and the structure and vibrational frequencies of the substrate depend on whether LDA or GGA is used. Our results and those of Ref.[34] suggest that this is related to the inability of LDA to describe the Cu-C bond (wrong adsorption site and overestimation of the binding energy[34]). Surprisingly, the value of ν_2 provided by LDA FD-FS calculations is closer to the experimental one than that by LDA-DFPT. It has been suggested the DFPT result may be corrected by using an appropriate choice of coordinates in the phonon calculation.[175] The reason, however, is apparently the cancellation of errors, since FD-FS calculations neglect the strong contribution of *covered* Cu atoms. We find that omission of the dynamics of the substrate lowers ν_2 by ∼8 meV in DFPT calculations. It is thus not surprising that the stiffening due to the overestimation by LDA of the C-Cu bond strength can be counterbalanced by the softening resulting from a

frozen substrate. Along the same lines, a much better estimation of ν_2 can be expected from DFPT GGA calculations since the adsorption site, the chemisorption energy, and d_{Cu-C} are in good agreement with experiment.

In this work, the unsuitably of LDA to describe this chemisorbed surface is evident from the instability of the FT mode that it produces almost everywhere inside the SBZ. GGA, in contrast, is able to reproduce the dispersion of the FT mode as measured by HAS.[16] More importantly, the close agreement between our GGA calculations and HAS measurements indicates that the harmonic approximation is apt to describe the Cu-CO bond, contrary to the conclusion drawn from LDA results.[175] Examination of the real space force constant matrices indicates that lateral interactions among CO molecules exist as well. They are at least 10 times smaller than those due to the perturbation to the C-O bond length, but enough to make the FT and the FR (to a lesser degree) modes to disperse and split their SH- and L- branches, which otherwise would be degenerate. Interestingly, the frequency of the SH-branch at X- which displacement pattern distends half of the CO-CO first NN bond-lengths - is 3 meV lower than that of the L-branch and than the frequency at Γ. Clearly, the SH-branch cannot explain the low branch observed experimentally, which is rather attributed to defects in the overlayer.[16] Finally, the frequency range of the FT mode allows for coupling to the substrate over a significant region around Γ. Such harmonic resonant coupling is manifested only through the broadening of the spectral line of the FT mode, but its frequency (the center of the distribution) is found to be independent of the dynamics of the substrate.

LDA displays a mild effect of CO chemisorption on the relaxation and force constants of the surface. Even so, the *back-folded* RW is significantly softened in such a way that LDA is able to closely reproduce HAS measurements. This feature is rather unexpected in consideration of the poor ability of LDA to describe the Cu-CO interaction and its less successful description of the acoustic modes of bulk Cu and the RW in Cu(001). GGA, on the other hand, finds that CO chemisorption significantly perturbs the structure and the

first NN force constants of the surface layer atoms. Softening of the RW is well reproduced; only slightly overestimated by ∼1 meV at Γ. It is surprising that, while LDA and GGA differ considerably in the response of the substrate to CO chemisorption, the actual percentage softening of the *back-folded* RW with respect to the clean surface is comparable. We find that softening of the RW along Σ and Δ is not necessarily connected with the vibration of *covered* atoms, which indicates that mass overloading cannot alone account for it. Were that the case, all surface modes involving the first layer would be softer. On the contrary, L_1, for example, does not soften, notwithstanding the leading involvement of first layer atoms. In fact, it slightly stiffens, perhaps because of the little hardening of intralayer force constants of the first layer. Moreover, softening/stiffening of the various modes is selective for layer, direction, and polarization, indicative of different modifications in Cu force constants. For example, S_2, V-mode in the second layer, stiffens and S_1 slightly softens (along Δ) while it is L-polarized - where it is totally localized in the first layer - but undergoes a stronger softening after it becomes V-polarized - where deeper layers are involved. Softening of the RW seems thus due not only to the mass of CO but also to longer range interactions, i.e. beyond first NN and involving deeper layers, that subdue differences in the local bonding of surface atoms and result in an overall softening of the RW, which is sometimes independent on whether *covered* or *bare* atoms are primarily involved.

We call attention to the folding of $\overline{Y}$ (of the 1x1 SBZ) onto Δ (of the c(2x2) SBZ), which displays *back-folded* modes along the latter. For example, *back-folded* S_1 and *back-folded* S_4 are found along Δ with changed polarization that may make them observable. In particular, S_1 acquires V-polarization close to Γ and L-polarization close to X. Ellis et al. observed some HAS peaks precisely at the region where *back-folded* S_1 is V-polarized. Without considering that $\overline{Y}$ is *back-folded* onto Δ, those peaks were associated to multi-phonon excitation bands.[16] Nevertheless, the excellent fit of their measurements to our *back-folded* S_1 suggests that this mode was observed rather than multi-phonon excitation bands. Perhaps more importantly, *back-folded* S_1 becomes as well discernible to scattering

spectroscopy techniques close to the zone boundary since it is changed from SH- (along $\overline{Y}$ of the (1x1) SBZ) to L- polarization (along $\overline{\Delta}$ of the c(2x2) SBZ) in that region. It means that the frequency of S_1 (SH-polarized in Cu(001)) can be indirectly measured at X via *back-folded* S_1. We believe that three of the *2T overtones*[16] observed by Ellis et al. along $\overline{\Delta}$ may also correspond to *back-folded* S_1, in the region where is L-polarized. The fact that S_1 has been predicted (along $\overline{\Delta}$) by theory since early studies of short-range interacting fcc structures,[197] and remained inaccessible to experiments due to its polarization, renders its detection and confirmation of the predicted frequency as an additional worthy verification of the success of DFT, the linear response theory, and the slab method in describing the fcc(001) surfaces.

Chapter 7

Conclusions

This thesis has presented our results of the geometric, electronic, vibrational and magnetic properties of several nanostructured systems. From the study of interparticle dipolar interactions on three-dimensional and two dimensional ensembles of magnets, we have solved the Landau-Lifshitz equation for 3D and 2D cubic lattices of nanomagnets, subject to dipole-dipole interactions and spin anisotropy. We find that a classical approach - applied to magnets in square arrays - produces stepped hysteresis curves, suggesting these do not have necessarily a quantum origin. The smaller the damping constant, the stronger the maximum induction required to produce hysteresis. The shape of the hysteresis loops also depends on the damping constant. We find further that the system magnetizes and demagnetizes at decreasing magnetic field strengths with decreasing sweep rates, resulting in smaller hysteresis loops. Variations of the lattice constant within realistic values in the show that the dipolar interaction plays an important role in the magnetic hysteresis by controlling the relaxation process. The temperature dependencies of the damping constant and of the magnetization are presented and discussed with regard to recent experimental data on nanomagnets. Magnetic anisotropy enhances the size of the hysteresis loops for external fields parallel to the anisotropy axis, but decreases it for perpendicular external fields. We show that its hysteretic behavior is only weakly dependent on the shape-anisotropy field and the sweep rate, but depends sensitively upon the dipolar interactions. Although in 3D systems, dipole-dipole interactions generally diminish the hysteresis, in two-dimensional

systems, they strongly enhance it.[14] We found that when qualitative changes in the $M(B)$ curves do not occur with decreasing lattice constants, the area of the hysteresis increases correspondingly. However, we also showed that at least one critical a value $a*$ can exist, at which qualitative changes in the $M(B)$ hysteresis curves appear, accompanied by an abrupt decrease in the hysteresis loop area.[95] With this understanding in hand, we were able to reconcile the apparent discrepancies between two earlier theoretical studies.[85,94,95] In the near future, although still using an oversimplified model of SMM's, our target in this subject continues towards the implementation of *ab initio* spin-polarized DFT calculations that allow us to obtain parameter-free results which are, as always, desirable.

Indeed, based on the fact that the functionality of *ab initio* DFT calculations is, up to the use and choice of a pseudopotential,[7] independent of the chemical environment, we have analyzed the $Ag_{27}Cu_7$ nanoalloy and bulk alloys, and draw the properties of alloyed structures in general. We conclude that size effects in single-element systems take place mainly due to the local coordination of the atoms which may differ considerably from that in the bulk environment. In such cases, along with structural changes (as those occurring in nanoclusters), bond lengths are expected to change from bulk bond lengths typically by a few percent. In binary system, however, we have found that the perspective is different since the strength of the binary bond, compared with that of the single-element bonds, is a decisive factor. First of all, it seems that binary bulk systems are present in nature either as ordered or amorphous alloys, or as segregated systems, depending on the strength of the binary bond as compared to the strength of the two single-element bonds, and depending as well on the difference between the optimum lengths of the two strongest bonds. The strength of the binary bond in a given ordered structure must not be weaker than the average of the two single elements bonds in bulk in order for the alloy to have a negative heat of formation. In the case of $Au-Cu$ alloys, for example, the cohesive energy of Cu_3Au is higher than that of bulk Cu and Au. In addition, the difference between the optimum bond-lengths that make possible for the two strongest bonds to exist may be required to be as small as

possible; otherwise, amorphous phases might be favored. In the nano-scale, however, for few tens of atoms and when the bulk structure is vanished, the main difference is that the later condition may be flexible. Namely, one can take advantage of the difference between the optimum lengths of the strongest bonds while playing with core-shell or layered structures, for example. Indeed, we have seen that one key factor for the relative stability of $Ag_{27}Cu_7$ is the freedom of $Ag-Cu$ bonds to be optimized. Contrastingly, in $L1_2$ $Ag-Cu$ alloys, the $Ag-Cu$ bonds play a minor role because the lattice parameter dictated by the Ag content in the ordered lattices strongly weakens the binary bond and never patches up for the cost of breaking $Ag-Ag$ bonds and, above all, $Cu-Cu$ bonds. Nevertheless, it is surprising that the cohesive energy of any of these two alloys is larger than that of bulk Ag. That is in fact the first hint indicating that $Ag-Cu$ bonds are stronger than $Ag-Ag$ bonds, and that $Cu-Cu$ bonds are stronger than $Ag-Cu$ bonds. It suggests thus an importance hierarchy of bonds as follows: $\{Cu-Cu$, $Cu-Ag$, and $Ag-Ag\}$. We noticed, however, that the actual strength of the bonds in a particular structure is simply the signature of the relaxed geometry; the equilibrium positions may or may not let the strongest bonds to realize. In $Ag_{27}Cu_7$, for example, the two-dimensional charge density plots suggest that $Ag-Cu$ bonds are stronger than $Cu-Cu$ bonds, while the trend in the formation energy of the nanoalloy family suggests the opposite. We find moreover that few Cu atoms immersed in Ag can create bonds stronger than those in bulk Cu. It is the stability what ultimately is contingent on whether the resulting geometry allows for the existence and maximization of the bonds that must be favored according to the hierarchy natural of the species. The best illustration of this assertion is the large bond-lengths found in bulk Ag_3Cu and Cu_3Ag , which stretch the $Cu-Cu$ and $Ag-Cu$ bonds by ~ 0.3 Å, with respect to those found in bulk Cu and in the $Ag_{27}Cu_7$ nanoalloy. In brief, it seems that there is a precise ladder order of maximum bond strengths and optimum bond lengths between atoms of the same and different species which may together unequivocally predict the most stable configuration and composition of a given system. Among noble metals, (given the heats of formation

and calculations of the dimmer binding energy and bond-length, not presented here for the sake of clarity), we conclude that for bond strength it is as follows: $\{Au-Cu$, $Au-Au$, $Au-Ag$, $Cu-Cu$, $Ag-Cu$, and $Ag-Ag\}$, while for the shortest optimum bond lengths it is: $\{Cu-Cu$, $Au-Cu$, $Ag-Cu$, $Au-Au$, $Au-Ag$, and $Ag-Ag\}$. Therefore, since the conclusions along this paper have been motivated by earlier studies of noble metal and $Ag-Ru$ alloys, and our results apparently do not depend on intrinsic properties of Ag or Cu other than the position of the d-band, it is interesting to investigate whether any binary system (at least non-magnetic) would obey a similar hierarchy that applies to any atomic environment, say bulk alloys, deposited surfaces, nanoalloys, etc. The stability of $Cu-Au$ alloys, for example, emerges naturally, while the conclusion of Darby et al.[97] indicating that in $Cu-Au$ nanoalloys is crucial to favor $Cu-Au$ and $Au-Au$ bonds to minimize the energy, properly fits into the proposed hierarchy.

In terms of the stability of $Ag_{27}Cu_7$ nanoalloy, the energy cost of breaking bulk bonds is perhaps an aspect that should not be considered for its feasibility, since it is not expected to occur by simply melting bulk Ag and Cu. The stability of arrays of $Ag_{27}Cu_7$ nanoalloys against the opposite process - dissociation of a hypothetical $Ag_{27}Cu_7$ array into the bulk segregated phase - represents thus the main concern regarding possible applications. We propose that, well down the melting temperature of $Ag_{27}Cu_7$,[15] the stability of the eventual core-shell nanoalloys in an array against decay into the bulk segregated phase also relies on the bond strength hierarchy. For a given array of such core-shell nanoalloys, the immediate interaction that occurs among nanoalloys is shell-shell interaction, that is, $Ag-Ag$ interactions, which has been found to be the weakest one. We can thus expect the cluster to be stable against single element bulk decomposition with no need to isolate them in matrices or coating surfactants[110] since core(Cu)-shell(Ag) interactions are much stronger that shell(Ag)-shell(Ag) interactions.

Future work will focus on the substitution of Ag atoms by Au atoms in the D_{5h} structure proposed in Ref.[15]. We expect $Au_{27}Cu_7$ nanoalloys to have enhanced stability because the

core-shell structure of $Ag_{27}Cu_7$ optimizes the binary bond - the strongest one for $Cu-Au$ alloys - and keeps $Ag-Ag$ in the typical bulk bond lengths, which in the case of $Au_{27}Cu_7$ would certainly be a very favorable since the $Au-Au$ bond is next in strength after the $Au-Cu$ bond. In addition, the energy distribution of the electronic states of Au and the short $Cu-Au$ bond-lengths furnished by the D_{5h}could provide better hybridization between $Cu-Au$ d-states than that of $Cu-Ag$ in $Ag_{27}Cu_7$ and that of between $Cu-Au$ d-states in ordered $Au-Cu$ alloys. We acknowledge that for larger core-shell nanocluster, say few nanometers, the bonds strength hierarchy might open the possibility of Au interpenetration and the consequent amorphization of the nanocluster. Nevertheless, that would imply a very unlikely simultaneous bond breaking of the two strongest and length optimized $Cu-Au$ (core-shell) and $Au-Au$ (intra-shell) bonds. Furthermore, experimental confirmation of the stability of 8-10 nm core-shell nanoparticles at room temperature evidence the low probability of such event.[199]

First principles calculations were also feasible and necessary to give one step further in the understanding of the enhanced reactivity of Pt-decorated Ru nanoparticles, which is relevant to the hydrogen economy. This project establishes the origination of an electric current based on the oxidation of hydrogen atoms. Such a process needs to be catalyzed in order to be suitable for technological applications, and while Pt atoms are known as the best catalyst for H-oxidation, traces of CO - always present in hydrogen reservoirs - poison their catalytic properties and vanish the outcoming current. At present Pt-Ru alloys are commercially-used catalysts exhibiting CO-tolerance over pure Pt. Recently, Ru nanoparticles decorated with small amounts of Pt were found capable to maintain the electric current for a considerable longer time period than commercial alloys. In order to understand the factors that render enhanced CO-tolerance to Pt-decorated Ru nanoparticles, we have first studied Pt deposition on $Ru(0001)$ and a Ru nanoparticle model. We have concluded that, unlike the Ru surface, Ru nanoparticles compel Pt atoms to remain scattered on their facets provided that, although Pt tend to coalesce (as in the case of $Ru(0001)$), their diffusivity

through the edges of the *Ru* nanoparticles is strikingly reduced as they grow larger.

Finally, we have addressed the vibrational dynamics of c(2x2)-CO on Cu(001) from *ab initio* methods to account for some of the interrogatives around this model system that have persisted after many years of research. Our GGA calculation has been able reproduce Helium Atom Scattering (HAS) measurements for the dispersion of the *frustrated translation* (FT) mode of CO-molecules and show that it is a normal mode of the system. Our results thus point to the harmonic nature of the Cu-C bond, which exhibits zero-temperature quartic anharmonicity within LDA. We find instead that the spectral line of the FT is broadened by a harmonic resonant coupling of the substrate over a large region around the Γ point, which nevertheless does not influence the FT mode frequency, and that LDA is, in fact, incapable to describe the dynamics of c(2x2)-CO on Cu(001). In addition, due to the relatively weak binding energy of CO to the surface and the distance separating CO molecules at half monolayer coverage, it has been considered that the dynamics of chemisorbed CO molecules on Cu(001) is negligibly coupled to neighboring molecules and the substrate. Our results, however, establish that CO-modes are considerably influenced by molecule-substrate and/or molecule-molecule interactions.

Regarding the effect of CO molecules on the Cu substrate, we concluded that CO mass overloading of the surface atoms cannot alone account for the softening of the Rayleigh wave. Softening of the RW seems thus due also to the *long-range* effects of CO on the force constants of the substrate. Furthermore, we have obtained the dispersion of surface phonons matching HAS measurements inside the SBZ, which have been associated to multi-phonon excitation bands. Nevertheless, the excellent fit of their measurements to our calculated *back-folded* S_1 suggests that this mode was observed rather than multi-phonon excitation bands. Perhaps more importantly, we find that *back-folded* S_1 becomes as well discernible to scattering spectroscopy techniques close to the zone boundary since its polarization is changed from SH- to L- polarization upon folding on the c(2x2) SBZ. The frequency of S_1 (SH-polarized in Cu(001)) can hence be indirectly measured at X via *back-folded* S_1. The fact

that S_1 has been predicted (along $\overline{\Delta}$) by theory since early studies of short-range interacting fcc structures and remained inaccessible to experiments due to its polarization renders its detection and confirmation of the predicted frequency as an additional worthy verification of the success of DFT, the linear response theory, and the slab method in describing the fcc(001) surfaces. The following step towards the understanding of the dynamics of chemisorbed metallic surfaces, the rate of diffusion, desorption, and reaction, etc., is the extension of this work to other Cu surfaces and other noble and transition metals. Currently, we are pursuing a similar investigations of c(2x2)-CO-Ag(001).

Bibliography

[1] M. G. Schultz, T. D. Diehl, G. P. Brasseur, and W. Zittel, Science **302**, 624 (2003).

[2] Z. P. Liu, S. J. Jenkins, and D. A. King, Phys. Rev. Lett. **94**, 196102 (2005).

[3] F. Alber and P. Carloni, Protein Science **9**, 2535 (2000).

[4] W. G. Minarik, F. J. Ryerson, and E. B. Watson, Science **272**, 530 (1996).

[5] J. Tersoff, Phys. Rev. Lett. **56**, 632 (1986).

[6] G. J. Ackland and R. Thetford, Philosophical Magazine A **56**, 15 (1987).

[7] M. Payne, M. Teter, D. Allan, T. Arias, and J. Joannopoulos, Rev. Mod. Phys. **64**, 1045 (1992).

[8] J. Ho, F. C. Khanna, and B. C. Choi, Phys. Rev. B **70**, 172402 (2004).

[9] J. Ho, F. C. Khanna, and B. C. Choi, Phys. Rev. Lett. **92**, 097601 (2004).

[10] J. Sinova et al., Phys. Rev. B **69**, 085209 (2004).

[11] E. M. Lifshitz and L. P. Pitaevskii, *Course of Theoretical Physics Vol.5: Statistical Physics*, volume 5, Pergamon, New York, 1980.

[12] T. L. Gilbert, Trans. Mag. **40**, 3443 (2004).

[13] M. Elstner et al., Phys. Rev. B **58**, 7260 (1998).

[14] M. Alcántara Ortigoza, R. A. Klemm, and T. S. Rahman, Phys. Rev. B **72**, 174416 (2005).

[15] G. Rossi et al., Phys. Rev. Lett. **93**, 105503 (2004).

[16] J. Ellis, J. P. Toennies, and G. Witte, J. Chem. Phys. **102**, 5059 (1995).

[17] G. Petersson, Theor. Chem. Acc. **103**, 190 (2000).

[18] R. Wangsness and F. Bloch, Phys. Rev. **89**, 728 (1953).

[19] D. Fredkin and A. Ron, PRB **61**, 8654 (2000).

[20] J. D. Jackson, *Classical Electrodynamics*, volume 3rd Ed., New York: John Wiley & Sons, Inc., 1998.

[21] E. Merzbacher, *Quantum Mechanics*, volume 3rd Ed., New York: John Wiley & Sons, Inc., 1998.

[22] M. d'Aquino, *Nonlinear magnetization dynamics in thin-films and nanoparticles*, PhD thesis, Universit degli studi di Napoli "Federico II", 2004.

[23] H. Goldstein, *Classical Mechanics*, volume 2nd Ed., Addison Wesley Publishing Company Inc., 1981.

[24] P. Anderson, Phys. Rev. **88**, 1214 (1952).

[25] J. Kohanoff and N. I. Gidopoulos, *Handbook of Molecular Physics and Quantum Chemistry*, volume 1st Ed., Chichester: John Wiley & Sons, Ltd., 2003.

[26] S. Baroni, S. de Gironcoli, and A. D. Corso, Rev. Mod. Phys. **73**, 515 (2001).

[27] D. H. Kobe, Phys. Rev. **188**, 1583 (1969).

[28] N. W. Ashcroft and N. D. Mermin, *Solid State Physics*, volume 1st Ed., Thomson Learning, Inc., 1976.

[29] P. Hohenberg and W. Kohn, Phys. Rev. **136**, B864 (1964).

[30] W. Kohn and L. J. Sham, Phys. Rev. **140**, A1133 (1965).

[31] P. O. Löwdin, Phys. Rev. **97**, 1474 (1955).

[32] J. P. Perdew and Y. Wang, Phys. Rev. B **45**, 13244 (1992).

[33] L. Hedin and B. I. Lundqvist, J. Phys. C **4**, 2064 (1971).

[34] F. Favot, A. D. Corso, and A. Baldereschi, J. Chem. Phys. **114**, 483 (2001).

[35] D. Langreth and M. Mehl, Phys. Rev. Lett. **47**, 446 (1981).

[36] J. P. Perdew and Y. Wang, Phys. Rev. B **45**, 13244 (1992).

[37] J. P. Perdew, S. Burke, and M. Ernzerhof, Phys. Rev. Lett. **77**, 3875 (1996).

[38] M. Alcántara Ortigoza, T. Rahman, R. Heid, and K. Bohnen, First-principles study of the lattice dynamics of CO-c(2x2) on $Ag(001)$, to be published.

[39] H. J. Monkhorst and J. P. Pack, Phys. Rev. B **13**, 5188 (1976).

[40] S. Hong, *First principles study of chemisorbed light gases on transition metal and transition metal oxides surfaces: structure, dynamics and reaction*, PhD thesis, Kansas State University, 2003.

[41] M. Methfessel and A. Paxton, Phys. Rev. B **40**, 3616 (1989).

[42] D. Newns, W. Donath, G. Martyna, M. Schabes, and B. Lengsfield, J. Appl. Phys. **95**, 3175 (2004).

[43] T. R. Koehler and D. R. Fredlin, IEEE Trans. Magn. **27**, 4763 (2001).

[44] W. Chen, D. R. Fredkin, , and T. R. Koehler, IEEE Trans. Magn. **29**, 2124 (1993).

[45] J. F. Smyth et al., J. Appl. Phys. **69**, 5262 (1991).

[46] D. R. Fredkin and T. R. Koehler, IEEE Trans. Magn. **24**, 2362 (1988).

[47] T. R. Koehler and D. R. Fredkin, IEEE Trans. Magn. **28**, 1239 (1992).

[48] D. R. Fredkin and T. R. Koehler, J. Appl. Phys. **63**, 3179 (1988).

[49] D. R. Fredkin and T. R. Koehler, J. Appl. Phys. **67**, 5544 (1990).

[50] T. R. Koehler, Physica B **233**, 302 (1997).

[51] T. R. Koehler and M. L. Williams, IEEE Trans. Magn. **31**, 2639 (1995).

[52] E. D. Boerner and H. N. Bertram, IEEE Trans. Magn. **33**, 3052 (1997).

[53] E. D. Boerner and H. N. Bertram, IEEE Trans. Magn. **34**, 1678 (1998).

[54] J. M. Deutsch, T. Mai, and O. Narayan, Phys. Rev. E **71**, 026120 (2005).

[55] K. Zhang and D. R. Fredkin, J. Appl. Phys. **87**, 4795 (2000).

[56] M. N. Leuenberger and D. Loss, Nature **410**, 789 (2001).

[57] F. Luis et al., Phys. Rev. B **55**, 11448 (1997).

[58] C. Sangregorio, T. Ohm, C. Paulsen, R. Sessoli, and D. Gatteschi, Phys. Rev. Lett. **78**, 4645 (1997).

[59] S. Hill et al., Phys. Rev. Lett **80**, 2453 (1998).

[60] S. M. J. Aubin, N. R. Dilley, M. B. Wemple, D. N. J. G. Christou, and Hendrickson, J. Am. Chem. Soc. **120**, 839 (1998).

[61] A. D. K. L. Bokacheva, Phys. Rev. Lett. **85**, 4803 (2000).

[62] T. Ohm, C. Sangregorio, and C. Paulsen, Europhys. J. B **6**, 595 (1998).

[63] J. A. A. J. Perenboom, J. S. Brooks, S. Hill, T. Hathaway, and N. S. Dalal, Phys. Rev. B **58**, 330 (1998).

[64] W. Wernsdorfer and R. Sessoli, Science **284**, 133 (1999).

[65] D. V. Efremov and R. A. Klemm, Phys. Rev. B **66**, 174427 (2002).

[66] R. Tiron, W. Wernsdorfer, D. Foguet-Albiol, N. Aliaga-Alcalde, and G. Christou, Phys. Rev. Lett. **91**, 227203 (2003).

[67] M. Soler, W. Wernsdorfer, K. Folting, M. Pink, and G. Christou, J. Am. Chem. Soc. **126**, 2156 (2004).

[68] D. H. W. Wernsdorfer, N. Aliaga Alcalde and G. Christou, Nature **416**, 406 (2002).

[69] J. V. Slageren.

[70] J. R. Friedman, M. P. Sarachik, J. Tejada, and R. Ziolo, Phys. Rev. Lett. **76**, 3830 (1996).

[71] L. Thomas et al., Nature **383**, 145 (1996).

[72] W. Wernsdorfer, S. Bhaduri, R. Tiron, D. N. Hendrickson, and G. Christou, J. Mag. Magn. Mat. **272**, 1109 (2004).

[73] W. Wernsdorfer, S. Bhaduri, R. Tiron, D. N. Hendrickson, and G. Christou, Phys. Rev. Lett **89**, 197201 (2002).

[74] H. D. Raedt, S. Miyashita, K. Michielsen, and M. Machida, PRB **70**, 064401 (2004).

[75] N. V. Prokof'ev and P. C. E. Stamp, Phys. Rev. Lett. **80**, 5794 (1998).

[76] J. F. Fernández and J. J. Alonso, Phys. Rev. Lett. **91**, 047202 (2003).

[77] I. S. Tupitsyn and P. C. E. Stamp, Phys. Rev. Lett. **92**, 119701 (2004).

[78] J. F. Fernández and J. J. Alonso, Phys. Rev. Lett. **92**, 119702 (2004).

[79] P. Santini et al., Phys. Rev. Lett. **94**, 077203 (2005).

[80] Y. Furukawa et al., Phys. Rev. B **64**, 094439 (2001).

[81] P. W. Anderson, Phys. Rev. **82**, 342 (1951).

[82] H. Margenau and W. W. Watson, Rev. Mod. Phys. **8**, 22 (1936).

[83] H. L. Huang, J. Phys. Chem **35**, 909 (1997).

[84] R. L. Stamps and R. E. Camley, Phys. Rev. B **60**, 11694 (1999).

[85] Y. Takagaki and K. H. Ploog, Phys. Rev. B **71**, 184439 (2005).

[86] M. Evangelisti et al., Phys. Rev. Lett. **93**, 117202 (2004).

[87] E. Z. Meĭlikhov and R. M. Farzetdinova, J. Exp. Theor. Phys. **98**, 1367 (2004).

[88] W. Wernsdorfer and R. Sessoli, Science **284**, 133 (1999).

[89] Y. Shapira, M. T. Liu, S. Foner, C. E. Dubé, and P. J. Bonitatebus, Phys. Rev. B **59**, 1046 (1999).

[90] Y. Shapira, M. T. Liu, S. Foner, R. J. Howard, and W. H. Armstrong, Phys. Rev. B **63**, 094422 (2001).

[91] D. V. Efremov and R. A. Klemm, 2005.

[92] A. Morello et al., Phys. Rev. Lett. **90**, 017206 (2003).

[93] M. Alcántara Ortigoza, R. A. Klemm, , and T. S. Rahman, Local spin anisotropy in smm, to be published.

[94] M. A. Kayali and W. M. Saslow, Phys. Rev. B **70**, 174404 (2004).

[95] M. Alcántara Ortigoza, R. A. Klemm, and T. S. Rahman, Phys. Rev. B **74**, 226401 (2006).

[96] T. Shibata et al., J. Am. Chem. Soc. **124**, 11989 (2002).

[97] S. Darby, T. Mortimer-Jones, R. Johnston, and C. Roberts, J. Chem. Phys. **116**, 1536 (2002).

[98] E. Cottancin et al., Phys. Rev. B **62**, 5179 (2000).

[99] H. Portales, L. Saviot, and E. Duval, Phys. Rev. B **65**, 165422 (2002).

[100] S. Giorgio and C. Henry, Eur. Phys. J. Appl. Phys. **20**, 23 (2002).

[101] M. Moskovits, I. Srnová-Šloufová, and B. Vlčková, J. Chem. Phys. **116**, 10435 (2002).

[102] H. Tada et al., J. Phys. Chem. B **106**, 8714 (2002).

[103] M. Valden, X. Lai, and D. Goodman, Science **281**, 1647 (1998).

[104] L. Molina and B. Hammer, Phys. Rev. Lett. **90**, 206102 (2003).

[105] M. Haruta, Catal. Today **36**, 153 (1997).

[106] A. Sanchez et al., J. Phys. Chem. **103**, 9573 (1999).

[107] B. Huber, P. Koskinen, H. Häkkinen, and M. Moseler, Nature Mat. **5**, 44 (2006).

[108] S. Lee, C. Fan, T. Wu, and S. Anderson, J. Chem. Phys. **123**, 124710 (2005).

[109] P. Jensen, Rev. Mod. Phys. **71**, 1695 (1999).

[110] C. Ashman and S. Khanna, Phys. Rev. B **55**, 15868 (1997).

[111] K. Kokko, E. Ojala, and K. Mansikka, J. Phys. Condens. Matter **2**, 4587 (1990).

[112] J. Doye and F. Calvo, Phys. Rev. Lett. **86**, 3570 (2001).

[113] K. Terakura, T. Oguchi, T. Morí, and K. Watanabe, Phys. Rev. B **35**, 2169 (1987).

[114] J. Sánchez, J. Stark, and V. Moruzzi, Phys. Rev. B **44**, 5411 (1991).

[115] A. van-de Walle and G. Ceder, Rev. Mod. Phys **74**, 11 (2002).

[116] R. Heid and K. Bohnen, Phys. Rep. **387**, 151 (2003).

[117] R. O. Jones and O. Gunnarson, Rev. Mod. Phys. **61**, 689 (1989).

[118] S. Baroni, A. Dal Corso, S. de Gironcoli, and P. Giannozzi, and others. Complete Quantum-ESPRESSO distribution, version 3.0 (2005), http://www.pwscf.org

[119] D. Vanderbilt, Phys. Rev. B **41**, 7892 (1990).

[120] J. P. Perdew, K. Burke, and M. Ernzerhof, Phys. Rev. Lett. **77**, 3865 (1996).

[121] H. Monkhorst and J. Pack, Phys. Rev. B **13**, 5188 (1976).

[122] S. Baroni, P. Giannozzi, and A. Testa, Phys. Rev. Lett. **58**, 1861 (1987).

[123] P. Giannozzi, S. de Gironcoli, P. Pavone, and S. Baroni, Phys. Rev. B **43**, 7231 (1991).

[124] D. Blat, N. Zein, and V. Zinenko, J. Phys. Condens. Matter **3**, 5515 (1991).

[125] K. Hellwege and A. Hellwege, *Numerical data and functional relationships in science and technology*, volume 2, K. H. Hellwege and A. M. Hellwege; Landolt-Börnstein-Group III Condensed Matter; New Series; Group III; Springer-Verlag; Berlin, 1969.

[126] A. Dal-Corso, Phys. Rev. B **64**, 235118 (2001).

[127] G. Cipriani, D. Loffreda, A. Dal-Corso, S.de-Gironcoli, and S. Baroni, Surf. Sci. **501**, 182 (2002).

[128] R. Ferrando, private communication.

[129] Y. Kong, J. Li, L. Kong, and B. Liu, Phys. Rev. B **72**, 024209 (2005).

[130] J. He et al., Phys. Rev. Lett. **89**, 125507 (2002).

[131] J. He, H. Sheng, P. S. C.L.Chien, and E. Ma, Phys. Rev. Lett. **86**, 2826 (2001).

[132] B. Liu, W. Lai, and Z. Zhang, Adv. Phys. **50**, 367 (2001).

[133] E. Peiner and K. Kopitzki, Nucl. Instrum. Methods Phys. Res. **34**, 173 (1988).

[134] A. Kara and T. Rahman, Surf. Sci. Rep. **56**, 159 (2005).

[135] P. Bogdanoff and B. Fultz, Phys. Rev. B **60**, 3976 (1999).

[136] P. Sharma and N. Singh, Phys. Rev. B **4**, 4636 (1971).

[137] M. Schmidt, R. Kusche, B. von Issendorff, and H. Haberland, Nature **393**, 238 (1998).

[138] U. Hild et al., Phys. Rev. A **57**, 2786 (1998).

[139] K. Kokko, J. Phys. Condens. Matter **11**, 6685 (1999).

[140] G. Wertheim, S. DiCenzo, and D. Buchanan, Phys. Rev. B **33**, 5384 (1986).

[141] S. DiCenzo, P. Citrin, E. Hartford-Jr., and G. Wertheim, Phys. Rev. B **34**, 1343 (1986).

[142] C. Sánchez, E. Leiva, and W.Schmickler, Electrochem. Comm. **5**, 584 (2003).

[143] F. Baletto, C. Mottet, and R. Ferrando, Eur. Phys. J. D **24**, 233 (2003).

[144] T. R. Ralph and M. P. Hogarth, Platinum Metal Rev. **46**, 117 (2002).

[145] S. R. Brankovic, J. X. Wang, and R. R. Adẑić, Electrochem. Solid State Lett. **4**, A217 (2001).

[146] S. R. Brankovic et al., J. Electroanalytical Chem. **524-525**, 231 (2002).

[147] T. M. Chang and E. A. Carter, J. Phys. Chem. **99**, 7637 (1995).

[148] J. Tersoff, Phys. Rev. Lett. **74**, 434 (1995).

[149] H. Hoster, B. Richter, and R. J. Behm, J. Phys. Chem. B **108**, 14780 (2004).

[150] S. R. Brankovic, J. McBreen, and R. R. Adẑić, J. Electroanalytical Chem. **523**, 99 (2001).

[151] B. Du and Y. Y. Tong, J. Phys. Chem. B Lett. **109**, 17775 (2005).

[152] M. T. Kopper, T. E. Shubina, and R. A. van Santen, J. Phys. Chem. B **106**, 686 (2002).

[153] M. C. Payne, M. P. Teter, D. C. Allan, T. A. Arias, and J. D. Joannopoulos, Rev. Mod. Phys. **64**, 1045 (1992).

[154] S. Baroni et al.

[155] D. Vanderbilt, Phys. Rev. B **41**, 7892 (1990).

[156] W. H. Press, S. A. Teukolsky, W. T. Vetterling, and B. P. Flannery, *Numerical Recipes in Fortran The Art of Scientific Computing*, volume 2nd Ed., Cambridge Cambridge University Press, 1992.

[157] A. Kokalj, Comp. Mater. Sci. **28**, 155 (2003).

[158] P. Morrow et al., J. Vac. Sci. Technol. A **24**, 237 (2006).

[159] M. Gajdos and J. Hafner, Surf. Sci **590**, 117 (2005).

[160] J. C. Tracy, J. Chem. Phys. **56**, 2748 (1972).

[161] S. P. Lewis and A. M. Rappe, Phys. Rev. Lett. **77**, 5241 (1996).

[162] C. Hirschmugl, G. Williams, F. Hoffmann, and Y. Chabal, Phys. Rev. Lett. **65**, 480 (1990).

[163] P. Fouquet, R. A. Olsen, and E. J. Baerends, J. Chem. Phys. **119**, 509 (2003).

[164] S. Andersson and J. B. Pendry, Phys. Rev. Lett. **43**, 363 (1979).

[165] C. F. McConville et al., Surf. Sci. **166**, 221 (1986).

[166] J. Stöhr et al., Phys. Rev. Lett. **51**, 2414 (1983).

[167] A. P. Graham et al., J. Chem. Phys. **108**, 7825 (1998).

[168] M. Head-Gordon and J. Tully, J. Phys. Rev. B **46**, 1853 (1992).

[169] A. Föhlisch et al., J. Chem. Phys. **112**, 1946 (2000).

[170] P. S. Bagus and G. Pacchioni, Surf. Sci. **278**, 427 (1992).

[171] K. Hermann, P. S. Bagus, and C. J. Nelin, Phys. Rev. B **35**, 9467 (1987).

[172] J. Casanovas and G. Pacchioni, Chem. Phys. Lett. **259**, 438 (1996).

[173] W. Miller and P. S. Bagus, J. Vac. Sci. Technol. A **3**, 1623 (1985).

[174] K. M. Ho and K. P. Bohnen, Phys. Rev. Lett. **56**, 934 (1986).

[175] S. P. Lewis and A. M. Rappe, J. Chem. Phys. **110**, 4619 (1999).

[176] G. Kresse, A. Gil, and P. Sautet, Phys. Rev. B **68**, 073401 (2003).

[177] S. G. Louie, K. M. Ho, and M. L. Cohen, Phys. Rev. B **19**, 1774 (1979).

[178] M. J. Gillan, J. Phys.: Condens. Matter **1**, 689 (1989).

[179] W. H. Press, S. A. Teukolsky, W. T. Vetterling, and B. P. Flannery, *Numerical Recipes in Fortran The Art of Scientific Computing*, volume 2nd Ed., Cambridge Cambridge University Press, 1992.

[180] R. Heid and K. P. Bohnen, Phys. Rev. B **60**, R3709 (1999).

[181] P. Gianozzi, S. Gironcoli, P. Pavone, and S. Baroni, Phys. Rev. B **43**, 7231 (1991).

[182] A. Khein, D. J. Singh, and C. J. Umrigar, Phys. Rev. B **51**, 4105 (1995).

[183] P. Eckerlin, H. Kandler, and A. Stegherr, *Structure Data of Elements and Intermetallic Phases*, volume 6, K. H. Hellwege and A. M. Hellwege; Landolt-Börnstein-Group III Condensed Matter; New Series; Group III; Springer-Verlag; Berlin, 1971.

[184] W. A. Harrison, *Electronic Structure and the Properties of Solids*, volume 1st Ed., Dover and New York, 1989.

[185] A. D. Corso and A. Baldereschi, Surf. Rev. Lett. **4**, 885 (1997).

[186] T. Rodach, K. P. Bohnen, and K. M. Ho, Surf. Sci. **286**, 66 (1993).

[187] D. M. Lind, F. B. Dunning, G. K. Walters, and H. L. Davis, Phys. Rev. B **35**, 9037 (1987).

[188] G. Blyholder, J. Phys. Chem. **68**, 2772 (1964).

[189] D. J. DeFrees, B. A. Levi, W. J. H. S. K. Pollack, J. S. Binkley, and J. A. Pople, J. Am. Chem. Soc. **101**, 4085 (1979).

[190] L. Peterson and S. Kevan, J. Chem. Phys. **94**, 2281 (1991).

[191] P. H. T. Philipsen, G. te Velde, and E. J. Baerends, Chem. Phys. Lett. **226**, 583 (1994).

[192] R. M. Nicklow, G. Gilat, H. G. Smith, L. J. Rauben-heimer, and M. K. Wilkinson, Phys. Rev. **164**, 922 (1967).

[193] E. C. Svensson, B. N. Brockhouse, , and J. M. Rowe, Phys. Rev. **115**, 619 (1967).

[194] G. Benedek, J. Ellis, N. Luo, A. Reichmuth, and R. Tatarek, Surf. Sci. **325**, 377 (1997).

[195] M. Wuttig, R. Franchy, and H. Ibach, Z. Phys. B **65**, 71 (1986).

[196] Y. Chen et al., Phys. Rev. B **44**, 11394 (1991).

[197] R. Allen, G. Alldredge, and F. de Wette, Phys. Rev. B **4**, 1661 (1971).

[198] V. Chis, B. Hellsing, G. Benedek, M.Bernasconi, and J. P. Toennies, J. Phys.: Condens. Matter **Proceedings of the 12th International Conference on Vibrations at Surfaces** (2007).

[199] H. Cai, N. Zhu, Y. Jiang, P. He, and Y. Fang, Biosens. Bioelectron. **18**, 1311 (2003).

Appendix A

Derivative of a Functional

Let us consider first a function $f(g)$. The the derivative of f with respect to g is

$$\frac{df}{dg} = \lim_{\epsilon \to 0} \frac{f(g+\epsilon) - f(g)}{\epsilon} \tag{A.1}$$

The integral of a function f(x) in the interval $[a, b]$ is

$$\int_a^b f(x)dx = \lim_{n\to\infty} \sum_{i=1}^{n} \frac{b-a}{n} f(x_i). \tag{A.2}$$

where $x_i = a + i\left(\frac{b-a}{n}\right)$.

Now, let us consider a function f of several variables, g_1, g_2, ., g_n. If the variables change from g_1^0, g_2^0, ., g_n^0 by dg_1, dg_2, ., dg_n, respectively. The differential of F, dF, is defined by its partial derivatives as follows,

$$df(g^0) = \frac{\partial f}{\partial g_1}\Big|_{g^0} dg_1 + \frac{\partial f}{\partial g_2}\Big|_{g^0} dg_2 + . + \frac{\partial f}{\partial g_n}\Big|_{g^0} dg_n = \sum_{i=1}^{n} \frac{\partial f}{\partial g_i}\Big|_{g^0} dg_i, \tag{A.3}$$

where $g^0 = \{g_1^0, g_2^0, ..., g_n^0\}$ and

$$\frac{\partial f}{\partial g_i} = \lim_{\epsilon \to 0} \frac{f(g_1, ..., g_i + \epsilon, ..., g_n) - f(g_1, ..., g_i, ..., g_n)}{\epsilon} \tag{A.4}$$

Let $G(x)$ be the continuous limit ($n \to \infty$) of the set of variables $\{g_0, ., g_i, ., g_n\}$, hence,

$f(\{g_0, ., g_i, ., g_n\})$ becomes a functional $F[G(x)]$, whose functional derivative is

$$\frac{\delta F[G(x)]}{\delta G(x')} \equiv \lim_{\lambda \to 0} \frac{F[G(x) + \lambda \delta(x - x')] - F[G(x)]}{\lambda} \tag{A.5}$$

$$= \lim_{\lambda \to 0} \lim_{n \to \infty} \frac{f(g_1, ..., g_i + \lambda \frac{n}{j-k}, ..., g_n) - f(g_1, ..., g_i, ..., g_n)}{\lambda} \tag{A.6}$$

where $\delta(x - x')$ is a Dirac's delta and i, j, and $k \in [1, n]$. Introducing the change of variable $\lambda = \epsilon \frac{(j-k)}{n}$, we obtain

$$\frac{\delta F[G(x)]}{\delta G(x')} = \lim_{n \to \infty} \lim_{\epsilon \to 0} \frac{f(g_1, ..., g_i + \epsilon, ..., g_n) - f(g_1, ..., g_i, ..., g_n)}{\epsilon \frac{(j-k)}{n}} \tag{A.7}$$

$$= \lim_{n \to \infty} \frac{n}{(j-k)} \lim_{\epsilon \to 0} \frac{f(g_1, ..., g_i + \epsilon, ..., g_n) - f(g_1, ..., g_i, ..., g_n)}{\epsilon} \tag{A.8}$$

Using Eq. A.4 we can rewrite Eq. A.8

$$\frac{\delta F[G(x)]}{\delta G(x')} = \lim_{n \to \infty} \frac{n}{(j-k)} \frac{\partial f}{\partial g_i} \tag{A.9}$$

From (A.3), we can write

$$dF[G(x)] = \lim_{n \to \infty} df(g_1, ..., g_i, ..., g_n) = \lim_{n \to \infty} \sum_{i=1}^{n} \frac{\partial f}{\partial g_i} \, dg_i \tag{A.10}$$

$$= \lim_{n \to \infty} \sum_{i=1}^{n} \frac{b-a}{n} \Big(\frac{n}{b-a} \frac{\partial f}{\partial g_i} \, dg_i \Big) = \lim_{n \to \infty} \sum_{i=1}^{n} \frac{b-a}{n} \Big(\frac{n}{j-k} \frac{\partial f}{\partial g_i} \, dg_i \Big) \tag{A.11}$$

Following the definition of the integral in A.2, we obtain

$$dF[G(x)] = \int_a^b dx' \frac{\delta F[G(x)]}{\delta G(x')} \delta G(x') \tag{A.12}$$

where $dg_i \to \delta G(x')$ as $n \to \infty$

Appendix B

Numerical integration of the Landau-Lifshitz equation

We rotate our reference frame at every integration time step in such a way that $\boldsymbol{B}_i^{c,\text{eff}}$ is along the z axis. In this case, we can easily solve the LL equation, Eq. (3.1). For simplicity of notation, we drop the subscripts i and superscripts c, and remember that we are describing the precession of the ith nanomagnet in the cth crystal. We define the axes to describe the magnetization direction of this particular nanomagnet, $\hat{\boldsymbol{M}}$, $\hat{\boldsymbol{\theta}}$, and $\hat{\boldsymbol{\phi}}$, where $\hat{\boldsymbol{\phi}} = \hat{\boldsymbol{M}} \times \hat{\boldsymbol{\theta}}$, and then write

$$\begin{aligned} \boldsymbol{B}^{\text{eff}} &= B_z \hat{\boldsymbol{z}} = B_z(\hat{\boldsymbol{M}} \cos\theta - \hat{\boldsymbol{\theta}} \sin\theta) \\ &= \hat{\boldsymbol{M}} B_M + \hat{\boldsymbol{\theta}} B_\theta. \end{aligned} \tag{B.1}$$

Since the magnitude of the dipole moment M_s is conserved, in spherical coordinates Eq.(1) leads to

$$\begin{aligned} \frac{d\hat{\boldsymbol{M}}}{dt} &= \hat{\boldsymbol{\theta}} \frac{d\theta}{dt} + \hat{\boldsymbol{\phi}} \sin\theta \frac{d\phi}{dt} \\ &= \hat{\boldsymbol{\theta}} \alpha B_\theta + \hat{\boldsymbol{\phi}} \gamma B_\theta. \end{aligned} \tag{B.2}$$

Finally, from

$$\frac{d\theta}{dt} = = -\alpha |\boldsymbol{B}^{\text{eff}}| \sin\theta, \tag{B.3}$$

$$\frac{d\phi}{dt} = -\gamma |\boldsymbol{B}^{\text{eff}}|, \tag{B.4}$$

we obtain for a very small time interval dt,

$$\phi(t_0 + dt) \approx \phi(t_0) - \gamma |\boldsymbol{B}^{\text{eff}}(t_0)| dt, \tag{B.5}$$

$$\theta(t_0 + dt) \approx \theta(t_0) - \alpha |\boldsymbol{B}^{\text{eff}}(t_0)| \sin[\theta(t_0)] dt. \tag{B.6}$$

These equations were used in our numerical calculations. In order to relate the angles to measurable quantities, however, we note that it is possible to integrate Eqs. (B.3) and (B.4) exactly, obtaining

$$\theta(t) = \cos^{-1}\Big[\tanh\Big(\tanh^{-1}(\cos[\theta(t_0)] + \alpha \int_{t_0}^{t} d\tau |\boldsymbol{B}^{\text{eff}}(\tau)|\Big)\Big], \tag{B.7}$$

$$\phi(t) = \phi(t_0) - \gamma \int_{t_0}^{t} d\tau |\boldsymbol{B}^{\text{eff}}(\tau)|, \tag{B.8}$$

which is equivalent to that obtained using a somewhat different technique.[44] We note that by expanding Eqs. (B.7) and (B.8) to leading order in dt, we recover Eqs. (B.6) and (B.5), respectively.

However, these more general forms for $\theta(t)$ and $\phi(t)$ lead to a more physical interpretation of our method. Since the dimensionless magnetization components along and perpendicular to $\boldsymbol{B}^{\text{eff}}$ are $M_z = \cos\theta$, $M_x = \sin\theta\cos\phi$, and $M_y = \sin\theta\sin\phi$, we have

$$M_z(t) = \tanh\Big(\tanh^{-1}[M_z(t_0)] + \alpha \int_{t_0}^{t} d\tau |\boldsymbol{B}^{\text{eff}}(\tau)|\Big), \tag{B.9}$$

$$M_x(t) = \sqrt{1 - [M_z(t)]^2}\cos[\phi(t)], \tag{B.10}$$

and

$$M_y(t) = \sqrt{1 - [M_z(t)]^2}\sin[\phi(t)]. \tag{B.11}$$

Independent of the coordinates, we must assure that (for the ith nanomagnet in the cth configuration) $\boldsymbol{M}$ changes its direction smoothly, in order to obtain a reliable calculation

for the overall $\overrightarrow{\mathcal{M}}$. Since each component of $\boldsymbol{M}$ cannot change dramatically, we must therefore require $\theta \ll 2\pi$ and $\phi \ll 2\pi$. These restrictions then require us to set the time integration step width dt sufficiently small. If for example, γ/α were on the order of 10^{+11} and $|\boldsymbol{B}^{\text{eff}}|$ were in the range $10^{-3} - 10^{-2}$ T, we would require $dt < 10^{-11}$ s. For sweep rate $\frac{\Delta B}{\Delta t} \approx 10^{-2}$T/s, where $\Delta t = N_t dt \approx 10^{-4}$ s, N_t must be on the order of 10^7. Since we would need to recalculate the direction of the magnetization of each nanomagnet N_t times in each ΔB step, this would be a significant challenge with present day computers.

One thing we can do to make our calculations feasible for the sweep rates used in SMM studies is to set α extremely small, say $\frac{\alpha}{\gamma} \lesssim 10^{-10}$, although such small α values have not been reported in experiments. Otherwise, to study much larger but perhaps more reasonable α values, we would have to use much faster sweep rates, as in KS.[94]